Search for jet interactions with quark-gluon plasma

A Dissertation Presented

by

Chin-Hao Chen

to

The Graduate School

in Partial Fulfillment of the

Requirements

for the Degree of

Doctor of Philosophy

in

Physics

Stony Brook University

August 2011

Stony Brook University

The Graduate School

Chin-Hao Chen

We, the dissertation committee for the above candidate for the **Doctor of Philosophy** degree, hereby recommend acceptance of this dissertation.

Professor Barbara V. Jacak , Thesis Advisor
Department of Physics and Astronomy

Professor Edward Shuryak, Chairman of the defense committee
Department of Physics

Professor Robert L. McCarthy
Department of Physics and Astronomy

Dr. David Morrison, Outside member
Department of Physics, Brookhaven National Laboratory

This dissertation is accepted by the Graduate School.

Lawrence Martin
Dean of the Graduate School

Abstract of the Dissertation

Search for jet interactions with quark-gluon plasma

by

Chin-Hao Chen

Doctor of Philosophy

in

Physics

Stony Brook University

2011

A hot, dense QCD medium is created in heavy ion collisions at the Relativistic Heavy Ion Collider at Brookhaven National Laboratory. This new type of matter is opaque to energetic partons, which suffer a strong energy loss in the medium. Two particle correlations are a powerful tool to study the jet properties in the medium and provide information about the energy loss mechanism and jet-medium interactions. When triggering on high p_T particles, the away-side shape depends strongly on the p_T of the associated particles.

In this analysis, we present the inclusive photon-hadron two particle azimuthal correlations measured in Au+Au collisions at $\sqrt{s_{NN}}$ = 200 GeV by PHENIX experiment. In order to study jet-medium interactions, we focus on intermediate p_T, and subtract particle pairs from the underlying event. Jet-like correlations appear modified in central Au+Au compared to p+p, in both the trigger and opposing jet. The trigger jet is elongated in pseudorapidity (the "ridge"), while the opposing jet shows a double peak

structure ("head" and "shoulder"). We decompose the structures in $\Delta\eta$ and $\Delta\phi$ to disentangle contributions from the medium and the punch-through and trigger jets. Upon correcting the underlying event for elliptic flow, the ridge is observed for associated particle p_T below 3 GeV/c; it is broad in rapidity and narrow in $\Delta\phi$. The away side correlated particle yield is enhanced in central collisions. The yield of particles in the shoulder grows with centrality while the away side punch-through jet is suppressed. Remarkably, the ridge closely resembles the shoulder in the centrality dependence of particle yield and spectra.

There has been great debate about the origin of the ridge and shoulder. A favored explanation is that the structure is due to features of the collective flow of particles in the underlying event, particularly the fluctuation-driven triangular flow, quantified by the third Fourier component, v_3. We measure higher order Fourier harmonics in two ways, and use the results to give the shape of particle correlations in the underlying event. We decompose the power spectrum for the medium and for jets measured in p+p collisions.

When including the higher harmonics of the collective flow (v_3, v_4) in the shape of the underlying events in two particle correlations, the ridge and shoulder no longer exist after subtraction. The jet function in Au+Au looks like p+p in which the away side jet is suppressed and broadened. There is also a pedestal-like structure in the jet function. Since the higher harmonics only change the shape of the underlying background, the pedestal is simply the redistribution of the ridge and shoulder particle yields.

In conclusion, when jets pass through the medium, the away side jet is suppressed and the shape is broadened. This also brings out extra particles with spectra slightly harder than the medium, but softer than jet fragments. These are probably from the jet-medium interaction.

To my parents.

Contents

List of Figures

List of Tables

Acknowledgements

PhD is a long journey, without help from people around me, this task will not be able to finish.

The first person I would like to thank is my thesis adviser, Prof. Barbara Jacak. Over the years, she always gave me useful suggestions and insightful comments on my work. All these point me to a clearer direction of analysis direction and sharper physics messages.

I would also like to thank Justin Frantz, who was a post-doc in the group during my first few years in group. With Justin's help, I can start my analysis rather smoothly, from a person who never wrote codes to be able to finish a big analysis.

People from the heavy ion group in Stony Brook always gave me all the supports. Professors Tom Hemmick, Axel Drees, and Abhay Deshpande all gave me helpful comments during my always never-ending presentations in group meetings.

Friends in the group are always fun to be with. I would like to thank Megan, who always listens to my complaints patiently. She also helps me corrects most of the English problems in most of my proceedings, which makes my writing much smoother. I'd like to thank Ali, she patiently read through this long thesis and gave me suggestions on English and physics messages.

Over the years, friends here and in Taiwan all give me all kinds of encouragement, either from email, instant messaging, or even Facebook. With all of you, even though I am working alone, I know I have a lot of friends surrounding me.

At the end, I would like to thank my parents. They just wait me patiently at home and give me support through phone calls and emails. The process is a bit long, but finally all this become fruitful. Without their understanding and support, I probably can not finish the study.

Part I

Introduction

Chapter 1

Physics Introduction and Motivation

1.1 Quantum Chromodynamics

All stable matter in the current universe consists of protons and neutrons. Protons and neutrons combined together form all the elements we see today. In the viewpoint of the Standard Model of particle physics, protons and neutrons are not the fundamental building blocks. Instead, quarks and gluons are the most fundamental building blocks. Protons and neutrons are baryons, which consist of three quarks. There are six kinds of quarks: up (u), down (d), strange (s), charm (c), bottom (b), and top (t). Quarks have color, which is a quantum number: red (R), green (G), and blue (B). The interaction between quarks is mediated by exchanging gluons. The theory used to describe quark and gluons is called Quantum Chromodynamics (QCD).

The strength of the interaction between quarks is described by the coupling constant of the strong interaction, α_s. The strength of α_s as a function of the momentum transfer Q of the interaction is shown in Fig. 1.1 [1, 2]. The horizontal axis, Q, is the momentum exchange. Large Q is reached in the high energy interactions. At the same time, high energy also corresponds to short distance.

The running of the coupling constant, α_s, with increasing Q leads to the phenomenon of "asymptotic freedom" [3, 4]. When the two quarks are separated by a large distance, the interaction strength will increase and tend to bring the two quarks together, which lowers the energy of the system. This is why quarks are bound inside the nucleon.

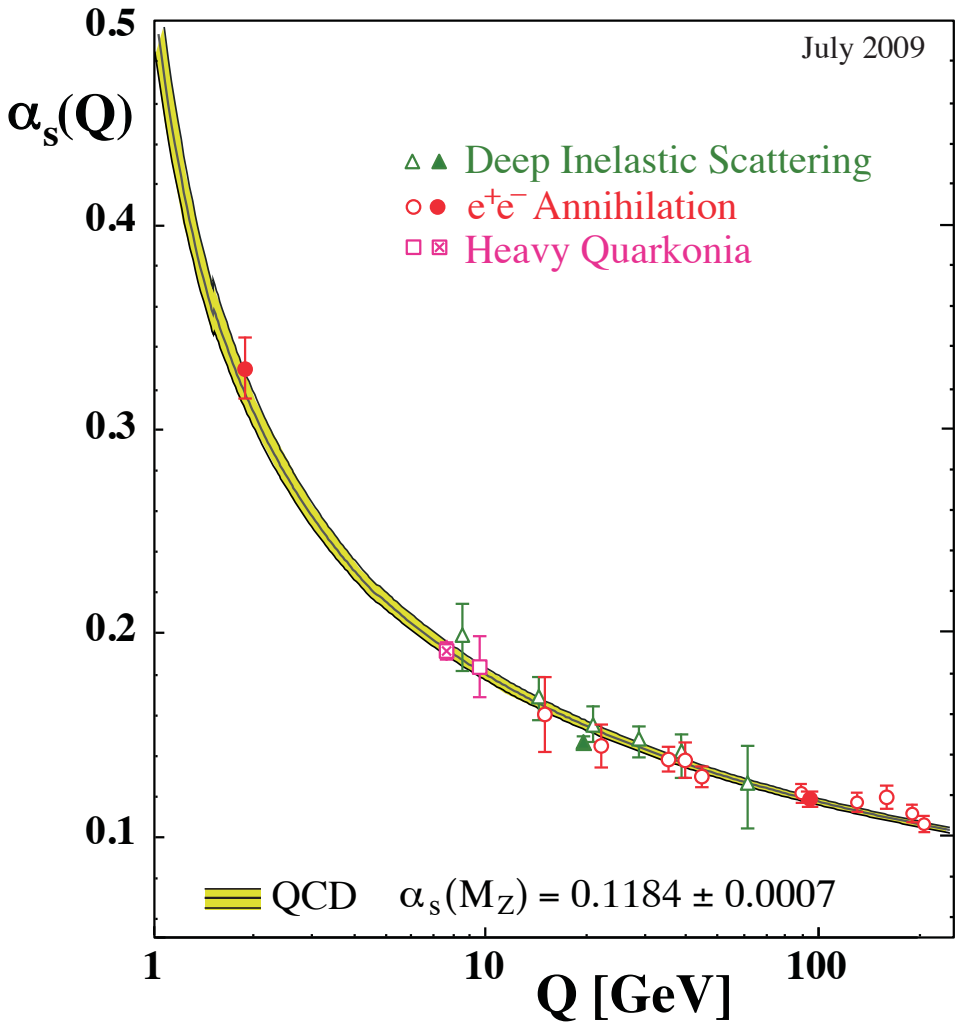

Figure 1.1: The QCD coupling constant, α_s, as a function of the momentum exchange, Q. [1, 2].

1.2 The Quark Gluon Plasma

From Fig. 1.1, we know that the strength of the interaction between quarks varies with energy. One might imagine that when the coupling constant α_s is small enough, quarks and gluons can move freely as gas.

There are two methods to achieve the condition of small α_s. First, one can "heat up" the nucleon. Second, one can reduce the distance between the quarks, i.e. "squeeze" the nucleon. Both of these conditions can be achieved by colliding large nuclei at relativistic energies.

QCD predicts a phase transition from hadronic gas to quark gluon plasma. The calculation from lattice QCD, as shown in Fig. 1.2 [5], indicates that with the sudden increase of the ratio of the energy density over the fourth power of the temperature, there is indeed a phase transition when temperature, T, is around the critical temperature, T_c. The high temperature phase is known as "quark gluon plasma" [6, 7]

When T $< T_C$, and by assuming $c = \hbar = k_B = 1$, the energy density, ε (in units of [GeV]^4), of the massless pion gas is given in Eq. 1.1

$$\varepsilon_\pi = 3d_\pi \frac{\pi^2}{90} T^4 \tag{1.1}$$

where d_π is the number of degrees of freedom of the pions, which can be calculated by Eq. 1.2:

$$d_\pi = N_f^2 - 1 \tag{1.2}$$

In the quark–gluon–plasma phase, we have the energy density

$$\varepsilon_{QGP} = 3d_{QGP} \frac{\pi^2}{90} T^4 + B \tag{1.3}$$

Here, d_{QGP} is number of degrees of freedom in the QGP phase, which is written as

$$d_{QGP} = d_g + \frac{7}{8} d_q \tag{1.4}$$

$$d_g = 2_{spin} \times (N_C^2 - 1) \tag{1.5}$$

$$d_q = 2_{spin} \times 2_{q\bar{q}} \times N_C \times N_f \tag{1.6}$$

For the case of three flavors of massless quarks, or $N_f = 3$, we have $d_\pi = 3^2 - 1 = 8$, $d_g = 2 \times (3^2 - 1) = 16$, $d_q = 2 \times 2 \times 3 \times 3 = 36$, $d_{QGP} = 8 + \frac{7}{8} \times 36 = 47.5$

So from hadron gas phase to QGP phase, there is a sudden increase of the number of degrees of freedom. This corresponds to the jump of ε/T^4 at T = T_C in Fig. 1.2. Note that this is true for all three assumptions of quark type and masses in the figure.

For T > T_C, ε/T^4 is approximately constant with temperature. In Fig. 1.2, the values of the Stefan–Boltzmann limit, ε_{SB}/T^4, which corresponds to the noninteracting gluon gas are also plotted. But ε/T^4 is below the energy density by assuming that the quarks and gluons are non–interacting, or the Boltzmann limit by about 20%. This is a hint that within quark–gluon plasma, quarks and gluons are strongly interacting.

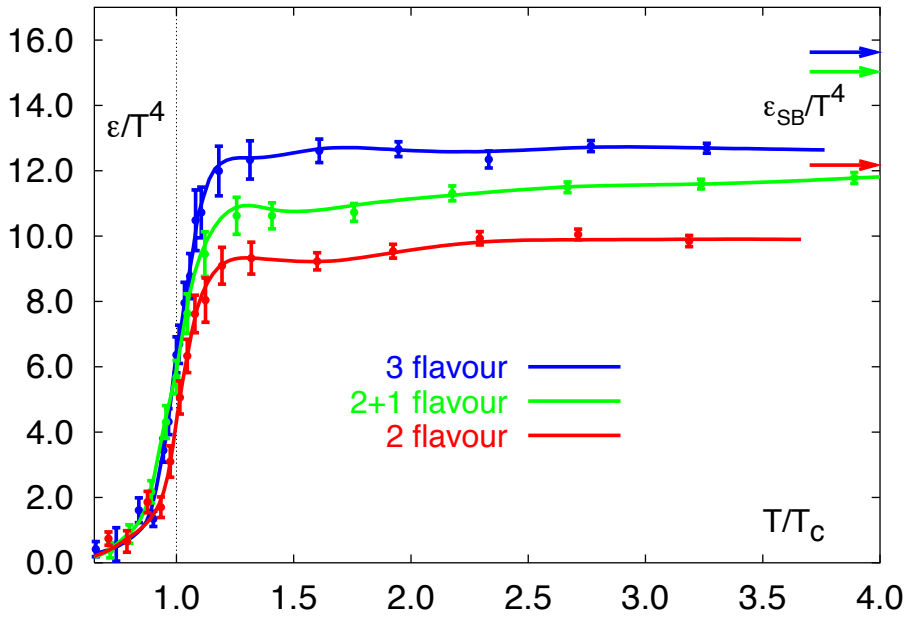

Figure 1.2: Energy density, ε, as a function of temperature from Lattice QCD calculations [5]. ε_{SB}/T^4 represent the Stefan–Boltzmann limit of non–interacting gluon gas.

1.3 Different Stages of Heavy Ion Collisions

The Relativistic Heavy Ion Collider (RHIC) at Brookhaven National Lab (BNL) collides gold nuclei and various nucleus systems at center of mass energies up to 200 GeV per nucleon pair ($\sqrt{s_{NN}}$ = 200 GeV). Under this condition,

a new type of hot dense matter, the quark–gluon plasma, is created. Here we describe the time history of the such collisions.

1.3.1 $0 < \tau < \tau_0$, Pre–equilibrium and Thermalization

At the top RHIC energy, due to Lorentz contraction, the nuclei will have longitudinal size $2R/\gamma_{cm}$, where $\gamma_{cm} = E_{cm}/2m_n \approx (200\text{ GeV})/(2\text{ GeV}) \approx 100$, where m_n is the nucleon mass. When the two nuclei collide, the resulting collisions of constituent partons produce many semi–hard partons, or mini–jets. A lot of entropy is also created at this stage. These mini–jets form an equilibrated parton plasma and interact with other partons. At this stage, local thermalization is achieved and creates the hydrodynamical initial conditions for $\tau > \tau_0$, where τ_0 is the characteristic proper time of the QGP. At RHIC, τ_0 is less than 1 fm/c under perfect fluid hydrodynamical models [8].

1.3.2 $\tau_0 < \tau < \tau_f$, Hydrodynamical Evolution and Freeze–out

At τ_0 the system is in local thermal equilibrium. The system expands both in longitudinal and transverse directions. This longitudinal expansion expands the volume of the system in the z direction (beam direction) and this process cools the system and decreases its temperature. When the temperature drops to the critical temperature, T_c, there will be a phase transition, the system will become a hot dense hadronic gas. After the phase transition, the hadron gas will still expand.

The relativistic hydrodynamics is used to describe the expansion of the system from the time that local thermal equilibrium is reached in the quark gluon plasma phase until freeze-out. . Under relativistic hydrodynamics, the energy–momentum is conserved, that is

$$\partial_\mu \langle T^{\mu\nu} \rangle = 0, \tag{1.7}$$

where $T^{\mu\nu}$ is the energy–momentum tensor of the fluid. By assuming the system is a perfect fluid, the system can be described by the energy density, ε, and the local pressure, P, and $T^{\mu\nu}$ can be written as

$$T^{\mu\nu}(x) = \begin{bmatrix} \varepsilon(x) & 0 & 0 & 0 \\ 0 & P(x) & 0 & 0 \\ 0 & 0 & P(x) & 0 \\ 0 & 0 & 0 & P(x) \end{bmatrix} \tag{1.8}$$

The energy density, ε and the local pressure, p, are linked by Equation of State, EoS. In the fluid, the number of baryon number is also conserved, where

$$\partial_\mu \langle j_B^\mu \rangle = 0. \tag{1.9}$$

and the baryon number current, j_B^μ is given by

$$j_B^\mu(x) = n_B(x) u^\mu(x) \tag{1.10}$$

where $n_B(x)$ is the baryon number density and $u^\mu(x)$ is the four velocity. The evolution can then be calculated with proper initial conditions, starting from $\tau = \tau_0$ to $\tau = \tau_f$, which is the freeze–out time, when the hadronic plasma stop interacting with each other.

1.3.3 $\tau_f < \tau$, Freeze–out and Post–equilibrium

The freeze-out of the hadronic plasma happens at this stage, $\tau_f < \tau$. The freeze–out is defined as the time when local thermalization breaks, or the mean free path of the hadrons is larger than the size of the system. The hadron gas is still very dense and the hadrons still interact with each other in a non-equilibrium way, where the system may be described by transport theories, such as UrQMD [9, 10].

1.4 Definition of terms

In order to describe the heavy ion collisions, we define the following terms.

The transverse momentum of the particle, p_T, is the momentum in the transverse plane, which is perpendicular to the beam direction. The magnitude of p_T is $p_T = |p| \sin\theta$, where p is the magnitude of the momentum, θ is the angle between the direction of the particle and the beam direction. The longitudinal momentum, p_L is the momentum along the beam direction.

The direction of the particle is typically described by two angles, the azimuthal angle on the transverse plane ϕ and θ. The pseudorapidity, η, is defined as $\eta = -\ln[\tan(\theta/2)]$, which is often used to describe the direction of θ.

The geometry in heavy ion collisions is an important parameter, which describe how much matter is colliding. The geometry for head–on collisions and peripheral collisions is very different. When two nuclei collide, the nucleons which participate the collision are called "participants", and the rest are called "spectators". These participants form the collision region. The collisions are

typically categorized by different "centralities". Centrality is defined by the total nucei-nuclei inelastic cross section, which is strongly correlated with the number of participants. The 5% events which have the largest total inelastic cross section is defined as centrality of 0–5%. Experimentally, centrality is determined by the density of the charged particles produced from the collisions, or $dN^{ch}/d\eta$. For example, the centrality of 0–5% events produces the highest multiplicity.

The Glauber model [11] has been used to calculate the colliding geometry. The Glauber model breaks the nuclei–nuclei interaction into numerous nucleon–nucleon interactions. It assumes the nucleon moves in a straight trajectory and not deflected after the collisions. Using the Glauber model, we can calculate N_{part} for the average number of participant of the certain centrality. The number of binary collisions, N_{coll}, is also used extensively to describe heavy ion collisions. When the two nuclei collide, many partons within colliding region may interact. The total number of binary collisions is N_{coll}, which can also be estimated with a Glauber simulation, is used extensively to describe heavy ion collisions.

1.5 General Properties of QGP

At RHIC, quark–gluon plasma is routinely created in central Au+Au collisions. There are several interesting properties of this new type of matter.

1.5.1 Temperature of QGP

One of the most important questions at RHIC has been the temperature achieved. This has been determined by measuring thermal radiation. When the quark–gluon plasma is produced in heavy ion collisions, it will radiate thermal photons. By measuring the spectra of the thermal photons, we can extract the temperature of the medium.

The hot quark–gluon–plasma should emit thermal radiation [12]. The partonic phase is predicted to be the major source of direct photons at $1 < p_T < 3$ GeV/c [13]. But at this p_T range, there is a large background of hadronic decay photons. Since any photon production can also emit virtual photons, which decay to electron-positron pairs, one can measure the virtual photons via di-electrons and require the mass of the electron pairs to be larger than the mass of the π^0 to suppress the background. PHENIX has measured low mass di–electrons in Au+Au and p+p collisions ($m_{e^+e^-} < 0.3$ GeV/c^2 and $1 < p_T < 5$ GeV/c) [14]. After removing all the pairs from hadronic

decays, an excess yield is found in central Au+Au collisions compared to p+p, as shown in Fig. 1.3.

Fig. 1.3 shows the spectra of di–electrons which come from direct photons in p+p and Au+Au collisions. The spectrum from p+p is fit with a modified power law function $[A_{pp}(1 + p_T^2/b)^{-n}]$. The same di–electron spectrum is measured in different centralities in Au+Au and compared with the p+p spectrum scaled by the total inelastic nucleus-nucleus cross section. An excess yield for $1 < p_T < 3$ GeV/c is found in central Au+Au collisions compared to p+p collisions. The low mass di–electrons excess in Au+Au is interpreted as coming from thermal radiation photons produced by the QGP. After fitting an exponential function, $Ae^{-p_T/T}$, to the spectra of the excess, or the thermal radiation, the slope of the exponential is extracted as $T = 221 \pm 19^{stat} \pm 19^{syst}$ MeV. If the source of this excess is from thermal photons, the inverse slope, T, is related to the initial temperature, T_{ini}. From hydrodynamical calculations, T_{ini} is 1.5 to 3 times T due to the space–time evolution of the fireball [15]. Several hydrodynamical calculations can reproduce the central Au+Au data within a factor of 2. These models were $T_{ini} = 300-600$ MeV, depending upon which thermalization time is assumed. τ_0 ranges from $\tau_0 = 0.6-1.5$ fm/c [16]. From Lattice QCD, the critical temperature of the QGP is $T_C = 170$ MeV [17]. This measurement clearly shows that the T_{ini} of the medium is above T_C, and we have indeed created quark–gluon plasma at RHIC.

1.5.2 Elliptic Flow

When two nuclei collide, most of the time the two nuclei do not overlap completely, but producing an almond–shape collision zone as shown in Fig. 1.4. The plane which connects the centers of the two nuclei is called the reaction plane, along the direction of the impact parameter of the collision. In order to study the spatial anisotropy of the collision, the particle azimuthal distribution, $dN/d(\phi - \psi)$ is measured with respect with the direction of the reaction plane (ψ). This distribution can be expanded as a Fourier series in ϕ:

$$\frac{dN}{d(\phi - \psi)} \propto 1 + \sum (2v_n \cos n(\phi - \psi_n)) \tag{1.11}$$

The elliptic flow, defined as the second Fourier coefficient, v_2, of the particle distribution, is used to describe the azimuthal anisotropy of the particle distribution and has been measured extensively and precisely [18, 19]. Fig. 1.5 shows the v_2 and v_4 measured with respect to the second event plane, ψ_2, which is the estimation of the reaction plane. If the QGP is weakly interacting, the whole system should expand like a gas, i. e. homogeneously in all directions.

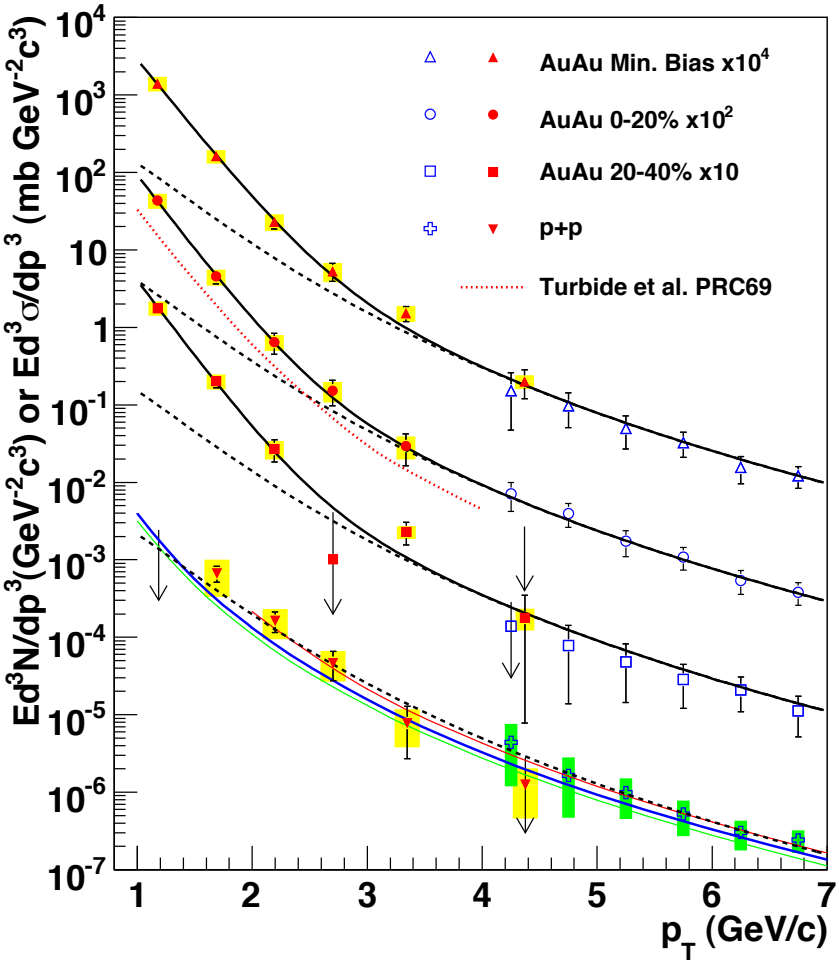

Figure 1.3: Invariant cross section (p+p) and invariant yield (Au+Au) of direct photons as a function of p_T. The black dashed curves are modified power law fit to the p+p data, scaled by the number of binary collisions. Low mass di–electrons excess in Au+Au shows the thermal radiation of QGP [14].

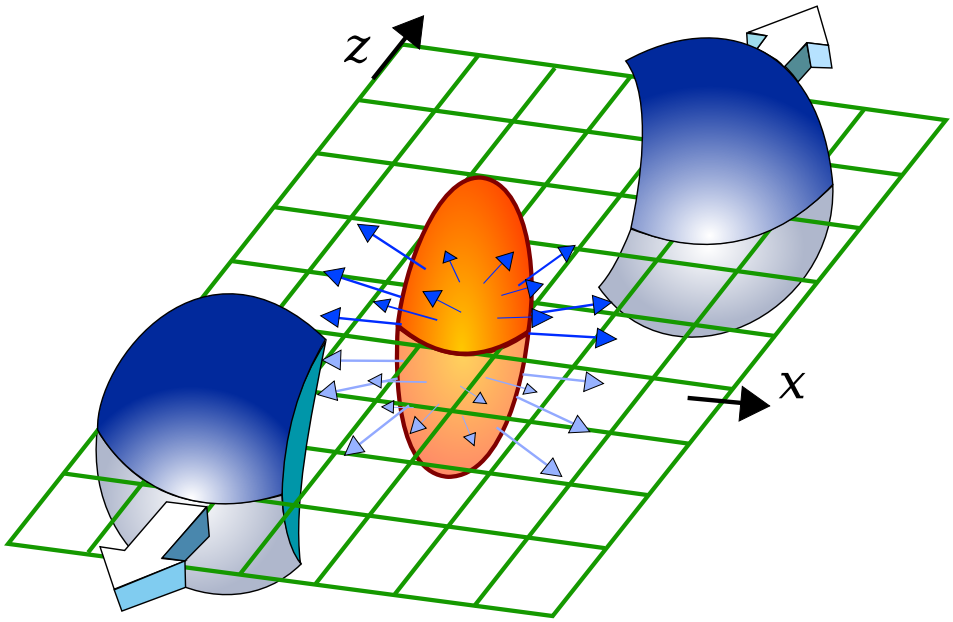

Figure 1.4: When two nuclei collide, the colliding area has an almond–like shape.

The large, non zero v_2 in Fig. 1.5 indicates that the medium expands faster in the short direction (in–plane) and slower in the long direction (out–of–plane). This implies that the system has a large pressure gradient and experiences a fast thermalization. More detail will be discussed in Chapter 5 and Chapter 7.

1.5.3 Jet Quenching

When two nucleon collides, the partons within the nucleon may experience a hard scattering, which can be illustrated by Fig. 1.6. Fig. 1.6 shows two high energy protons collides (blue arrows). During the collision, the partons in protons scattered into a pair of high energy partons (red arrows) in opposite directions due to conservation of momentum. The partons will hadronized into high p_T particles or fragment into a shower of particles in a small cone in ϕ and η, which become jets. In heavy ion collisions, this hard process happened in the early stage of the collisions, so the energetic parton will interact with the quark gluon plasma before the parton leaves the medium.

A key question in heavy ion collisions is how partons interact with the medium as they travel through. By measuring the properties of the high p_T

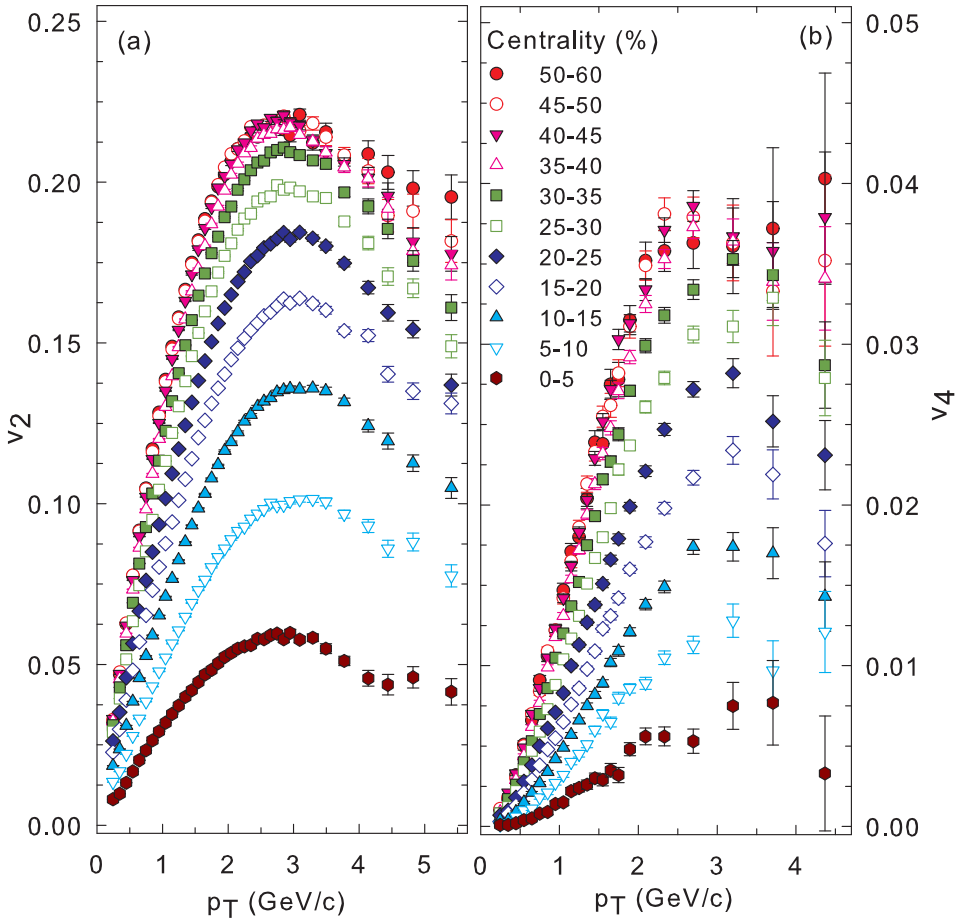

Figure 1.5: v_2 and v_4 of inclusive charged hadrons vs p_T of several centralities [19].

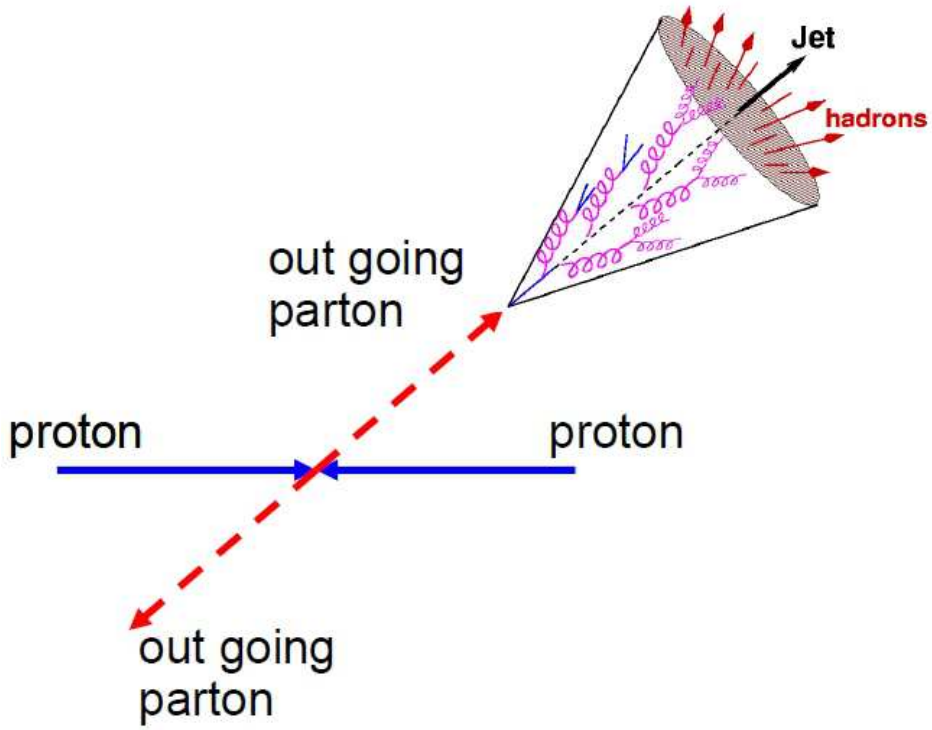

Figure 1.6: Hard scattering in a proton-proton collision. The blue arrows are the direction of the protons, the red arrows are the outgoing partons. The upper out going parton fragment into a jet.

particles or jets, we can have the information on how partons interact with the quark gluon plasma. By measuring the spectra of high p_T hadrons in Au+Au collisions, where the medium is produced, and comparing with p+p collisions, where there is no medium produced, we can gain some insight on the effect of the medium and the study the parton–medium interaction.

One parameter used to quantify the medium modification is the medium modification factor, R_{AA}, which is defined in Eq. 1.12:

$$R_{AA}(p_T) = \frac{d^2N^{AuAu}/dp_Td\eta}{N_{coll}d^2N^{pp}/dp_Td\eta} \tag{1.12}$$

where $d^2N/dp_Td\eta$ is the particle spectrum in Au+Au/p+p, and N_{coll} is the total number of binary nucleon–nucleon collisions in Au+Au at a given impact parameter. If the particle spectrum in Au+Au is simply given by the spectrum in p+p scaled by the number of binary collisions in Au+Au, then R_{AA} should be equal to 1. $R_{AA} < 1$ means the spectra in Au+Au are suppressed compared to p+p.

PHENIX has measured π^0 spectra in Au+Au in various centralities and over a broad range of p_T [20]. The results are shown in Fig. 1.7. At $p_T > 5$ GeV/c, R_{AA} in central collisions (0–10%) is about 0.2, which means the π^0 yields are suppressed by a factor of 5. This is strong evidence that partons are losing energy in the medium. At higher p_T, R_{AA} shows a weak rising trend with p_T. In Fig. 1.8, R_{AA} at $p_T > 5$ GeV/c shows that R_{AA} decreases with increasing N_{part} , i.e. from peripheral to central collisions. This indicates that larger medium volume results in larger suppression.

1.6 Two Particle Correlations

1.6.1 The Definition of Two Particle Correlations

In section 1.5.3, hard partons will produce high p_T particles or jets. Jets are important probes for understanding the properties of the quark–gluon plasma. But in central heavy ion collisions, thousands of particles are produced, making jet finding an extremely difficult task. Instead, two particle azimuthal correlations are used as a proxy for studying properties of jets in the medium.

This correlation function method is a statistical method. When high energy partons are produced in hard collisions, they will fragment into hadrons which are confined to a cone of small $\Delta\phi$ and $\Delta\eta$. So the idea of two particle correlations is to select a high p_T particle, known as the trigger particle, which is supposed to be fragment from a jet and roughly in the direction of the

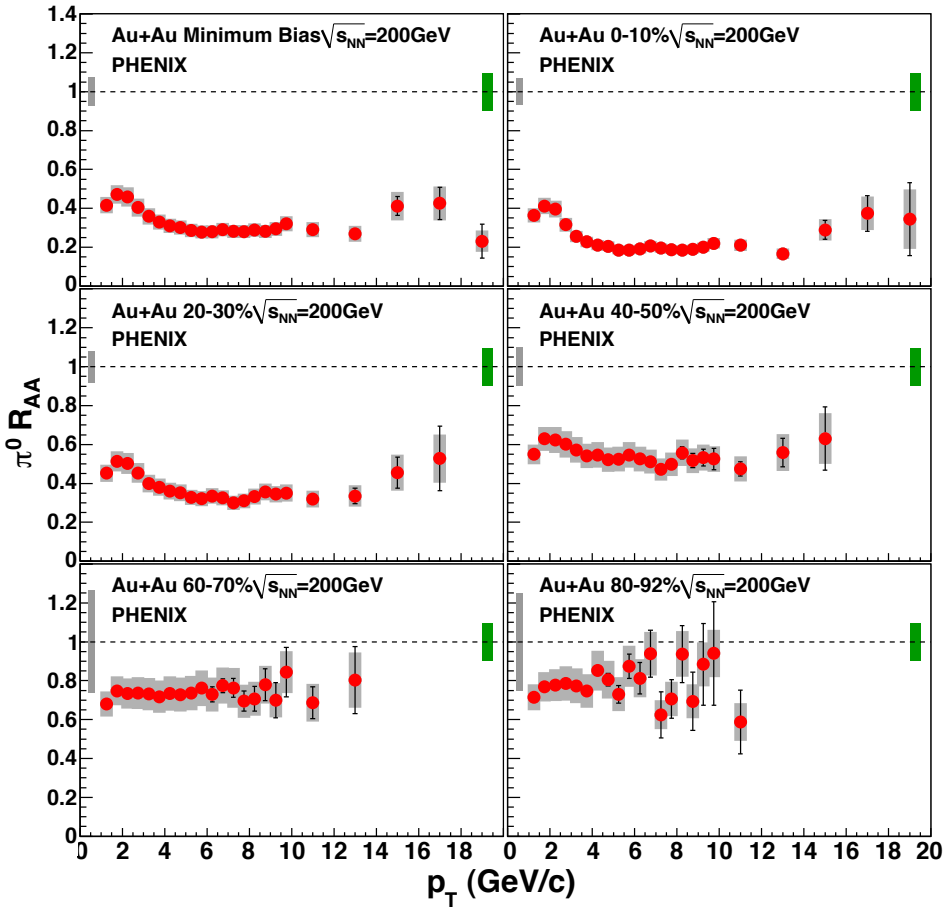

Figure 1.7: R_{AA} of π^0 vs p_T in various centralities [20]. Error bars are statistical and p_T–uncorrelated errors, boxes around the points indicate p_T–correlated errors. Single box around $R_{AA} = 1$ on the left is the error due to N_{coll}, whereas the single box on the right is the overall normalization error of the p+p reference spectrum.

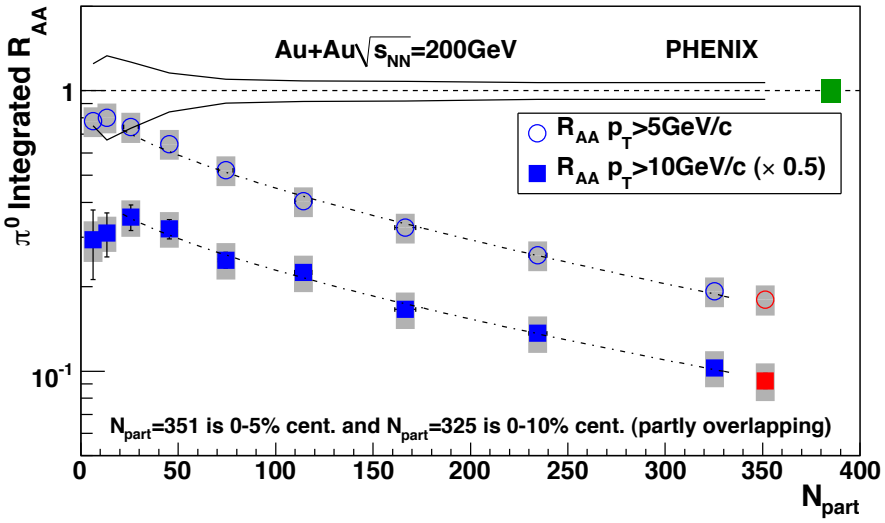

Figure 1.8: Integrated R_{AA} of π^0 vs N_{part} [20]. The error bars/bands are the same as in Fig. 1.7. The two lines at unity show the errors on N_{coll}. The last two points correspond to partially overlapping centrality bins.

original parton, and correlate it with lower p_T associated particles in ϕ or η. When the difference of the azimuthal angle between the trigger and associated particles is $\Delta\phi \approx 0$, this means both particles arise from the same jet. If $\Delta\phi \approx \pi$, this means the associated particle is coming from the opposing jet, which is due to the conservation of momentum.

A typical correlation function looks like Fig. 1.9. The two particle correlation function has two components: contributions from jet pairs and the underlying event. In order to extract the jet signal, we need to determine the level and also the shape of the underlying event background. After the shape and the level are properly determined, we can subtract the background and extract the jet signal. The peak at $\Delta\phi = 0$ is the near side jet, which is the jet where the trigger particle comes from. The peak at $\Delta\phi = \pi$ is the opposing jet. So with two particle correlations, we can study the properties of dijet events.

1.6.2 High p_T Correlations

PHENIX has performed extensive studies with two–particle correlations [21, 22, 23]. Fig. 1.10 [24] shows the π^0–h correlations in central Au+Au collisions. When both particles are at high p_T, such as 7–9 GeV/c for trigger particles, and 3–5 GeV/c associated particles, the near side ($\Delta\phi = 0$) in

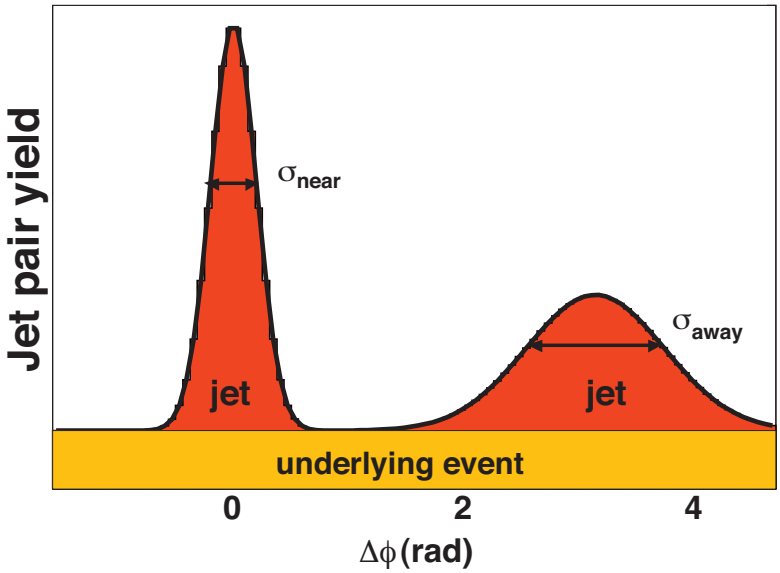

Figure 1.9: A typical correlation function. On the top are the jet pairs. On the bottom are uncorrelated underlying backgrounds

Au+Au (solid circles) behaves just like p+p (empty circles). However, on the away side ($\Delta\phi = \pi$), the jet like structure in Au+Au is significantly suppressed compared to p+p, which is the evidence of jet quenching inside the medium at high p_T. At low partner p_T, the away side jet is modified and comprises more particle than p+p, as shown in upper left of Fig. 1.10. From the two–particle correlations shown in Fig. 1.10, we can clearly see that the suppression happens when the away side jet goes through the medium. By selecting the high p_T particle as the trigger, we are biased by selecting the trigger particles emitted from the surface, which suffers no or little energy loss. But the opposing jet had to pass through the medium, suffering energy loss. This is known as trigger bias.

1.6.3 Intermediate p_T correlations

When the momentum range for both trigger and associated particles is decreased, interesting features comes out. Fig. 1.11 [22] shows the jet function from Au+Au and Cu+Cu collisions at various centralities. In peripheral collisions, the correlation function looks like unmodified p+p, which shows peaks at 0 and π in $\Delta\phi$. In central collisions, we see the near side peak still sits at $\Delta\phi = 0$, but on the away side, instead of a peak at $\Delta\phi = \pi$, a dip appears,

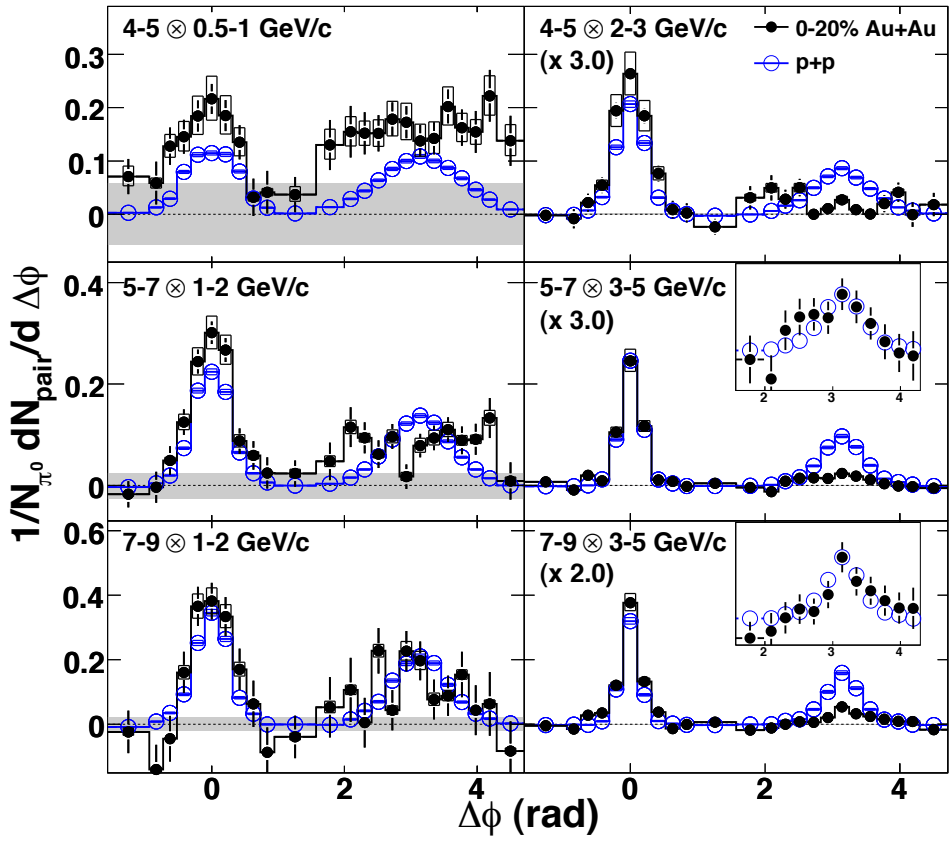

Figure 1.10: High p_T π^0–h jet correlations in central Au+Au (0–20%) in solid circles and p+p collisions in empty circles [24].

and the peak shifts to $\Delta\phi \approx 2$. This strange shape is found in different colliding systems and different colliding energies, and the position of the away side peak, parametrized by D, is the same for all $N_{part} > 50$. Fig. 1.12 [22] summarizes the centrality dependence of the peak location, D, at the bottom, and shows how the peak shape changes on the top panel.

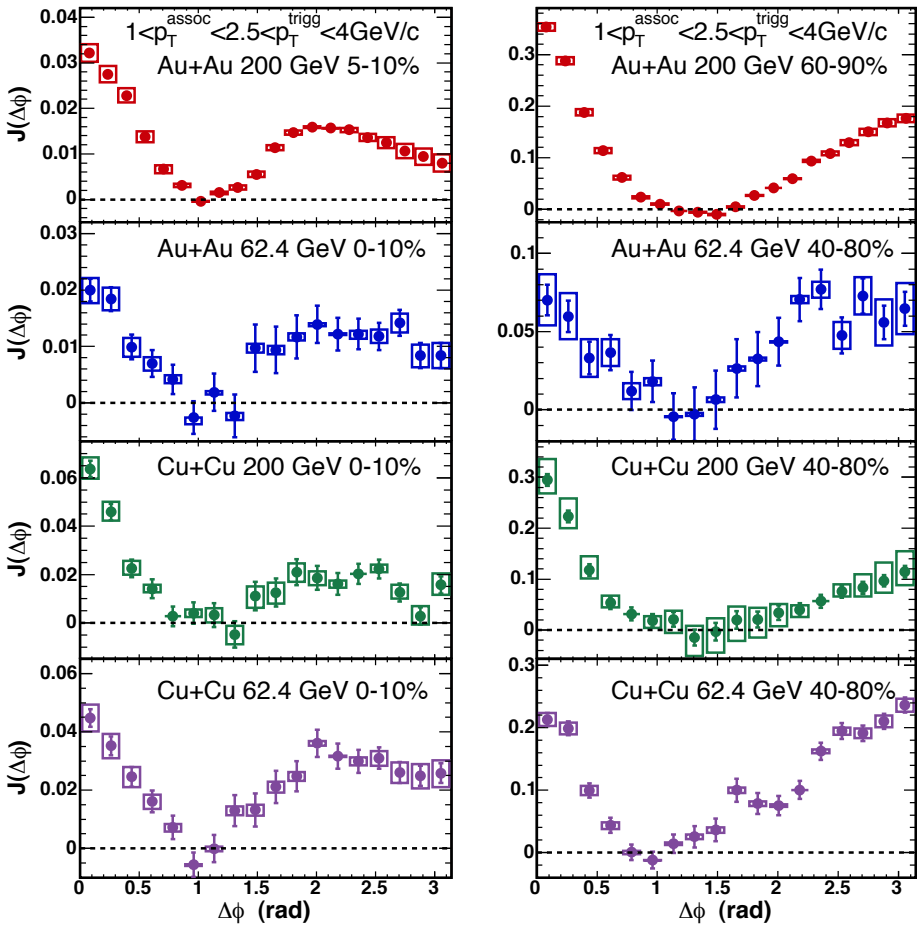

Figure 1.11: Shape of jet functions in Au+Au/Cu+Cu at $\sqrt{S_{NN}}$ = 200/62.4 GeV/c at intermediate p_T [22].

1.6.4 $\Delta\eta$–$\Delta\phi$ Correlations

The near side correlation is found to be modified not only in $\Delta\phi$, but also in $\Delta\eta$, which is defined as $\eta = -\ln[\tan(\theta/2)]$, where θ is relative to the beam direction. Fig. 1.13(a) shows the $\Delta\eta$–$\Delta\phi$ correlation function in central

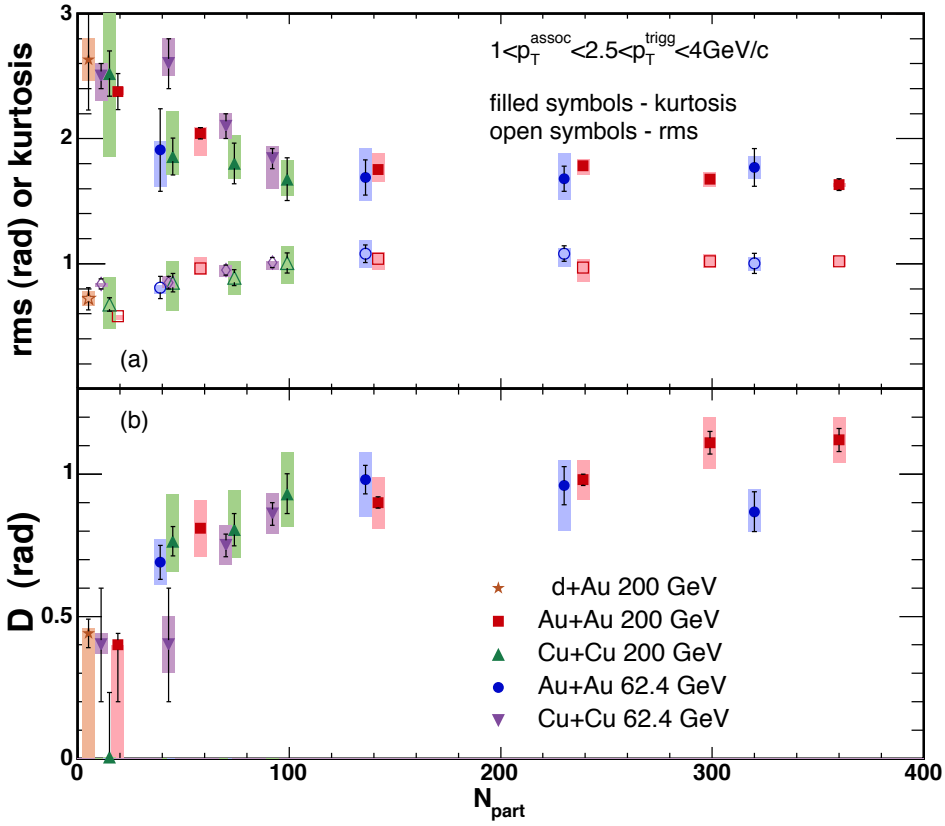

Figure 1.12: Shape parameters of jet functions in various colliding systems and energies [22]. RMS(kurtosis) in top panel describes the shape of the away side jet function. D in the bottom panel is used to describe the peak position of the double peak structure.

Au+Au collisions [25]. Fig. 1.13(b), shows the correlation function in d+Au collisions, which has no medium effect. Fig. 1.13(a) shows the correlation in central Au+Au, an enhancement along $\Delta\eta$ at $\Delta\phi \approx 0$ is found. This structure is called the "ridge". Together with the cone–like double–peak structure, we see that the effect of the quark gluon plasma in Au+Au upon jets appears to be very complicated.

1.7 Motivation for this Dissertation Work

We have performed a study aimed at understanding the exotic structures seen in two particle correlations in heavy ion events, and using properties of the ridge in the near side and the double peak structure in the away side to learn about the response of the quark–gluon plasma to the energy deposited by fast partons. There are several theoretical interpretations of each structure, but very few theoretical approaches treat them together. Furthermore, new insights from higher harmonic Fourier coefficients have also triggered new interpretations of these structures.

In this analysis, we study the two particle correlations with the PHENIX detector. First, we extract the ridge and shoulder from the correlation functions and study their centrality and p_T dependence. In order to understand the effects of higher harmonics of the collective flow of the underlying event, we measured the higher harmonics in correlations of two low p_T particles, as well as for intermediate p_T particles, and applied those measurements back to the background subtraction in the correlation analysis to gain new insights into the source of the ridge and shoulder structures.

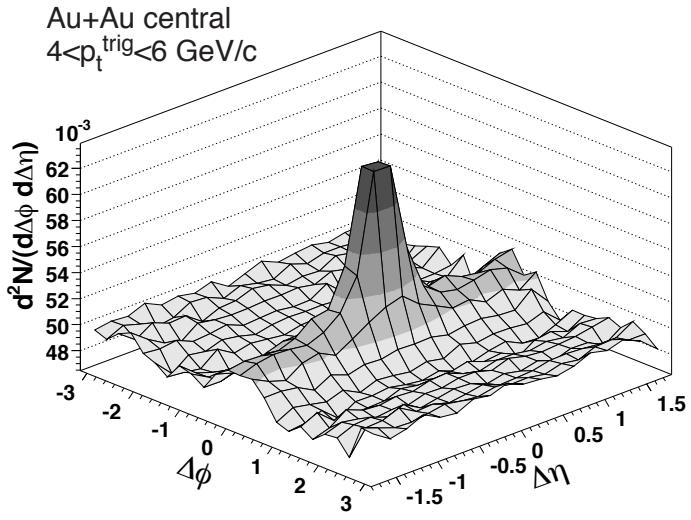

(a) Au+Au (0–12%)

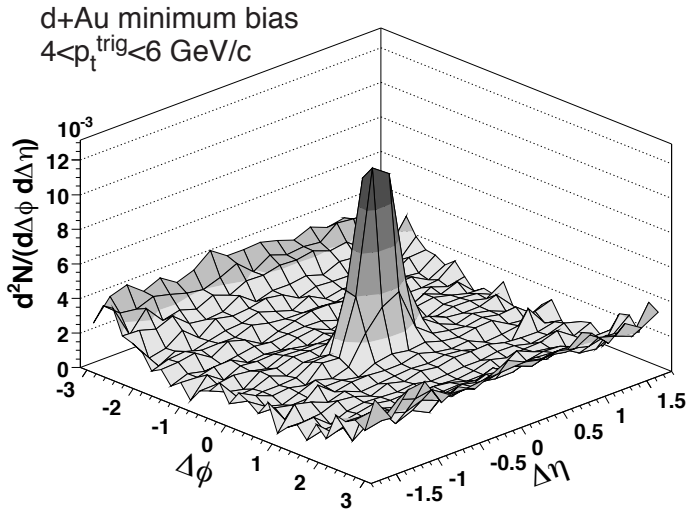

(b) d+Au

Figure 1.13: $\Delta\eta$–$\Delta\phi$ jet function in central Au+Au (a) and in d+Au (b) [25].

Chapter 2

Experiment

2.1 RHIC

From Sec. 1.2, we know the way to create the quark-gluon plasma is to create a high temperature, a high energy density state. In order to achieve this condition, the Relativistic Heavy Ion Collider (RHIC) at Brookhaven National Laboratory (BNL) [26] accelerates gold nuclei up to 100 GeV per nucleon along its 2.4 mile ring. When full energy gold nuclei collide, violent interactions happen. RHIC is capable of colliding various species of nuclei, such as gold, copper, deuteron and proton at various energies. This makes RHIC a unique machine to explore the properties of the QGP under different conditions.

These collisions are detected and have been studied extensively by four dedicated experiments: BRAHMS [27], PHOBOS [28], STAR [29] and PHENIX [30].

With good particle identification capability, the Broad RAnge Hadron Magnetic Spectrometers Experiment (BRAHMS) [27] at RHIC was designed to measure the identified charged hadron spectra over wide pseudorapidity and transverse momentum range. It consisted of two spectrometers. One at mid–rapidity was used to measure the low p_T particles. The other was at forward rapidity, where the momentum of the particle will be boosted. BRAHMS experiment started taking data in 2000 and completed data taking in 2006.

The PHOBOS experiment [28] focused on the global properties of the quark–gluon plasma, such as particle multiplicity distributions and elliptic flow. PHOBOS placed silicon sensors around the interaction region, allowing precision measurements of the number of particles and their angular distributions in Au+Au collisions. The PHOBOS experiment started taking data in 2000 and completed data taking in 2005.

The Solenoidal Tracker at RHIC (STAR) [29] is a multi purpose particle detector. The main component of STAR is a time projection chamber (TPC) which can track thousands of particles at the same time. The full azimuth and

large rapidity acceptance makes it ideal for studying the hadron production and global properties of the medium.

2.2 PHENIX

PHENIX stands for "Pioneering High Energy Nuclear Interaction Experiment" [30]. This is the detector used for this work. Fig. 2.1 is the detector configuration of PHENIX during the 2004 run. There are two central arm spectrometers covering pseudorapidity $|\eta| < 0.35$. These are optimized for measuring electrons, photons and charged hadrons with great precision. There are also two muon spectrometers ($1.0 < |\eta| < 2.2$), which measure muons in the forward direction. The analysis in this thesis was done with the central arms only.

The coordinate system of the PHENIX follows the right hand rule. Z axis is along the beam direction, where the north is the positive direction. X direction points to west.

2.2.1 Beam Beam Counter and Zero Degree Calorimeter

The Beam–Beam counter (BBC) [31] is used to determine the position and timing of collisions. The BBC has two identical counters, sitting 144 cm away from the collision center in the north and south direction, called BBCN and BBCS. The position of the two BBC is equivalent to $3.0 < |\eta| < 3.9$. Each BBC consist of two arrays of Cerenkov detectors with quartz radiators and photomultiplier readouts. Each counter has 64 mesh–dynode photo–multiplier tubes with 1–inch diameter, with a 3 cm quartz radiator on the head of the photo–multiplier tube.

When a collision happens, prompt hadrons hit the BBCs. The average hit time at BBCN and BBCS are T_N and T_S. The average arrival time, T_0, is calculated for both BBCs. This is used as the start time of the Time of Flight and to determine the collision vertex position along the beam direction (ZVTX).

The Zero Degree Calorimeter (ZDC) [32] is used to measure the neutrons emitted during the heavy ion collisions. ZDCs are located on both sides of the beam direction and is 18 m away from the collision point. The coincidence between both ZDCs can be used to for selection of minimum bias events. The information can also be used to determine the vertex of the collision.

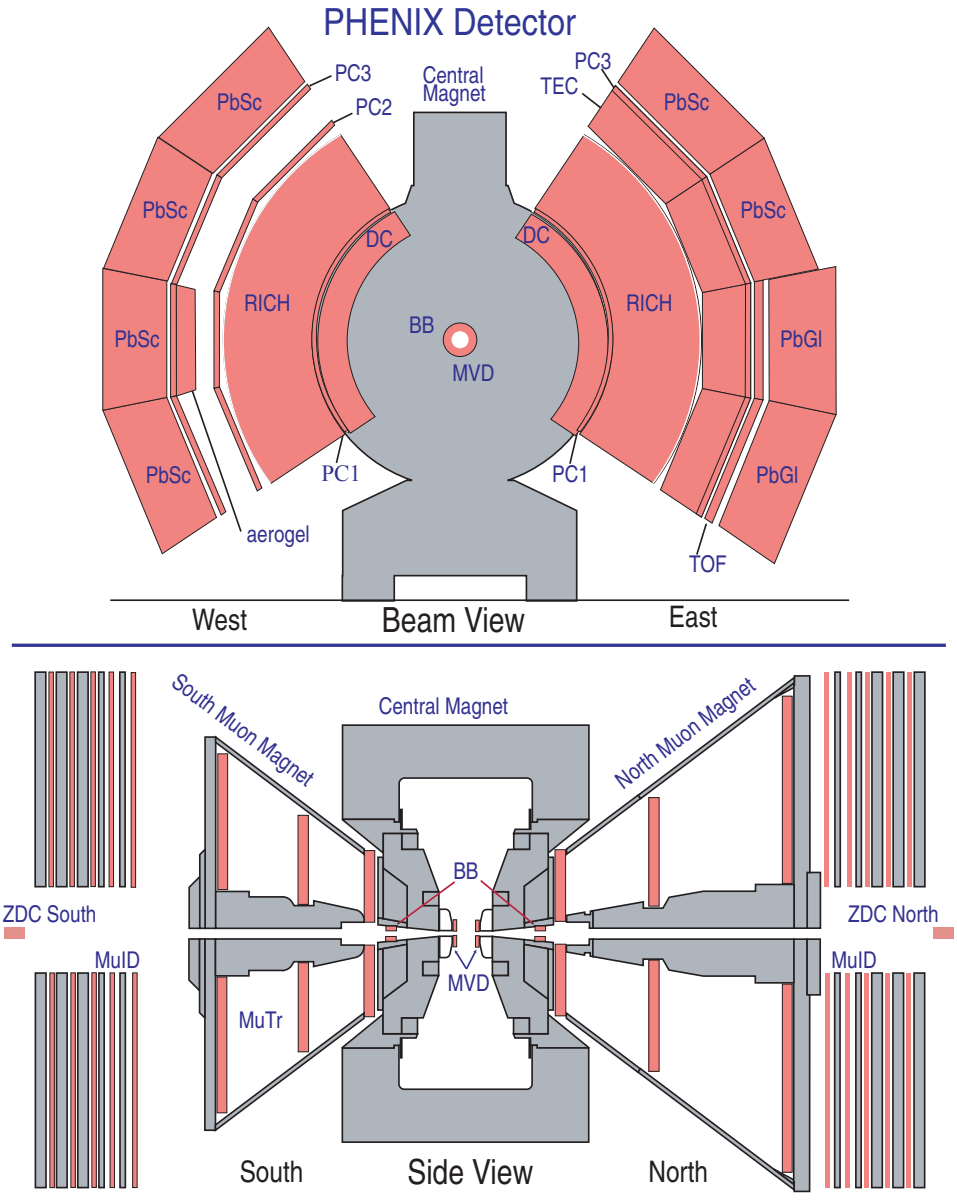

Figure 2.1: Detector configuration of PHENIX during the 2004 run. Top panel: Beam view; bottom panel: side view.

When combined with the ZDC, the centrality of the events can be determined. The centrality describes the degree of the overlap of the two nuclei during the collision. When the two nuclei collide, the nucleons which do not participate in the collision, or the spectators, will travel at forward angles. The the neutrons will be detected by ZDC. For central collisions, most nucleons participate the collision, which means the number of spectators seen at ZDC is small but the number of prompt hadrons hitting the BBC is large. By sorting the events with respect to the response of BBC and ZDC, the centrality of the events can be determined, as shown in Fig. 2.2

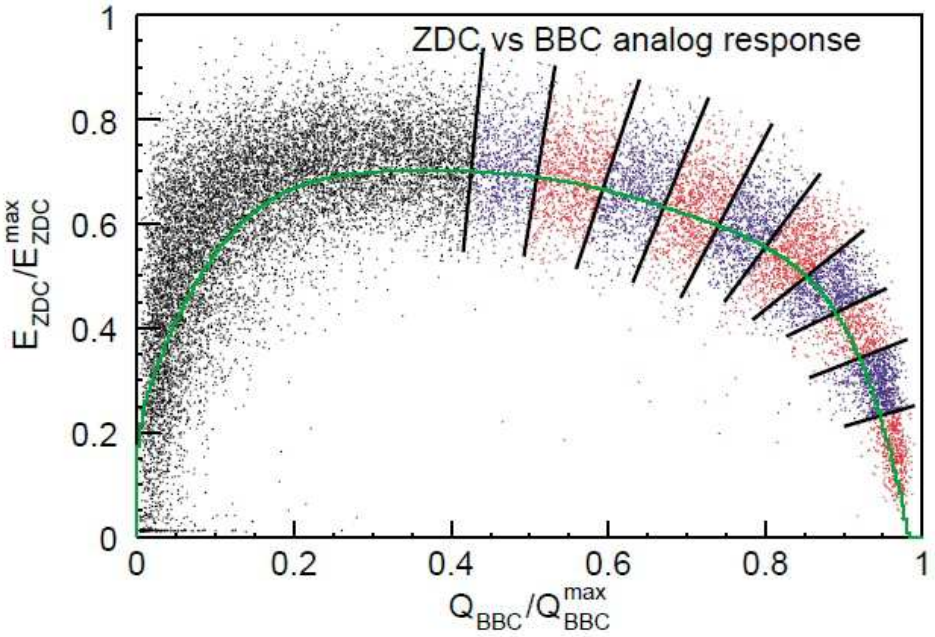

Figure 2.2: The correlations between the charge sum in BBC and the energy in ZDC. The line contains the centrality interval of 5%. The far right region corresponds to centrality 0–5%.

2.2.2 Central Arm

There are two central spectrometers in PHENIX [33], each covers $|\eta| < 0.35$ and $\pi/2$ in azimuth, as shown in Fig. 2.1. The central arms have layers of different detectors. The innermost layer is the drift chamber (DC) [33], followed by the first layer of pad chamber (PC) [33]. After the pad chamber is the ring imaging Cherenkov detector (RICH). In east arm, there are time

expansion chambers (TEC) and time of flight detector (TOF) in the east arm. In the west arm, there is a second layer of pad chamber behind the RICH. There are also aerogel detectors in the west arm. Both arms contain an additional layer of pad chambers in front of the electromagnetic calorimeters (EMCAL), which is the last layer of the central arm [34]. In this analysis, we use the information from the drift chamber and pad chamber to determine the direction and the momentum of the charged tracks and the electromagnetic calorimeter to measure the energy of the photon.

Drift Chamber

The Drift chambers [33] are two cylindrically shaped detectors with titanium frames, as shown in Fig. 2.3. The locations of the drift chambers are between 2 to 2.4 m radially from the beam pipe. They extend 2m in the beam direction in both the east and west arm. Each drift chamber is used to measure the position of the tracks in the r–ϕ direction and to provide p_T information.

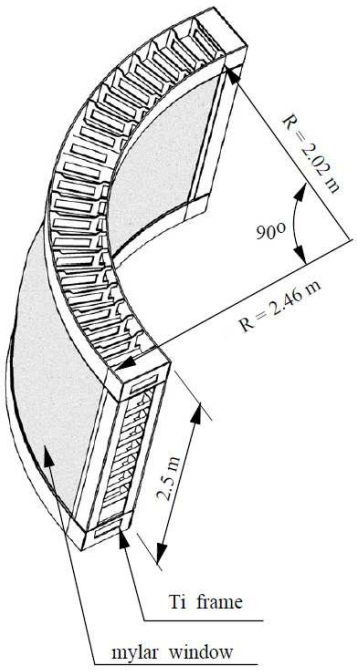

Figure 2.3: Shape of the frame of the drift chamber [33].

The draft chamber is filled with a mixture of 50% argon and 50% ethane gas. When charged tracks pass through the drift chamber, the gas mixture

will be ionized. The ionized electrons drift to the anode wires of the drift chamber and are registered as a hit. Each drift chamber has 20 sectors in the ϕ direction. The layout of a sector is shown in the left hand side of Fig. 2.4. Each sector covers 4.5^0 in ϕ and has 6 wire modules, which are X1, U1, V1, X2, U2 and V2. Each wire module has 4 anode planes, and has 4 cathode planes.

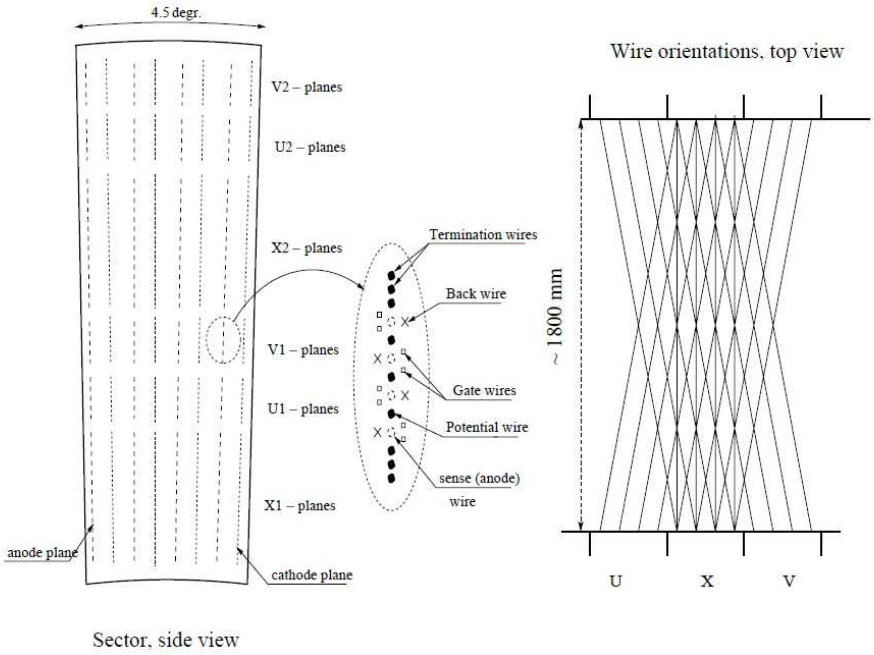

Figure 2.4: Left: Wire position of a sector of drift chamber. Also a map of the anode plane. Right: Top view of the wire orientation in a sector [33].

The position of the wire modules are the following. The wires in the X1 and X2 modules lie parallel to the beam direction, and are used to measure the direction in r–ϕ precisely. The U1, U2, V1, V2 modules are inclined by 6^0 degrees with respect to X the modules, as shown in the right hand side of Fig. 2.4, in order to give information about the z position of the track. For each anode plane, there are 12 anode wires in the X modules and 4 anode wires in the U and V modules each. In total, there are about 6500 anode wires in each of the drift chamber arms.

The set up of each anode plane is shown in the right hand side of Fig. 2.4. The anode wires are separated by potential wires which have strong electric potentials. The potential wires separate the sensitive region of each anode wire. Each anode wire is surrounded by two gate wires and a back wire on

the opposite side of the gate wires. Gate wires help focus the ionized electrons drift toward the anode wire and minimize the track sample length to about 3 mm. The back wire has a relatively lower potential, which terminates most of the drift lines from the other direction and can avoid the left–right ambiguity.

To reconstruct the transverse momentum and direction of the track in the drift chamber, the technique "combinatorial Hough transform" is used. To use this method, one looks for tracks hit both the X1 and X2 plane, then the track can be reconstructed. Those tracks with hits in X1 and X2 modules are plotted in the x–y plane. The polar angle, ϕ, is defined from the center to the intersection of the track with the reference circle with a radius of 220 cm, which is close to the mid–point of the drift chamber. The inclination of the track relative to the intersection is defined as α. All these features are shown in Fig. 2.5. With ϕ and α, the direction of the track is also defined. Since the tracks bend in the magnetic field, the inclination angle, α, is proportional to the inverse of the transverse momentum. With the direction of the track, specified by ϕ and α, the p_T of the track can be determined.

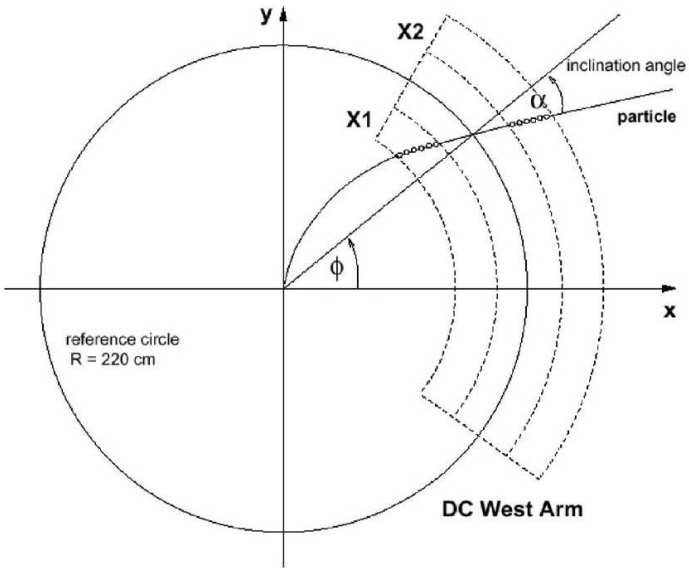

Figure 2.5: Illustration of the Hough transform parameters for drift chamber track reconstruction. The outline shows the drift chamber active volume. The circles represent drift chamber hits along the particle trajectory. [35].

Pad Chamber

The pad chambers (PC) are three layers of multi–wire proportional chambers [33]. The positions of the pad chambers are shown in Fig. 2.1. The first layer of pad chambers (PC1) are located right behind the drift chambers. The second layer of pad chambers (PC2) are in the west arm, behind the RICH detector. The third layer of pad chambers (PC3) are in both arms, in front of the electromagnetic calorimeter. The combined information from DC and PC1 provides the z position information of the track, and gives the direction vectors to the RICH, which is crucial for electron identification. The PC2 and PC3 information is important to reject the particles produced from particle decays, which do not point back to the collision vertex. They also reject conversion electrons after or outside the DC acceptance.

Each pad chamber has a similar structure. The vertical structure of the pad chamber is shown in Fig. 2.6. It consists of a anode layer in the gas chamber and sandwiched by two cathode layers. One of the cathode layers is made of solid copper and the other is finely segmented into pixels. When the charged tracks pass through the chamber, the anode wire will start to avalanche, which causes charge to be induced on the pixels. This signal is read out through the readout electronics.

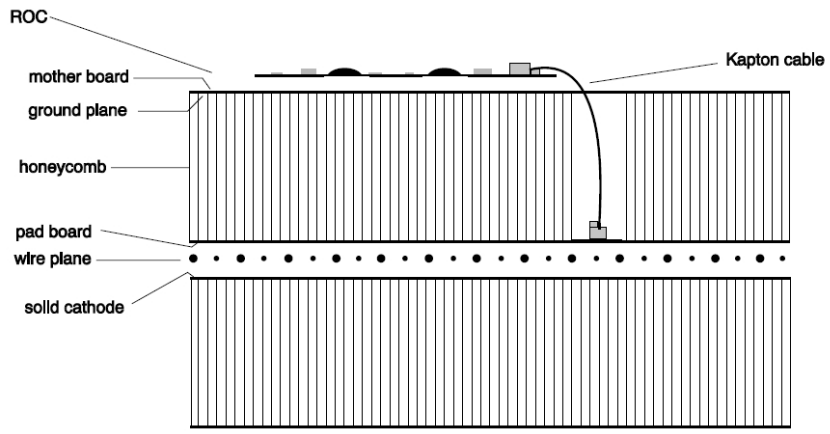

Figure 2.6: Vertical view of the pad chamber [33].

Electromagnetic Calorimeter

Electromagnetic calorimeters (EMCal) are used to measure the energy and the position of photons and electrons. There are eight sectors of EMCal in the

central arms of PHENIX [34]. There are two different kinds of EMCal used in PHENIX. One is lead scintillator (PbSc), which has good timing resolution. The other is lead glass (PbGl), which has better energy resolution. In the west arm, there are four sectors of lead scintillator, while in east arm there are two lead scintillator and two lead glass sectors.

The lead scintillator electromagnetic calorimeter measures the energy by detecting the shower light coming from the deposited energy from the photons or the electrons. Lead scintillator calorimeter is a shashlik detector, which uses layers of lead as absorber and scintillator for calorimetry. When a photon or electron hits the lead absorber, it showers and is detected by the scintillator. The radiation length of lead scintillator is $18X_0$ deep.

Each tower in the PbSc calorimeter contains 66 cells, each consisting of alternating layers of lead and plastic scintillator, with the edges covered with aluminum. Four towers are combined into a module, as shown in Fig. 2.7. In total, there are 15552 towers in the PbSc calorimeter. Every 36 modules will be walled by stainless steel to form a super module. Every 18 super modules are grouped as a sector.

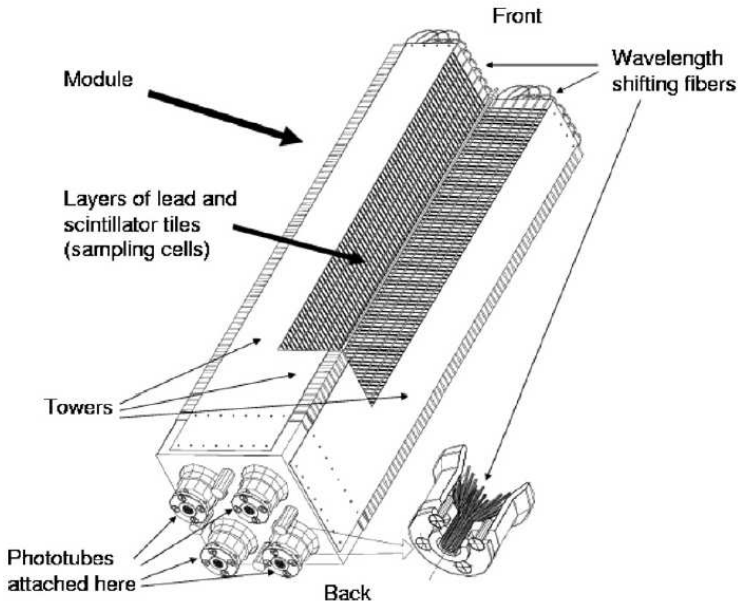

Figure 2.7: The structure of the lead scintillator electromagnetic calorimeter [34].

The lead glass calorimeter is a Cherenkov radiation detector. When photons or electrons pass through the calorimeter, Cherenkov radiation will be

generated and detected. Hadrons with momentum above the Cherenkov threshold also generate Cherenkov radiation, the threshold is 106 MeV/c for pions and 751 MeV/c for protons. Once the momentum of the hadron is below the threshold, the radiation light will be absent.

Each PbGl module is 40mm x 40mm x 400mm in size. A group of 6x4 PbGl Modules is a supermodule. For each sector, it has 16x12 supermodules as shown in Fig. 2.8.

When measuring photons with the calorimeter, we exclude the photon clusters which are identified as hot towers or unresponsive regions of the EMCAL. Each photon cluster also must pass shower shape cuts to remove showers from charged particles. The position information from PC3 is used to ensure that there are no charged particles in the cluster in the calorimeter. Time of flight of the particle is also used to remove neutral particles, such as neutrons.

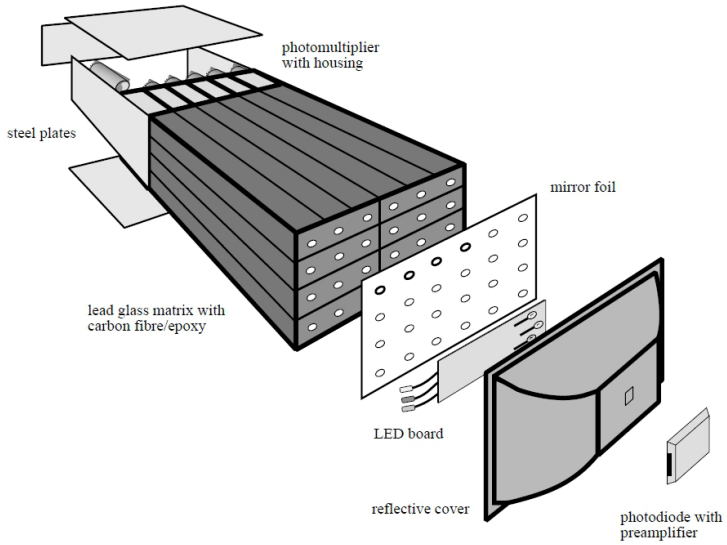

Figure 2.8: The structure of the lead glass calorimeter [34].

Part II

Analysis: correlation function

Chapter 3

Correlation Function

3.1 Introduction

Two particle azimuthal correlations have provided a lot of insight into how jets interact with the quark gluon plasma. In p+p collisions the azimuthal angular difference between two particles, $\Delta\phi$, shows jet fragmentation peaks at $\Delta\phi = 0$ when both particles are from the fragmentation of the same jet, and at $\Delta\phi = \pi$ when the particles arise from a back to back di–jet. In Au+Au collisions, high p_T (p_T >7GeV/c) back–to–back azimuthal correlations are suppressed, while the near side jet remains nearly unmodified from p+p collisions [36, 24]. At intermediate transverse momentum (2< p_T <5GeV/c), in the transition region from soft (hydro) to hard (jet fragment), several new structures have been been observed: the *ridge* [37, 25] and the *shoulder* [21, 22].

There have been several physical pictures proposed to explain the production of the ridge. Jet–medium interactions may result in a momentum kick to particles in the bulk medium, boosting their momentum and producing a correlation with a traversing fast parton [38]. A correlated emission model describes radiation of soft gluons by a parton penetrating the medium; these gluons and their resulting hadronic fragments are boosted by longitudinal flow of the medium [39]. The Glasma model treats the ridge as arising from the flux tube formed early in the collision; expansion of the quark gluon plasma along the longitudinal direction elongates the ridge in η [40]. The shoulder structure has been suggested to arise from passage of a sound wave as the medium responds to shocks deposited by jet energy loss [41, 42, 43]. However there is considerable debate as to whether it is possible to observe the resulting Mach cone–like structure [44, 45].

Until now, analyses of data have typically addressed properties of either the ridge or the shoulder. We address both the modification to the near side and to the away side in the same analysis. Theoretical investigations have

also considered the structures separately. While their origins might in fact be unrelated, they do both appear in the transition region from the low p_T, hydrodynamical region to the high p_T energy loss dominated region. Both phenomena could be sensitive to the same properties of the produced matter, or perhaps even be from related physical processes. Consequently, detailed comparison between the near and away side modifications, particularly their evolution with centrality is of prime interest. In this paper we present systematic data on the centrality and transverse momentum dependence of both the ridge and the shoulder.

3.2 Definition of Correlation Function

Jets are important probes to understand the properties of the quark–gluon plasma. But in central heavy ion collisions, thousands of particles are produced in the final state, making jet finding an extremely difficult task. Instead, two particle azimuthal correlations provide a simpler method to study the properties of jet in the medium.

This correlation function method is a statistical method to study two particle correlations. When jets are produced in hard collisions, they will fragment into high p_T particles which are confined to a small range of azimuthal angle $\Delta\phi$ and pseudorapidity $\Delta\eta$, where $\eta = -ln(tan(\theta/2))$ and θ is the polar angle relative to the beam direction. The size of the jet cone, $R = \sqrt{\Delta\phi^2 + \Delta\eta^2} \approx 0.3$. So the idea of two particle correlations is to select a high p_T particle, known as the trigger particle, presumed to be a jet fragment, and correlate it with lower p_T particles (the partner or associated particle) in ϕ or η. Then the pair distribution is plotted in the difference in azimuthal angle, $\Delta\phi$, and pseudorapidity, $\Delta\eta$, of trigger and associated particles. When the difference of the azimuthal angle between trigger and associated particles, $\Delta\phi \approx 0$, both particles are fragments of the same jet. If $\Delta\phi \approx \pi$, the associated particle comes from the opposing jet. By looking at these correlations, we can study the properties of the near ($\Delta\phi \approx 0$) and away ($\Delta\phi \approx \pi$) side jets statistically.

A typical correlation function looks like Fig. 3.1. The two particle correlation function has contributions from two sources: jet pairs and the underlying event. In order to extract the jet signal, we need to determine the level and also the shape of the underlying event background. After the shape and the level are properly determined, we can subtract out the background and extract the jet signal.

In this analysis, we measure the two particle $\Delta\eta$–$\Delta\phi$ correlations. We select a photon as the trigger particle and a charged hadron as the associated

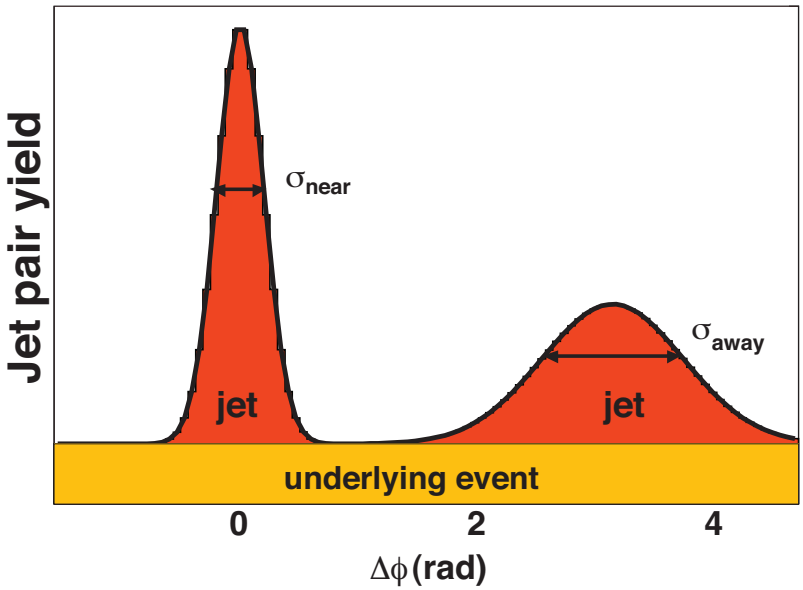

Figure 3.1: A typical correlation function. On the top are the jet pairs. On the bottom are uncorrelated underlying backgrounds

particle, and measure the difference between the trigger and associated particle azimuthal angles and pseudo–rapidities, η. The p_T range of the photons in this analysis is 2–3 GeV/c, which are primarily from the decay of π^0 mesons. This also avoid the low π^0 signal to background ratio of low p_T π^0s due to huge combinatorial background. Using photon as a trigger particle provides the advantage of removing correlations coming from triggering baryons and anti–baryons which have less associated meson yields than associated meson yields in meson triggered collisions in central Au+Au collisions in this p_T range [46]. Due to the geometry of the PHENIX central arms, the acceptance is non uniform in both $\Delta\phi$ and $\Delta\eta$. We use the shape of the mixed event background to correct the $\Delta\phi$ and $\Delta\eta$ acceptance. The idea of event mixing is that by forming pairs with trigger particles from one event and associated particles from another event, the two particles will be totally uncorrelated. Hence, the only effect which will change the shape of the mixed event distribution is the acceptance of the detector. By measuring the mixed event background properly, therefore we can correct for the acceptance in $\Delta\eta$ and $\Delta\phi$.

We define the 2D correlation function, C($\Delta\eta$,$\Delta\phi$), as:

$$C(\Delta\eta, \Delta\phi) = \frac{N^{same}(\Delta\eta, \Delta\phi) \int N^{mixed}(\Delta\eta, \Delta\phi) d\Delta\eta d\Delta\phi}{N^{mixed}(\Delta\eta, \Delta\phi) \int N^{same}(\Delta\eta, \Delta\phi) d\Delta\eta d\Delta\phi} \tag{3.1}$$

where $N^{same}(\Delta\eta,\Delta\phi)$ is for the measured correlated pairs, and $N^{mixed}(\Delta\eta,\Delta\phi)$ is for the pairs from the mixed events.

The resulting C($\Delta\eta$, $\Delta\phi$) is then both $\Delta\eta$ and $\Delta\phi$ acceptance corrected. A typical distribution is shown in Fig. 3.2(a).

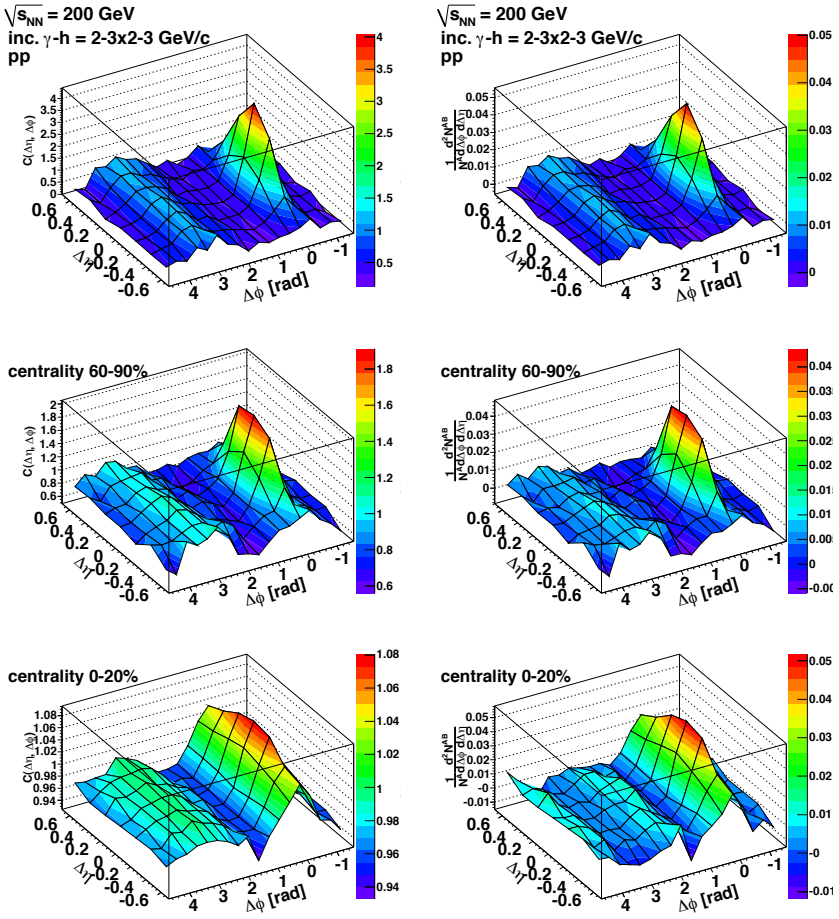

(a) Correlation function (b) after flow subtraction

Figure 3.2: $\Delta\eta$–$\Delta\phi$ correlation functions of trigger 2–3 GeV/c, partner 2–3 GeV/c, in p+p, Au+Au at 60–90% and 0–20%. (a): Correlation function before remove the combinatorial background; (b): conditional yield per trigger.

3.3 Data Selection

3.3.1 Data and Selection

In this analysis, we use the data taken during the 2004 and 2005 runs (Run4 and Run5). After quality assurance checks, 8.8 x 10^8 events are used in Au+Au, and 1.3 x 10^9 events are used in p+p.

All data has been calibrated. Events are removed if the vertex is more than 30 cm from the center, where the magnetic field is uniform within this region.

Single Particle Selection

We use the electro–magnetic calorimeter (EMCAL) to measure the photons. We remove the photon clusters that hit the hot towers and unresponsive regions of the EMCAL. Each photon cluster also must pass shower shape cuts to remove showers from charged particles. The position information from PC3 is used to ensure that there are no charged particles in the cluster. We also require a time of flight cut to remove the neutral particles, such as neutrons (TOF $<$ 1.35 ns).

For charged particles, we require $|zed_{DC}| < 75$ cm to remove drift chamber edge effects. We also require a 2σ PC3 matching cut in both z and ϕ. We group charged particles in 5 different p_T bins, which are 1–1.5, 1.5–2, 1–2, 2–3, 3–5 GeV/c.

3.3.2 Analysis Scheme

In this analysis, we use the standard mixing scheme of PHENIX, which is called "CabanaBoy". In two particle correlation analysis, the signal, or the foreground, is formed by pairing trigger and partner particles in the same event. The mixed event background is formed by pairing trigger particles from one event and partner particles from another event. Since the two events are independent, this mixed event describes the uncorrelated event shape and detector acceptance. In order to apply the same cuts to both foreground and background, we apply the same pair cuts in mixed events. In CabanaBoy, we group the events into 20 centrality bins (0–100%, 5% per bin), 12 z vertex bins ($-30 < z < 30$ cm, 5 cm per bin). We do the mixing for events which have similar centrality and z–vertex.

The centrality bins used in this analysis are 0–5%, 5–10%, 10–20%, 20–40%, 40–60%, 60–90%. The most central bins are merged into 0–20% for

more statistics. Trigger p_T = 2–3 GeV/c, partner p_T = 1–1.5, 1.5–2, 2–3, 3–5 GeV/c. The same p_T bins also applied to p+p analysis.

3.4 Background Subtraction

In order to estimate the yield of the jet–induced pairs in the correlation functions, we assume a two component model [21]. The two component model assumes that the measured pairs are either from jet fragments or combinatorial background from the underlying event.

For the underlying events, we must correct for the correlations created by the collective flow described before. To do this, we assume the distributions of both trigger and partner particle are proportional to $1 + 2\langle v_2 \rangle \cos 2(\phi - \psi_{RP})$, where ψ_{RP} is the angle of the reaction plane. The uncorrelated pairs in the underlying events are then proportional to $1 + 2\left\langle v_2^A v_2^B \right\rangle \cos(2\Delta\phi)$, where A and B correspond to trigger and associated particles, respectively. Based on the results of PHOBOS [47] and PHENIX [48], the v_2 of inclusive photons and charged hadrons are treated as constant along the η direction, within the PHENIX central arm η acceptance ($|\eta| < 0.35$).

In the two source model, the correlation function, CF($\Delta\eta$, $\Delta\phi$) can be rewritten as

$$CF(\Delta\eta, \Delta\phi) = b_0(1 + 2\left\langle v_2^A v_2^B \right\rangle \cos(2\Delta\phi)) + JF(\Delta\eta, \Delta\phi) \qquad (3.2)$$

where JF($\Delta\eta$,$\Delta\phi$) is the correlation of the jet pairs, or the jet function. The b_0 determines the level of the underlying events.

The v_2 of inclusive photons and charged hadrons used in this analysis are measured by the standard reaction–plane method. Details will be presented in the following sections.

In order to determine the contribution from the jet, J($\Delta\eta$,$\Delta\phi$), we need to determine b_0. We apply the "Zero Yield at Minimum" or ZYAM method [23], which assumes that after subtraction the yield is zero at the minimum of the jet function. This technique determines the maximum possible background level. The point where the yield is zero is called the ZYAM point. Since v_2 is constant along η within the PHENIX acceptance, then the combinatorial background should also be flat within the PHENIX acceptance. Since the single particle distribution in η, $dN/d\eta$, is uniform with the PHENIX η acceptance [49], we assume the ZYAM level, b_0, is constant within the PHENIX $\Delta\eta$ acceptance. We project the correlation function, C($\Delta\eta$,$\Delta\phi$), on the $\Delta\phi$ direction to maximize the statistics, and then determine the ZYAM level. This ZYAM level is applied to the whole $\Delta\eta$ range.

The result of the subtracted correlation function is shown in Fig. 3.2(b). The detail of the subtracted correlation function will be described in Chapter 4.

3.5 Measurement of v_2

In this analysis, we measured v_2 of inclusive photons and inclusive charged hadrons, to ensure precise values in the centrality and p_T bins for which we construct correlation functions. The results are compared with other existing PHENIX analysis.

We use the event plane method [50] to measure the azimuthal anisotropy. The definition of v_2 is Eq. 3.3

$$v_2 = \langle \cos(2\phi - \psi_{RP}) \rangle \tag{3.3}$$

where ψ_{RP} is the direction of the reaction plane. Experimentally we can not measure ψ_{RP} precisely. We define the event flow vector $\vec{Q_n} = (Q_x, Q_y)$. Then the event plane ψ_n for the n–th harmonic is defined as

$$Q_x \equiv |\vec{Q_n}| \cos(n\psi_n) = \sum_i^M w_i \cos(n\phi_i), \tag{3.4}$$

$$Q_y \equiv |\vec{Q_n}| \sin(n\psi_n) = \sum_i^M w_i \sin(n\phi_i), \tag{3.5}$$

$$\psi_n = \frac{1}{n} \tan^{-1}\left(\frac{Q_y}{Q_x}\right), \tag{3.6}$$

where M is the number of particles used to determine the event plane, ϕ_i is the azimuthal angle of each particle, and w_i is the weight to optimize the reaction plane resolution. From Eq. 3.6, we can reconstruct the event plane ψ_2 event by event. This is known as the event plane for the second harmonic. The event plane for higher harmonics will not necessarily be exactly the same.

After determining ψ_2, v_2 can be measured as

$$v_2 = \frac{v_2^{obs}}{\Delta} = \frac{\langle \cos(2(\phi - \psi_2)) \rangle}{\langle \cos(2(\psi_2 - \psi_{RP})) \rangle} \tag{3.7}$$

where

$$\Delta = \langle \cos(2(\psi_2 - \psi_{RP})) \rangle \tag{3.8}$$

is the resolution of the reaction plane.

3.5.1 Reaction plane resolution, Δ

We measured the reaction plane resolution, Δ, using the beam–beam counter (BBC). The systematic error is the difference in the resolution given by BBC north and BBC south. The values of Δ used in this analysis are listed in Table 3.1.

Table 3.1: The reaction plane resolution, Δ, in various centrality

Centrality	Δ	stat. err	sys. err
0–5	0.2109	0.0005	0.0011
5–10	0.3094	0.0004	0.0038
10–20	0.3852	0.0002	0.0067
20–40	0.3867	0.0001	0.0067
40–60	0.2580	0.0002	0.0020
60–90	0.0909	0.0005	0.0015
0–10	0.2649	0.0003	0.0022
0–20	0.3310	0.0002	0.0042

3.5.2 v_2 of Inclusive Photons

We measured the v_2 of inclusive photons using the event plane method described above. The measured results in this analysis are shown as red points (CHC) and compared with with PHENIX preliminary Run4 result (shown as blue points, AN518) [51] as shown in Fig 3.3(a), Fig 3.3(b) and Fig 3.3(c). The v_2 of inclusive photons used in this analysis are listed in Table 3.2. The systematic error for the photon v_2 is dominated by the reaction plane resolution.

Table 3.2: v_2 of the inclusive photon in various centrality at p_T = 2–3 GeV/c

Centrality	v_2	stat. err	sys. err
0–5	0.0618	0.0015	0.0003
5–10	0.0950	0.0011	0.0012
10–20	0.1346	0.0007	0.0023
20–40	0.1780	0.0006	0.0031
40–60	0.1966	0.0014	0.0015
60–90	0.1825	0.0069	0.0030
0–10	0.0783	0.0008	0.0007
0–20	0.1038	0.0005	0.0013

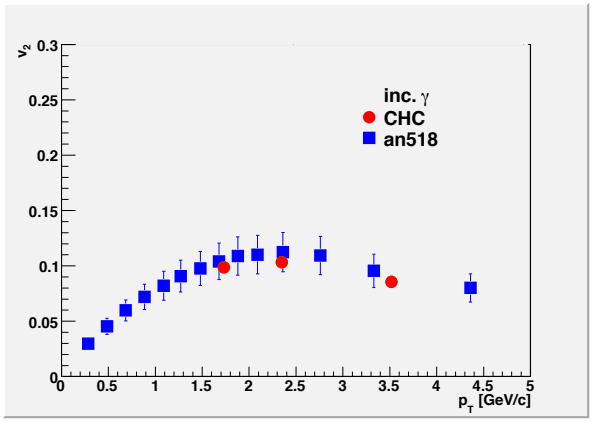

(a) 0–20%

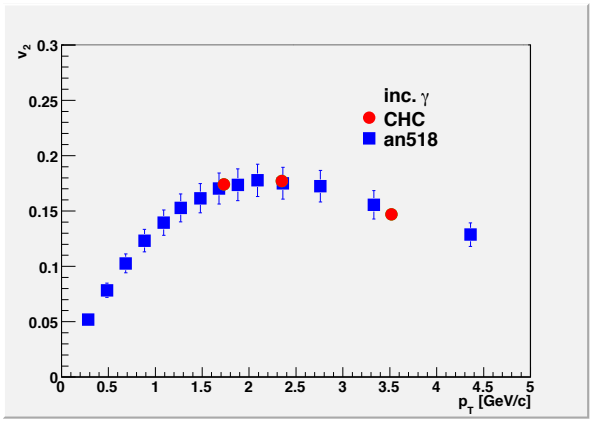

(b) 20–40%

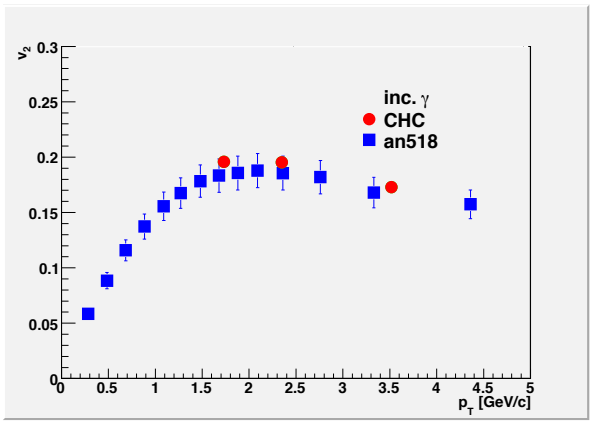

(c) 40–60%

Figure 3.3: v_2 of the inclusive photon at centrality 0–20%. Red points (CHC) are measurement from this analysis; blue points (an518) are measurements from PHENIX preliminary results [51]. (a): 0–20%; (b): 20–40%; (c): 40–60%;

3.5.3 v_2 of inclusive charged hadron

We measured the v_2 of the inclusive charged hadrons with the event plane method described in Sec. 3.5.1. The particle selection cuts are consistent with the cuts used in the correlation analysis. The measured values are compared with PHENIX preliminary 2004 result [52]. Selected comparisons are shown in Fig 3.4(a) to Fig 3.4(c). The v_2 measurement in this analysis is in good agreement with the PHENIX preliminary results. The v_2 of inclusive charged hadrons used in this analysis are listed in Table 3.3 to Table 3.7. The systematic error on this measurement is again dominated by the reaction plane resolution.

Table 3.3: v_2 of the inclusive charged hadron in various centrality at p_T = 1.0–1.5 GeV/c

Centrality	v_2	stat. err	sys. err
0–5	0.0419	0.0002	0.0019
5–10	0.0627	0.0002	0.0016
10–20	0.0915	0.0001	0.0034
20–40	0.1296	0.0001	0.0045
40–60	0.1558	0.0002	0.0029
60–90	0.1613	0.0014	0.0063
0–10	0.0520	0.0001	0.0010
0–20	0.0695	0.0001	0.0021

Table 3.4: v_2 of the inclusive charged hadron in various centrality at p_T = 1.5–2.0 GeV/c

Centrality	v_2	stat. err	sys. err
0–5	0.0543	0.0004	0.0017
5–10	0.0821	0.0003	0.0021
10–20	0.1198	0.0002	0.0045
20–40	0.1666	0.0002	0.0059
40–60	0.1950	0.0004	0.0032
60–90	0.1982	0.0023	0.0108
0–10	0.0680	0.0002	0.0013
0–20	0.0912	0.0001	0.0028

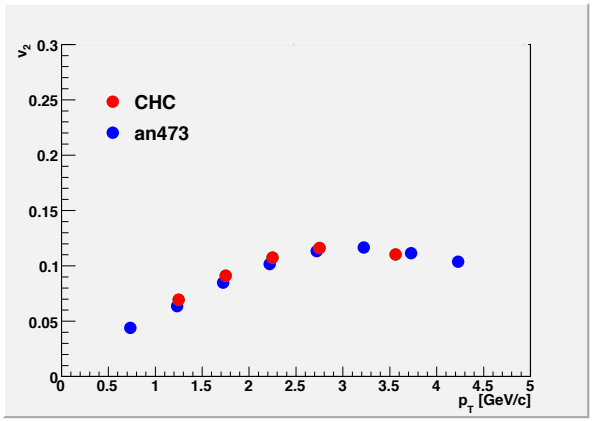

(a) 0–20%

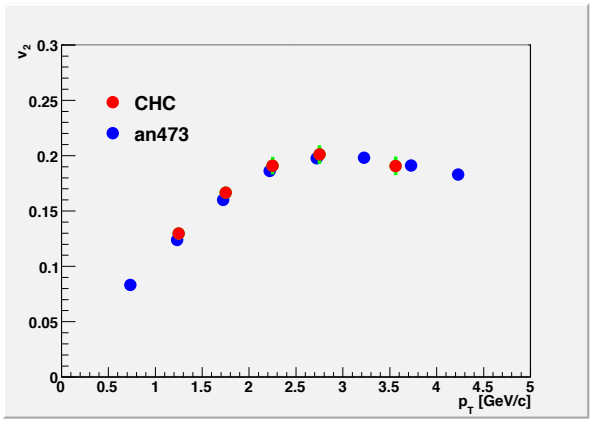

(b) 20–40%

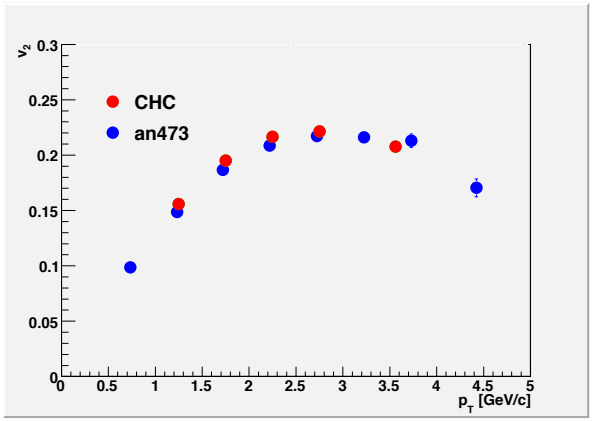

(c) 40–60%

Figure 3.4: v_2 of the inclusive charged hadron at centrality 0–20%. Red points (CHC) are measured in this analysis; blue points (an473) are from PHENIX preliminary results. [52]. (a): 0–20%; (b): 20–40%; (c): 40–60%;

Table 3.5: v_2 of the inclusive charged hadron in various centrality at p_T = 1.0–2.0 GeV/c

Centrality	v_2	stat. err	sys. err
0–05	0.0448	0.0002	0.0019
5–10	0.0672	0.0002	0.0017
10–20	0.0981	0.0001	0.0037
20–40	0.1382	0.0001	0.0048
40–60	0.1647	0.0002	0.0029
60–90	0.1694	0.0013	0.0072
0–10	0.0557	0.0001	0.0010
0–20	0.0745	0.0001	0.0022

Table 3.6: v_2 of the inclusive charged hadron in various centrality at p_T = 2.0–3.0 GeV/c

Centrality	v_2	stat. err	sys. err
0–5	0.0654	0.0006	0.0014
5–10	0.0992	0.0004	0.0026
10–20	0.1424	0.0003	0.0053
20–40	0.1934	0.0002	0.0067
40–60	0.2177	0.0006	0.0036
60–90	0.2151	0.0035	0.0073
0–10	0.0823	0.0004	0.0017
0–20	0.1095	0.0002	0.0034

Table 3.7: v_2 of the inclusive charged hadron in various centrality at p_T = 3.0–5.0 GeV/c

Centrality	v_2	stat. err	sys. err
0–5	0.0643	0.0017	0.0028
5–10	0.0989	0.0012	0.0025
10–20	0.1438	0.0008	0.0060
20–40	0.1907	0.0007	0.0070
40–60	0.2078	0.0016	0.0041
60–90	0.2052	0.0085	0.0123
0–10	0.0817	0.0010	0.0013
0–20	0.1104	0.0006	0.0035

3.6 Photon Distribution

Inclusive photons with $2 < p_T < 3$ GeV/c are dominated by decay photons from π^0s. It is important to know the p_T distribution of the parent π^0s.

The method used here is similar to the "shark fin" method used in direct γ–h analyses in PHENIX [53]. The idea is to calculate the probability of a π^0 with the momentum at $p_T^{\pi^0}$ has a decay photon which has transverse momentum p_T^γ. We use an analytic approach to directly calculate the probability of a π^0 with transverse momentum $p_T^{\pi^0}$, decaying to a photon with p_T^γ between 2 and 3 GeV/c.

The probability of a photon parent with $p_T^{\pi^0}$, Prob($p_T^{\pi^0}$) is

$$\begin{aligned} Prob(p_T^{\pi^0}) \quad &= 0, \text{if } p_T^{\pi^0} < p_T^\gamma|_{low} \\ &= 2\frac{p_T^{\pi^0} - p_T^\gamma}{p_T^{\pi^0}}, \text{if } p_T^\gamma|_{low} < p_T^{\pi^0} < p_T^\gamma|_{high} \\ &= 2\frac{p_T^{\pi^0} - p_T^\gamma|_{high}}{p_T^{\pi^0}}, \text{if } p_T^\gamma|_{high} < p_T^{\pi^0} \end{aligned} \tag{3.9}$$

Here the p_T^γ is between 2–3 GeV/c. The resulting decay probability distribution is shown in Fig 3.5. As an example, for a 3 GeV π^0, the probability to have a 2–3 GeV/c decay photon is about 0.66.

This probability distribution is weighted by the π^0 spectra from p+p [54], and Au+Au in various centralities [20]. The π^0 spectra in [20] are measured mainly in 10% centrality bins, and properly combined to be consistent with the centrality bins used in this analysis. We only consider π^0 p_T below 10 GeV/c, since the yields for high p_T π^0 are several orders of magnitude smaller and have essentially no contributions in the yields of the decay photons. When p_T of π^0 is below 2 GeV/c, the π^0 has no contribution to decay photons between 2–3 GeV/c.

We use the π^0 spectrum of Au+Au at 0–20%, Fig 3.6, as an example. Fig 3.6 has two spectra. The black spectrum is the measured π^0 spectrum in Au+Au [20]. The red points show the measured spectrum weighted by the probability in Fig 3.5. It is clear that in the weighted spectra (red), 2–3 GeV/c π^0s are still the dominant source of photons at 2–3 GeV/c.

From these weighted spectra , we can measure the average p_T of the parent π^0s, which is tabulated in Table 3.8. For comparison, we also list the mean p_T of π^0s at p_T 2–3 GeV/c. The overall trend is that the mean p_T of the parent π^0s is higher than the mean p_T from the unweighted π^0 spectra.

Table 3.8: The average p_T of π^0 which decays to a 2–3 GeV/c photon

Centrality	mean parent π^0 p_T [GeV/c]	mean π^0 p_T at 2–3 GeV/c
0-5	2.60729	2.34511
5-10	2.62896	2.35626
10-20	2.64737	2.35876
20-40	2.66607	2.36175
40-60	2.69527	2.36674
60-90	2.71375	2.3706
0-10	2.61747	2.35025
0-20	2.63031	2.35382
p+p	2.71317	2.36951

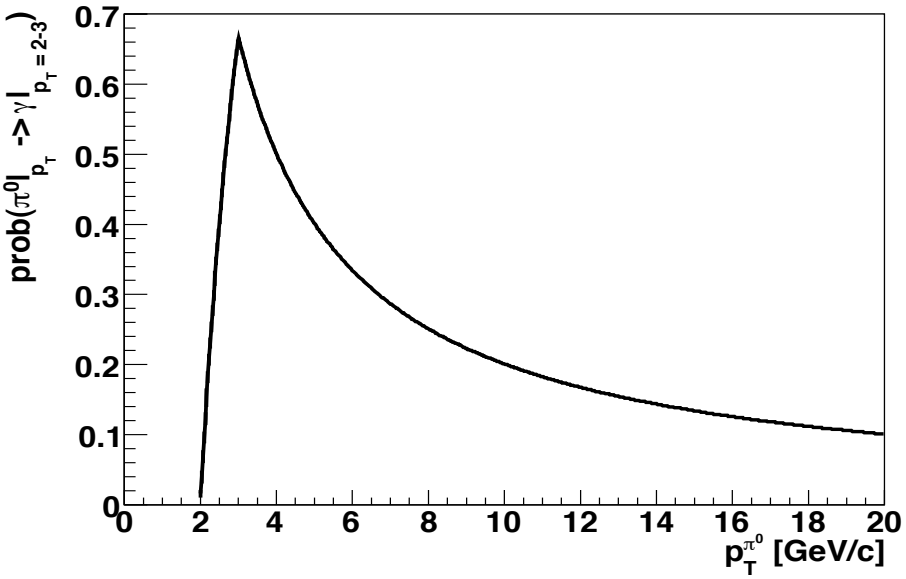

Figure 3.5: Probability distribution of π^0 generating a 2–3 GeV/c decay photon.

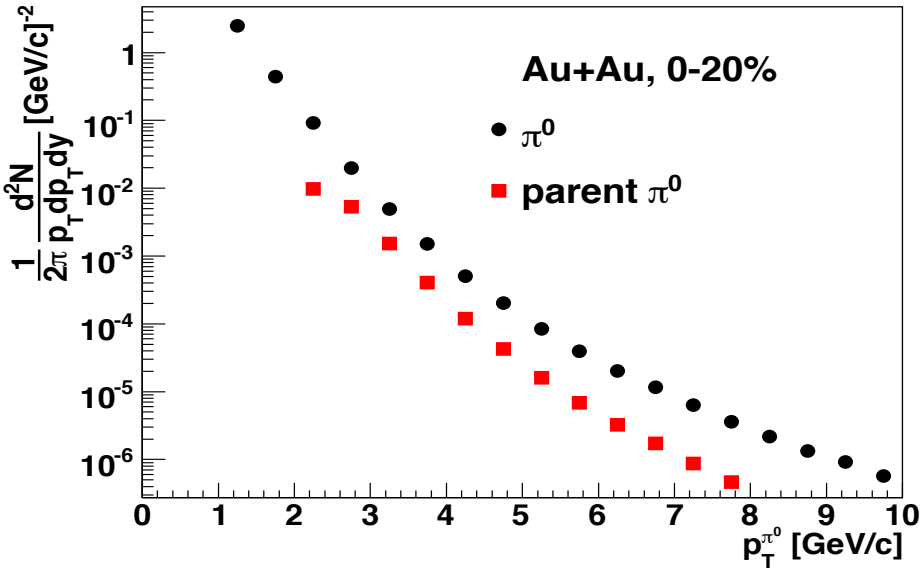

Figure 3.6: π^0 spectra (black) and the π^0 spectra weighted by the sharkfin (red) at centrality 0–20%

3.7 Normalization

For standard two particle azimuthal $\Delta\phi$ correlations, the conditional yield is an important quantity which measures the number of associated particles when there exists a trigger particle. This conditional yield is also called the "per trigger yield". Eq. (3.10) is used to calculate this per trigger yield:

$$\frac{1}{N^A}\frac{dN^{AB}(\Delta\phi)}{d(\Delta\phi)} = \frac{1}{\epsilon_B}\frac{N^{AB}_{Real}}{N^A_{Real}}\frac{1}{\int d(\Delta\phi)}J(\Delta\phi) \tag{3.10}$$

In Eq. (3.10), ϵ_B is the single particle efficiency of the associated particles. N^{AB}_{Real} (and N^A_{Real}) is the true number of pairs (triggers) measured in the analysis.

For $\Delta\phi$ correlations, the integral $\int d(\Delta\phi)$ is π (2π) if the $\Delta\phi$ is from 0 to π (2π). This is because $\Delta\phi$ is a cyclic function.

To get the per trigger yield of in $\Delta\eta$–$\Delta\phi$ correlation functions, we extend Eq. (3.10):

$$\frac{1}{N^A}\frac{d^2N^{AB}(\Delta\eta,\Delta\phi)}{d(\Delta\eta)d(\Delta\phi)} = \frac{1}{\epsilon_B}\frac{N^{AB}_{Real}}{N^A_{Real}}\frac{1}{\int d(\Delta\eta)\int d(\Delta\phi)}J(\Delta\eta,\Delta\phi) \tag{3.11}$$

In this analysis, $\Delta\phi$ is from $-\pi/2$ to $3\pi/2$, so $\int \Delta\phi$ is 2π, which is the same as the one–dimensional case.

In the $\Delta\eta$ direction, both the trigger and the partner distributions are flat within the PHENIX η acceptance ($|\eta| < 0.35$). If we convolve two flat distribution between $|\eta| < 0.35$, we can find a simple triangular shape for the $\Delta\eta$ acceptance, $acc(\Delta\eta) = (0.7 - |\Delta\eta|)/0.7$ [55]. This means we only have 50% pair efficiency in the $\Delta\eta$ direction. In Eq. (3.11), $\int d(\Delta\eta)$ should be written as $\int_{-0.7}^{0.7} acc(\Delta\eta)d(\Delta\eta) = 0.7$.

Similarly, if both trigger and partner distributions are flat in ϕ from 0 to 2π, we can show that $acc(\Delta\phi) = 1$.

The equation to calculate the per trigger yield in 2D $\Delta\eta$ $\Delta\phi$ correlation, or Eq. (3.11), should be re–written in the form of

$$\frac{1}{N^A}\frac{d^2N^{AB}(\Delta\eta,\Delta\phi)}{d(\Delta\eta)d(\Delta\phi)} = \frac{1}{\epsilon_B}\frac{N^{AB}}{N^A}\frac{1}{\int acc(\Delta\eta)d(\Delta\eta)\int acc(\Delta\phi)d(\Delta\phi)}J(\Delta\eta,\Delta\phi) \tag{3.12}$$

where $\int_{-0.7}^{0.7} acc(\Delta\eta)d(\Delta\eta) = 0.7$ and $\int_{-\pi/2}^{3\pi/2} acc(\Delta\phi)d(\Delta\phi) = 2\pi$.

3.8 Efficiency Correction

In order to obtain the per trigger yield of the correlation function, we need to know the efficiency of detecting the associated charged hadrons, ϵ_B, in Eq. 3.11. We determine this efficiency by comparing the measured charged particle spectra in this analysis with the published spectra [56], which has been corrected for the detector acceptance and all the efficiencies.

In [56], PHENIX published the spectra for inclusive charged hadrons, $\frac{(h^+ + h^-)}{2}$, in units of $\frac{1}{2\pi p_T N_{evt}}\frac{dN^2}{dp_T d\eta}$. In order to get the corrected number of particles inside the PHENIX central arm η acceptance, we convert the spectrum to the number of particles expected in a certain p_T bin in this measurement. To do this, we multiply 2π, p_T and dp_T for each p_T bin in the spectrum. We then apply $d\eta$ =0.7, a factor of 2 for h^+ and h^-, and the number of events, N_{evt}, in our measurement.

Using the number of particles expected from the published spectra, $N^{publish}$, and number of particles we measured, $N^{measured}$, we can calculate the associated particle efficiency, ϵ, for this measurement, defined as

$$\epsilon = \frac{N^{measured}}{N^{publish}} \tag{3.13}$$

For p+p, the inclusive charged hadron spectra is taken from PHENIX paper [57]. By comparing the measured spectra with the published ones in [57], we can determine the efficiency in p+p. The spectrum in [57] is absolutely normalized; we use Eq.(3.14) to convert the cross section to number of particles:

$$E\frac{d^3\sigma_x^{unbiased}}{d^3p} = \sigma_x^{unbiased}\frac{1}{2\pi}\frac{1}{p_T}\frac{1}{N_X^{TotalUnbiased}}\frac{d^2N_X^{Unbiased}}{dp_T dy} \tag{3.14}$$

$\sigma_x^{unbiased} = 42.5$ mb is the total p+p inelastic cross section at $\sqrt{s} = 200$ GeV. There is also a BBC trigger bias effect, which is $N_x^{unbiased} = C_{p+p}^{BBC} N_x^{totalbiased}$. The value of $1/C_{p+p}^{BBC}$ =0.75. With all the parameters, we can calculate $N_x^{totalbiased}$. From Eq.(3.14), we transform the cross section of inclusive charged particles to an invariant yield.

The efficiency in our measurement in Au+Au and p+p is shown in Table 3.9.

Table 3.9: Efficiency of AuAu and pp in various p_T and centrality bins.

centrality	partner p_T [GeV/c]				
	1.0 – 1.5	1.5 – 2.0	1.0 – 2.0	2.0 – 3.0	3.0 – 5.0
0–5	0.1954	0.2011	0.1966	0.2143	0.2522
5–10	0.2033	0.2097	0.2048	0.2236	0.2535
10–20	0.2158	0.2241	0.2177	0.2371	0.2618
20–40	0.2297	0.2399	0.2320	0.2531	0.2758
40–60	0.2469	0.2608	0.2499	0.2745	0.2971
60–90	0.2589	0.2773	0.2627	0.2986	0.3187
0–10	0.1986	0.2047	0.2000	0.2180	0.2520
0–20	0.2057	0.2129	0.2073	0.2258	0.2563
p+p	0.2061	0.2172	0.2082	0.2299	0.2610

3.9 Multiplicity Cross Check

To make sure that we applied the correct factor when calculating the per trigger yield, we perform a multiplicity crosscheck. The idea is that the total multiplicity obtained from $\Delta\eta$–$\Delta\phi$ correlation should be the same as from $\Delta\phi$ correlations times the $\Delta\eta$ bin width. Since we applied the same method in all centrality and p_T bins, we only select one particular example here.

We use trigger p_T = 2–3 GeV/c, partner p_T = 1–2 GeV/c, centrality 0–20% as an example. When we integrate the $\Delta\eta$–$\Delta\phi$ correlation function, Fig 3.7,

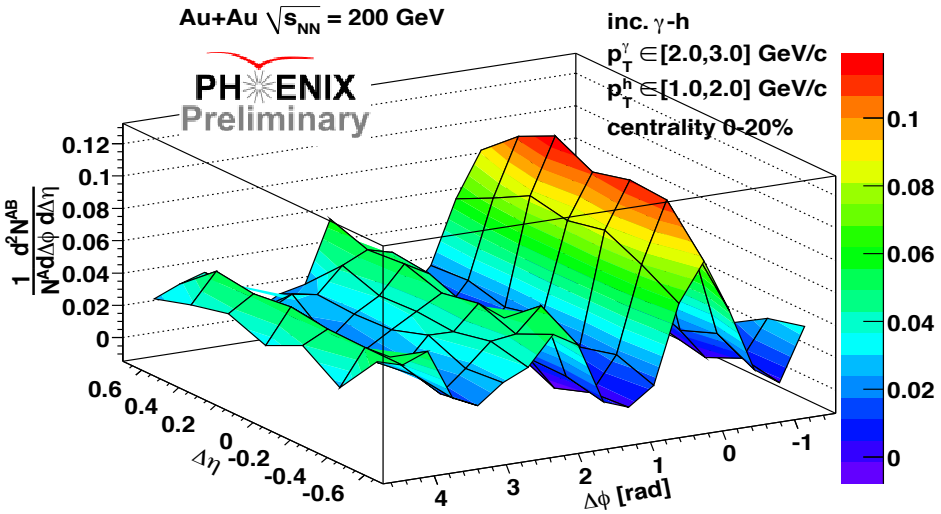

Figure 3.7: $\Delta\eta$–$\Delta\phi$ jet function of 2–3x1–2 GeV/c, centrality 0–20%, with v_2 modulated underlying event background subtracted.

times the bin width in $\Delta\phi$ and $\Delta\eta$, the total multiplicity is 0.660 pairs per trigger. Integrating the correlation function along $\Delta\phi$ for the $0.0 < |\Delta\eta| < 0.7$, Fig 3.8, yield the total multiplicity of 0.471 * 1.4 = 0.660, showing that the two results are consistent.

We also check in finer $\Delta\eta$ bins. Integrating 4 $\Delta\eta$ bins separately and summing $0.0 < |\Delta\eta| < 0.1$, $0.1 < |\Delta\eta| < 0.3$, $0.3 < |\Delta\eta| < 0.5$, and $0.5 < |\Delta\eta| < 0.7$, (Fig 3.9, Fig 3.10, Fig 3.11 and Fig 3.12), then the total multiplicity of $0.495 * 0.2 + 0.481 * 0.4 + 0.494 * 0.4 + 0.427 * 0.4 = 0.660$. This verifies that the result is consistent between 1D $\Delta\phi$ and 2D $\Delta\eta$–$\Delta\phi$ correlation functions.

3.10 Systematic Error

In this analysis, systematic errors arise from four different sources: v_2, ZYAM, hadron efficiency, and hadron contamination of the photon trigger.

The shape of the underlying event background is $b_0(1 + 2c_2\cos(2\Delta\phi))$, where b_0 is the level of the background, and c_2 is the modulation defined as $c_2 = v_2^{trig} \times v_2^{part}$. The v_2 systematic error of the subtracted jet function is by fixing background level, b_0 and varying the v_2 by the 1σ systematic error.

The ZYAM error is the uncertainty of the ZYAM level, or b_0. To estimate

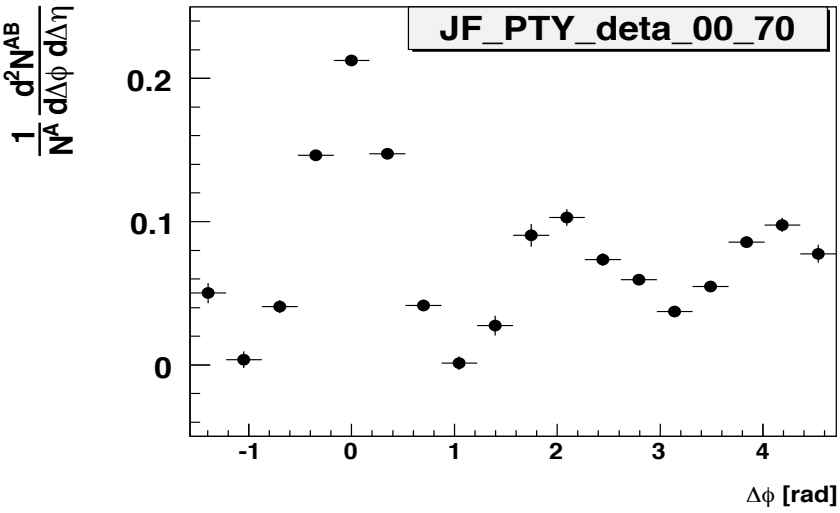

Figure 3.8: $\Delta\phi$ correlation function of 2–3x1–2 GeV/c, centrality 0–20%, $0.0 < |\Delta\eta| < 0.7$

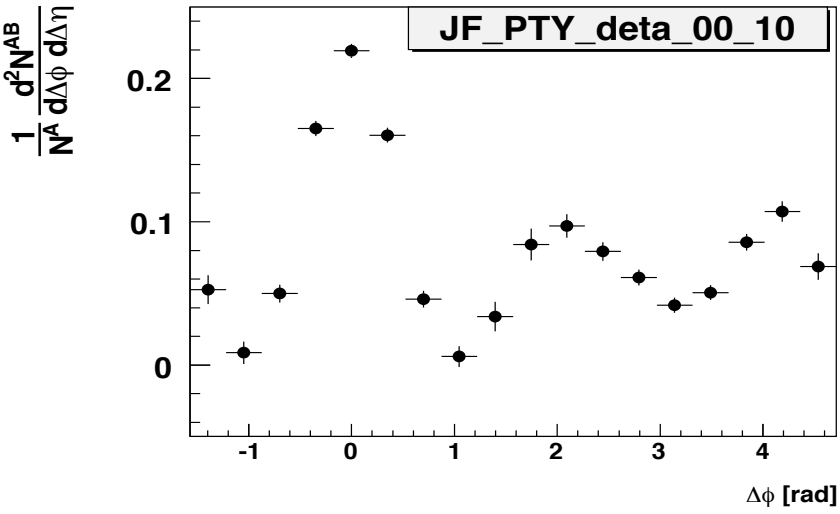

Figure 3.9: $\Delta\phi$ correlation function of 2–3x1–2 GeV/c, centrality 0–20%, $0.0 < |\Delta\eta| < 0.1$

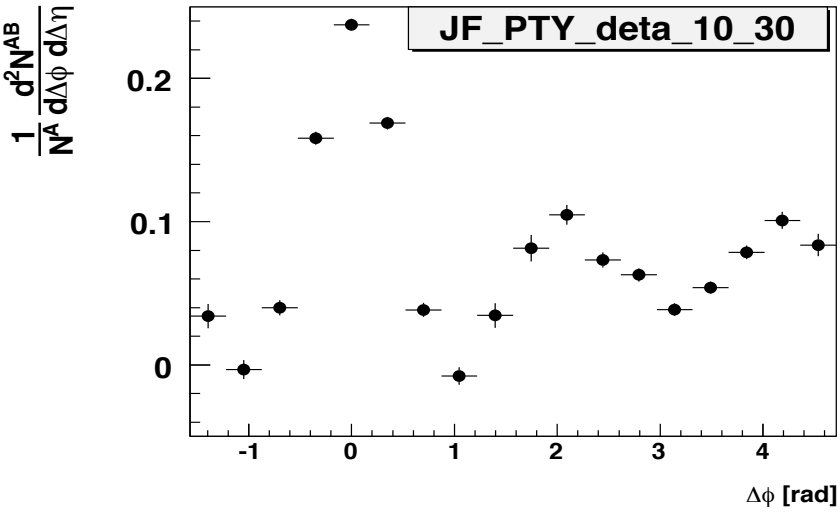

Figure 3.10: $\Delta\phi$ correlation function of 2–3x1–2 GeV/c, centrality 0–20%, $0.1 < |\Delta\eta| < 0.3$

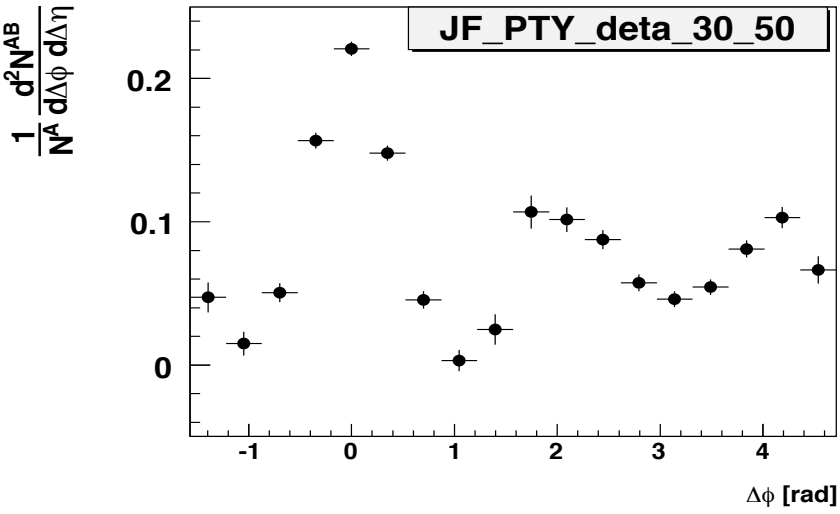

Figure 3.11: $\Delta\phi$ correlation function of 2–3x1–2 GeV/c, centrality 0–20%, $0.3 < |\Delta\eta| < 0.5$

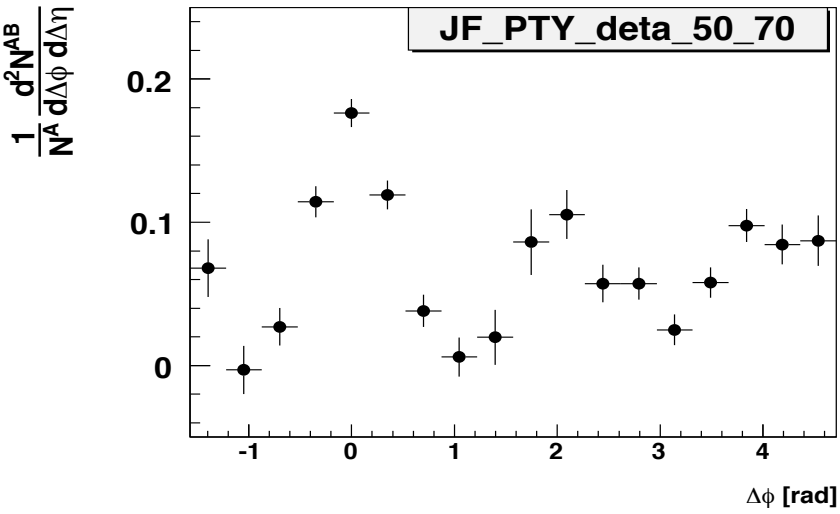

Figure 3.12: $\Delta\phi$ correlation function of 2–3x1–2 GeV/c, centrality 0–20%, $0.5 < |\Delta\eta| < 0.7$

this value, use a Monte Carlo simulation by varying the data points of the correlation function by their statistical errors. The ZYAM error is determined by the the variation of the ZYAM level.

The systematic error due to the hadron efficiency comes from comparing the measured inclusive hadron spectra with the published spectra. This value is between 7.1% – 9.4%, depending on centrality and partner p_T.

In order to estimate the hadron contamination of the trigger, we removed the PC3 veto cut. in Fig. 3.13, we compare the correlation function with and without veto cut. by comparing the per trigger yield after removing the PC3 veto cut, we can estimate the effect of the hadron contamination in the trigger photons. The level of the contamination is about 5%

All four different systematic are summed in quadrature.

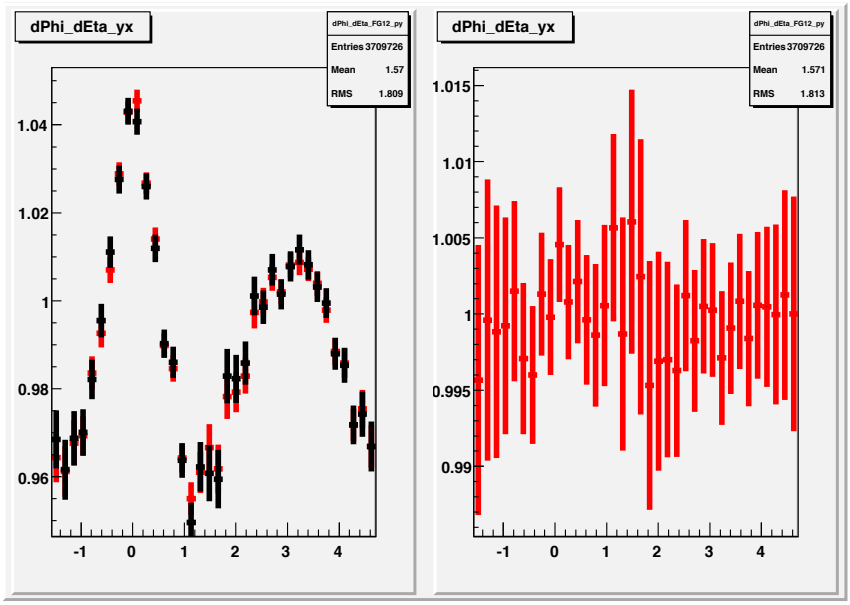

Figure 3.13: Left: correlation function with (black) and without pc3 veto cut (red). Right: the ratio of the correlation function of (without veto)/(veto). trigger p_T =2–3 GeV/c, partner p_T =1–2 GeV/c, and centrality = 0–90.

Chapter 4

Decomposing the Correlation Functions

4.1 Introduction

In this chapter, we assume the collective flow induced modulation of the underlying background is described by v_2 ($\cos 2\Delta\phi$). Effects of higher harmonics will be discussed in Chapter 5 and 6. After subtracting the underlying events, we study the $\Delta\eta$–$\Delta\phi$ correlation functions in detail. We decompose the jet functions by fitting the different components to extract the yield of the pp–like away side jet and the shoulder, which corresponds to the possible medium modification. The shoulder is also compared with the ridge in the nearside.

4.2 $\Delta\eta$–$\Delta\phi$ Correlation Functions

$\Delta\eta$–$\Delta\phi$ correlations are measured for various centralities in Au+Au collisions and in p+p. By applying the normalization and the efficiency correction discussed in Chapter 3, and the ZYAM method, we obtain the $\Delta\eta$–$\Delta\phi$ conditional yields of the associated particles per photon trigger.

In left hand side of Fig. 4.1 and Fig. 4.2, we present correlation functions from p+p, peripheral and central Au+Au collision before removing the combinatorial background. Before subtracting the underlying event background, the p+p correlation function has a clear peak on the nearside ($\Delta\phi \approx 0$ and $\Delta\eta \approx 0$). There is an awayside peak at $\Delta\phi \approx \pi$ which extends along $\Delta\eta$. This extension along $\Delta\eta$ is due to k_T smearing. The correlation function in the 60–90% centrality range looks like that in p+p. In central Au+Au collisions, an enhancement is seen along the $\Delta\eta$ direction on the near side ($\Delta\phi \approx 0$), this is the ridge which is significantly different from peripheral Au+Au or p+p cases. .

The right hand side of Fig. 4.1 and Fig. 4.2 show the correlation functions after subtraction of the flow modulated background. Both p+p and peripheral Au+Au collisions (60–90%) show similar dijet structure. In 0–20%, the near-side enhancement along $\Delta\eta$ in nearside is significant. This ridge was reported by STAR [25] and PHOBOS [37] previously. On the awayside, where $\Delta\phi \approx \pi$, p+p peaks at $\Delta\phi = \pi$, but central Au+Au shows a local minimum. The peaks shift to $\Delta\phi \approx \pi \pm 1$ and extend along $\Delta\eta$. This double peak structure, the shoulder, is consistent with previous PHENIX results [21, 22, 23].

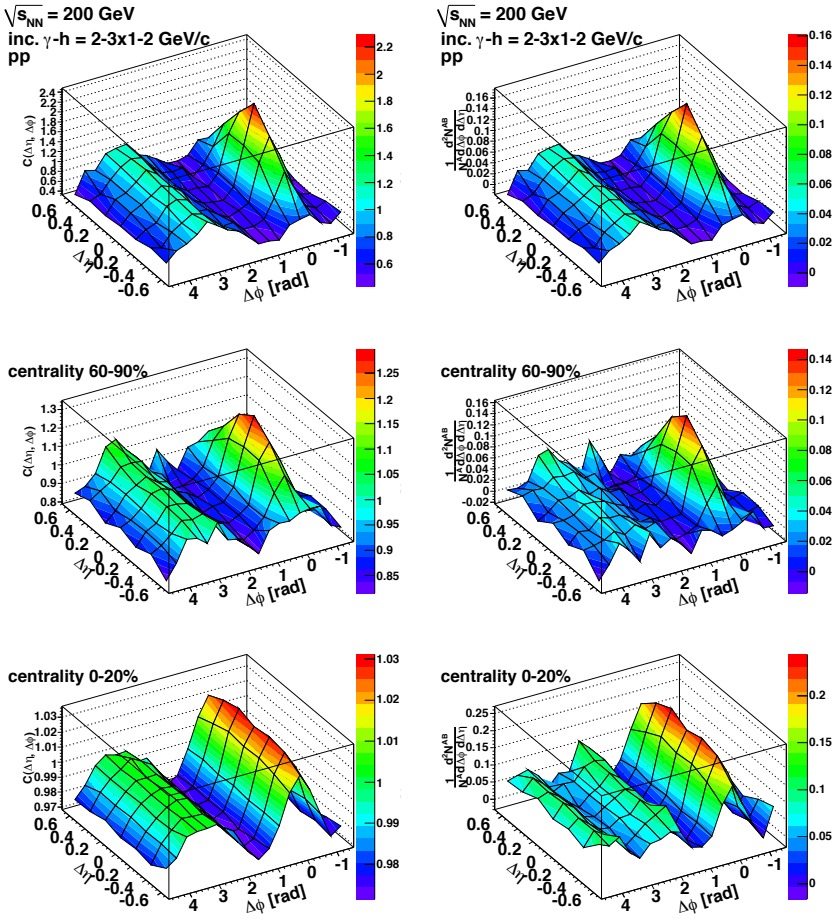

(a) Correlation function (b) after flow subtraction

Figure 4.1: $\Delta\eta$–$\Delta\phi$ correlation functions of trigger 2–3 GeV/c, partner 1–2 GeV/c, in p+p, Au+Au at 60–90% and 0–20%. (a): Correlation function before removing combinatorial background; (b): conditional yield per trigger.

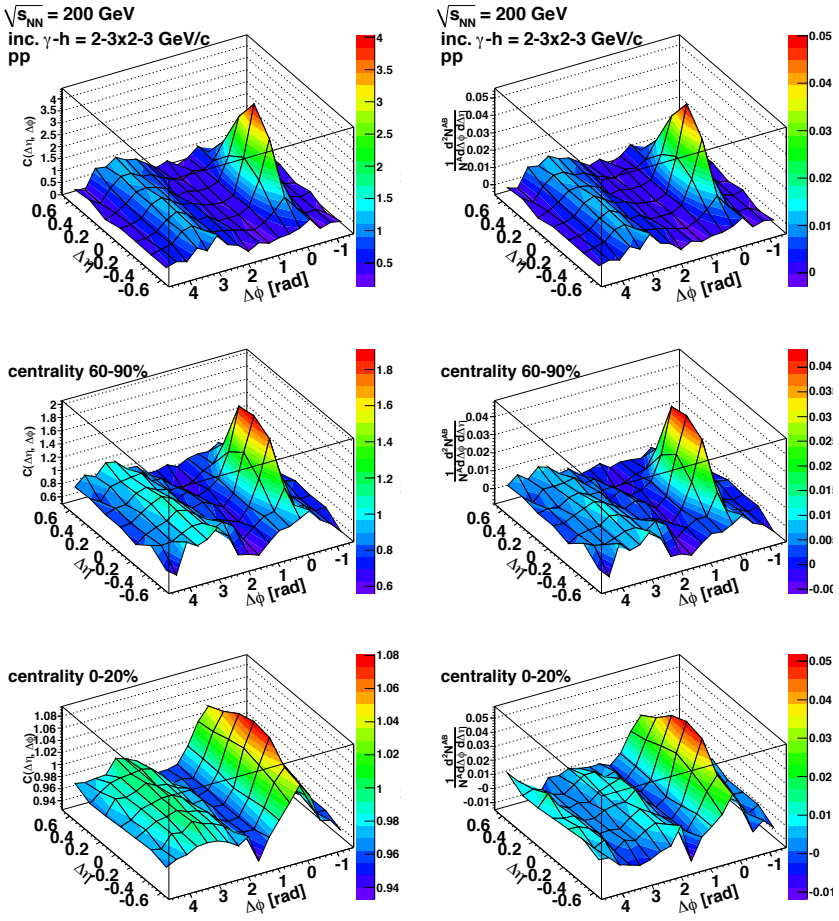

(a) Correlation function (b) after flow subtraction

Figure 4.2: $\Delta\eta$–$\Delta\phi$ correlation functions of trigger 2–3 GeV/c, partner 2–3 GeV/c, in p+p, Au+Au at 60–90% and 0–20%. (a): Correlation function before remove the combinatorial background; (b): conditional yield per trigger.

4.2.1 $\Delta\phi$ Correlation Functions in Different $\Delta\eta$ Region

In order to trace the modification from p+p to Au+Au collisions, we slice the $\Delta\phi$ correlation in 4 $\Delta\eta$ ranges: $|\Delta\eta|$ = 0–0.1, 0.1–0.3, 0.3–0.5 and 0.5–0.7. In peripheral Au+Au collisions (60–90%), shown in Fig.4.3, the $\Delta\phi$ shape is consistent with p+p collisions for all 4 $\Delta\eta$ regions. The near side yield decreases as the $\Delta\eta$ slice moves from $\Delta\eta = 0$ to larger $\Delta\eta$, which is consistent with the fact that the nearside jet has a Gaussian shape in the $\Delta\eta$ direction and peaks at $\Delta\eta = 0$. In contrast, the away side peak remains roughly the same in all $\Delta\eta$ regions.

However, in central Au+Au collisions at large $\Delta\eta$ on the near side, we see a clear difference from p+p, as shown in Fig.4.4. In the rapidity range $0.5 < |\Delta\eta| < 0.7$, substantial yield is seen in Au+Au, while in p+p there is very little yield on the near side. At smaller $\Delta\eta$ in Au+Au collisions there is also some enhancement compared to the jet peak in p+p. In all measured $\Delta\eta$ regions on the away side, the double peak structure away from $\Delta\phi \approx \pi$ is clearly seen in central Au+Au, in contrast to the single peak in p+p collisions. This is consistent with previous observations [21].

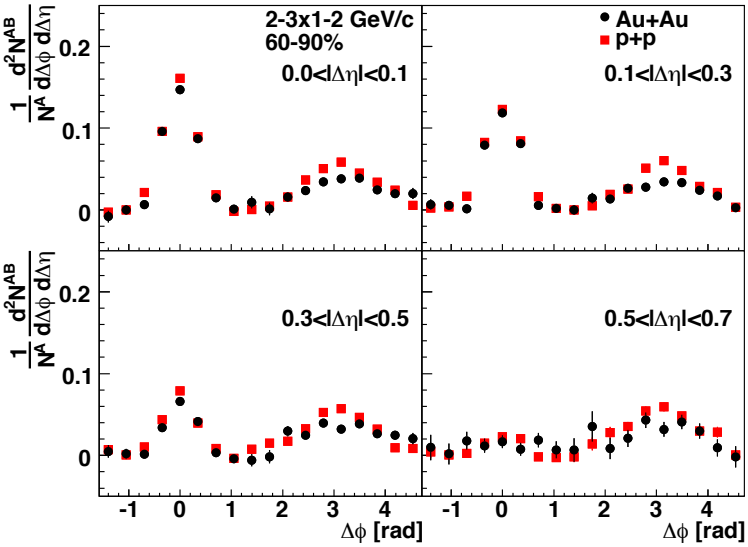

Figure 4.3: Peripheral Au+Au (60–90%) and p+p conditional per trigger yield in different $\Delta\eta$ regions for trigger p_T = 2.0 – 3.0 GeV/c and partner p_T = 1.0 – 2.0 GeV/c. Au+Au (p+p) data are shown by solid circles (squares).

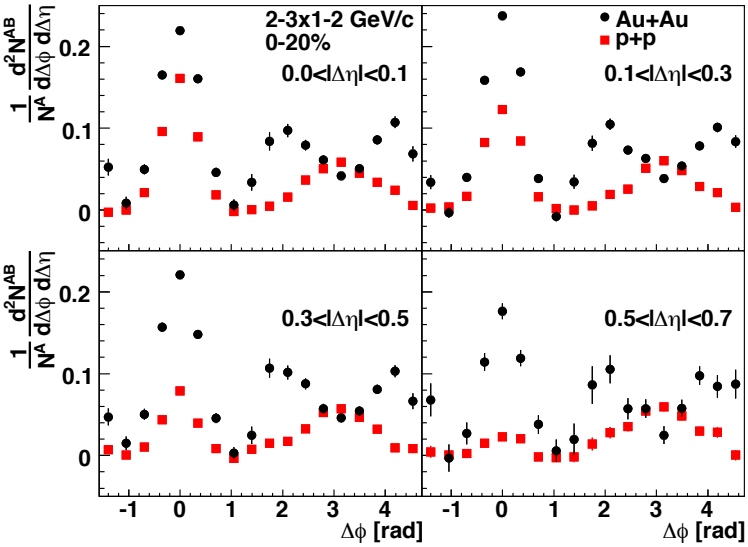

Figure 4.4: The same as Fig. 4.3, but for central Au+Au collisions (0–20%).

4.3 Near Side Projection along $\Delta\eta$ Direction

To focus on the modification of the near side yield along $\Delta\eta$ in Au+Au, the two–particle $\Delta\eta$–$\Delta\phi$ correlation function is integrated in $|\Delta\phi| < 7\pi/18$ and is projected in the $\Delta\eta$ direction, shown in Fig. 4.5(a). We choose $|\Delta\phi| < 7\pi/18$ because in p+p, this is the size of the near side jet. In central Au+Au collisions the near side is wider along $\Delta\eta$ and is enhanced compared to p+p. Moving from central to peripheral Au+Au collisions, the near side enhancement along $\Delta\eta$ decreases, and the peak becomes more consistent with the jet–like shape in p+p. This indicates that the yield of the ridge strongly correlates with the size of the medium.

To investigate the partner p_T dependence, we present the $\Delta\eta$ projections for four partner p_T ranges in the most central Au+Au (0–20%) collisions in Fig. 4.5(b). The effect of the ridge is the strongest in central collisions compared to p+p At partner p_T below 3 GeV/c, the enhancement is significant in Au+Au, and the peak is wider than in p+p. At larger partner p_T = 3–5 GeV/c, there is no obvious enhancement in Au+Au and the Au+Au shape is consistent with p+p. Therefore near side enhancement along $\Delta\eta$ decreases significantly for high partner p_T. The ridge is most significant at partner p_T below 3 GeV/c.

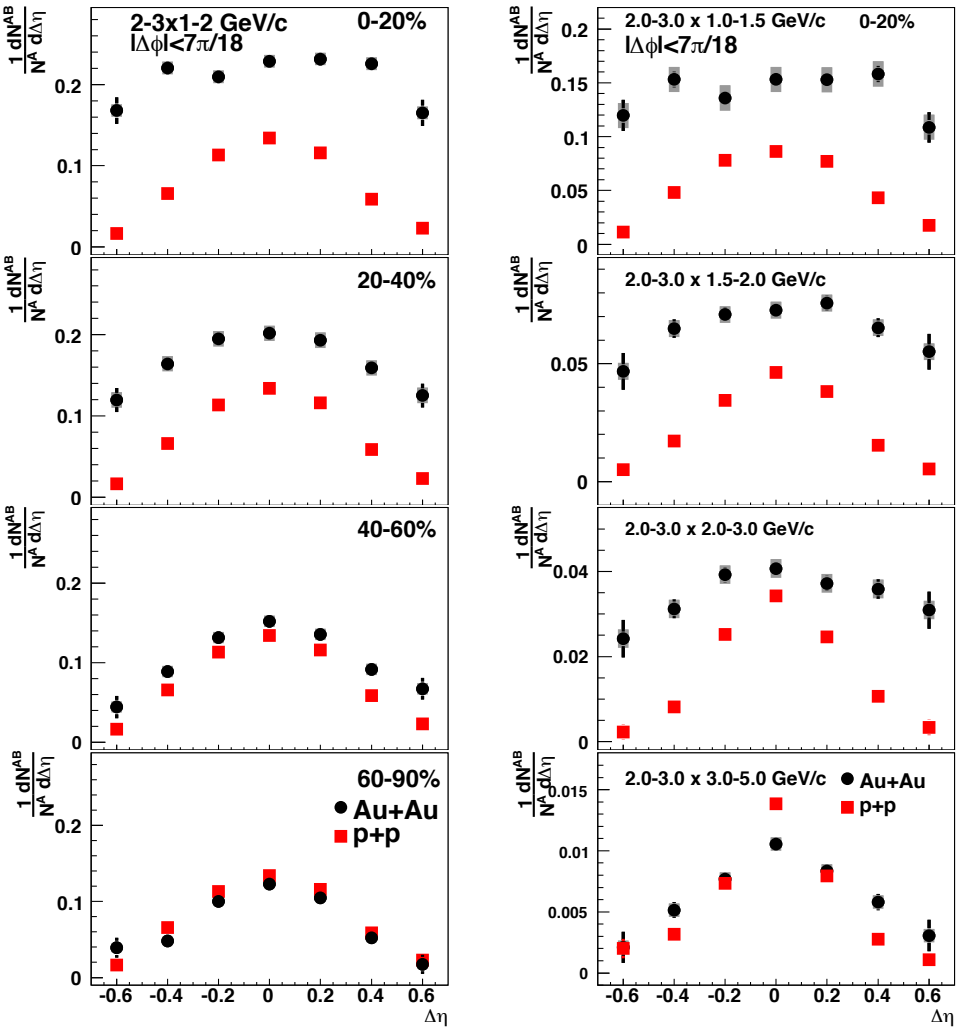

(a) centrality dependence (b) centrality dependence

Figure 4.5: Near side $\Delta\eta$ correlations of Au+Au (circles) and p+p (squares). (a): various centralities for trigger p_T = 2.0 – 3.0 GeV/c, partner p_T = 1.0 – 2.0 GeV/c; (b): Au+Au at 0–20% and p+p for for various partner p_T bins.

4.4 Extracting the Near Side Yield

In Fig. 4.6, the near side per trigger yield is plotted as a function N_{part}, which is the number of nucleons participating the collisions, for different partner p_T. Since we are using the ZYAM method to determine the background level, it is natural to use ZYAM point to separate the near and away side. In this analysis, we adapt the idea of the ZYAM point, but more closely follow previous PHENIX analysis [23]. We define the near side within a fixed $\Delta\phi$ region as $|\Delta\phi| < 7\pi/18$. The selection of this $\Delta\phi$ range is due to the bin width in the correlation function histogram. However, it is consistent with the previous result using the ZYAM point to separate the near and away side. The systematic error of the nearside yield is coming from the determination of the ZYAM level and from the v_2 modulations.

Different symbols correspond to sequential slices in $|\Delta\eta|$. The p+p near side yields are plotted as the left most symbols and serve as a baseline measurement. In p+p collisions, the yield decreases gradually for ranges from $|\Delta\eta|$ = 0–0.1 to 0.5–0.7. This is consistent with a typical jet structure, which peaks at $\Delta\eta \approx 0$ and decreases at larger $\Delta\eta$. In the range of $0.5 < |\Delta\eta| < 0.7$ the yield in p+p is very small.

For partner p_T below 3 GeV/c, the conditional yield monotonically increases with N_{part} up to $N_{part} \approx 240$ in all $\Delta\eta$ regions. For Au+Au collisions the largest enhancement relative to p+p collisions is seen in the $0.5 < |\Delta\eta| < 0.7$ region where the p+p yield (from jets) is small. This enhancement is clear evidence of the ridge. At N_{part} larger than 240, the yield at $0.5 < |\Delta\eta| < 0.7$ levels off. For partner p_T above 3 GeV/c the yield does not change with N_{part} within the errors.

4.5 Ridge Extraction

4.5.1 Definition of Ridge in PHENIX

From Fig. 4.5(a) and Fig. 4.5(b), we know that the near side correlation consists of a jet–like correlation which peaks at $\Delta\phi = 0$, and a ridge like correlation which is flat in $\Delta\eta$. The ridge is flat along the $\Delta\eta$ direction to 4 units of pseudorapidity [37]. In two particle correlation analysis, the width of the near side jet when fitting with a Gaussian function is about 0.3 in $\Delta\phi$ direction. Assume the jet shape is symmetric in $\Delta\eta$ and $\Delta\phi$ direction, then the width in $\Delta\eta$ is about 0.3. However, since the PHENIX $\Delta\eta$ acceptance is limited ($|\Delta\eta| \sim 0.7$, which contains more than 95% of the near side jet) there

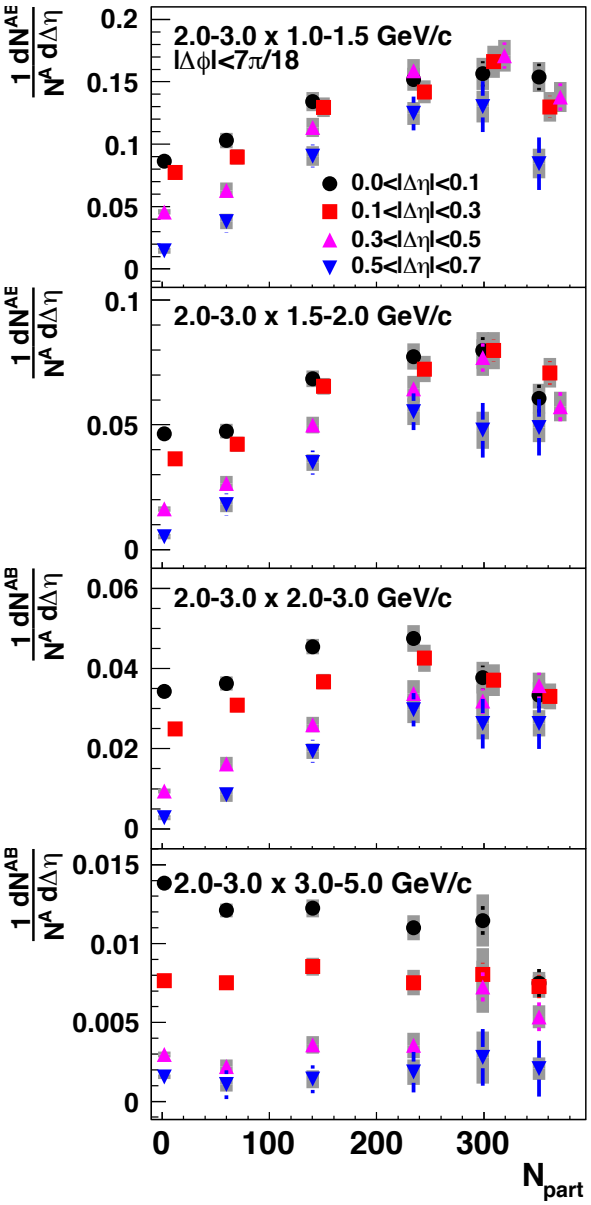

Figure 4.6: The Near side per trigger yields for various partner p_T and in different regions $\Delta\eta$ versus N_{part}. Trigger photon $p_T = 2.0 - 3.0$ GeV/c. Gray shade bands are the systematic errors from ZYAM and v_2 (Au+Au). The data points are shifted a bit to avoid overlap.

is always a non–negligible jet contamination. The level of jet contamination to any ridge characterization of the enhancement can be estimated from the non–zero yield in p+p at the same $\Delta\eta$ region, which is quite small in the outermost $0.5 < |\Delta\eta| < 0.7$ bin. Thus in what follows, we define our ridge yield as the excess of the near side yield in Au+Au compared to p+p for $0.5 < |\Delta\eta| < 0.7$:

$$Y_{ridge} = Y^{near}_{AuAu}|_{0.5<|\Delta\eta|<0.7} - Y^{near}_{pp}|_{0.5<|\Delta\eta|<0.7} \tag{4.1}$$

The potential effect of an interplay between near side jet modification and ridge yield is investigated, and an extra systematic uncertainty from this source is assigned to Y_{ridge}. To do this, different possible scenarios for the near side are assumed, including (i) jet broadening, (ii) jet suppression, and (iii) dilution–meaning a lowering of the per–trigger yield by the presence of the ridge or other non–jet trigger particles.

Here we discuss these three possible scenarios separately. The first is when the near side jet interacts with the medium, the number of associated particles in the jet–like correlation in Au+Au is the same as in p+p, but with a wider Gaussian width in $\Delta\eta$; we call this situation as "jet broadening". The second case assumes that the jet medium interaction does not change the shape of the jet, but the yield is modified. This is the case of near side jet suppression. We can simply write this as:

$$Y_{AuAu} = xY_{pp} + Y_{ridge} \tag{4.2}$$

where Y_{AuAu} is the total near side yield in Au+Au, Y_{pp} is the jet like yield in p+p and Y_{ridge} is the ridge yield. The factor x is the suppression in Au+Au, which is a function of centrality. In p+p collisions, Eq. 4.2 automatically leads to x =1 and $Y_{ridge} = 0$. The third case is near side jet dilution. In this analysis, the p_T of our trigger particle is between 2–3 GeV/c, where the medium response dominates, so some of our trigger particles may not come from jets, but instead arise the ridge. If the trigger particle is from the jet, then associated particles will come from both jet and ridge. If the trigger particle is from the ridge, then the associated particle will come from ridge only. We define this situation as jet dilution, which indicates the trigger from the jet is 'diluted' by triggers from the ridge. Since we report per trigger yields, we assume that x triggers are from jets, which carry x times $(Y_{pp} + Y_{ridge})$. There will be (1-x) triggers from the ridge, with associate particles (1-x) times Y_{ridge}. So the over all effect is

$$\begin{aligned} Y_{AuAu} &= x \times (Y_{pp} + Y_{ridge}) + (1 - x) \times Y_{ridge} \\ &= xY_{pp} + Y_{ridge} \end{aligned} \tag{4.3}$$

By comparing Eq. 4.2 and Eq. 4.3, we see that the jet dilution effect is equivalent to jet suppression. We will treat the two situations as one scenario. We fit the jet function to evaluate the yield of the ridge. The $\Delta\eta$ correlation functions are fitted by Eq. 4.4:

$$Y_{AuAu}(\Delta\eta) = \frac{Y_{jet}}{\sqrt{2\pi}\sigma_{jet}} \exp(-\frac{(\Delta\eta)^2}{2\sigma_{jet}^2}) + Y_{ridge} \tag{4.4}$$

There are three parameters in Eq. 4.4: the yield of jet like correlation, Y_{jet}, the jet width in the $\Delta\eta$ direction, σ_{jet}, and the yield of ridge, Y_{ridge}. The first step is to fit the p+p correlation with Eq. 4.4 by fixing $Y_{ridge} = 0$, as there is no ridge in p+p collisions at RHIC. Then we can extract the yield and Gaussian width in $\Delta\eta$ of p+p collisions.

In order to consider the scenarios of jet broadening and jet suppression, we use Eq. 4.4 to fit the $\Delta\eta$ correlation, but must fix different parameters according to different assumptions. In the jet broadening case, we fixed the jet yield to be equal to the yield in p+p, or $Y_{jet} = Y_{pp}$, and leave the jet width and ridge yield as free parameters. In the jet suppression case, we fix the jet $\Delta\eta$ width to p+p (i.e. $\sigma_{jet} = \sigma_{pp}$), and let the jet yield and ridge yield as free parameters.

$\Delta\eta$ correlation functions in various associated particle p_T and centrality bins such as Fig. 4.5(a) and Fig. 4.5(b) are fitted using Eq. 4.4. When testing the jet broadening scenario, where we fix the jet yield to p+p, the near side jet width increases with N_{part} as shown in Fig. 4.7. On the other hand, if we fit with the jet suppression scenario, where we fix the jet width to p+p, the near side jet yield in Au+Au decreases when increasing N_{part}, as shown in Fig. 4.8. The χ^2 of two different assumptions are tabulated in Table 4.1. From Table 4.1, the assumption of jet broadening generally gives smaller χ^2 value. But both assumptions give reasonable χ^2 values. So it is hard to say which assumption is better than the other. More important, either method gives a substantial ridge yield in central collisions, providing supporting evidence that the ridge has been observed in PHENIX.

In addition to the two extreme cases mentioned above, we also estimate the ridge yield through another method. We assume that the $Y_{Au+Au,near} = Y_{p+p,near} + Y_{ridge}$, or $Y_{ridge} = Y_{Au+Au,near}$ - $Y_{p+p,near}$, which assumes that near side Au+Au is simply a p+p like jet yield plus a ridge yield which is flat $\Delta\eta$. The ridge yield is simply the excess in Au+Au compare to p+p in different $\Delta\eta$ region.

This systematic uncertainty coming from this physical assumptions describes previously is included in Fig. 4.9 and other figures as the thin solid

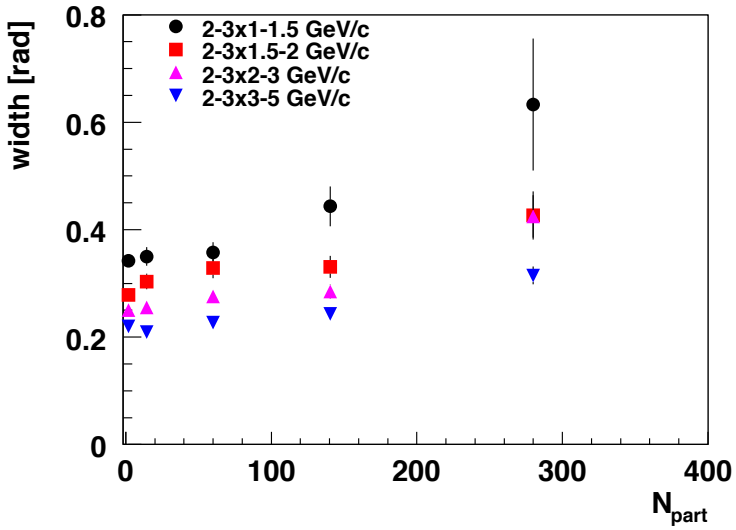

Figure 4.7: Jet broadening case, where the jet yield in the nearside is fixed and fit the jet width of the near side. Near side jet widths are plotted as a function of N_{part} and partner p_T

Table 4.1: χ^2 table for different fitting method (Degrees of freedom = 5)

assoc. p_T	Centrality	jet broadening	jet suppression
1.0–1.5	Cent–00–20	15.94	17.26
1.0–1.5	Cent–20–40	1.75	2.40
1.0–1.5	Cent–40–60	2.67	2.67
1.0–1.5	Cent–60–90	3.98	3.73
1.5–2.0	Cent–00–20	3.83	5.99
1.5–2.0	Cent–20–40	3.14	4.91
1.5–2.0	Cent–40–60	1.50	1.70
1.5–2.0	Cent–60–90	7.57	7.40
2.0–3.0	Cent–00–20	4.05	5.05
2.0–3.0	Cent–20–40	6.55	5.39
2.0–3.0	Cent–40–60	3.14	4.53
2.0–3.0	Cent–60–90	10.22	10.17
3.0–5.0	Cent–00–20	4.40	4.78
3.0–5.0	Cent–20–40	2.12	1.57
3.0–5.0	Cent–40–60	10.77	9.48
3.0–5.0	Cent–60–90	4.33	4.39

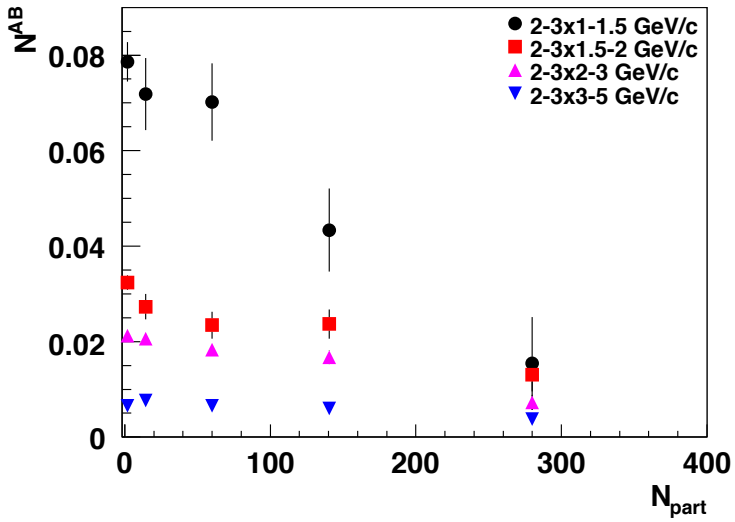

Figure 4.8: Near side jet suppression case. The jet width in near side is unmodified and fit the nearside jet yield Near side jet yields, N^{AB} are plotted as a function of N_{part} and partner p_T

brown lines which bracket the Y_{ridge} ($0.5 < |\Delta\eta| < 0.7$) data points.

The ridge yield defined by Eq. 4.1 can also be applied to the entire $\Delta\eta$ range, $0.0 < |\Delta\eta| < 0.7$. While the $0.5 < |\Delta\eta| < 0.7$ p+p jet like contribution is relatively small, the $\Delta\eta$ region $0.0 < |\Delta\eta| < 0.7$ contains approximately the full near side jet. The ridge yield per unit $\Delta\eta$ extracted in the $\Delta\eta$ regions ($|\Delta\eta| = 0.5$–0.7 and 0–0.7) are compared in Fig. 4.9. The ridge yield extracted from the two different $\Delta\eta$ regions are consistent with each other, indicating that the ridge yield is relatively flat in $\Delta\eta$ around $\Delta\eta = 0$.

4.5.2 Results

The final results of the ridge yield as a function of N_{part} in different partner p_T bins are shown in Fig. 4.9. At partner p_T below 3 GeV/c, the ridge yield is consistent with 0 at $N_{part} \approx 14$. The ridge yield increases with N_{part} up to $N_{part} \approx 250$. When $N_{part} > 250$, the ridge yield is constant, or even decreasing with increasing with N_{part} for the most central collisions. Similar trends in N_{part} have been observed previously by PHENIX [21]. At partner $p_T > 3$ GeV/c, the ridge yield is consistent with zero.

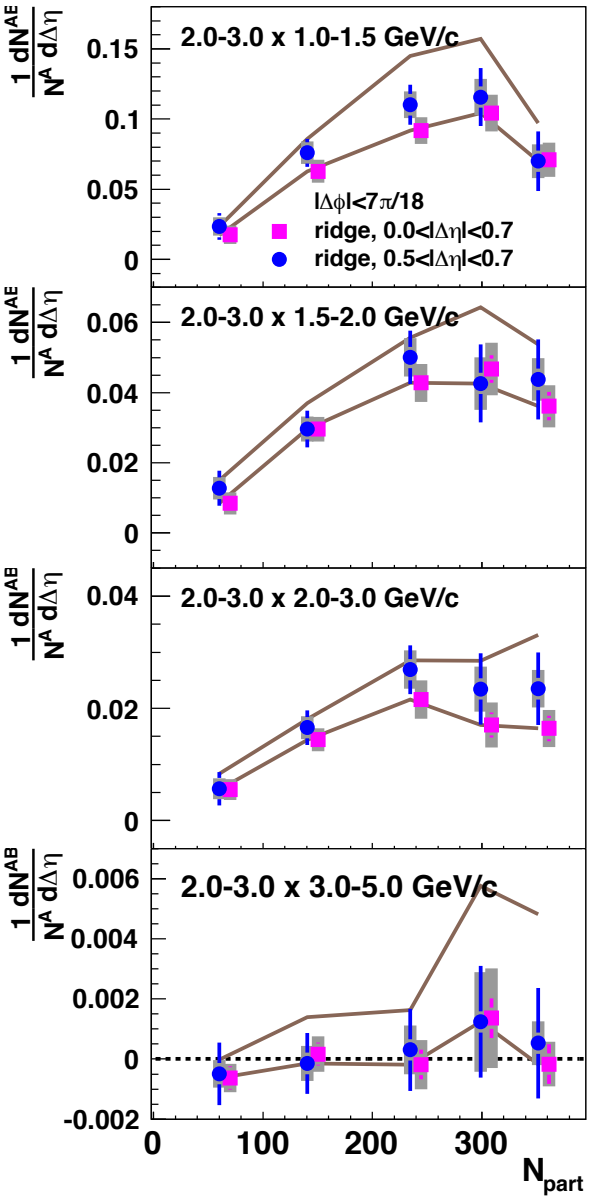

Figure 4.9: Ridge yields extracted by $Y_{ridge} = Y_{Au+Au,near}$ - $Y_{p+p,near}$ for trigger $p_T = 2.0 - 3.0$ GeV/c and various partner p_T in two different $\Delta\eta$ region ($0 < |\Delta\eta| < 0.7$ and $0.5 < |\Delta\eta| < 0.7$. The brown lines apply to $0.5 < |\Delta\eta| < 0.7$ and is the systematic error due to physics assumptions regarding ridge/jet modification interplay described in the text .

4.6 Extracting the Away Side Yields

4.6.1 Decomposing Different Components

We fit the jet functions to extract the contribution of different components of the away side correlation. This allows separating the two components, which we refer to as the *head* of the jet at $\Delta\phi = \pi$ and *shoulder* at $\Delta\phi \approx 2$ rad.

Eq. 4.5 is used to fit the full $\Delta\phi$ jet correlation function:

$$\begin{aligned} J(\Delta\phi) = \quad & \frac{Y_n}{\sqrt{2\pi}\sigma_n}\exp(-\frac{(\Delta\phi)^2}{2\sigma_n^2}) \\ & + \frac{Y_s}{\sqrt{2\pi}\sigma_s}\exp(-\frac{(\Delta\phi-\pi-D)^2}{2\sigma_s^2}) \\ & + \frac{Y_s}{\sqrt{2\pi}\sigma_s}\exp(-\frac{(\Delta\phi-\pi+D)^2}{2\sigma_s^2}) \\ & + \frac{Y_h}{\sqrt{2\pi}\sigma_h}\exp(-\frac{(\Delta\phi-\pi)^2}{2\sigma_h^2}) \end{aligned} \tag{4.5}$$

Eq. 4.5 has four terms. The first term describes the near side jet. The second and third term describe the shoulder, which has been considered a possible medium response due to the jet. These two terms peak at $\Delta\phi = \pi \pm D$. The last term is motivated by [24, 58], where the away side jet reappears at large p_T at $\Delta\phi = \pi$. We assume there is a remnant of a p+p like away side jet, which is called the "head".

In Eq. 4.5, we assume each component has a Gaussian shape. Y_n, Y_s, and Y_h (σ_n, σ_s, and σ_h) are the yield (width of the Gaussian) of the near side, shoulder and head respectively. D is the position of the shoulder to describe the displacement of the peak.

In order to reduce the number of fit parameters, we checked whether the width of the head could be fixed. We use Eq. 4.5 to fit the jet function in Au+Au to extract the width of the head component, σ^{head}. The result is shown in Fig. 4.10. We see the extracted width in Au+Au is consistent with p+p. Consequently, we fix the width of the head component to the width of the away side jet in the corresponding p_T bin in p+p collisions. The p+p away side width is tabulated in Table 4.2.

After fixing the width of the head component, we also tried to fix the position of the shoulder, parametrized by D in Eq. 4.5. After fixing the head width, we fit the correlation function to obtain the D in Eq. 4.5. In Fig. 4.11, D is plotted as a function of N_{part} at trigger p_T = 2–3 GeV/c, partner p_T

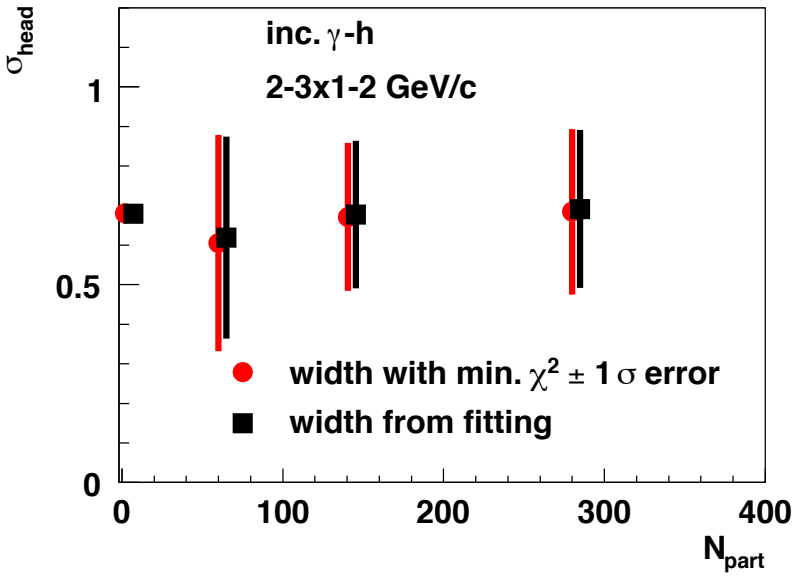

Figure 4.10: The width of the head component (punch through jet), σ^{head}, by fitting jet function with Eq. 4.5. trigger p_T = 2.0 – 3.0 GeV/c, partner p_T = 1.0 – 2.0 GeV/c.

= 1–2 GeV/c. The D does not vary significantly with N_{part}. Similar results are also found in other p_T bins. Based upon this study, we fix the position of the shoulder, D, to that obtained in the 0–20 % centrality bin, where the modification is most statistically significant. The values of D used in this analysis is tabulated in Table 4.3

Now we can fix the head width and the position of the shoulder, we are able to decompose the away side associated particle yields. $\Delta\phi = 7\pi/18$ is used as the separation point between the near and the away side. In the away side decomposition, fit only in between $7\pi/18 < \Delta\phi < (2 - 7/18)\pi$. The jet function of different centrality and $\Delta\eta$ bins is fitted by Eq. 4.5 without the term describing the near side:

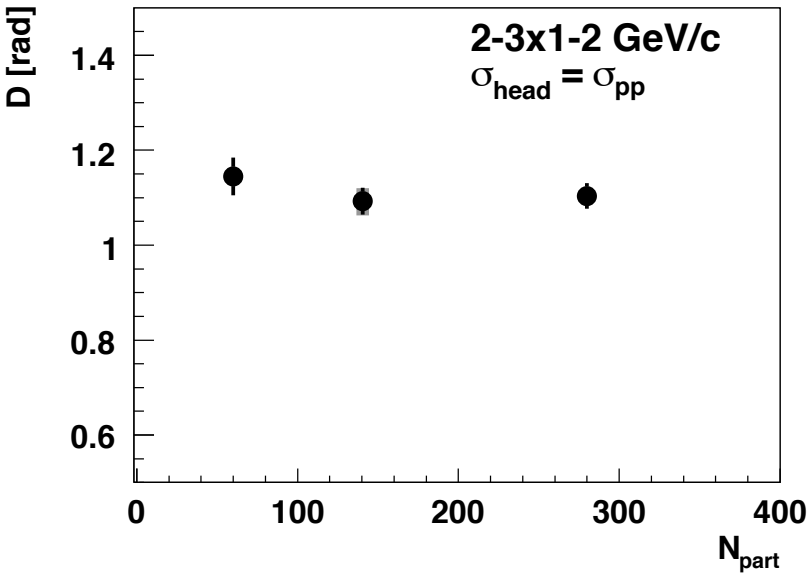

Figure 4.11: The position of the shoulder, D, from fitting with Eq. 4.5. Trigger p_T = 2.0–3.0 GeV/c, partner p_T = 1.0–2.0 GeV/c

$$
\begin{aligned}
J(\Delta\phi) = \quad & \frac{Y_s}{\sqrt{2\pi}\sigma_s}\exp(-\frac{(\Delta\phi-\pi-D)^2}{2\sigma_s^2}) \\
& + \frac{Y_s}{\sqrt{2\pi}\sigma_s}\exp(-\frac{(\Delta\phi-\pi+D)^2}{2\sigma_s^2}) \\
& + \frac{Y_h}{\sqrt{2\pi}\sigma_h}\exp(-\frac{(\Delta\phi-\pi)^2}{2\sigma_h^2})
\end{aligned} \tag{4.6}
$$

Eq. 4.6 is used to fit both Au+Au and p+p jet functions. When used to fit p+p, Y_s is fixed to 0 because this structure is not observed in p+p. As previously described, the width of the head region is fixed to the away side width in p+p, and the position of the shoulder is fixed by D in Table 4.2 and Table 4.3. Finally, there are only 3 free parameters in the fitting function: the yield of the head region, the yield of the shoulder region, and the width of the shoulder. We do not set any limit on these parameters.

A typical fit is shown in Fig 4.12. The left hand side of the plot shows a fit to the full $\Delta\phi$ range ($-\pi/2$ to $3\pi/2$) with Eq. 4.5, while the right hand side

Table 4.2: The p+p away side width in different partner p_T bins. Trigger p_T = 2–3 GeV/c

partner p_T [GeV/c]	width [rad]
1.0–1.5	0.702 ± 0.025
1.5–2.0	0.622 ± 0.031
1.0–2.0	0.679 ± 0.019
2.0–3.0	0.581 ± 0.031
3.0–5.0	0.532 ± 0.028

Table 4.3: The shoulder displacement, D(p_T), in different partner p_T bins at centrality 0–20. Trigger p_T = 2–3 GeV/c

partner p_T [GeV/c]	D [rad]
1.0–1.5	1.125 ± 0.030
1.5–2.0	1.030 ± 0.068
1.0–2.0	1.104 ± 0.027
2.0–3.0	1.166 ± 0.047
3.0–5.0	1.274 ± 0.132

shows a fit to the away side only, from $7\pi/18$ to $29\pi/18$, with Eq. 4.6. The magenta curve is the complete fit function, the red curve is the head, the blue is the shoulder, and the green is the near side. On left hand side, p1 is the near side yield, p2 is the near side width, p3 is the yield of one shoulder, p5 is the width of shoulder, and p6 is the yield of head. For right hand side, p3 is the yield of one shoulder, p5 is the width of shoulder, and p6 is the yield of the head, which has the same definition as left hand side. After fitting, we obtain the yield of head, shoulder and total away side yield by integrating the fitting function. The statistical error for these yield is obtained from the error matrix. The systematic error of the away side yield is coming from the determination of the ZYAM level and from the v_2 modulations.

4.6.2 Results

In Fig. 4.13 the two components of the away side yield along with the total yield are plotted versus N_{part}. As a crosscheck, the away side yield was also measured via direct integration over $|\Delta\phi| > 7\pi/18$. The result is consistent with the away side yield determined from the fits. The centralities used in the fitting analysis are 0–20%, 20–40% and 40–60%.

In Fig. 4.13, when the partner p_T is below 3 GeV/c, the total away side

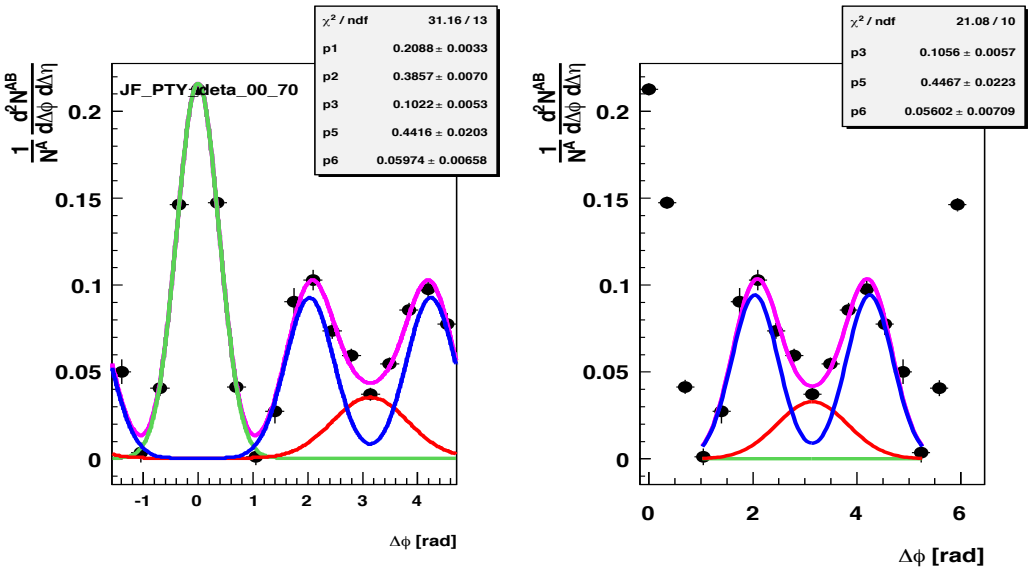

Figure 4.12: Fitting of the per trigger yield in the away side. Trigger p_T = 2.0–3.0 GeV/c, partner p_T = 1.0–2.0 GeV/c, centrality 0–20%

yield increases with N_{part}. This happens to be the p_T region where the shoulder is significant. There is also an obviously different trend in shoulder and head region versus N_{part}.

The decreasing trend of the head with increasing N_{part}, discussed above, is generally interpreted as the away side jet becoming more and more quenched inside the formed matter as the size of the medium increases [23, 58, 59, 60]. Similarly, the appearance of the shoulder has also been commonly attributed to this process, as the jet is quenched, particles appear at larger angle with respect to the jet axis to form the shoulder

For associated particles with $p_T > 3$ GeV/c, the total away side yield in Au+Au collisions is smaller than in p+p. This unambiguous suppression of the total away side yield in heavy ion collision is due to the the overwhelming domination of the jet–like "head" correlation with increasing p_T, and thus is another confirmation of the jet quenching effect.

4.7 Punch Through I_{AA}

$I_{AA}$is defined as the ratio of the yield between Au+Au and p+p jet yields [23]. The key drawback of I_{AA} is that it does not account for the crosstalk between

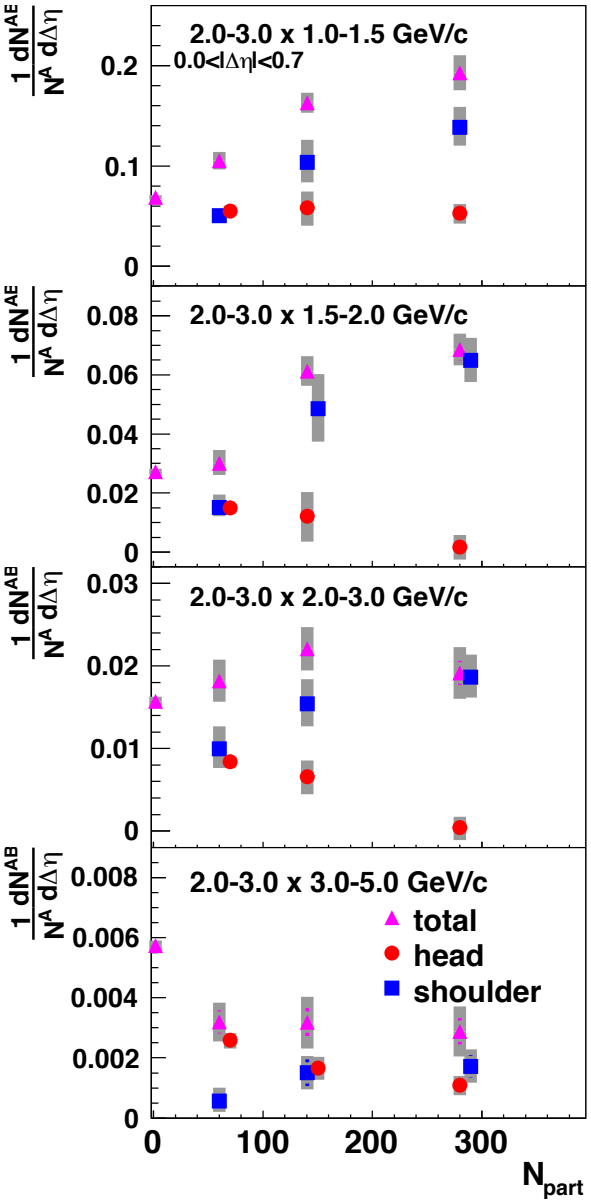

Figure 4.13: Per trigger yield of away side components: head, shoulder and total away side, vs N_{part}. Trigger p_T = 2.0 – 3.0 GeV/c and various partner p_T. Gray shaded band represents the combined systematic error from ZYAM and v_2.

the head and shoulder properly. To quantify the suppression of the punch through jet, we introduce a new parameter, the "punch through I_{AA}". The idea of the punch through I_{AA} is to quantify the suppression of the punch through jet, or head, in the medium. It is defined as

$$I_{AA,punch} = Y^{head}_{AuAu}/Y^{away-side}_{pp} \tag{4.7}$$

Fig. 4.14 shows the punch throgh I_{AA} as a function of N_{part} for different partner p_T bins. Punch through I_{AA} decreases from mid central to central Au+Au collisions. This indicates that increasing the medium increases the suppression of the punch through jet. To compare the suppression level, the π^0 R_{AA} (defined by Eq. eq:RAA) [20] for same p_T range (same as partner p_T)is plotted as well.

We also plot the punch through I_{AA} as a function of partner p_T in different centralities in Fig. 4.15. Here the punch through I_{AA} decreases with increasing partner p_T. The higher the partner p_T, the more suppression in the punch through jet.

4.8 Comparison of the Ridge, the Shoulder and the Underlying Event Background

In Fig. 4.6, at partner $p_T < 3.0$ GeV/c, the near side yield in Au+Au collisions is significantly larger than that in p+p collisions for rapidity $0.5 < |\Delta\eta| < 0.7$, due to the existence of the ridge. On the away side, the shoulder is also a sign of jet–medium interaction.

In two particle correlations, the combinatorial background increases with the number of participants. In order extract the jet signal, this background needs to be removed, leading one to wonder whether the ridge and shoulder structures arise from artifacts in the combinatorial background subtraction.

If the ridge is part of the combinatorial background, then the ridge yield should scale with the particle multiplicity in the underlying events. We study this via the ratio of the ridge yield to the yield of the combinatorial background integrated over the same $\Delta\phi$ range between the ZYAM points. Fig. 4.16 shows the ratio between the ridge yield and the yield of the underlying event, plotted as a function of N_{part} for different partner p_T. The ridge yield constitutes only a few percent of the underlying event. Furthermore, the ratio decreases at $N_{part} > 240$, which means the combinatorial background in the underlying event increases faster than multiplicity, or N_{part}. Therefore the non–flatness of the ratio means that the ridge yield is not produced by unsubtracted com-

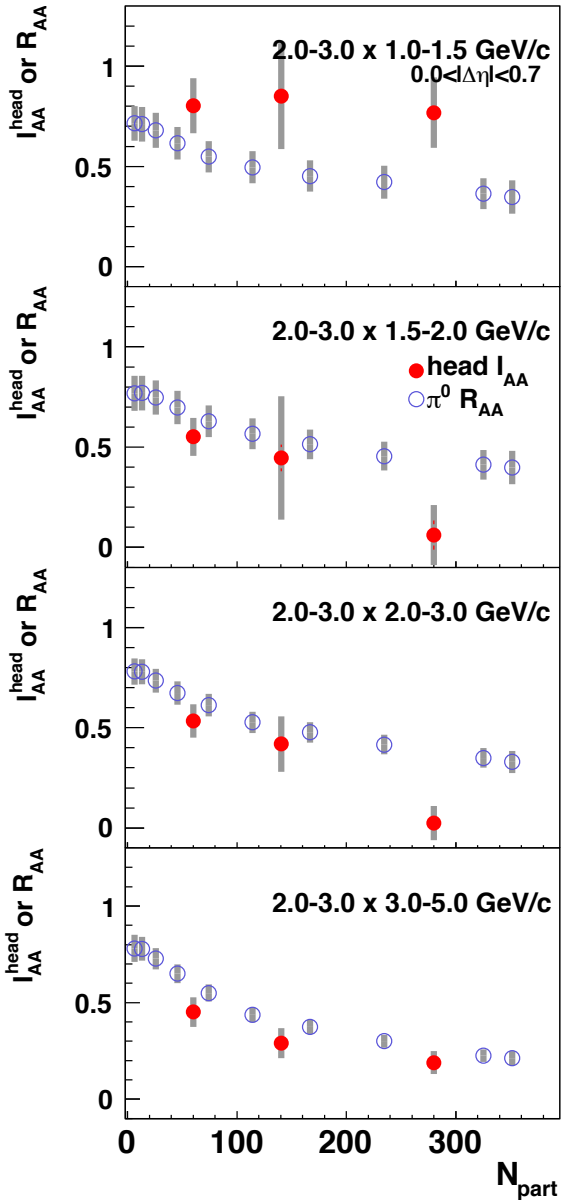

Figure 4.14: Punch through I_{AA} for trigger $p_T = 2.0 - 3.0$ GeV/c and various partner p_T vs N_{part}

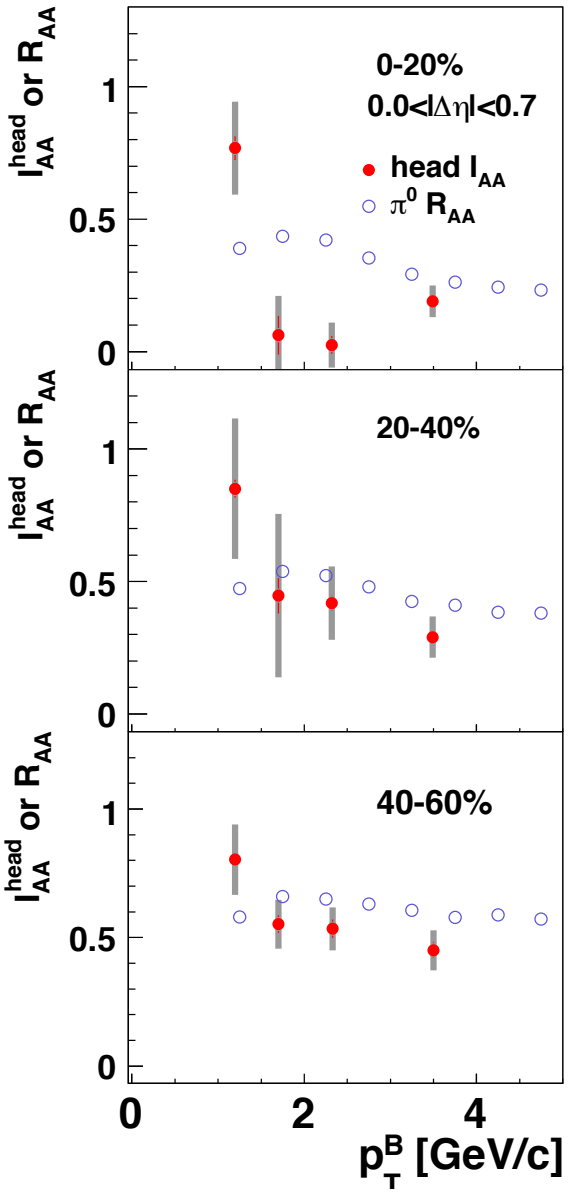

Figure 4.15: Punch through I_{AA} for trigger $p_T = 2.0 - 3.0$ GeV/c in various centrality vs partner p_T

binatorial background in the underlying event. We also observe that this ratio increases with partner p_T. This does not follow the particle spectrum, which decreases with momentum in the underlying event. From these observations it is clear that the ridge cannot simply be due to uncorrelated combinatorial background.

Similar procedures have been applied to the shoulder. The ratios of the shoulder to the combinatorial background on the away side are plotted as a function of N_{part} for different partner p_T, as shown in Fig. 4.17. The ratio decreases with increasing N_{part}, and increases with partner p_T, as was seen for the ridge.

We compare the two ratios together, as shown in Fig. 4.18. At partner p_T below 2 GeV/c, the two ratios are consistent with each other. At p_T larger than 2 GeV/c, the ratio of the shoulder to background is smaller than the ratio of the ridge at large N_{part}.

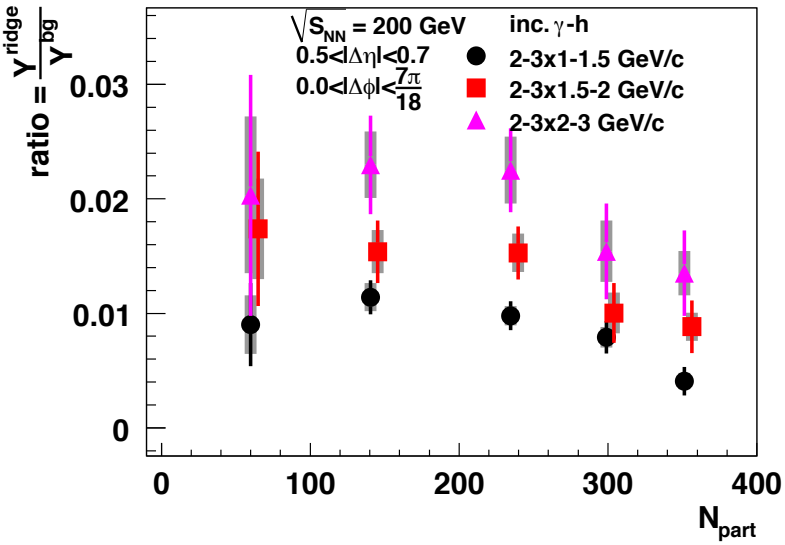

Figure 4.16: Ratios of the ridge yield to the underlying event in near side as a function of N_{part} for different partner p_T bins.

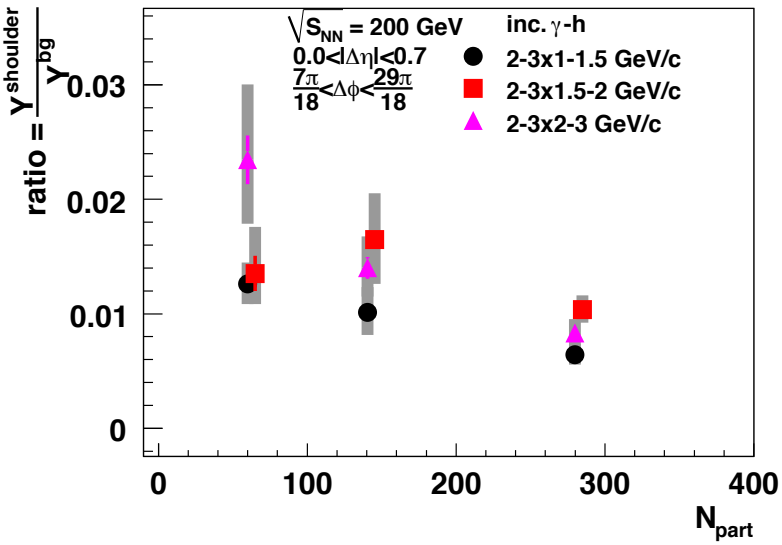

Figure 4.17: Ratios of the shoulder yield to the underlying event in away side as a function of N_{part} for different partner p_T bins.

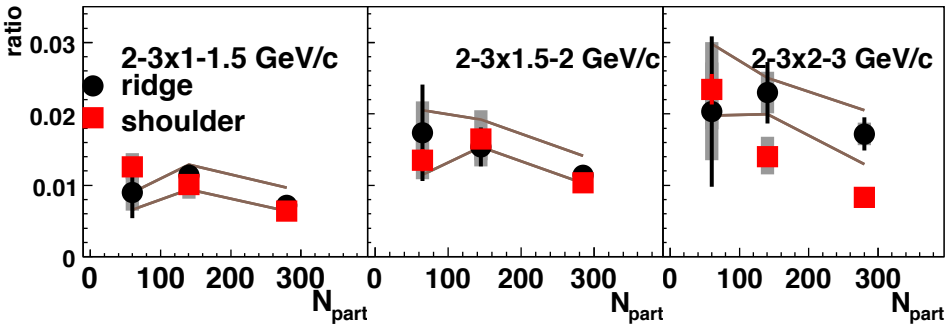

Figure 4.18: Ratios of the ridge (shoulder) yield to the underlying event as a function of N_{part} for different partner p_T bins.

4.8.1 Medium Modification and Comparison of Near–side and Away–side

The decomposition of the away–side allows comparison of the two jet induced modifications: ridge in the near–side and shoulder in the away–side. The two phenomena share many qualitative features. For example, as discussed above, the ridge appears to be constant over $\Delta\eta$. Fig. 4.4 suggests this is true for the shoulder as well. In fact, both of the preceding statements have been confirmed over much larger $\Delta\eta$ ranges by other experiments [25, 37]. Thus, the two phenomena seem to share this feature, as also previously noted in [61]. They are both "exotic" (compared to elementary collisions) and appear in similar p_T and centrality ranges. Thus it is very natural to look for more quantitative connections between the two phenomena.

Fig. 4.19 compares the yields of the ridge and shoulder as a function of N_{part}, in various partner p_T bins. When normalized per unit pseudo–rapidity, the yields are similar, both rising in the most central collisions to the level of about 0.2 charged particles above 1 GeV/c (integrating over all p_T bins shown) per trigger. At partner p_T below 2 GeV/c, the yield of the shoulder is larger than the ridge, but still consistent with the ridge, within systematic uncertainty. At partner p_T larger than 2 GeV/c, the two yields are even consistent numerically but uncertainties are increasing. At the highest partner p_T, 3–5 GeV/c, the ridge and shoulder are compatible within large systematic uncertainties, although the yield of ridge is approximately consistent with zero.

To further investigate the partner p_T dependence, we investigate the p_T and centrality trends of the ridge and shoulder separately. In Fig. 4.20, we normalized the ridge yield to that in the most central collisions, 0–5%. The normalized ridge yields are plotted as a function of N_{part} for different partner p_T bins. The centrality dependence of the ridge yield vs N_{part} is consistent from 1 to 3 GeV/c. This indicates that the centrality trend scales almost the same way for all p_T bins. A similar plot for shoulder yield is shown in Fig. 4.21. In this case, the N_{part} dependence is approximately the same over the whole p_T range, albeit with fewer centrality selections to reliably examine all three p_T bins.

At lower partner p_T, better statistics allows for the fitting decomposition in the away–side in finer centrality bins, especially in the most central collisions. Since the previous plots show no dependence on p_T, we compare the ridge and shoulder yields as a function of N_{part} at partner p_T = 1–2 GeV/c in Fig. 4.22. The most central collisions corresponds to 0–5% centrality. The two yields are numerically close and show a very similar p_T trend for N_{part} up to 250. At $N_{part} \approx 250$, the trend of the two yields start to deviate–the yield of the

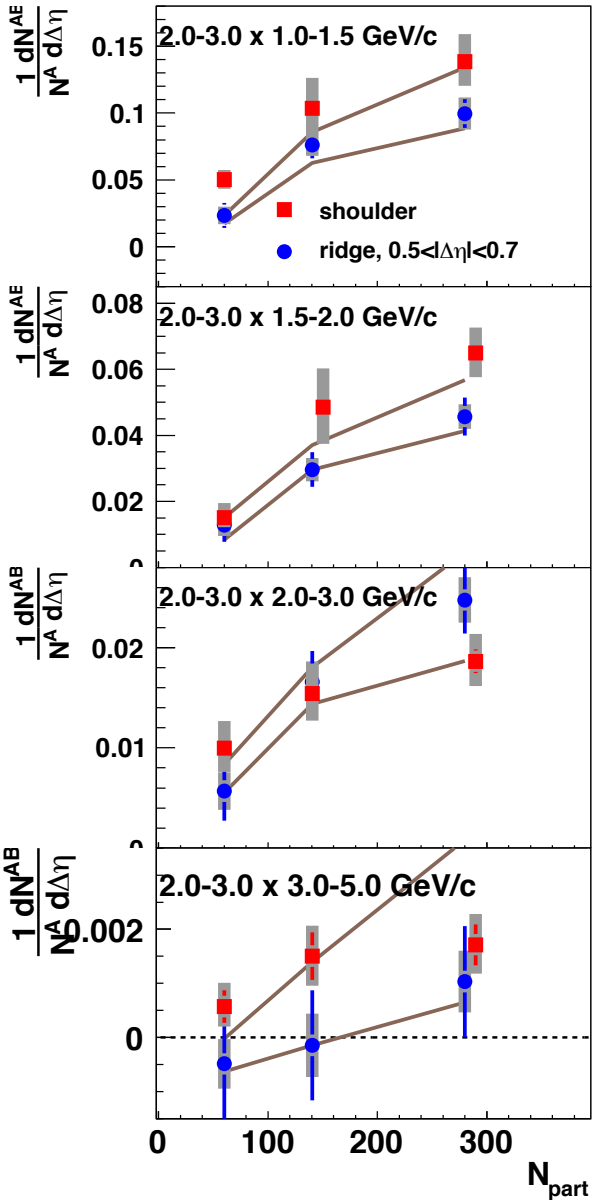

Figure 4.19: Yields of ridge and shoulder vs. N_{part} at trigger $p_T = 2.0 - 3.0$ GeV/c and various partner p_T. The green lines are the estimated systematic error of the ridge yields due to physics assumptions regarding the jet contamination and modification discussed in the text.

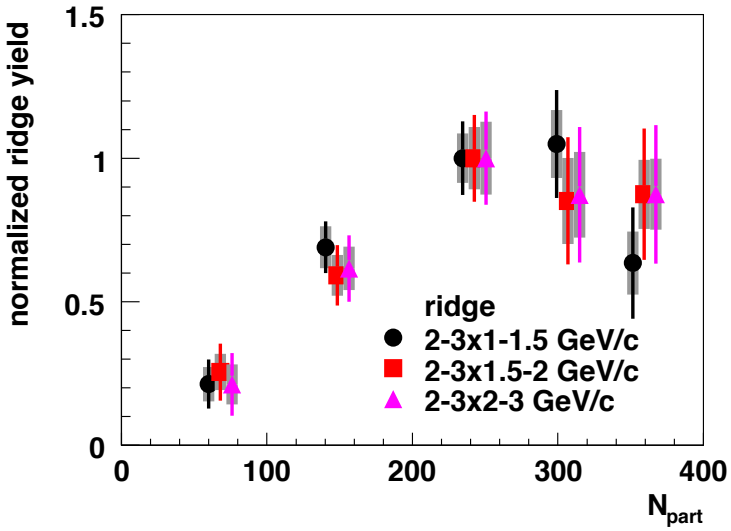

Figure 4.20: Normalized ridge yield vs N_{part}. The green lines are the estimated systematic error of the ridge yields due to physics assumptions regarding the jet contamination and modification discussed in the text

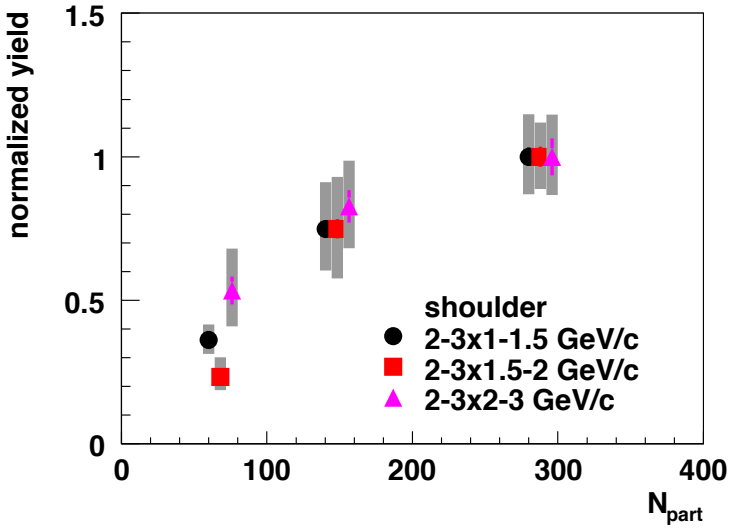

Figure 4.21: Normalized shoulder yield vs N_{part} in different partner p_T

shoulder keeps increasing while the yield of ridge shows hints (within the larger extra systematic) of flattening or even decreasing. However, this effect hinges on the single 0–5% point, where in other observables such as the baryon excess [62], deviations from an otherwise monotonic increase with centrality have also been observed.

Finally, by taking the ratio between the yield of shoulder and ridge which also cancels part of the systematic errors, we can best examine whether or not the two modifications scale the same way with centrality. The result is shown in Fig. 4.23. Although hinting at more complex behavior, the ratio is consistent with being constant in centrality within systematic uncertainties. The average value of the ratio across all centralities is 1.29 ± 0.08 (stat. only). So, although numerically close, they are not exactly the same–the shoulder yield is about 30% higher on average than that of the ridge across all centralities. It should be noted that given the discussion above about the $\Delta\eta$ independence of both phenomena, this ratio value is not specific to the PHENIX acceptance.

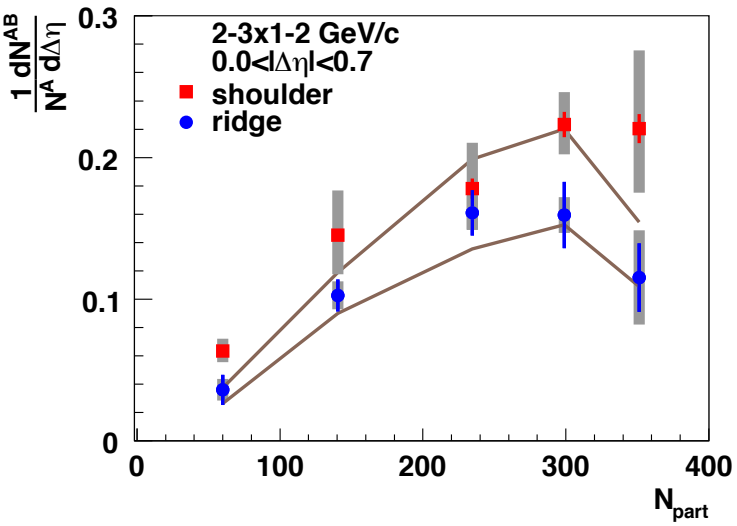

Figure 4.22: Yields of ridge and shoulder vs. N_{part} at trigger $p_T = 2.0 - 3.0$ GeV/c and partner $p_T = 1.0 - 2.0$ GeV/c. The brown lines are the estimated systematic error of the ridge yields due to physics assumptions regarding the jet contamination and modification discussed in the text.

In Fig. 4.24, we calculate the average per–trigger transverse momentum by integrating the per trigger yield weighted by the transverse momentum,

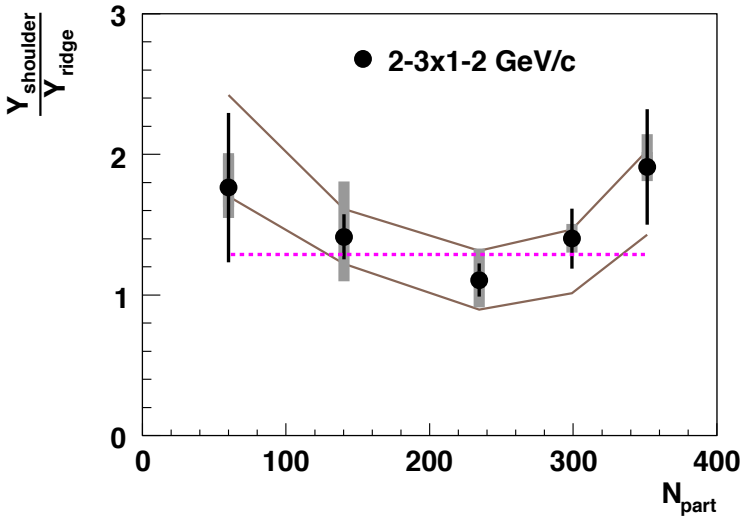

Figure 4.23: Ratio of the yields of shoulder over ridge vs. N_{part} at trigger p_T = 2.0 – 3.0 GeV/c and partner p_T = 1.0 – 2.0 GeV/c. The green lines are the estimated systematic error of the ridge yields due to physics assumptions regarding the jet contamination and modification discussed in the text. The average value of the ratio shown by the straight line is 1.29.

relative to the direction of the trigger particle. A weight factor of $p_T^B \cos\Delta\phi$ is used, where $\Delta\phi$ is the azimuthal angular difference between trigger and partner particle and the weighted yields are then integrated over p_T and $\Delta\phi$:

$$\frac{1}{N^A}\frac{d\langle p_T\rangle}{d\Delta\eta} = \int \frac{dN}{dp_T^B} p_T^B \cos\Delta\phi d\Delta\phi dp_T^B \tag{4.8}$$

By weighting with p_T, one can see how much transverse momentum is carried by the ridge and shoulder respectively. After weighting with p_T, the relative strength between the ridge and shoulder is changed. The p_T carried by shoulder is consistently *lower* than the p_T carried by ridge. The most important reason for this change is because the shoulder peaks at $\Delta\phi \approx 1.1$, so after weighting with a factor of $\cos\Delta\phi$, the contribution is more suppressed. Furthermore, one might argue that the p_T of the trigger itself should be added to the ridge total, and thus the imbalance could presumably be even larger.

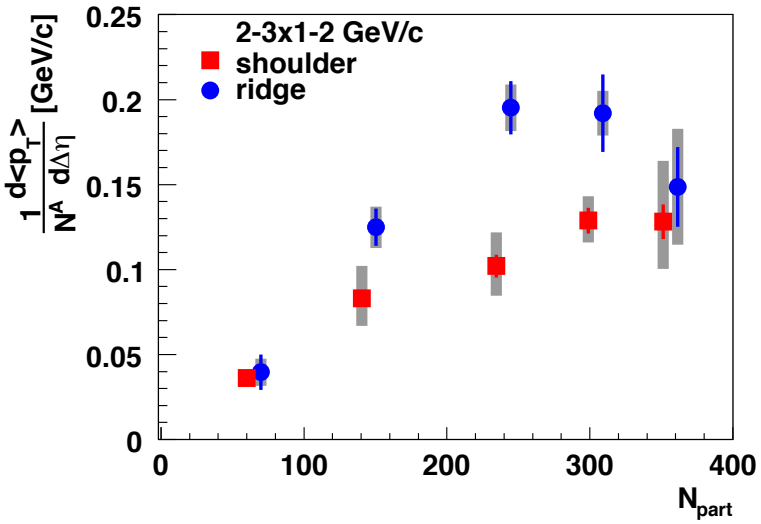

Figure 4.24: p_T weighted yields of ridge and shoulder vs. N_{part} at trigger p_T = 2.0 – 3.0 GeV/c and partner p_T = 1.0 – 2.0 GeV/c

4.8.2 Transverse Momentum in Near and Away side

In Fig. 4.13, the away side yield is suppressed at partner $p_T > 3$ GeV/c and is enhanced below 3 GeV/c. This leads to a fundamental question: where does

the energy lost by those high p_T particles go and does that energy reappear as the enhancement of the lower p_T particles?

In order to answer this question, we again use transverse momentum as our observable. In hard scattering, transverse momentum is a conserved quantity. In reality, it is impossible to collect all the particles. But we can use p+p collisions as a reference for the collisions without medium effects, and see how much transverse momentum is carried in both the near and away side in a certain p_T range. When the hard scattering happens inside the medium, the jet–medium interaction may redistribute the transverse momentum. Comparing the transverse momentum in the near and away side between Au+Au and p+p in the same p_T range may offer more information about the medium.

The per trigger yields in Fig. 4.6 and Fig. 4.13 were weighted with the mean partner p_T along the direction of the trigger particles of each p_T bin according to Eq. 4.8. We first look at partner p_T between 1–2 GeV/c in Fig. 4.25. The transverse momentum in both near and away side are plotted as a function of N_{part}. In the left panel, we see, as expected, that the mean p_T carried in the near side in heavy ion collisions is significantly larger than in p+p. This enhancement is mostly due to the existence of the ridge.

In the right panel, the awayside is plotted with its different components, where the head corresponds to the jet like correlation, the shoulder represents the medium modification, and the sum of the two is the total transverse momentum in the away side within the p_T range. We see that the p_T carried in the head region decreases with increasing N_{part}, which means the p_T carried by the head region is lost inside the medium. This is consistent with the jet suppression observed in previous measurements. For the shoulder region, the trend of the transverse momentum is similar to the ridge yields, which increases with N_{part}.

Adding the p_T carried in head and shoulder together gives the p_T carried in total away side. The transverse momentum carried in the away side increases with N_{part}. This indicates that in this partner p_T range, 1–2 GeV/c, even though the p_T carried in the head region is suppressed, the p_T lost in the head region apparently reappears in the shoulder region. The excess of total away side momentum in central Au+Au collisions also indicates that the away side may even pick up additional momentum from the medium. Another possibility for the enhancement may be that the momentum lost by high p_T particles due to jet quenching reappears in the lower p_T region.

In Fig. 4.13, at partner p_T of 3–5 GeV/c, the away side is suppressed. In order to see if the lost momentum at high p_T reappears as the transverse momentum enhancement at low p_T, we summed over partner p_T between 1–5 GeV/c, which also includes the p_T region where the away side is suppressed

and the result is plotted as a function of N_{part} in Fig. 4.26. The trends in Fig. 4.25 all hold here. The near side carries more p_T in Au+Au than in p+p. On the away side, the total transverse momentum in central Au+Au collisions is larger than p+p. Even though the momentum in the away side is smaller than p+p at p_T = 3–5 GeV/c due to jet quenching, the total away side transverse momentum in away side is still larger than p+p when summed over 1–5 GeV/c.

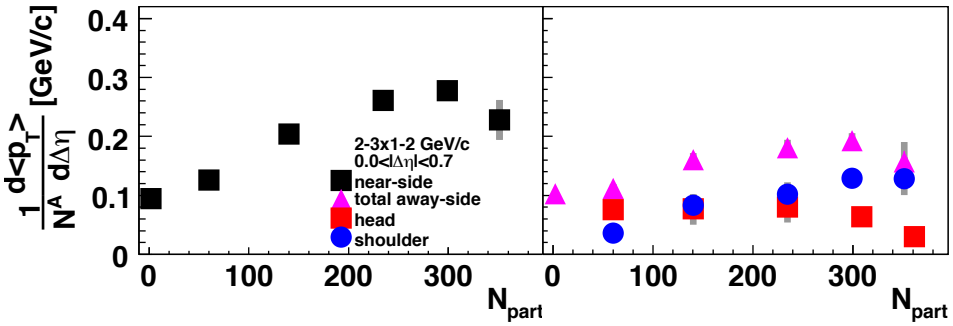

Figure 4.25: p_T weighted yields of near and away side vs. N_{part}. Trigger p_T = 2.0 – 3.0 GeV/c and partner p_T = 1.0 – 2.0 GeV/c

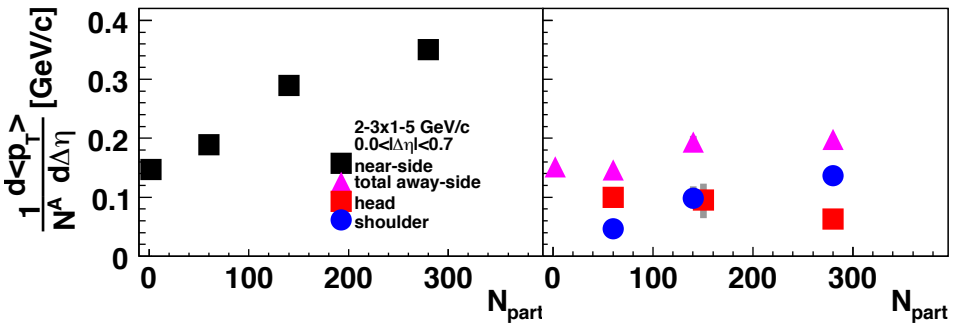

Figure 4.26: p_T weighted yields of near and away side vs. N_{part}. Trigger p_T = 2.0 – 3.0 GeV/c and partner p_T = 1.0 – 5.0 GeV/c

Thus the p_T lost by the head appears to be recovered as the p_T gained in the shoulder. This could be the first evidence of a direct connection between the awayside jet correlation and the shoulder enhancement, such that the quenched jet p_T is pushed or redirected into the shoulder, as would be the case in many of the speculated enhancement sources [42, 63, 64, 65, 66].

On the other hand, since the total transverse momentum summed over 1–5 GeV/c in the away side is enhanced in Au+Au compared to p+p, this implies that the momentum enhancement in low partner p_T is more than the transverse momentum lost in the away side at high partner p_T. Since the momentum lost at high p_T can not account for the enhancement of transverse momentum at low p_T, this suggests that the jet may also carry out some particles from the medium.

In this analysis, the partner p_T range is 1–5 GeV/c. Even though we did not include the full possible p_T range, the result does not change if we extend the measured p_T range. In [23], for partner p_T above 5 GeV/c, the conditional yield is about 2 orders of magnitude smaller than the conditional yields at 1 GeV/c, so even weighted with momentum, the contribution to the total transverse momentum is negligible. Also in [23], for partner p_T below 1 GeV/c, the away side yield in Au+Au is consistently larger than in p+p. When we weighting with p_T, the away side in Au+Au still carries more p_T than p+p. So this does not change the conclusion that the total transverse momentum in away side in Au+Au is larger than in p+p.

4.9 Spectra and Truncated Mean p_T

The spectra of the ridge, head and shoulder are measured and plotted in Fig. 4.27. In order to measure the trend of the spectra, we use the truncated mean p_T, $< p'_T >$ to describe the shape of the spectra. The truncated mean p_T is defined as

$$< p'_T >= \frac{\sum_{p_T^{min}}^{p_T^{max}} p_T \frac{dN}{dp_T} dp_T}{\sum_{p_T^{min}}^{p_T^{max}} \frac{dN}{dp_T} dp_T} - p_T^{min} \tag{4.9}$$

Here the partner p_T range is 1–5 GeV/c. The truncated mean p_T as a function of N_{part} for each component is shown in Fig. 4.28. Both the near and away–side yield for p+p are measured as well as a reference for the hard scattering. The truncated mean p_T of the inclusive hadrons is used to represent the medium. Within the large ridge uncertainties, ridge and shoulder are consistent as is expected from previous discussions. Despite the large uncertainties, it appears that the most probable value for the ridge $< p'_T >$ is in fact the same as the shoulder. Both are consistently softer than their p+p counter part, which likely means neither comes purely from hard scattering processes. But when comparing with the spectra of the inclusive charged hadrons, the shoulder is slightly harder while the ridge is consistent with the inclusive charged

hadrons. This is in contrast to the the head region, where in central collisions, $< p'_T >$ is even lower than inclusive charged hadrons. As in [23], this should be interpreted as the punch through jet being so suppressed that the yield is in fact close to completely gone. Going from central to peripheral, the $< p'_T >$ rises, which is consistent with decreasing suppression.

4.10 Summary

In this analysis, we present the inclusive photon–hadron two particle $\Delta\eta$–$\Delta\phi$ correlations measured in Au+Au collisions at $\sqrt{s_{NN}} = 200$ GeV. We decompose correlation function in $\Delta\eta$ and $\Delta\phi$ to disentangle contributions from the medium and the punch–through and trigger jets. Upon correcting the underlying event for elliptic flow, the ridge is observed for associated particle p_T below 3 GeV/c; it is broad in rapidity and narrow in $\Delta\phi$. The away side correlated particle yield is enhanced in central collisions. The yield of particles in the shoulder grows with centrality while the away side punch–through jet is suppressed. Remarkably, the ridge closely resembles the shoulder in the centrality dependence of particle yield and spectra. The truncated mean p_T of the ridge and shoulder are also consistent with the inclusive charged hadrons from the medium, which indicates the two structures are strongly related with the medium. With more understanding of the shape of the underlying event background, the shape of the subtracted correlation function may be changed as well, and so does our understanding of jet–medium interaction.

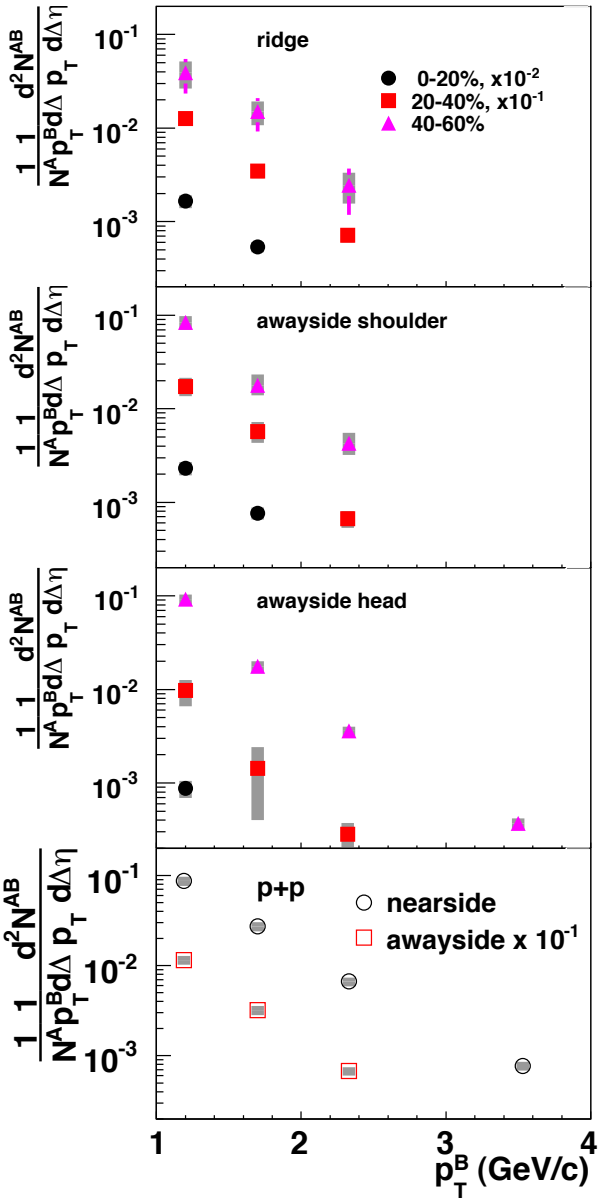

Figure 4.27: Spectra of ridge, shoulder and head for trigger $p_T = 2.0 - 3.0$ GeV/c.

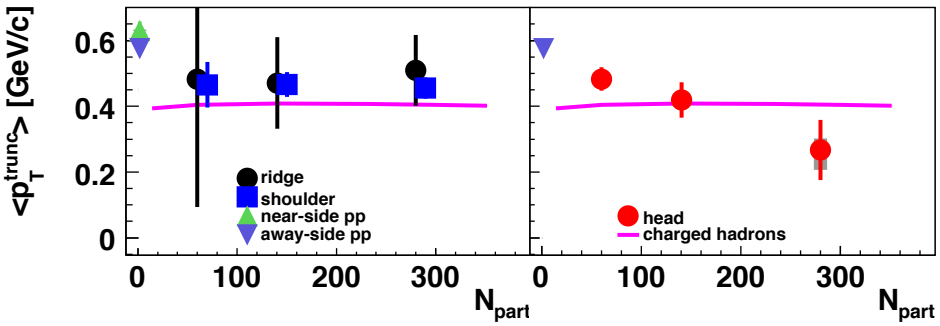

Figure 4.28: Truncated mean p_T of spectra of ridge, shoulder and head for trigger p_T = 2.0 – 3.0 GeV/c and partner p_T = 1–5 GeV/c.

Part III

Analysis: v_n

Chapter 5

Measurement of Effects on Higher Harmonics of the Collective Flow Correlations

5.1 Introduction

There are several explanations for the ridge and shoulder structures (see Sec. 3.1. However, higher harmonics of the collective flow have recently attracted a lot of attention [67]. v_3 is the third harmonic of the particle angular distribution, which corresponds to $\cos 3\Delta\phi$. v_3 has an intrinsic three peak structure over 2π, so it is natural to link v_3 with both the ridge and shoulder [67].

In a collision between two identical nuclei, by definition, at mid–rapidity there should be no odd harmonics in the particle distributions due to left–right symmetry. But in reality, the shape of the nuclei are not perfectly spherical. The fluctuations of the shape breaks the left right symmetry, the odd moments of the harmonics, such as v_3 become possible. Elliptic flow, or v_2, has become a standard measure of collective flow. v_2 is measured with respect to the direction of the reaction plane, ψ, with the forward detectors, such as the Reaction Plane Detector (RXN), Beam Beam Counter (BBC), or Muon Piston Calorimeter (MPC), which is a forward electromagnetic calorimeter located at $3.1 < |\eta| < 3.7$. Then we can measure the particle azimuthal angular distribution with respect to the reaction plane and extract the v_2 [19].

One way to measure v_3 is to measure the orientation of the third event plane, ψ_3, then follow a similar method to that used to measure v_2 [68]. Two particle correlations provide another way to measure v_n. The two particles come from the same event, so must share the same reaction plane direction ψ. By taking the relative azimuthal angle of the two particles, the direction of the reaction plane cancels out automatically. So there is no need to measure the direction of the reaction plane. The Fourier analysis of the correlation

function yields explicitly all n–th order Fourier coefficients. This method was first applied in early PHENIX v_2 measurements [69]. We have now applied Fourier expansions on two particle correlations to extract the first four flow coefficients, v_1, v_2, v_3 and v_4.

5.2 v_n in Event Plane Method

As mentioned above, there are two major methods to measure v_n: by reconstructing the event plane and by analysis of two particle correlations. Here we briefly describe v_n measurements with the event plane method. This is a well established approach to extract v_2 [48, 18, 19], as described in Sec. 3.5. PHENIX now extends the event plane method to higher harmonics. The event plane has been determined with the Reaction Plane Detector (RXN, $1 < |\eta| < 2.8$, the Beam–Beam Counter (BBC, $3.1 < |\eta| < 3.9$) and the Muon Piston Calorimeter (MPC, $3.1 < |\eta| < 3.7$). The nth event plane is determined by the following relation

$$Q_x \equiv |\vec{Q_n}| \cos(n\psi_n) = \sum_i^M w_i \cos(n\phi_i), \tag{5.1}$$

$$Q_y \equiv |\vec{Q_n}| \sin(n\psi_n) = \sum_i^M w_i \sin(n\phi_i), \tag{5.2}$$

$$\psi_n = \frac{1}{n} \tan^{-1}\left(\frac{Q_y}{Q_x}\right), \tag{5.3}$$

which is the same as Eq. 5.16. The v_n with respect of the event plane ψ_n can be measured as

$$v_n(\psi_n) = \frac{\cos(n[\phi - \psi_n])}{\Delta\{\psi_n\}} \tag{5.4}$$

where $\Delta\{\psi_n\}$ is the event plane resolution.

The correlation strength, $\left\langle \cos(j[\psi_n^A - \psi_m^B]) \right\rangle$ between various forward detectors are measured as a function of centrality. Here A, B are sub–events in forward detectors in different directions, separated by at least 5 units of pseudorapidity. The results are displayed in Fig. 5.1. Fig. 5.1(a) and (b) are cases where $m = n$. Strong correlations are found in all those cases. Note for n = 1, there is a anti–correlation, which is expected as a result of conservation of momentum in transverse direction.

The results are shown for $n \neq m$ in Fig. 5.1(c) and (d). We see that the first and second event planes are correlated with each other. The second and fourth planes have similar correlations, but with smaller strength. This agrees with our understanding that the even harmonics are strongly correlated with each other because the shape of the colliding region is close to an almond shape, for which ψ_2 and ψ_4 should line up together if the shape is perfectly symmetric. But when correlating the with second and third plane, which is shown in Fig. 5.1(d) and the correlation strengths are scaled by a factor of 20, we find that the second and third plane are basically uncorrelated. This shows that ψ_3 does not correlate with ψ_2, since the origin of ψ_3 is from fluctuations.

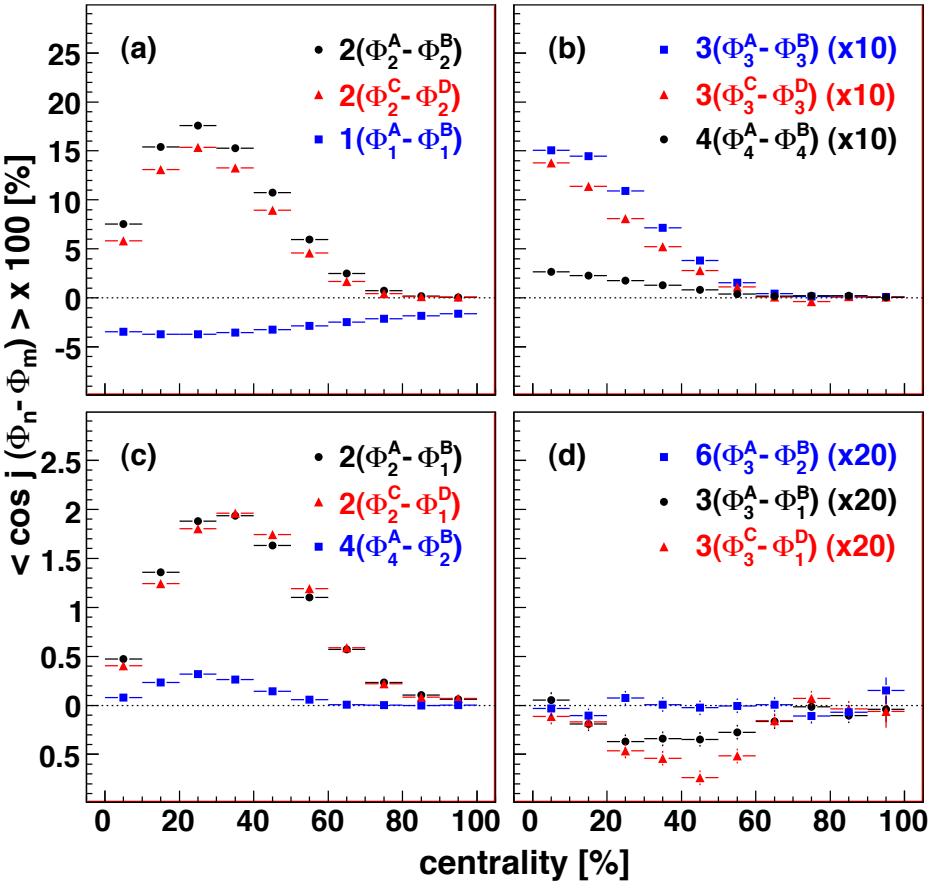

Figure 5.1: Raw correlation strengths of the event planes for various detector combinations as a function of collision centrality. The event planes are measured with the following forward detectors: (a) RXN North, (b) BBC South, (c) MPC North, and (d) MPC South.

The results of $v_2(\psi_2)$, $v_3(\psi_3)$ and $v_4(\psi_4)$ as a function of p_T in various centralities are shown in Fig. 5.2. Here the event plane is determined with the Reaction Plane Detector (RXN). We see a significant non–zero values for v_3 and v_4, increasing with p_T, similar to v_2. For v_2 and v_4, the values increase from central to mid–peripheral collisions, as expected from increasing shape anisotropy. v_3 does not show a similar trend. The value of v_3 in all centralities is very similar. The measured v_2 and v_3 are compared with two hydrodynamic models [67] and [70]. These models will be described in detail in Chapter 7. Both models agrees with data very well, especially for p_T below 1 GeV/c.

5.3 Analysis

The data is taken from the 2007 run (run7) with Au+Au at $\sqrt{s_{NN}} = 200$ GeV. Some special runs such as zero field runs, converter runs are removed. We also remove runs which has fewer than 1 million events. The event selection is similar to previous studies, which require the event centralities between 0–92% and the z–vertex measured by BBC is within 30 cm. For this two particle correlation measurement, both particles are charged hadrons.

We also applied $\Delta\eta$ cuts between particle pairs. From previous analysis, we know in the η acceptance of the PHENIX central arms ($|\eta| < 0.35$ or $|\Delta\eta| < 0.7$, there is a strong jet contribution at this η region. In order to remove the jet contributions as much as possible while still keeping enough singles, the η difference between the pairs with $\Delta\eta < 0.3$ are removed.

5.4 v_n from Correlation Function Method

5.4.1 Fourier Expansion

In a typical elliptic flow analysis, the particle distribution is written as Eq. 5.5

$$f(\phi) = \frac{dN(p_T)}{d\phi} = b_0 \sum (1 + 2v_n \cos(n(\phi - \psi_n))) \tag{5.5}$$

, where ψ_n is the direction of the reaction plane. Here v_n is defined as

$$< e^{in\phi} >= \int f(\Delta\phi) e^{in\phi} d\phi = v_n e^{i\psi_n} \tag{5.6}$$

For particle pairs, where $\phi_1 = \phi$, $\phi_2 = \phi + \Delta\phi$, the distribution is sensitive to v_n, where

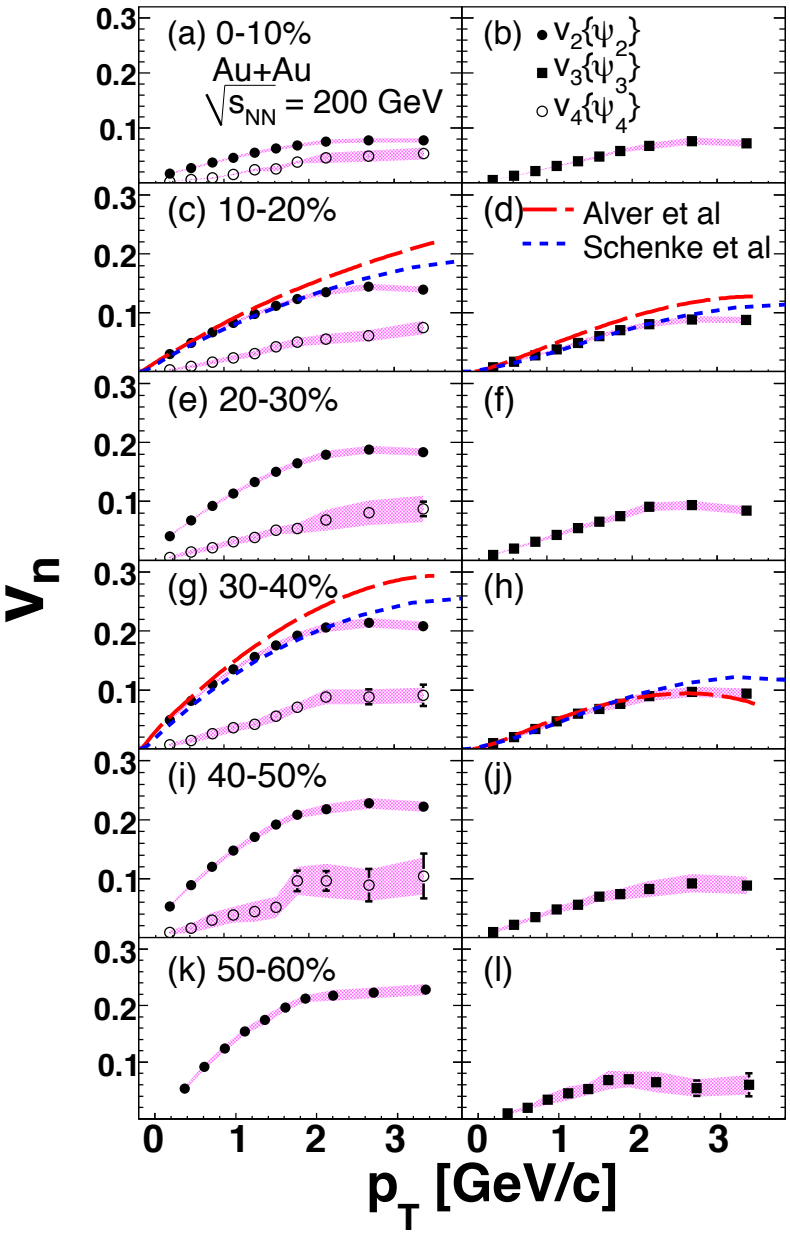

Figure 5.2: $v_n\{\Psi_n\}$ vs. p_T measured via the event plane method. The curves are calculations from two hydrodynamic models: Alver *et al.* [67] and Schenke *et al.* [70].

$$< e^{in\Delta\phi} >=< e^{in\phi_1} e^{-in\phi_2} >=< e^{in\phi_1} >< e^{-in\phi_2} >= (v_n)^2 \tag{5.7}$$

When both trigger and partner particles are below 1 GeV/c, the contribution from jet particle correlations can be ignored. And the two particle azimuthal correlations can be expanded as

$$\frac{dN^{pair}(p_T)}{d\Delta\phi} \propto \sum (1 + 2c_n \cos(n\Delta\phi)) \tag{5.8}$$

From Eq. 5.8, it is clear that there is no need to determine the direction of the reaction plane, ψ, when using the correlation function method. This simplification is because both particles are from the same event, and therefore share the same reaction plane. When calculating the difference of the azimuthal angle of the two, ψ cancels out naturally.

In standard two particle correlation analyses in PHENIX [21, 22, 23, 24], the combinatorial background is assumed to be factorisable, that is

$$c_2(p_T^a, p_T^b) = v_2(p_T^a) \times v_2(p_T^b) \tag{5.9}$$

We follow the same assumption, for the higher harmonics,

$$c_n(p_T^a, p_T^b) = v_n(p_T^a) \times v_n(p_T^b) \tag{5.10}$$

When the p_T of the trigger is the same as the partner p_T, then Eq. 5.10 can be reduced to Eq. 5.11

$$c_n(p_T^a, p_T^a) = v_n^2(p_T^a) \tag{5.11}$$

Upon extracting the Fourier Coefficients of the correlation functions at low p_T, we obtain v_n.

The analysis is constructed in the following order:

- measure the correlation functions in various p_T and centrality bins
- extract the Fourier coefficients, c_n
- obtain the v_n coefficients

5.4.2 Correlation Functions

The Correlation functions are constructed for particle p_T from 0.5 to 3.0 GeV/c, in six centrality bins from 0–10% to 50–60%. Some of the correlation functions are shown as examples in Fig. 5.3 and Fig. 5.4. The two plots are for particle p_T between 0.5–0.6 and 1.5–2.0 GeV/c in six centralities.

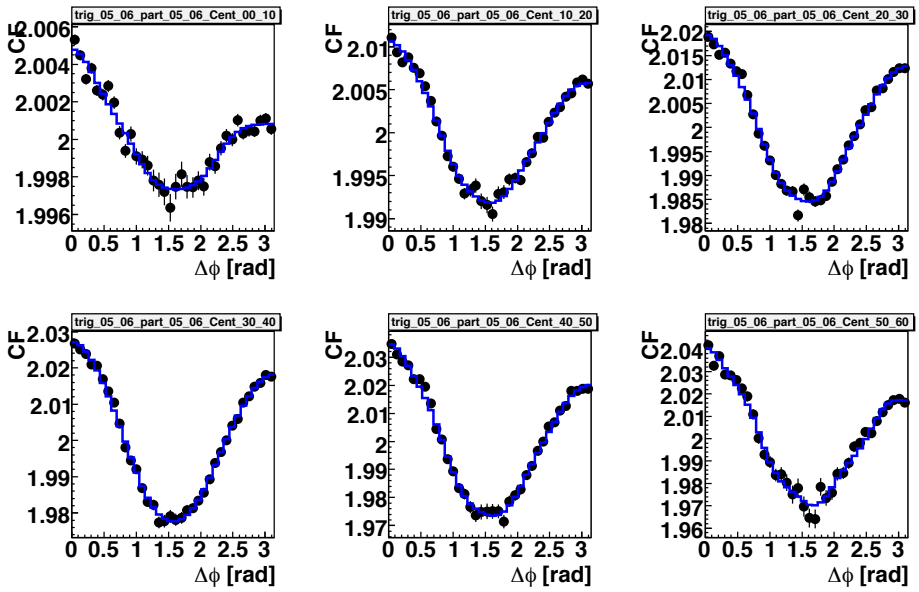

Figure 5.3: Correlation functions for trigger and partner at 0.5–0.6 GeV/c at various centralities. The blue curve is the sum of the Fourier spectra.

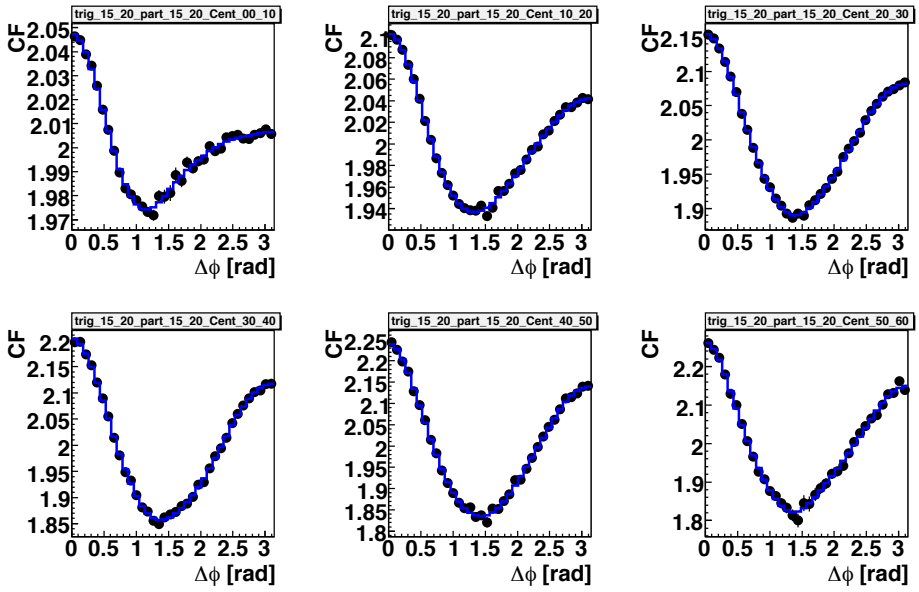

Figure 5.4: Correlation functions for trigger and partner at 1.5–2.0 GeV/c at various centralities. The blue curve is the sum of the Fourier spectra.

5.4.3 Extracting c_n

For the correlation functions shown in Fig. 5.3 and Fig. 5.4, we use Eq. 5.8 to extract the Fourier coefficients, c_n. Typical results for c_n are shown in Fig. 5.5, where the horizontal axis indicates the nth Fourier Coefficients. In these plots, we see that the second Fourier coefficients, which are equivalent to v_2, are significantly larger than the other coefficients. However the first and third components are also significant.

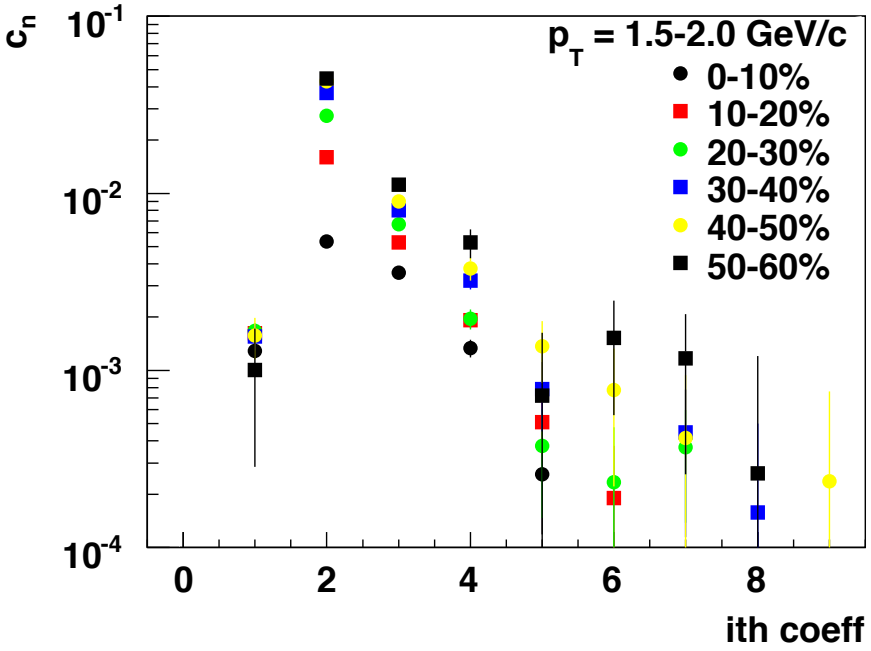

Figure 5.5: c_n for trigger and partner at 1.5–2.0 GeV/c at various centralities.

5.4.4 Extracting v_n

Since the correlation functions used to obtain c_n are symmetric in trigger and partner p_T, we can apply Eq. 5.11 to go from c_n to v_n. We will focus on the first four Fourier moments, v_1, v_2, v_3 and v_4.

We plot each v_n as a function of N_{part} and p_T. The results of v_n vs N_{part} are shown as Figures 5.6 to 5.9. v_1 shown in Fig. 5.6, is independent of p_T and decreases when going from peripheral to central collisions. For v_2 shown

in Fig. 5.7, the results are compared with previous PHENIX measurements [19] and shows good agreement. Fig. 5.8 shows a non–zero value of v_3 for all centralities and all p_T. The general trend here is (i)v_3 decreases with increasing N_{part}; (ii) v_3 increases with p_T. For v_4 (Fig. 5.9), due to statistics, v_4 fluctuates much more than lower v_ns. And because some of the c_4 values are negative, we set them to be zero to avoid taking the square root of a negative value.

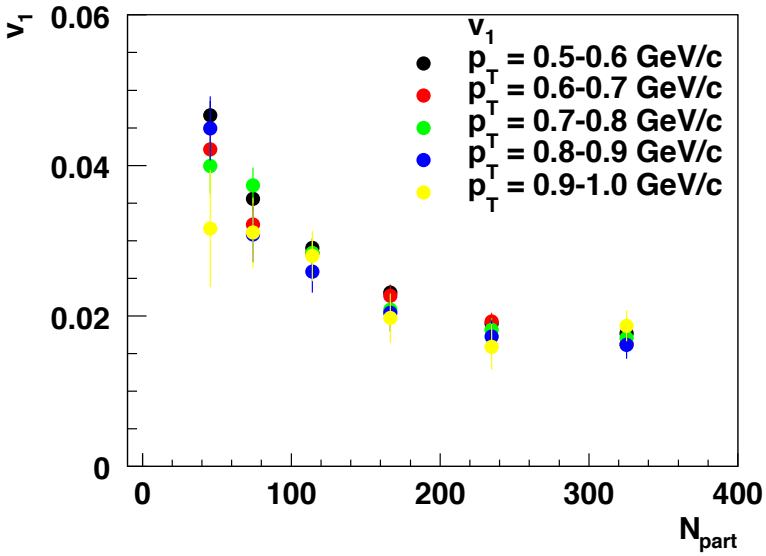

Figure 5.6: v_1 of various p_T as a function of N_{part}.

In Fig. 5.10 to Fig. 5.13, we plot the v_n as a function of p_T. Fig. 5.10 shows the trend of v_1. The v_1 is flat below 1 GeV, and increases with p_T at $p_T > 1$ GeV/c. There is no obvious difference between different centralities at $p_T > 1$ GeV/c. Fig. 5.11 plots v_2 vs p_T. The result is also compared with previous PHENIX measurement, which is measured by reaction plane method [19]. Both measurement agrees well at $p_T < 1$ GeV/c. At $p_T > 1$ GeV/c, there v_2 from two particle correlation method are slightly larger than the reaction plane method. The deviation increases from central to mid–peripheral collisions. The larger deviation at mid–peripheral and high p_T may come from the larger jet contamination. The result of v_3 is shown in Fig. 5.12. v_3 is non–zero and increases with p_T. v_3 also increases from central (centrality 0–10%) to mid–peripheral (centrality 50–60%) collisions. The v_4 measurement shown in Fig. 5.13 is similar to v_2, which also increases with p_T.

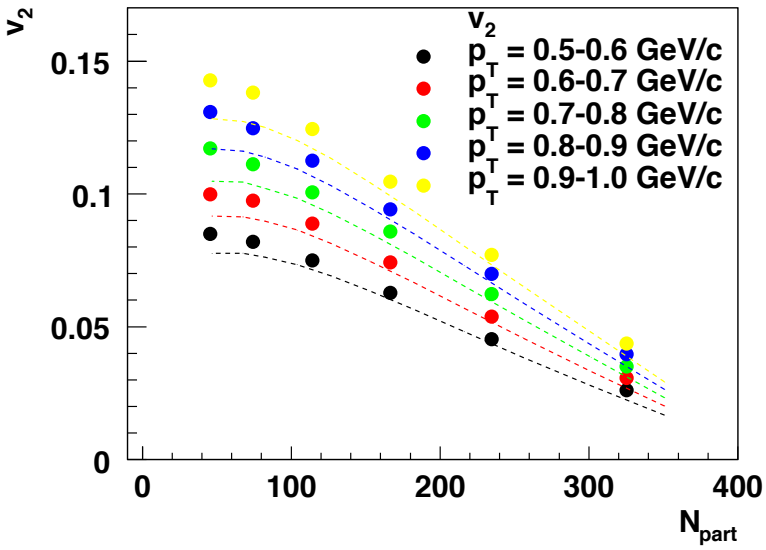

Figure 5.7: v_2 of various p_T as a function of N_{part}. The dash lines are v_2 measurements from [19].

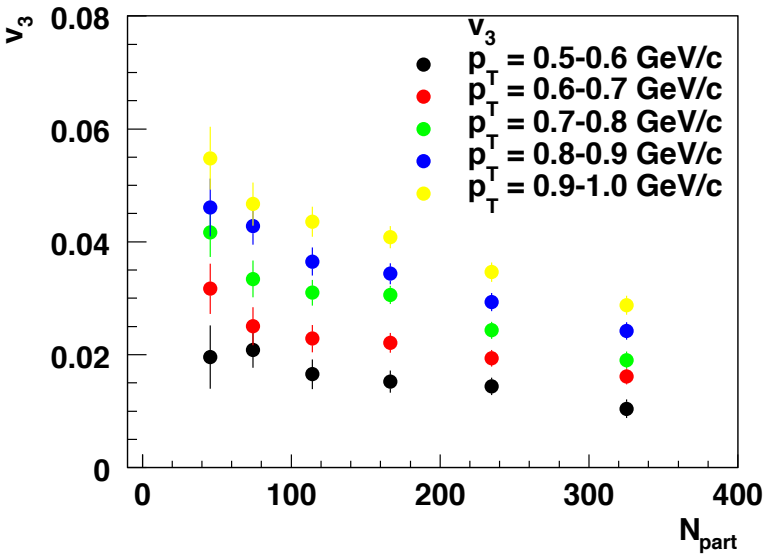

Figure 5.8: v_3 of various p_T as a function of N_{part}.

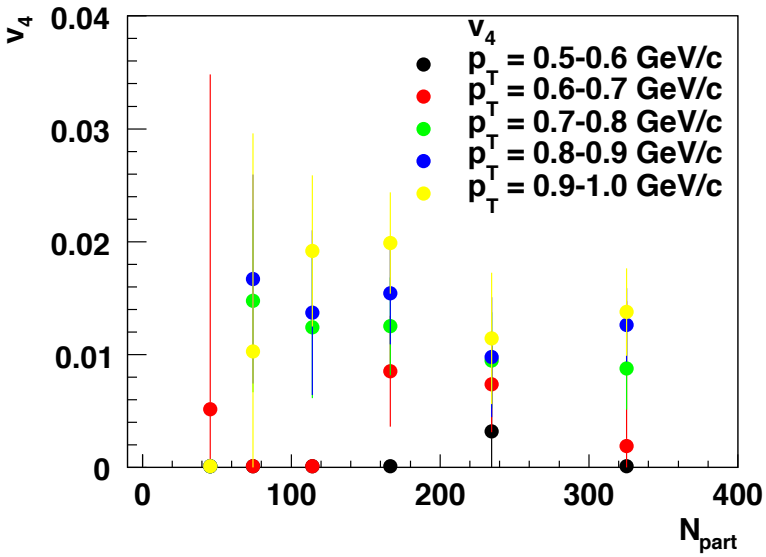

Figure 5.9: v_4 of various p_T as a function of N_{part}.

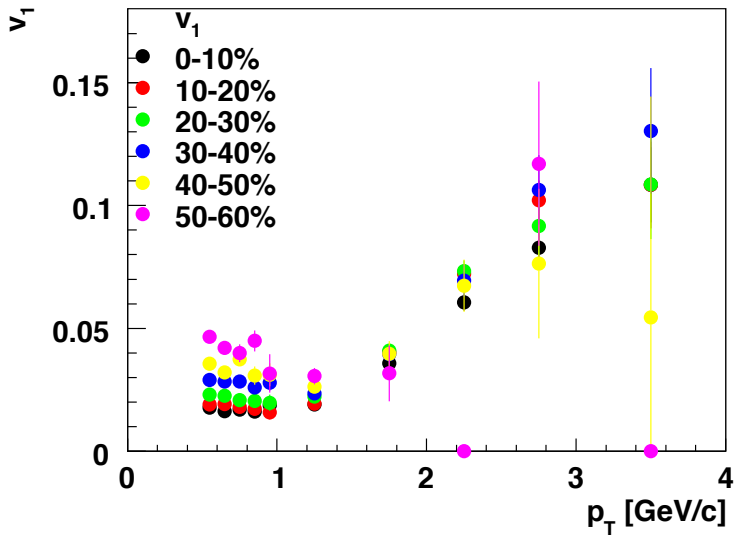

Figure 5.10: v_1 of various centralities as a function of p_T.

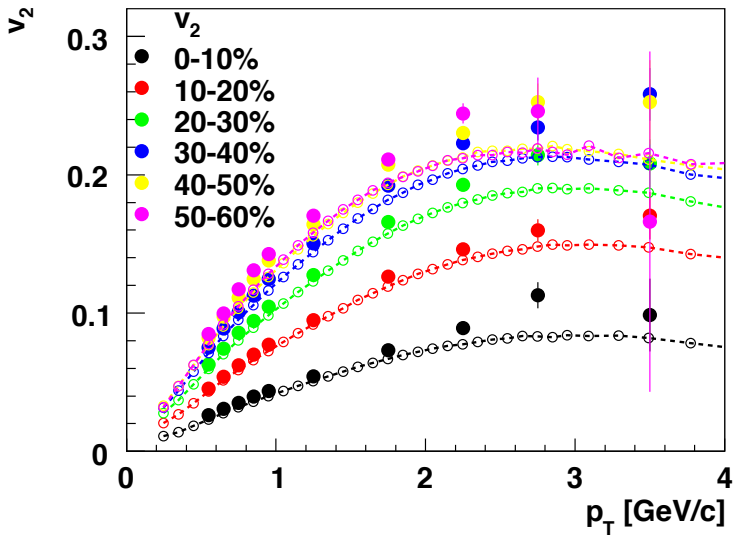

Figure 5.11: v_2 of various centralities as a function of p_T. The dash lines are v_2 measurements from reference [19].

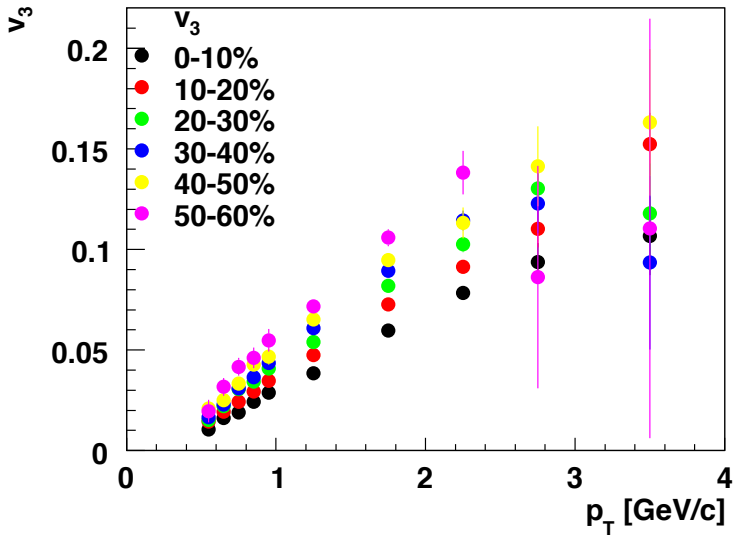

Figure 5.12: v_3 of various centralities as a function of p_T.

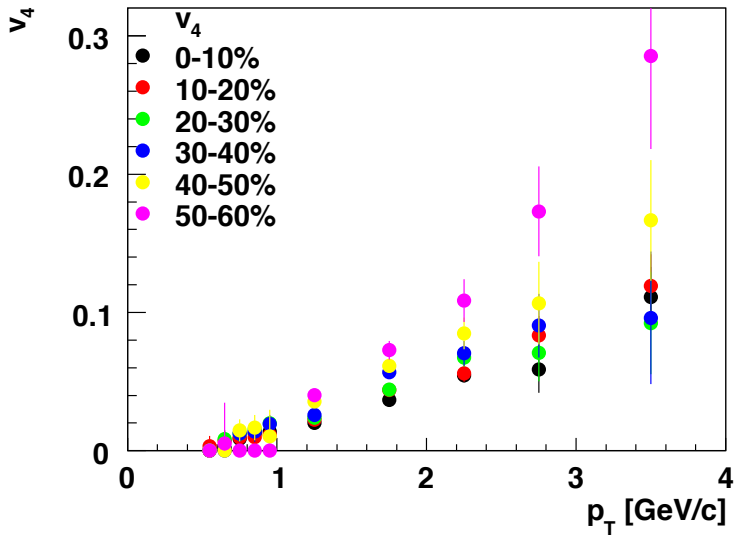

Figure 5.13: v_4 of various centralities as a function of p_T

5.5 Factorization of v_n

In the previous section, we made an assumption that

$$c_n(p_T^{trig}, p_T^{part}) = v_n(p_T^{trig}) \times v_n(p_T^{part}) \tag{5.12}$$

So when the trigger and the associated particle are at the same p_T, Eq. 5.12 can be reduced to

$$c_n(p_T) = v_n(p_T)^2 \tag{5.13}$$

Here we directly test this assumption. Eq. 5.13 is called the symmetric p_T method and Eq. 5.12 is the asymmetric p_T method. For the symmetric p_T method, both the trigger and the associated particles have the same p_T. In the case of the asymmetric p_T method, the p_T of the trigger particle is fixed at 0.5–1.0 GeV/c and the correlation function is measured with the associated particle in various p_T bins.

The v_2 and v_3 values of both the symmetric and asymmetric p_T methods are presented in Fig. 5.14 for v_2 and Fig. 5.15 for v_3 respectively. The top panel of Fig. 5.14 compares the v_2 measured by the symmetric (asymmetric) p_T method in red (black) in six different centrality bins. Both methods show

good agreement. The value ($v_2^{asymmetric}/v_2^{symmetric}$)-1 is plotted in the lower panel. This ratio shows the two measurements agree within better than 1% at low p_T and deviate at the 5% level at highest p_T. Similar comparison for v_3 is shown in Fig. 5.15. Both methods agree well at $p_T < 2.5$ GeV/c. The deviation is the largest at 50–60% and at $p_T > 2.5$ GeV/c.

5.6 $\Delta\eta$ dependence

In two particle azimuthal correlations, the $\Delta\eta$ separation between the particle pairs is important. At particle p_T below 1 GeV/c, the $\Delta\eta$ cut can help remove the HBT peak.

At higher particle p_T, the jet start to contribute in two particle correlations. The nearside jet has a Gaussian jet cone size about 0.3 in $\Delta\eta$ and $\Delta\phi$ direction. By requiring the particle pairs separate by 0.3 units of pseudorapidity, we can remove about 67% of the correlated near side pairs which are coming from jets. On the other hand, the ridge is constant along the η direction, so it will not be effected by the η cut.

For the awayside, the awayside jet swings along the full $\Delta\eta$ acceptance of PHENIX central arm, $|\Delta\eta| < 0.7$, as shown in Fig. 4.1(b). So the $\Delta\eta$ cut can not remove the awayside jet contributions, which will bias the v_n measurement.

In the current analysis, we require the two particles are separated by 0.3 unit in $\Delta\eta$, or $|\Delta\eta| > 0.3$. We vary the $\Delta\eta$ cut to 0.5 to further reduce the contribution of the nearside jet. Fig. 5.16, Fig. 5.17 and Fig. 5.18 show good agreement between v_n values from two $\Delta\eta$ cuts, which indicates we have removed a significant amount of nearside jet pairs with $|\Delta\eta| > 0.3$ cut.

5.7 Comparison with v_2 measurements from PHENIX

The v_2 measurement in this analysis, or the two particle correlation method, is compared with the latest v_2 measurement from PHENIX [19]. In [19], PHENIX uses the reaction plane method to measure v_2.

5.7.1 p_T vs N_{part}

We compare the v_2 measured via two particle correlations with the v_2 measurement from Fig. 2 in [19] as a function of N_{part}. The p_T bin used here is 0.5–0.8 GeV/c, and with various centralities from 0–5% up to 40–50%, or

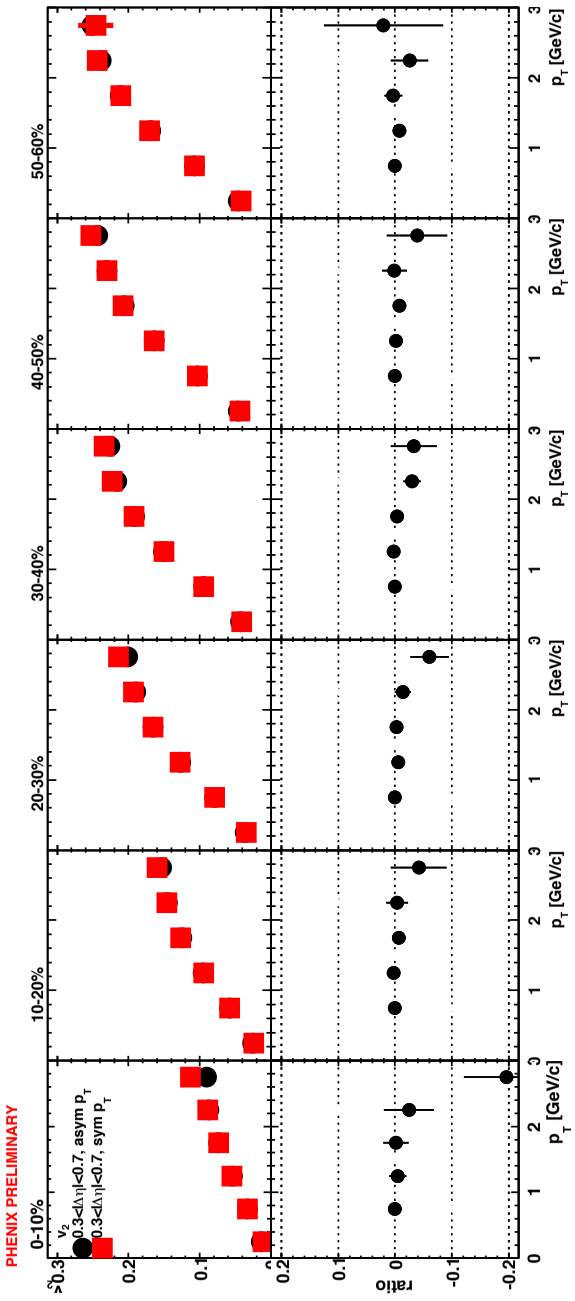

Figure 5.14: Comparison between v_2 values from method 1 (symmetric p_T, red) and method 2 (asymmetric p_T, black). Centralities from 0–10% to 50–60%. The bottom panel shows the ratio between black and red (black/red-1).

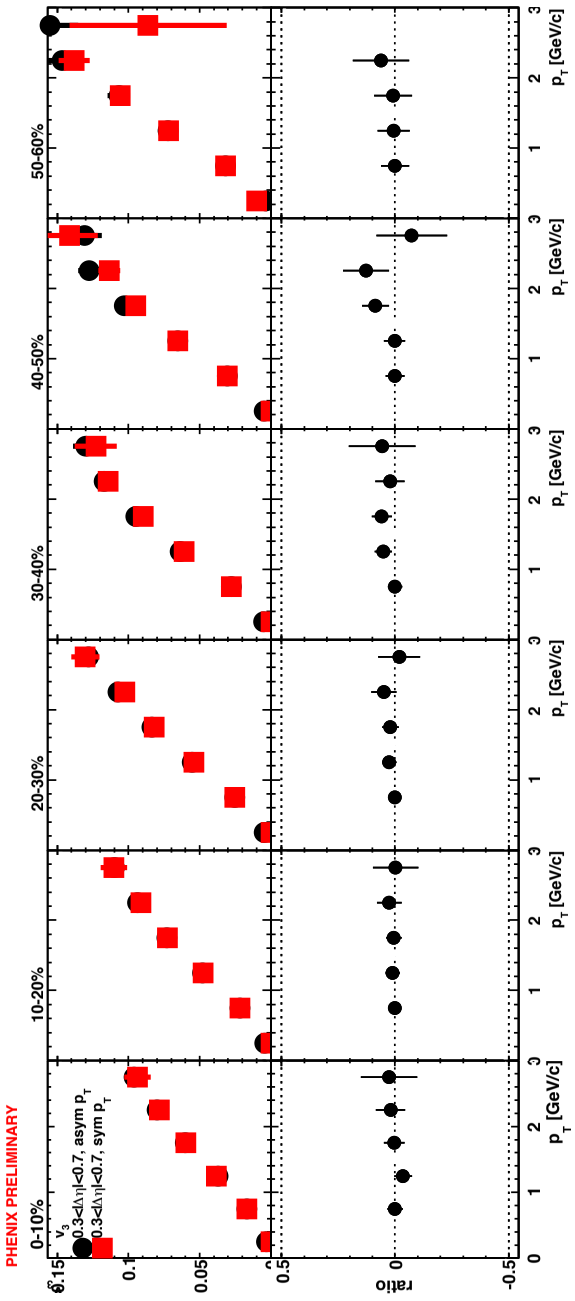

Figure 5.15: Comparison between v_3 values from method 1 (symmetric p_T, red) and method 2 (asymmetric p_T, black). Centralities from 0–10% to 50–60%. The bottom panel shows the ratio between black and red (black/red-1).

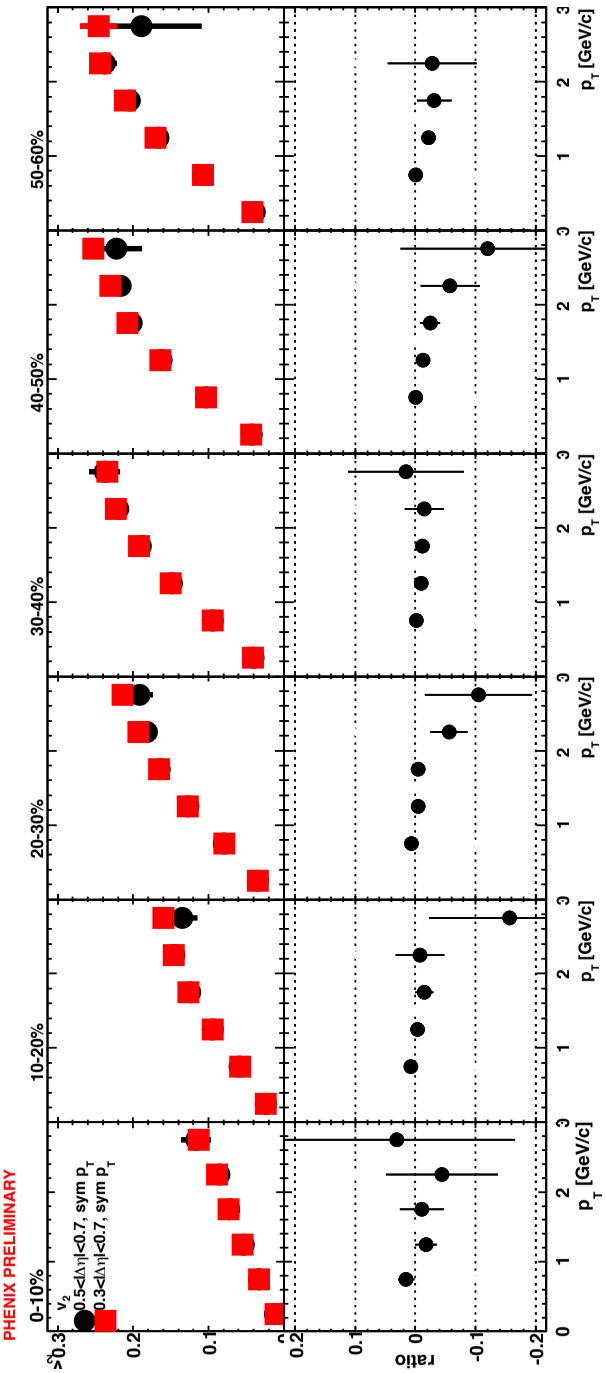

Figure 5.16: Comparison between v_2 values from $\Delta\eta = 0.3$ (red) and $\Delta\eta = 0.5$ (black). Centralities from 0–10% to 50–60%. The bottom panel shows the percentage deviation from $\Delta\eta = 0.3$.

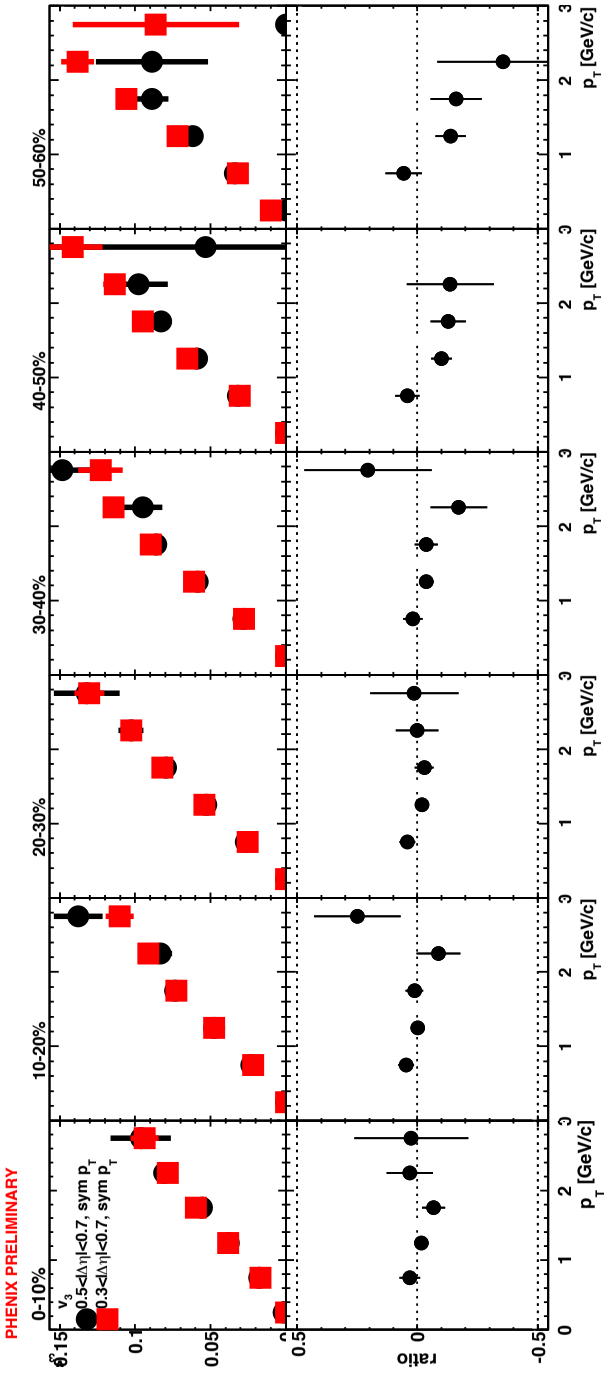

Figure 5.17: Same as Fig. 5.16, but comparing v_3.

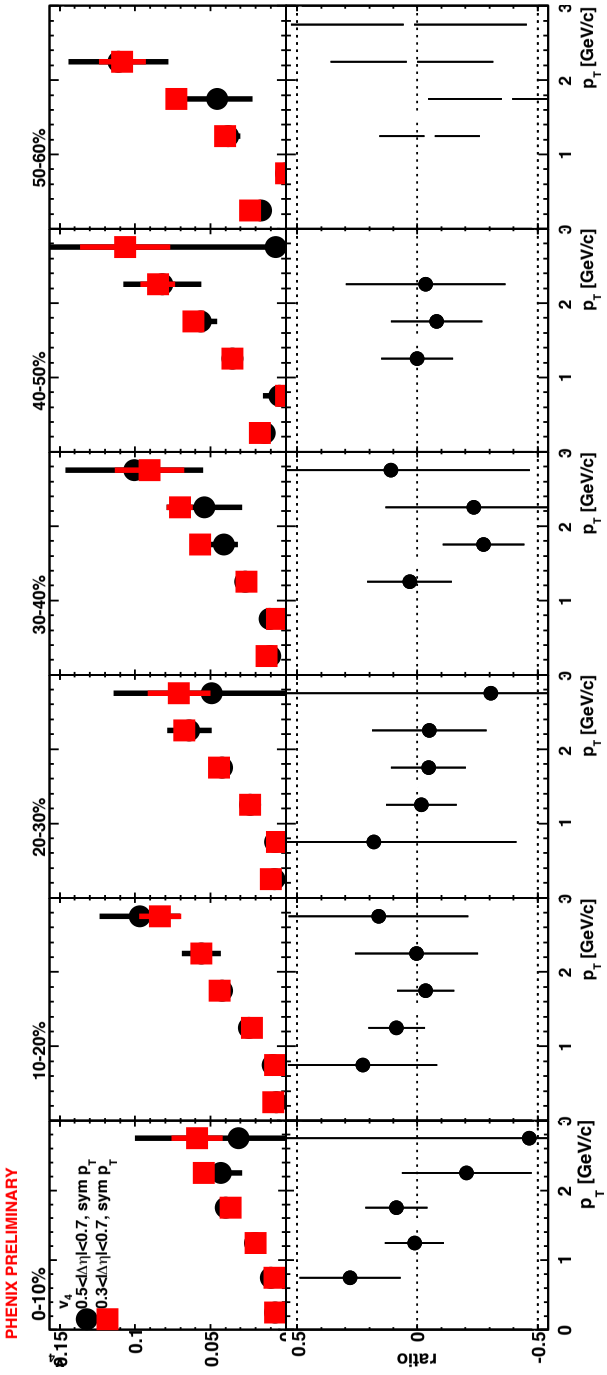

Figure 5.18: Same as Fig. 5.16, but comparing v_4.

$N_{part} \approx 60$. The comparison is shown in Fig. 5.19. The v_2 in this analysis is consistent with v_2 values from [19] for $N_{part} > 140$. When N_{part} decreases from 140, we see v_2 values are larger than data from [19].

In [19], the reaction plane is determined by several different detectors. Then the v_2 is measured with respect to each of these reaction planes. We compare our results with the v_2 obtained using the Muon Piston Calorimeter (MPC) and the outer layer of the Reaction Plane Detector (RXNo). The MPC covers η from 3.1–3.7, while RXNo has an η from 1–1.5. When determining the reaction plane ψ_2, the η position of the forward detector matters. This is because at smaller η, there is a stronger influence from jet particles which will bias the measurement of the reaction plane This bias is known as the "non–flow" effect. Consequently, reaction plane determined at smaller η tend to have higher v_2 values.

We take the ratio between the v_2 measured in this analysis via the two particle correlation method, $v_2\{2P\}$, and v_2 determined with the MPC, $v_2\{\psi_2^{MPC}\}$. The results are shown in Fig. 5.20. Fig. 5.21 is a similar plot comparing with v_2 determined with RXNo, $v_2\{\psi_2^{RXNo}\}$. We see that for N_{part} below 260, $v_2\{2P\}$ is larger than $v_2\{\psi_2^{MPC}\}$ ($v_2\{\psi_2^{RXNo}\}$) by 6 (2)%. The largest difference is for most central collisions, where the deviation is 25 (12)%. In two particle correlation measurements, both particles are detected within the PHENIX central arms, where the maximum $\Delta\eta$ separation is $\Delta\eta = 0.7$. On the other hand, when using a forward detector to determine the reaction plane and correlated with charged particles in central arm, the η separation is larger than 1. So with smaller η separation, we expect a somewhat higher v_2 value in the two particle correlation case.

5.7.2 v_2 vs p_T

We also compare the centrality dependence of v_2 vs p_T with previous results [19], using the same centrality bins as in Fig. 3 of Reference [19]. The p_T range used in the comparison is from 0.5–1.0 GeV/c. We take the ratio between the measurements and values from [19]. The results are plotted in Fig. 5.22. Fig. 5.23 is the same plot as Fig. 5.22, the only difference is the range of the Y axis is adjusted to focus the range between 0.98–1.15. The ratio is very flat with p_T. The largest deviation is for 0–5% central collisions, which has about a 20–30% higher v_2 than in [19]. For other centralities, the ratios are near 5 to 7%, except at 50–60% centrality, where the difference is about 10%. This shows that at low p_T, the v_2 from the two particle correlation method is consistent with v_2 from the reaction plane method.

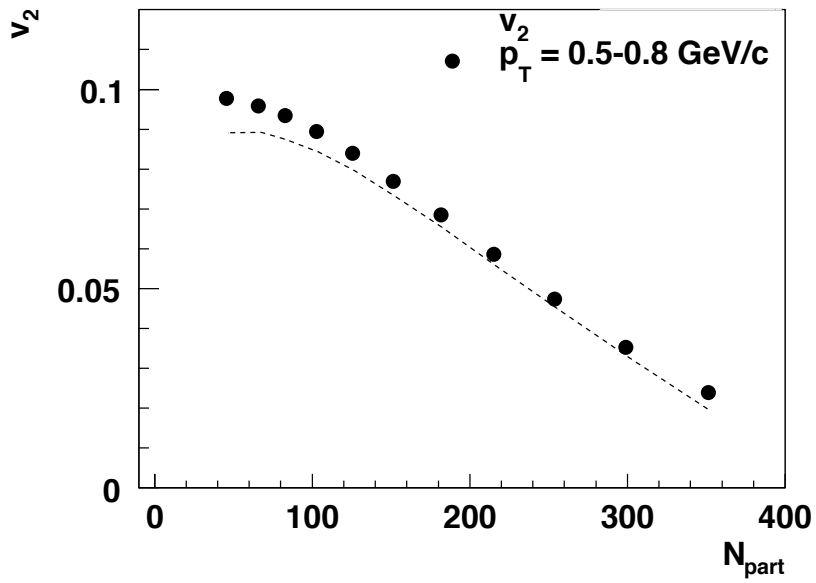

Figure 5.19: v_2 in this analysis (black points) compared with v_2 measured by reaction plane method (dashline) [19]. Inclusive charged hadrons with p_T = 0.5–0.8 GeV/c.

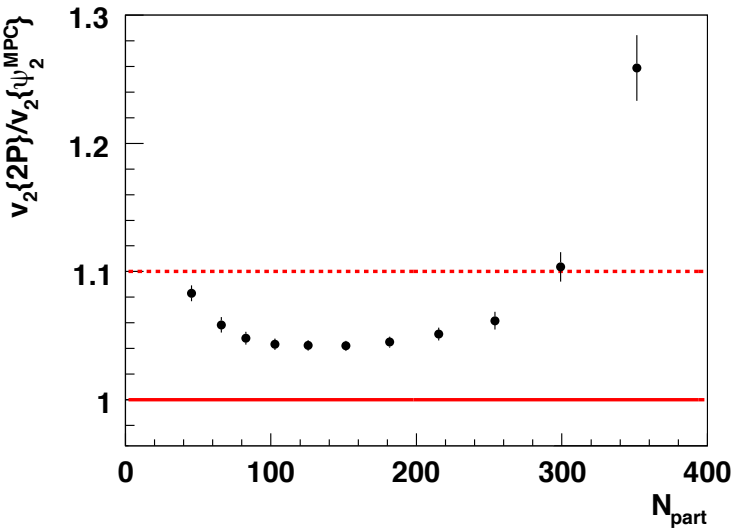

Figure 5.20: Ratio between $v_2\{2P\}$ value in this analysis and $v_2\{\psi_2^{MPC}\}$, where the second event plane, ψ_2, is determined by the Muon Piston Calorimeter (MPC) in [19].

5.7.3 Systematic Uncertainties of v_n

In the previous discussion, we used two particle correlations to measure v_n where n = 1, 2, 3, 4. However, there are four different variations. We have two different $|\Delta\eta|$ cuts (0.3 and 0.5), as well as symmetric and asymmetric p_T pairs. We use these four measurements to get our v_n and the corresponding systematic error. The the mean v_n is the average of the four measurements. The statistical error is the larger of the symmetric and asymmetric pairs, for the $\Delta\eta$ cut of 0.3. We use this instead of $\Delta\eta = 0.5$, because the statistics between the two is almost a factor of 10. The highest and lowest non–zero points are used to determine the systematic error. The final v_2 and v_3 values are plotted in Fig. 5.24 and Fig. 5.25.

5.7.4 $v_n\{2P\}$ vs $v_n\{\psi_n\}$

We also compared with the PHENIX published result [68], as shown in Fig. 5.26 and Fig. 5.27.

In general, the measurement is higher than results from [68] but still consistent within the systematic error.

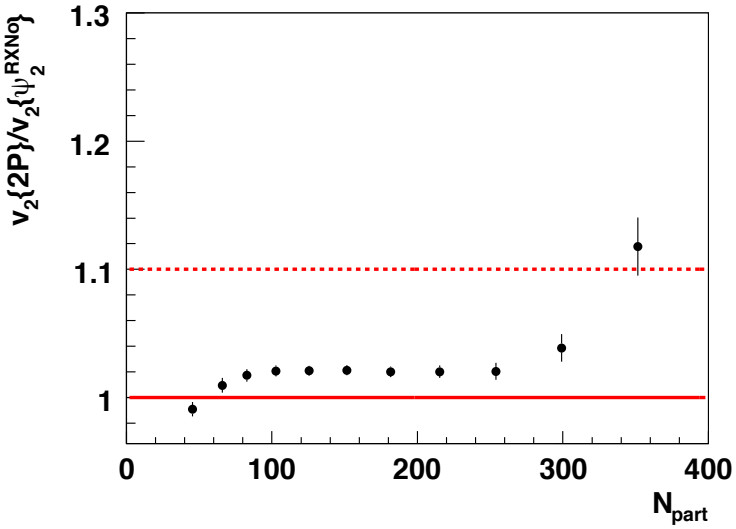

Figure 5.21: Ratio between $v_2\{2P\}$ value in this analysis and $v_2\{\psi_2^{RXNo}\}$, where the second event plane, ψ_2, is determined by the outer sector of the Reaction Plane Detector (RXNo)in [19].

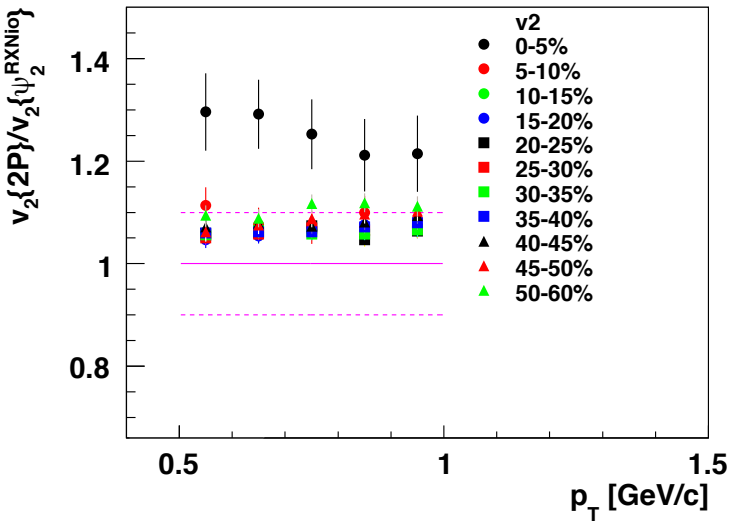

Figure 5.22: Ratio between $v_2\{2P\}$ value in this analysis and $v_2\{\psi_2^{RXNio}\}$ in [19] with various centralities.

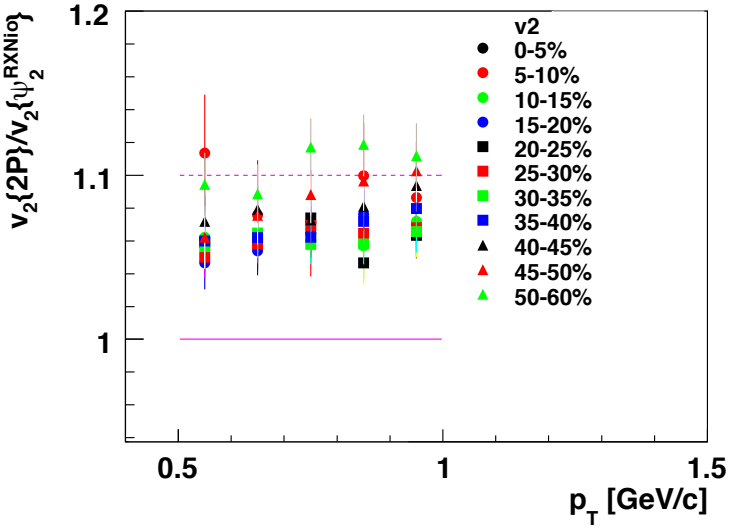

Figure 5.23: Same as Fig. 5.22, only the Y range is changed.

v_2 from this analysis, $v_2\{2P\}$, with the result from reference [68] as $v_2\{\psi_2\}$, which is shown in Fig. 5.26. For points with p_T from 0.5–1.0 GeV/c in all centralities, the measurements agree within 5%. As p_T goes up, the two methods begin to deviate significantly by as much as 10% in mid–central collisions and more than 20% at central collisions at 3 GeV/c.

We are not surprised by this result for several reasons. At $p_T > 1$ GeV/c, the jet contribution starts to increase. In the current analysis, we only have an η cut, which removes particle pairs with $|\Delta\eta| < 0.3$. This pair cut removes some of the jet, or "non–flow" pairs, but there is still a significant contribution from non–flow which is not being removed. Reference [19], showed that when the reaction plane is determined with detectors at smaller η, the v_2 value becomes slightly larger.

Fig. 5.27 compares $v_3\{2P\}$ values from this analysis with values from [68], $v_3\{\psi_3\}$, at $p_T = 0.5$–3.0 GeV/c. The two measurement agree within 5%, but deviate to about 20% at high p_T. We know that at high p_T, the jet contribution is significant in two particle correlations [23]. Furthermore, jet suppression will increase the third harmonic, since it decreases the correlation strength at $\Delta\phi = \pi$.

This comparison demonstrate two things. First, in the low p_T region, $p_T =$ 0.5–1.0 GeV/c, v_2 and v_3 measured by the reaction plane method, $v_n\{\psi_n\}$, and

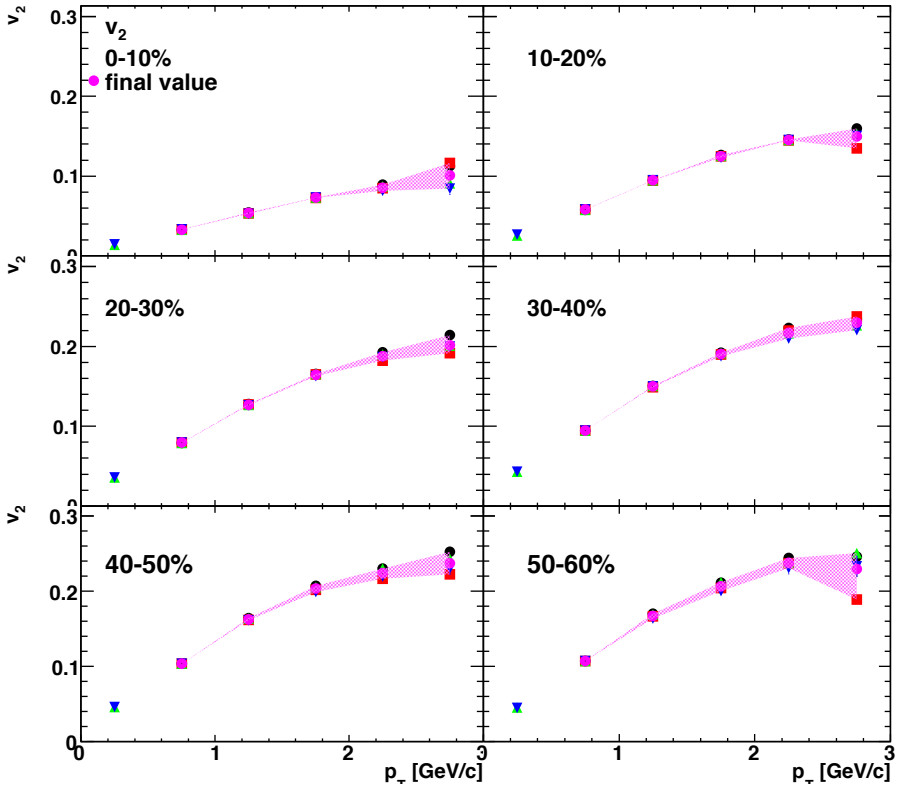

Figure 5.24: v_2 vs p_T. The final v_2 curve is plotted in pink, along with 4 other methods.

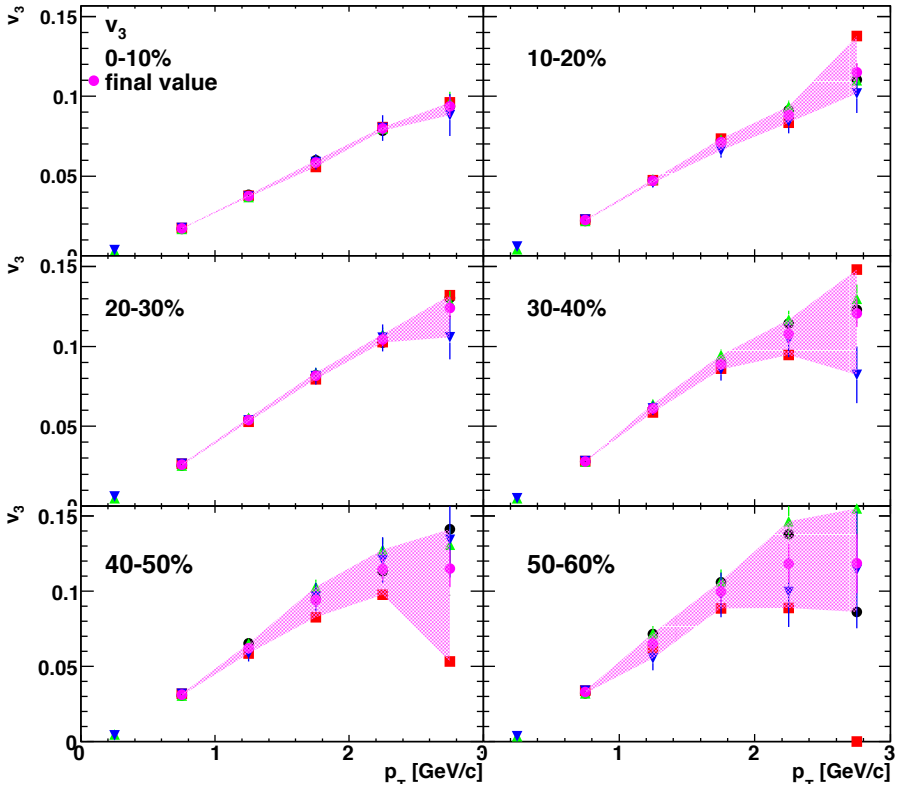

Figure 5.25: v_3 vs p_T. The final v_3 curve is plotted in pink, along with 4 other methods.

two particle correlation method, $v_n\{2P\}$, are consistent in all centralities from 0–10% to 50–60%. Second, at particle p_T above 1 GeV/c, since jet fragments are not completely removed, larger $v_n\{2P\}$ values compared to reaction plane methods, $v_n\{\psi_n\}$, however the methods still agree within systematic errors. This also indicates the jet contributions at high p_T needs proper treatment.

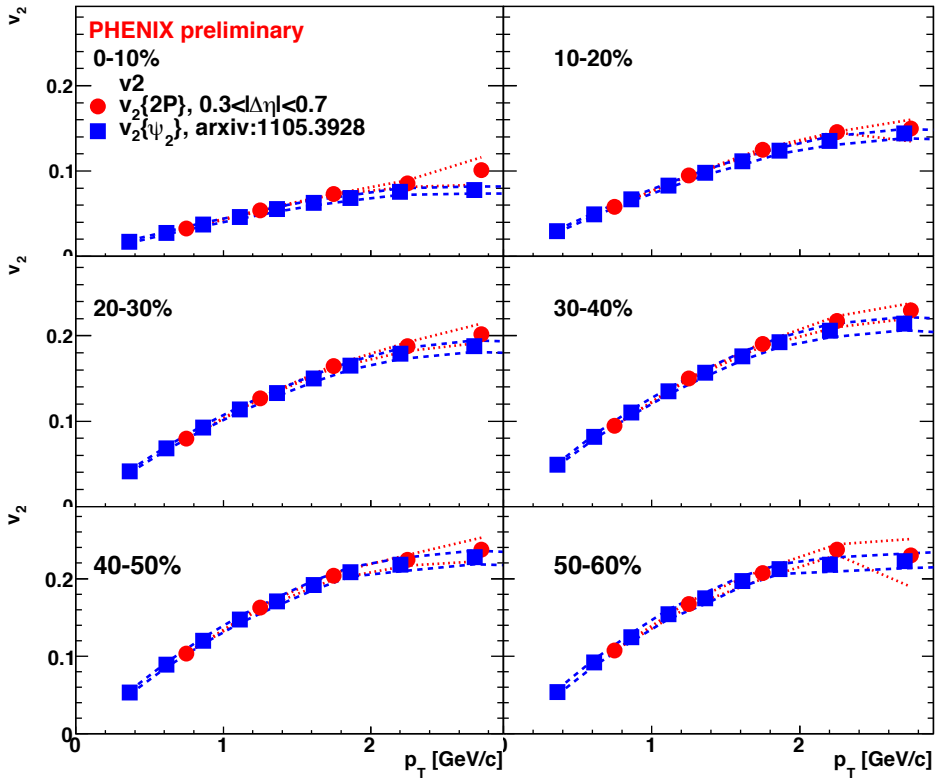

Figure 5.26: v_2 measured by this analysis,$v_2\{2P\}$ (red) and from reference [68], $v_2\{\psi_2\}$(blue) with systematic error.

5.8 Glauber Monte Carlo Simulation

In relativistic hydrodynamic models, the elliptic flow comes from the pressure gradient due to geometrical anisotropy or eccentricity, ε_2=< y^2-x^2 >/< y^2+x^2 >. One of the important prediction is v_2/ε_2, which takes out the geometrical effect, should be independent on centrality [71]. Previously, PHENIX has shown that there is a v_2/ε_2 scaling as shown in Fig. 5.28 [18]. When v_2/ε_2

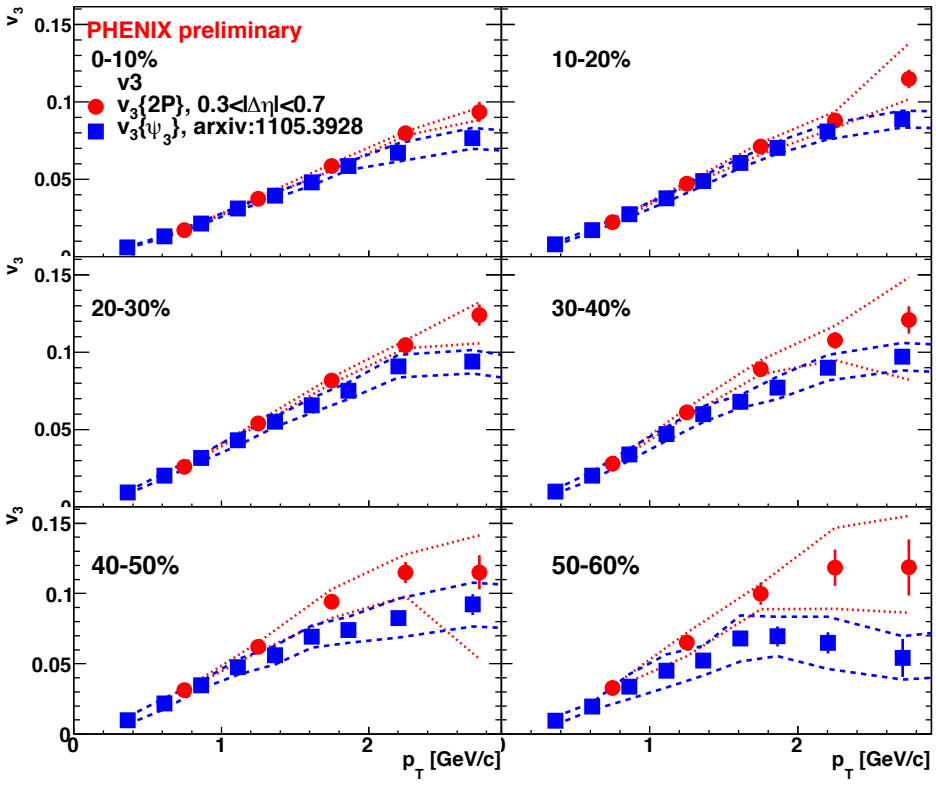

Figure 5.27: v_3 measured by this analysis,$v_3\{2P\}$ (red) and from reference [68], $v_3\{\psi_3\}$(blue) with systematic error.

is plotted as a function of p_T, all curves are following a universal curve independent of colliding systems and centralities. Along this line, there are several predictions which extend similar trend into v_3 [67, 72]. In order to test the prediction of v_n/ε_n scaling, we use Glauber Monte Carlo simulations to calculate the eccentricity (ε_2) or triangularity (ε_3).

5.8.1 Eccentricity and Triangularity

There are two kinds of eccentricity. The first kind is the "standard eccentricity", $\varepsilon_2^{standard}$, where the x–axis is along the direction of the impact parameter, and the y–axis goes through the origin, which is defined as the center of the impact parameter. $\varepsilon_2^{standard}$ is defined as

$$\varepsilon_2 = \frac{\langle y^2 - x^2 \rangle}{\langle y^2 + x^2 \rangle} \tag{5.14}$$

There is another kind of eccentricity, the "participant eccentricity", where the origin is shifted to the center of the mass makes $< x >= 0$ and $< y >= 0$. Eq. 5.14 can be written as Eq. 5.15:

$$\varepsilon_2 = \frac{\sqrt{\langle r^2 \cos(2\phi_{part}) \rangle^2 + \langle r^2 \sin(2\phi_{part}) \rangle^2}}{\langle r^2 \rangle} \tag{5.15}$$

where r and ϕ_{part} are the polar coordinates of the participant nucleons, nucleons involved in the collision, relative to the center of the mass. The short axis of the ellipse, ψ_2 is pointing to the direction

$$\psi_2 = \frac{tan^{-1}(\frac{\langle r^2 \sin(2\phi_{part}) \rangle}{\langle r^2 \cos(2\phi_{part}) \rangle}) + \pi}{2} \tag{5.16}$$

Since the pressure gradient is the largest in the direction of short axis, or direction of ψ_2, the strength of the collective flow should also be the largest in this direction.

In order to test the prediction of the scaling property v_3/ε_3, we need to calculate the triangularity, ε_3. We adopt the definition of ε_3 used in [67], which is the natural extension of Eq. 5.15. ε_3 is defined as

$$\varepsilon_3 = \frac{\sqrt{\langle r^2 \cos(3\phi_{part}) \rangle^2 + \langle r^2 \sin(3\phi_{part}) \rangle^2}}{\langle r^2 \rangle} \tag{5.17}$$

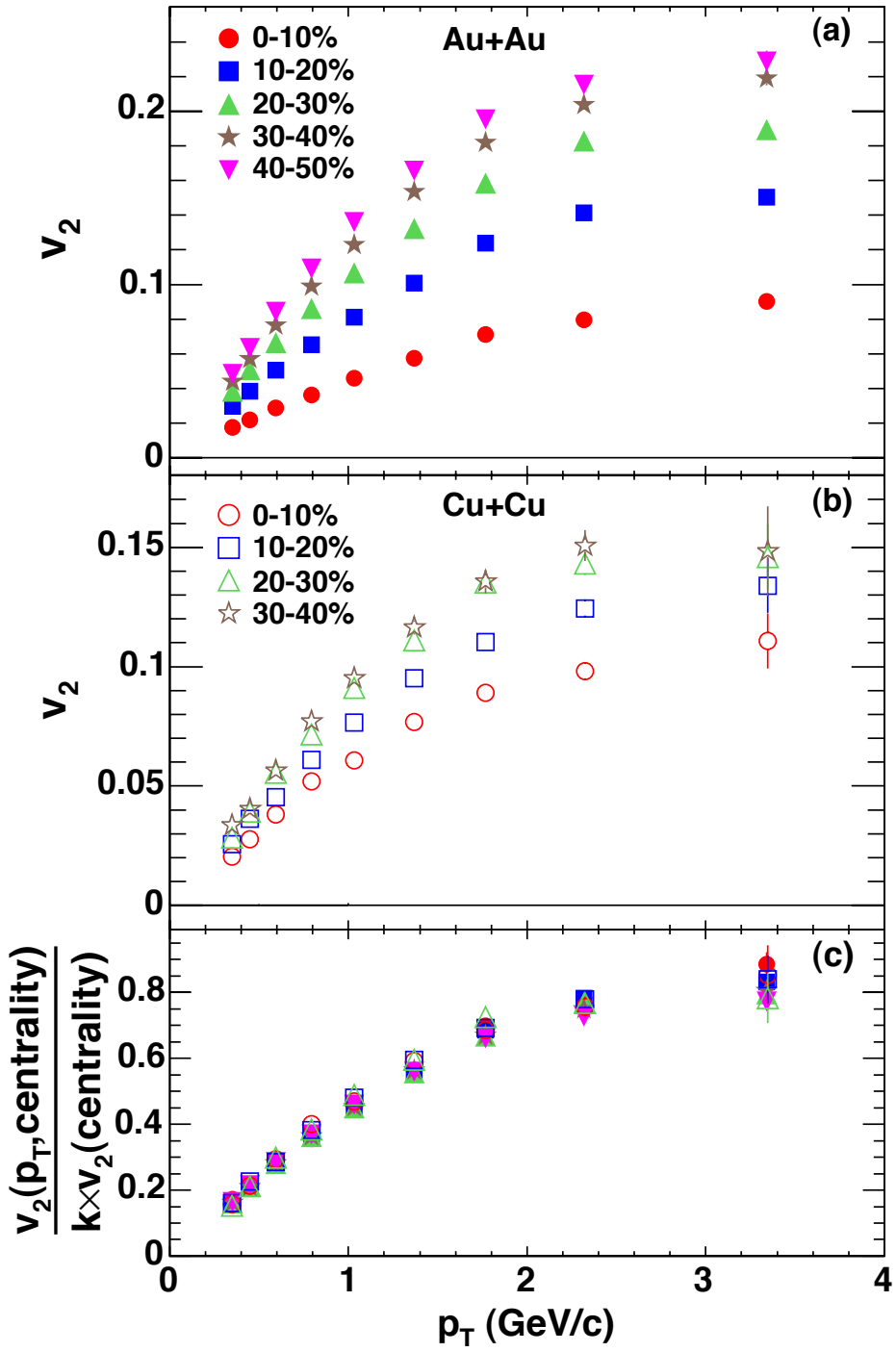

Figure 5.28: v_2 measurement in (a)Au+Au; (b)Cu+Cu; (c)v_2 scaled with p_T integrated v_2 [18]

We can also define the direction of the event plane for the n–th moment, ψ_n. The general equation of ψ_n is an generalized form of Eq. 5.16, which is defined as Eq. 5.18:

$$\psi_n = \frac{tan^{-1}(\frac{\langle r^2 \sin(n\phi_{part})\rangle}{\langle r^2 \cos(n\phi_{part})\rangle}) + \pi}{n} \tag{5.18}$$

5.8.2 Glauber Monte Carlo Simulation

Glauber model is used to calculate the geometrical related quantities, such as ε_2, ε_3, ψ_2 and ψ_3. Glauber model assumes the nuclei consists of individual nucleons. Each nucleon is distributed randomly within the radius of the nucleus. This introduces shape fluctuations naturally. In order to estimate the initial collision geometrical parameters, we run Monte Carlo simulations event–by–event and measure these quantities statistically. In this analysis, we use the PHOBOS Glauber Monte Carlo Simulation [73] to measure the eccentricity and triangularity. We simulated 600,000 events. Some key parameters are listed below

- The inelastic nucleon–nucleon cross section at 200 GeV is $\sigma_{NN} = 42$ mb
- The minimum nucleon separation distance = 0.4 fm
- The nuclear charge density is described by a Woods–Saxon function in the form with three parameters: $\rho(r) = \rho_0 \frac{1+w(\frac{r}{R})^2}{1+\exp\frac{r-R}{a}}$, where ρ_0 is the nuclear density, R is the nuclear radius, a is the skin depth and w is the shape deviation from a spherical shape. For Au nuclei, R = 6.38 fm, a = 0.535 fm, w = 0

A typical example of a Au+Au collision in Glauber simulations is shown in Fig. 5.29. The number of participants and number of binary nucleon–nucleon collisions are calculated for each event. The direction of the n–th event plane ψ_n, ε_2 and ε_3 are also calculated with Eq. 5.15, Eq. 5.17 and Eq. 5.18. From this example, it is clear to see that the nuclei consists of randomly distributed nucleons. The colliding area is not a perfect almond shape. The direction of ψ_2 is roughly long the direction of the impact parameter. ψ_3 is pointing to a random direction which is because the origin of ψ_3 is due to geometrical fluctuations.

With 600000 events, Fig. 5.30 and Fig. 5.31 are the participant eccentricity ε_2 and ε_3 plotted as a function of N_{part}. In both cases, even though the events

have the same N_{part}, but because of the event–by–event nucleon distribution fluctuations, we have a distribution of ε_2 and ε_3.

We also calculated the average ε_1, ε_2 and ε_3 as function of N_{part}, shown in Fig. 5.32. We see all three ε_n are the smallest at highest N_{part}. This is because at this situation, the two nuclei collide almost completely, which the collision region is almost like a circular shape. When N_{part} decreases, all ε increases, because the anisotropy of the colliding area becomes larger. We also note the ε_2 is consistently larger than ε_3, because ε_2 is mostly due to the geometrical shape, but ε_3 comes from fluctuations.

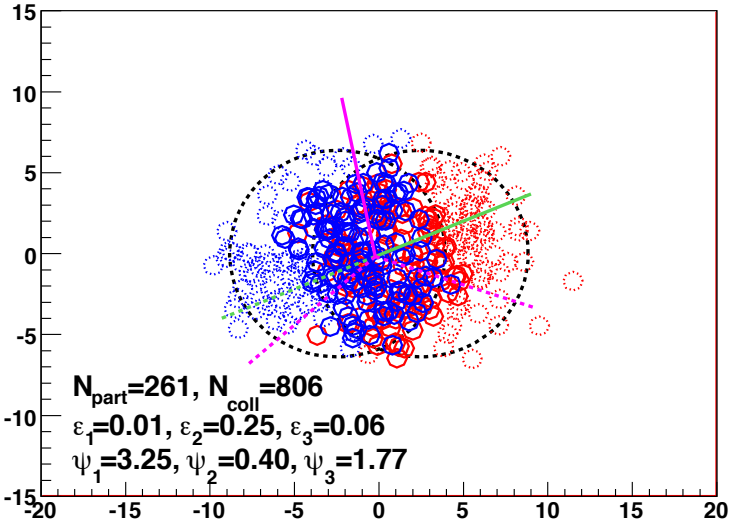

Figure 5.29: An example of collision of two gold nuclei in Glauber model. The solid circles are nucleons partipating the collision; the dash circles are spectators which do not participating the collision. The solid green (magenta) line is pointing to the direction of ψ_2 (ψ_3). The dashlines are the 2 (3) fold symmetry directions of ψ_2 (ψ_3).

5.8.3 Calculating Eccentricity from Glauber Simulation

Here we extract average eccentricity in different centralities. Here the centrality is defined by the distribution of number of participants. The most central 5% collisions or 0–5% centrality is defined as top 5% of events which has the largest number of participants. Then we can use this distribution to

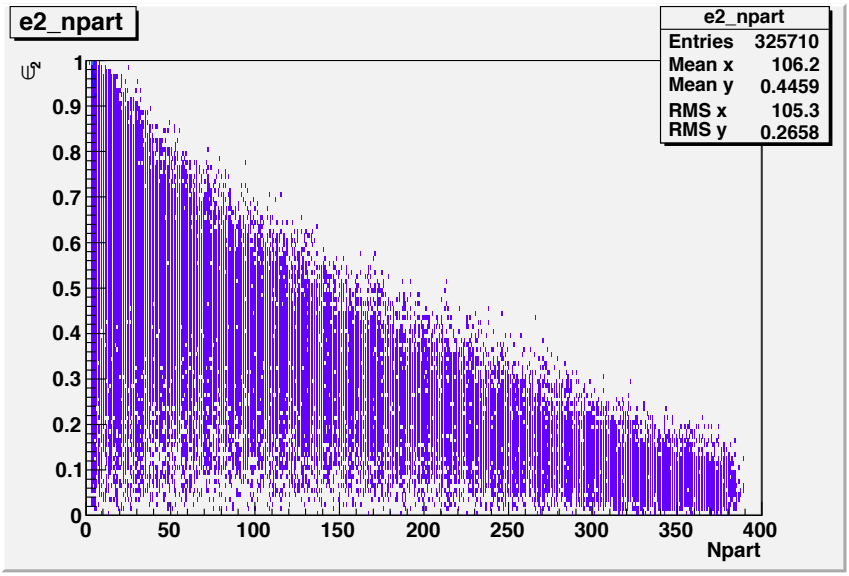

Figure 5.30: Participant eccentricity ε_2 vs N_{part}

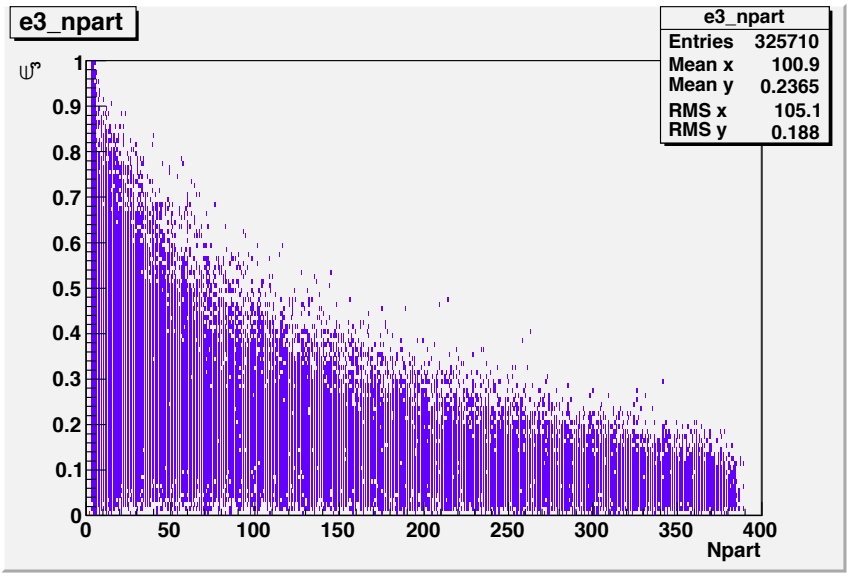

Figure 5.31: Participant eccentricity ε_3 vs N_{part}

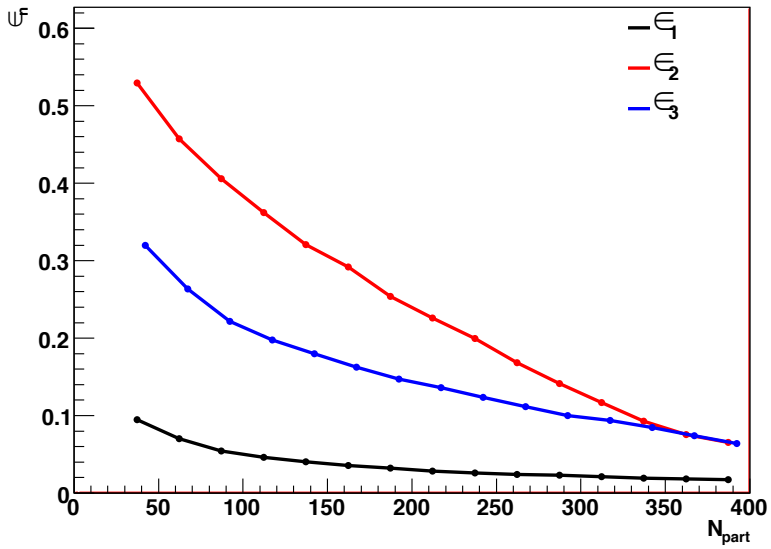

Figure 5.32: Average participant eccentricity ε_1 to ε_3 as function of N_{part}.

determine the centrality binning. The central value of the eccentricity is the average eccentricity in the centrality bin.

The ε_2 and ε_3 as a function of centrality are calculated from Fig. 5.30 and Fig. 5.31, and are tabulated in Table 5.1 and Table 5.2. Values in Table 5.1 are consistent with internal PHENIX measurements.

5.8.4 Systematic Error of ε_n

We estimate the systematic error of ε_2 and ε_3 by varying the following parameters:

- Change the nucleon–nucleon cross section from 42 mb to 39 mb.
- Change the nucleon–nucleon cross section from 42 mb to 45 mb.
- Change the Woods–Saxon function parameters from R = 6.38 fm, a = 0.535 fm to R = 6.65 fm, a = 0.55 fm
- Change the Woods–Saxon function parameters from R = 6.38 fm, a = 0.535 fm to R = 6.25 fm, a = 0.53 fm
- Change the minimum distance between nucleons from 0.40 fm to 0.36 fm

- Change the minimum distance between nucleons from 0.40 fm to 0.44 fm

The comparison of these systematic checks are shown in Fig. 5.33 and Fig. 5.35. The ratio between the systematic checks and the default value shows that the systematic error due to the description of the nuclear geometry of $\varepsilon_2(\varepsilon_3)$ is about 2–4%(2–6%).

The final systematic error of $\varepsilon_2(\varepsilon_3)$ for the given centrality is the quadratic sum of all differences compare to the values from default parameters. Systematic errors in both directions are calculated separately, and the larger of the two is used as the final systematic errors. The results are listed in Table 5.1 and Table 5.2.

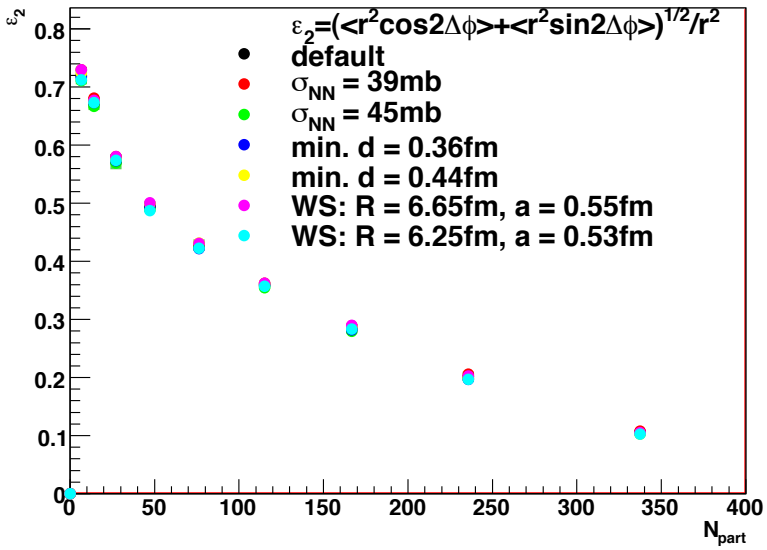

Figure 5.33: Participant eccentricity ε_2 compared with various systematic checks

5.9 Scaling

When assuming there is no shear viscosity, ideal hydrodynamic calculation predicts when v_2 scales with eccentricity, that is v_2/ε_2 as a function of p_T is a universal curve, which is independent of centrality and collision species [71]. This relation can be written as

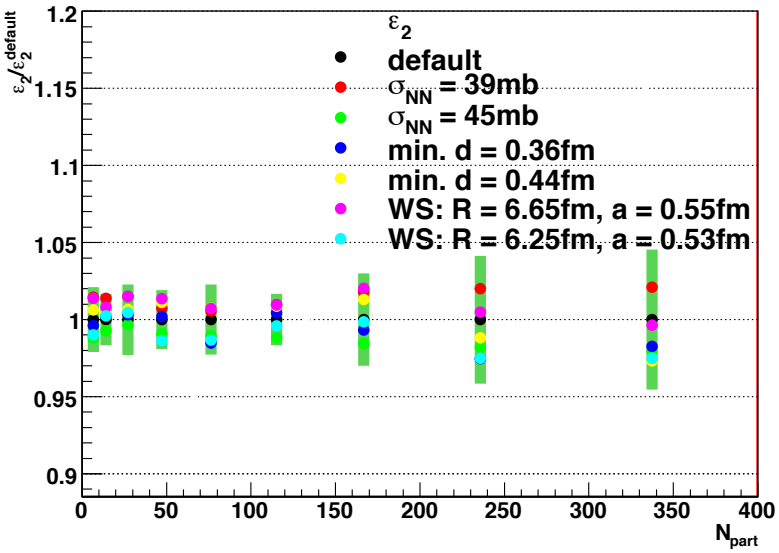

Figure 5.34: Ratios of Participant eccentricity ε_2 compared with various systematic checks. The green band is the final systematic errors

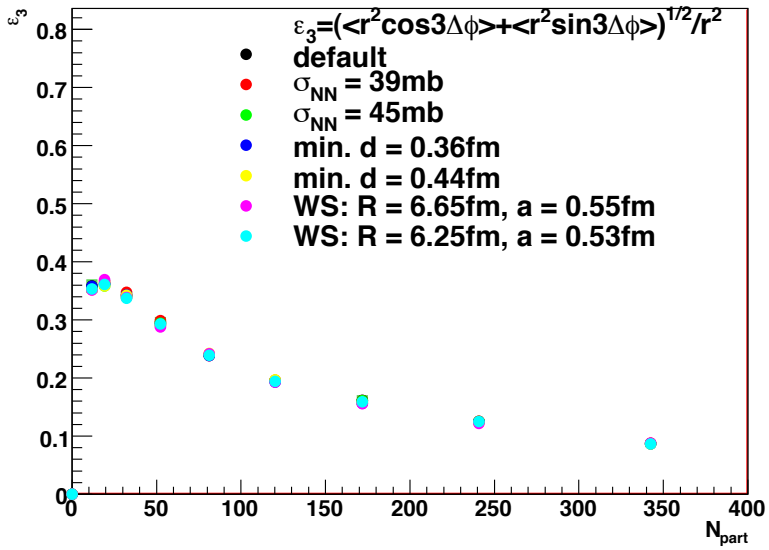

Figure 5.35: Participant eccentricity ε_3 compared with various systematic checks

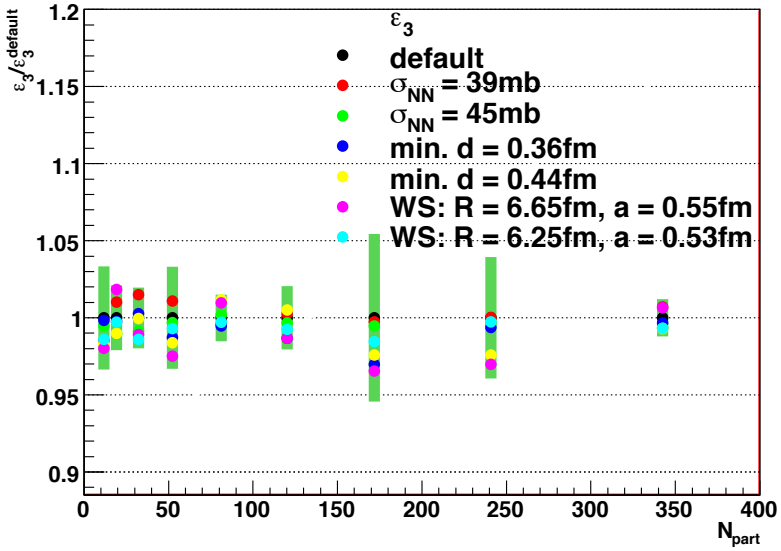

Figure 5.36: Ratios of Participant eccentricity ε_3 compared with various systematic checks. The green band is the final systematic errors

$$v_2(cent, p_T) = \varepsilon \times v_2(p_T) \tag{5.19}$$

where $v_2(cent, p_T)$ is the centrality and p_T dependent v_2, and $v_2(p_T)$ only depends on p_T. From Eq. 5.19, if we integrated over p_T, what remains should be proportional to the eccentricity, ε.

This property has been shown in previous PHENIX measurement of v_2 [18]. In [18], eccentricity is not calculated explicitly. In hydro predictions, the eccentricity is proportional to the p_T integrated v_2 ($\varepsilon = v_2 \times k$). So, reference [18] uses p_T the integrated v_2 times a factor of k = 3.1 as a proxy for the eccentricity. In reference [18], when v_2 is rescaled by ε or p_T integrated v_2 times a constant factor of k = 3.1, all v_2 vs p_T curves follow an universal trend.

In various hydrodynamical calculations [67, 72, 74], the v_3 value should be proportional to the magnitude of the triangularity or the ε_3. Therefore a trend similar to v_2/ε_2 for v_3 has also been shown, which says that v_3/ε_3 also follows a similar scaling. Or $v_3(p_T$, centrality$) = \varepsilon_3 \times v_3(p_T)$.

Following the methods described in [18], we test the v_2/(int. v_2) scaling and extend the study to v_3/(int v_3). We also use the ε_2 and ε_3 value from the Glauber Monte Carlo described in the previous section to search for the existence of scaling. In this scaling analysis, we use the v_n values from

Table 5.1: ε_2 measured via Glauber Monte Carlo simulations in different centralities.

centrality	ε_2	variance	sys. error
0–10%	0.105499	0.0582523	0.0048
10–20%	0.20173	0.0855551	0.0084
20–30%	0.283996	0.106145	0.0085
30–40%	0.358557	0.131047	0.0060
40–50%	0.428096	0.15094	0.0098
50–60%	0.494127	0.172629	0.0094
60–70%	0.571483	0.199686	0.013
70–80%	0.671808	0.207904	0.011
80–90%	0.719405	0.221362	0.015

Table 5.2: ε_3 measured via Glauber Monte Carlo simulations in different centralities.

centrality	ε_3	variance	sys. error
0–10%	0.0870931	0.047212	0.0010
10–20%	0.125344	0.0659116	0.0049
20–30%	0.161643	0.0837192	0.0088
30–40%	0.195772	0.101686	0.0040
40–50%	0.239647	0.12418	0.0036
50–60%	0.295354	0.14581	0.0098
60–70%	0.342285	0.169247	0.0067
70–80%	0.362377	0.183709	0.0077
80–90%	0.358197	0.215002	0.012

Chapter 5.7.3.

5.9.1 Scaling with p_T Integrated v_n

The p_T integrated v_n is calculated by Eq. 5.20:

$$int.v_n = \frac{\int v_n(p_T)\frac{dN}{dp_T}dp_T}{\int \frac{dN}{dp_T}dp_T} \tag{5.20}$$

v_2 and v_3 is summed over 0.5–3.0 GeV/c. The spectra for inclusive charged hadrons, dN/dp_T, are obtained from the published charged hadron spectra measured by PHENIX [56]. The integrated v_2 (v_3) are listed in Table 5.3 and Table 5.4.

Fig. 5.37 shows v_2 as function of p_T in different centralities as measured in this analysis. The dash lines are v_2 measurements from PHENIX **??**. The agreement between the two measurement are good. We rescale the v_2 by the p_T integrated v_2, which is tabulated in Table 5.3. The result is shown in Fig. 5.38, clearly that all six centrality bins, from 0–10% to 50–60%, follow a universal trend. The universality is also visible in Fig. 5.39, where the scaled v_2 is plotted vs N_{part}. The flatness of the curves show the consistency of the scaled v_2. This suggest the system is locally thermalized rapidly.

Similar properties are also found in v_3. Fig. 5.40 is v_3 vs p_T in six centrality bins. After scaled with p_T integrated v_3, as shown in Fig. 5.41, all $v_3/(p_T$ integrated $v_3)$ curves again lined up together as the v_2 case shown in Fig. 5.38. Same trend is also seen when scaled v_3 is plotted vs N_{part} as plotted in Fig. 5.42.

This analysis shows that if we assume $v_2(cent, p_T)$ $(v_3(cent, p_T))$ all follows a universal curve, $v_2(p_T)$ $(v_3(p_T))$, which is modulate by the centrality dependent eccentricity (triangularity).

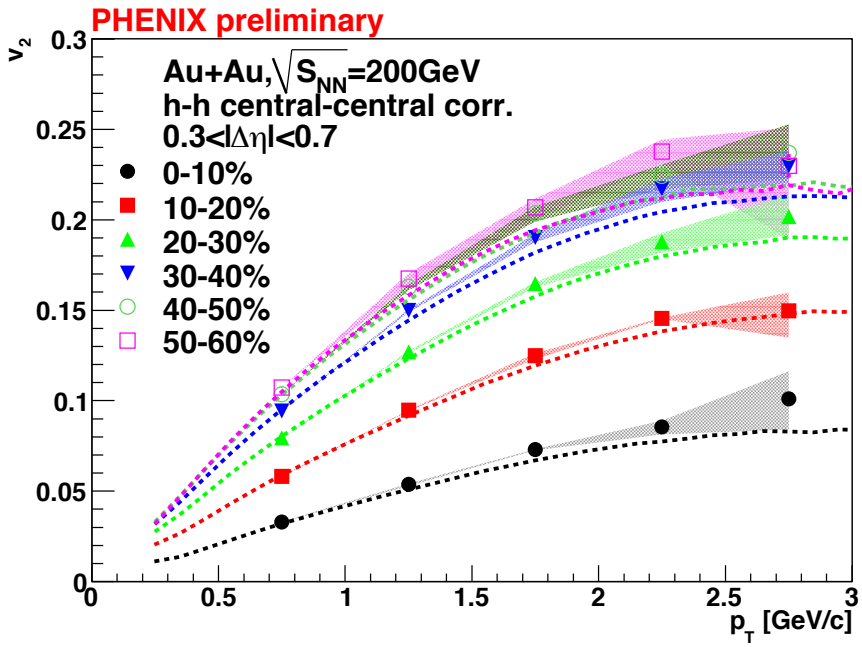

Figure 5.37: v_2 of various centralities as a function of p_T. Dash lines are PPG098 measurement.

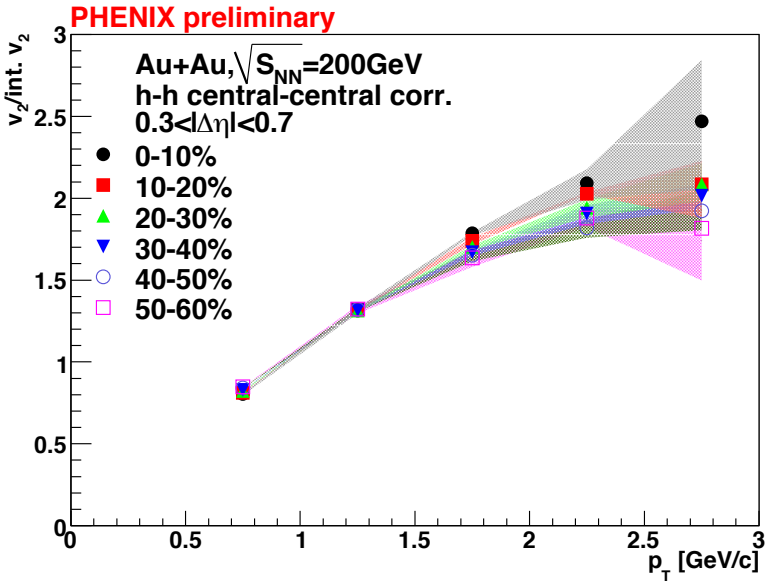

Figure 5.38: $v_2/(p_T$ integrated $v_2)$ vs p_T in various centralities

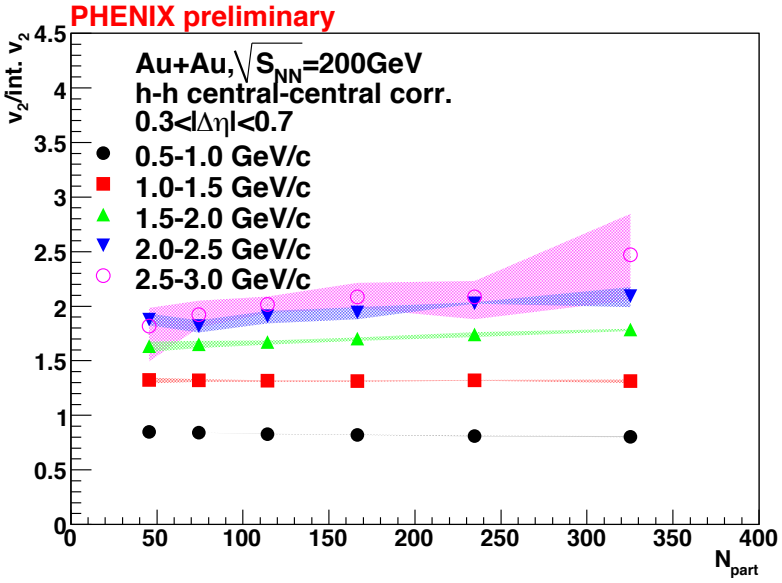

Figure 5.39: $v_2/(p_T$ integrated $v_2)$ vs N_{part} in various p_T bins.

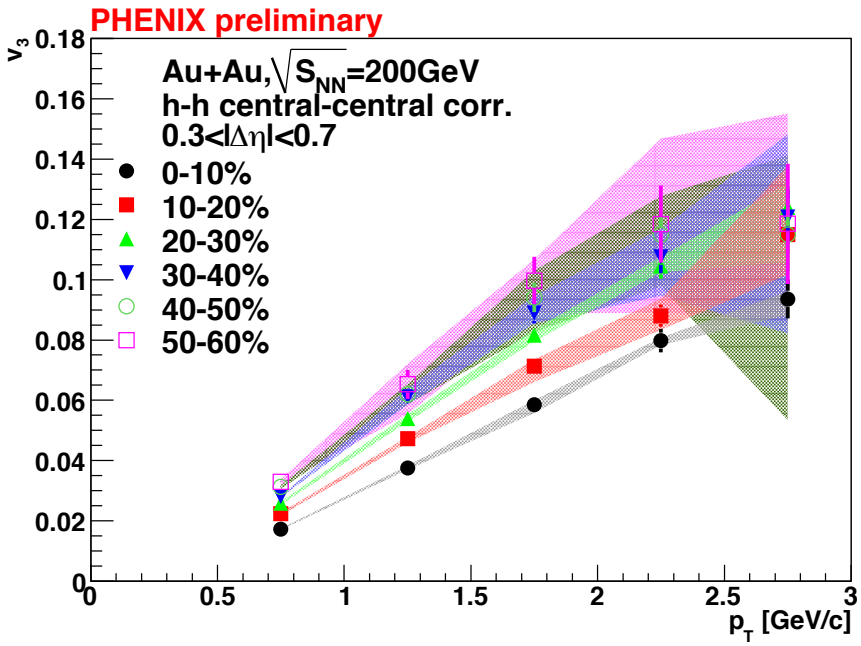

Figure 5.40: v_3 of various centralities as a function of p_T.

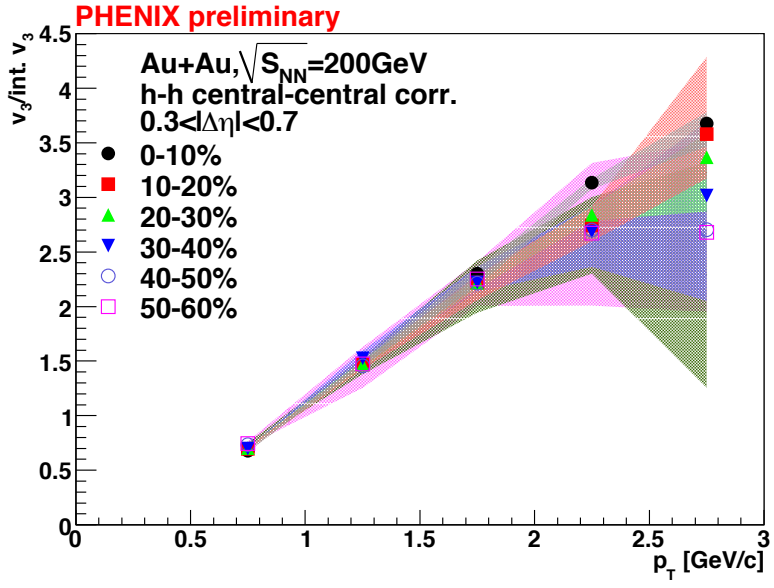

Figure 5.41: $v_3/(p_T$ integrated $v_3)$ vs p_T in various centralities

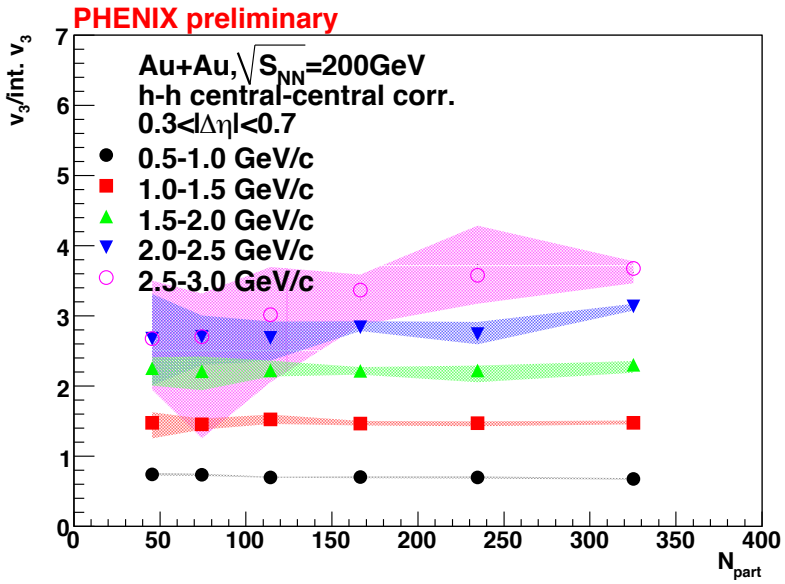

Figure 5.42: $v_3/(p_T$ integrated $v_3)$ vs N_{part} in various p_T bins.

5.9.2 Scaling with Glauber ε_2 and ε_3

We use the ε_2 and ε_3 measured by Glauber Monte Carlo simulations listed in Table 5.1 and Table 5.2 as an alternative way to study scaling by plotting v_n/ε_n. The results are shown in Fig. 5.43, Fig. 5.44 (v_2), and Fig. 5.45, Fig. 5.46 (v_3).

v_2/ε_2 as a function of N_{part} is plotted in Fig. 5.44. Scaling would be indicated by a flat distribution of v_2/ε_2. The scaling holds approximately at low p_T when N_{part} is larger than 100, but not for the most central collisions

Table 5.3: p_T integrated v_2 values (0.5–3.0 GeV/c) from two particle correlation method in this analysis.

centrality	int. v_2	stat err
0–10%	0.0409	0.0003
10–20%	0.0717	0.0002
20–30%	0.0967	0.0002
30–40%	0.1139	0.0002
40–50%	0.1233	0.0003
50–60%	0.1265	0.0005

Table 5.4: p_T integrated v_3 values (0.5–3.0 GeV/c) from two particle correlation method in this analysis.

centrality	int. v_3	stat err
0–10%	0.0255	0.0005
10–20%	0.0321	0.0005
20–30%	0.0368	0.0006
30–40%	0.0401	0.0010
40–50%	0.0425	0.002
50–60%	0.0443	0.002

(0–10% or $N_{part} \approx 330$). When p_T increases, this scaling does seem to work. The scaled v_2 also increases with N_{part}. This is not exactly the same as we see in [18] or Fig. 5.38. But a similar trend has been seen by [75], where the scaling holds between $N_{part} = 100$ and 300.

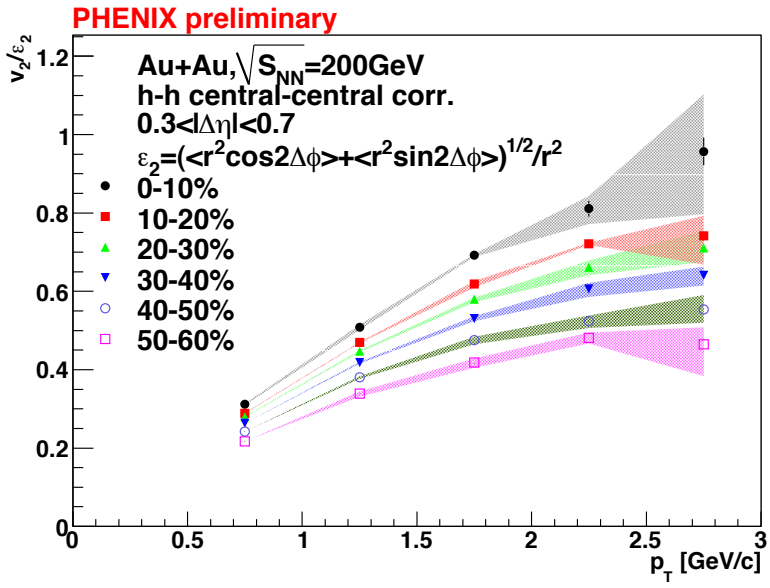

Figure 5.43: v_2/ε_2 vs p_T in various centralities.

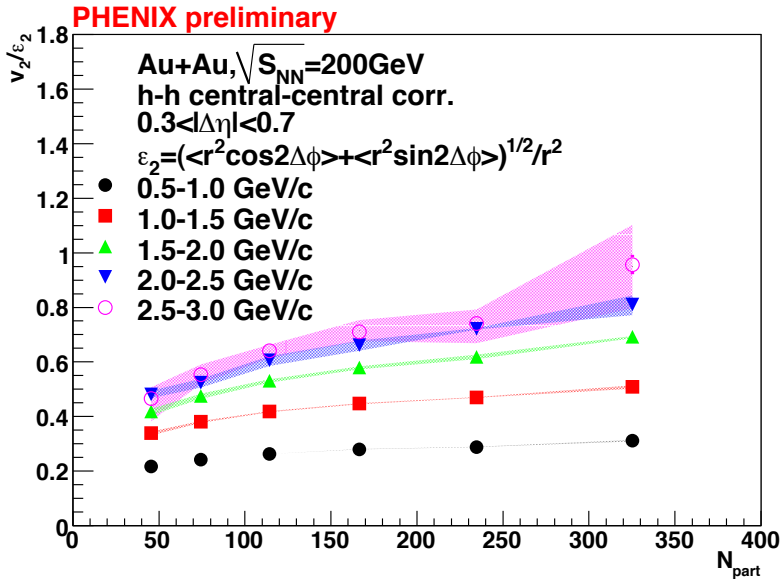

Figure 5.44: v_2/ε_2 vs N_{part} in different p_T bins.

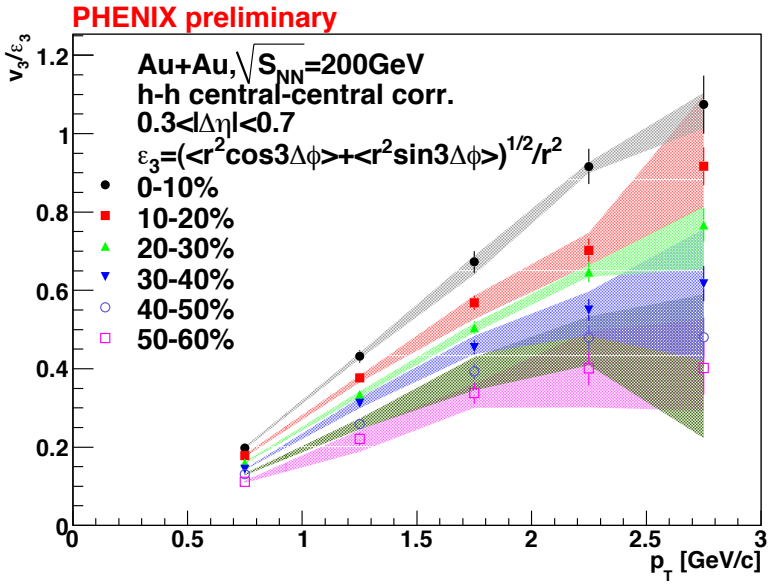

Figure 5.45: v_3/ε_3 vs p_T in various centralities.

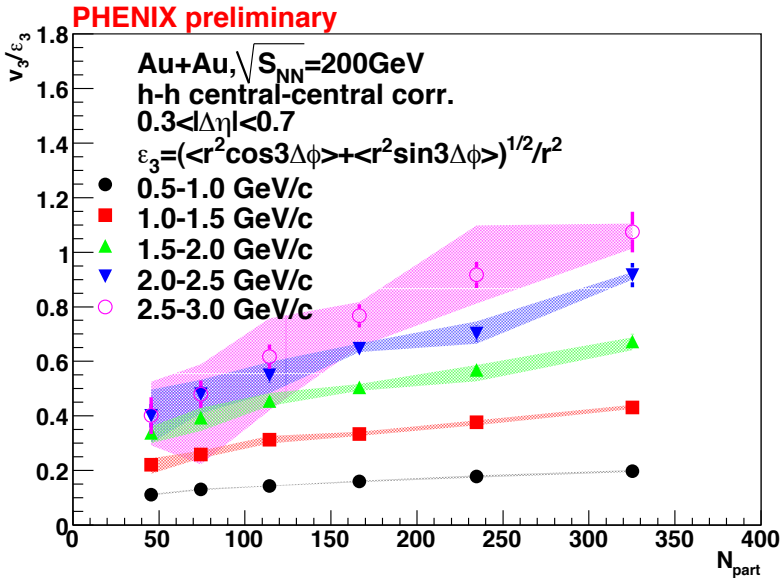

Figure 5.46: v_3/ε_3 vs N_{part} in different p_T bins.

Chapter 6

Fourier Spectra and Jet Quenching

6.1 Introduction

The exotic structures of the ridge and shoulder are discussed in detail in previous chapters, and several theories have been proposed to explain these phenomena. One explanation is that these two structures have nothing to do with jets, and are due to the presence of the third harmonic of collective flow, v_3 [67]. This v_3 proposal has a natural appeal, since it provides three separate peaks, and the peak location ($\Delta\phi = 0$, $2\pi/3$ and $4\pi/3$ roughly correspond to the locations of the ridge ($\Delta\phi = 0$) and shoulder ($\Delta\phi \approx \pi \pm 1$). Furthermore, this explains the similarity of the p_T spectra of the the ridge and shoulder and the bulk. The question then is whether evidence for jet modification remains.

In this chapter, we use an approach which is different from the fitting decomposition described in the previous chapter. We take the higher order harmonics v_3 and v_4 measured by PHENIX [68] and include those in the background subtraction, to have a better description of the shape of the background. Since those v_n are Fourier coefficients of the underlying background, we can further use the Fourier series of the correlation function to study the jet modification and gain more insight.

To study what, if any, evidence remains of jet modification, we now modulate the uncorrelated background with higher harmonics beyond v_2. After subtracting this background, we study the jet function by Fourier analysis. In the resulting Fourier spectra, all jet structures will be mixed together. There is no way to separate the near and away side jets, ridge and shoulder using the Fourier power spectra, so we compare to the power spectrum by Fourier analysis of p+p collisions. In central Au+Au collisions, the situation is further complicated by awayside jet quenching.

In order to understand the Fourier spectra in Au+Au, we make the following assumption. The correlation function in Au+Au can be separated into

two parts: p+p–like jet structures and possible jet–medium interactions.

From both PHENIX [24] and STAR [58], we know that the near–side jet is consistent with the nearside jet in p+p, with very little modification. We also know that the awayside jet is suppressed in Au+Au. But the problem is that we don't really know the level of suppression of the awayside jet. To describe the p+p like jet in Au+Au, we consider two extreme case scenarios. The first is that the p+p like jet is unmodified in Au+Au. This can be represented by the p+p jet correlation function, where there is no medium modification at all. The second is that the awayside jet is fully quenched in the medium. To mimic this situation, we set all points on the away side of the p+p jet function to zero. This can be regarded as equivalent to fully quenching the away side jet in Au+Au with no other structures present.

The true awayside jet in Au+Au should be in between these two cases. When the Fourier spectra of the Au+Au correlation function is measured, the spectra are compared with these two baselines. Any Fourier coefficients beyond the description of these two cases must come from sources more complicated than unmodified or fully absent jets.

6.2 Measuring the Fourier Coefficients of the Correlation Function

6.2.1 Fourier Coefficients and Correlation Function

We transform the efficiency corrected jet functions from this analysis to determine the Fourier spectra. We use the $\Delta\eta$ range from 0–0.7, which is the full $\Delta\eta$ acceptance of the PHENIX. The reason for using this $\Delta\eta$ range, instead of 0.5–0.7 is that this range includes the full near side jet, which is important for studying jet physics.

First, we analyze the jet function obtained by subtracting out the underlying events modulated only by v_2. The resulting jet function is expanded in a Fourier series by the following:

$$J(\Delta\phi) = \sum C_n \cos(n\Delta\phi) \tag{6.1}$$

The Fourier coefficients are measured from the zeroth term up to the ninth term (C_0 to C_9 in Eq. 6.1). Fig. 6.1 and Fig. 6.2 compare the correlation functions with the Fourier expansion results in various centralities. The 10 terms of Fourier expansion describe the data very well.

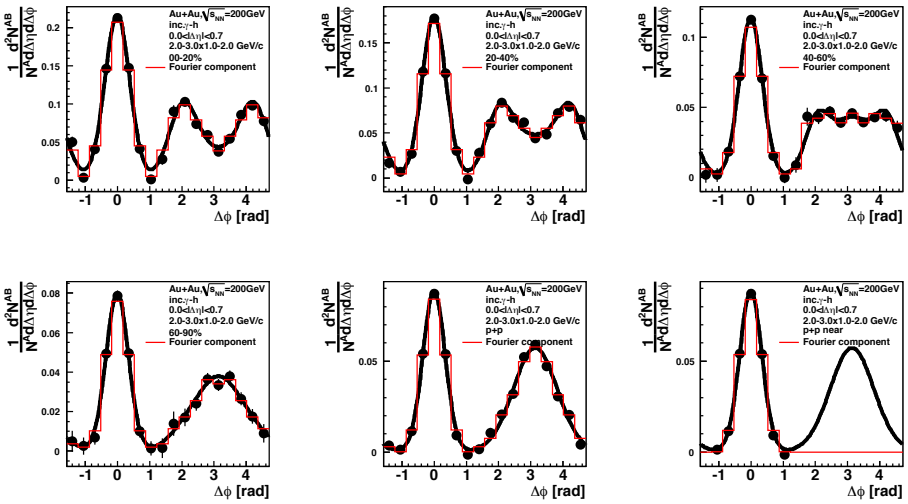

Figure 6.1: Per trigger yield jet function of various centralities (black) are compared with Fourier expansion results (red). Trigger p_T = 2.0–3.0 GeV/c and partner p_T = 1.0–2.0 GeV/c

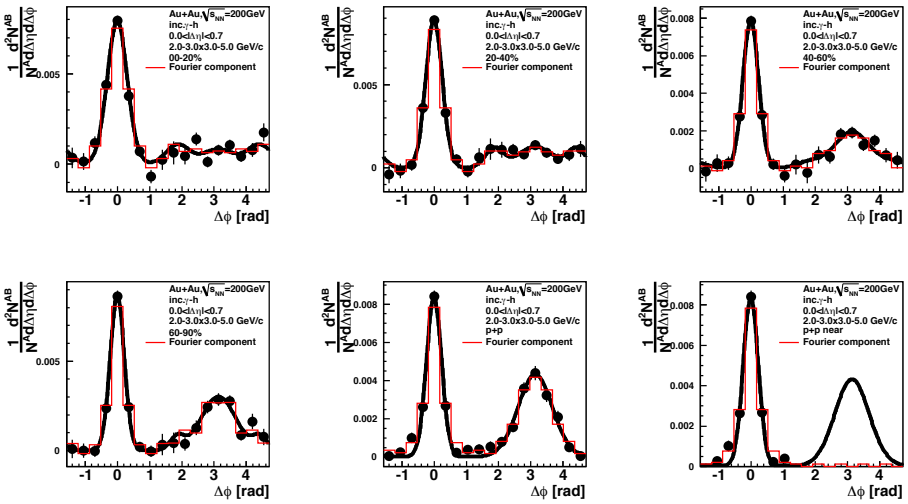

Figure 6.2: Per trigger yield jet function of various centralities (black) are compared with Fourier expansion results (red). Trigger p_T = 2.0–3.0 GeV/c and partner p_T = 3.0–5.0 GeV/c

6.2.2 Fourier Spectra of the Jet Function

Fig. 6.3 show the Fourier coefficients of jet function in various centralities extracted from Fig. 6.1. The solid line in the figure is the Fourier spectrum of pp jets. The green dashed line represents the case will fully quenching the awayside of pp–like jets. In this case, we observed that for the even terms (C_0, C_2, C_4), the full pp jet has larger coefficients than the fully quenched awayside pp–jet, since these even terms have peaks at $\Delta\phi = \pi$. On the other hand, the odd terms (C_1, C_3) in the full pp jet are smaller than the fully quenched awayside pp–jet, as these odd terms are negative at $\Delta\phi = \pi$. So jet quenching itself will increase the value of odd harmonic components.

Next, we look at the centrality dependence. For the Fourier coefficients larger than C_5, the values are very small in all centralities, indicating lesser importance of the higher harmonics.

The zeroth coefficient, C_0, is equivalent to the total yield integrated over 2π. At low associated particle p_T, where most central Au+Au collisions have higher yield than pp. Consquently, C_0 from Au+Au should exceed that for p+p. This can be seen clearly in Fig. 6.1. When moving from central to peripheral collisions, the total yield drops and approaches to the pp value.

The C_1 value of the most central collisions is closer to the fully quenched jet. With increasing centralities, C_1 is approaching the full p+p jet. This is consistent with the general picture that the more central the collision is, the more the jet is quenched.

In C_2, since we use ZYAM to remove most of the combinatorial background in Au+Au, what is left in the jet function should contain a significant portion of the jet. C_2 is very similar to C_2 observed in p+p collisions.

The third harmonic, C_3, shows strong enhancement in central collisions. The coefficients decrease with increasing centrality. It should be noted that, as described above, fully quenched away side jets cause the magnitude of the C_3 to increase comparing to unmodified p+p jets. C_3 in central collisions is much larger than the expectation from jet quenching, which means that there must be some other process causing an enhancement. A similar enhancement is observed in the fourth harmonic, C_4, but is less significant compared to C_3.

In Fig. 6.4, where associated particle $p_T = 3 - 5$ GeV/c, the situation is a little bit different. The C_0 term here is between that for full pp jets and awayside quenched pp jets. We know there is a strong jet quenching in this associated particle p_T region. (See Fig. 6.2). For this region, the structures from the medium effects such as ridge and shoulder are not strong, and the distribution is mostly dominated by jet quenching. Nevertheless, we still see some enhancement of C_3 in the 0–20% and 20–40% centrality bins.

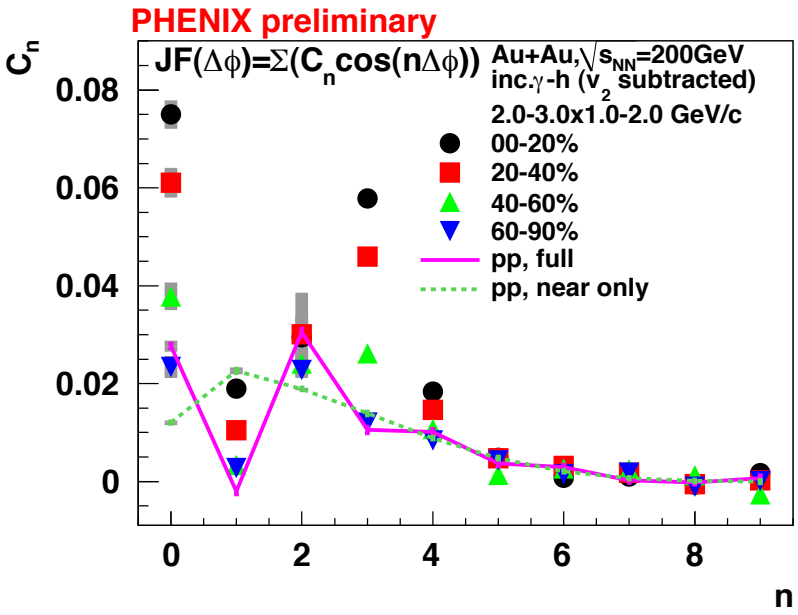

Figure 6.3: Fourier spectra for various centrality in Au+Au collisions. Trigger p_T = 2.0–3.0 GeV/c and partner p_T = 1.0–2.0 GeV/c, with v_2 modulated background shape subtracted.

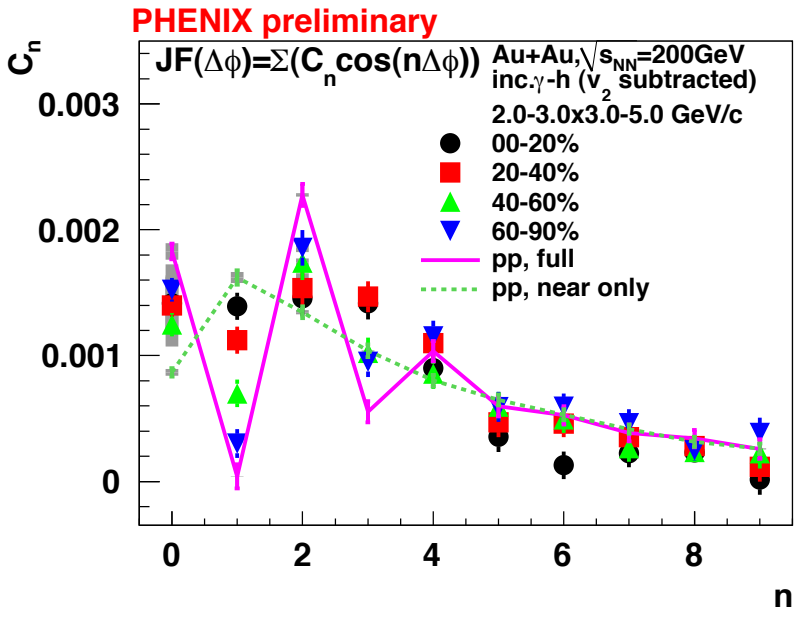

Figure 6.4: Fourier spectra for various centrality in Au+Au collisions. Trigger p_T = 2.0–3.0 GeV/c and partner p_T = 3.0–5.0 GeV/c, with v_2 modulated background shape subtracted.

6.3 Background Subtraction with Modulations from Higher Harmonics

From the previous chapter, we learned that there are higher harmonic components of collective flow. PHENIX has measured v_n with respect to ψ_n for low p_T particles arising from the flowing bulk, which forms the underlying event for this analysis [68]. Those v_n values are now used to better describe the background shape in two particle correlations. The reason to use v_n values from [68] instead of v_n from two particle correlation methods is to avoid the non–flow contribution in v_n when both particles are measured at mid–rapidity

To demonstrate the effect of higher harmonics in the underlying event, we take the following steps. First we rescale the correlation function (without background subtraction) so the y–axis is the per trigger yield. Then we subtract out the flow background with the shape described by Eq. 6.2. The background level, b_0, is determined by absolute normalization (ABS) [76]. The absolute normalization method assumes the level of the uncorrelated underlying event pairs is proportional to the particle production rate of the trigger and associated particles with a centrality dependent factor. Unlike ZYAM, ABS determines the background level independent from the shape of the background, which is important since we only change the shape, but not the level of the background. We add v_n one by one to Eq. 6.2, to see how each term changes the shape of the subtracted correlation function. The correlation function is then compared with the jet function in p+p, which represents the unmodified jet–function. The last step is to measure the Fourier spectrum of the subtracted Au+Au jet function, and compare to the Fourier spectra of the two p+p baselines (unmodified and awayside fully quenched), thus allowing us to quantify how the jet function is modified.

The full underlying event background shape is defined as

$$FL(\Delta\phi) = b_0(1 + 2c_2\cos(2\Delta\phi) + 2c_3\cos(3\Delta\phi) + 2c_4\cos(4\Delta\phi)) \tag{6.2}$$

where

$$c_n = v_n^{trig}(\psi_n)v_n^{part}(\psi_n) \tag{6.3}$$

The details of how Eq. 6.2 is obtained are described in Appendix A. The v_n used here are from [68], as shown in Fig. 6.5. For this analysis, the trigger particle is inclusive photons with p_T at 2–3 GeV/c, which is mainly the π^0 decay photon. The parent π^0 mean p_T is about 2.6 GeV/c, so as a proxy, we use the inclusive charged hadron at 2.5–3.0 GeV/c as a proxy for the inclusive photon v_3 and v_4.

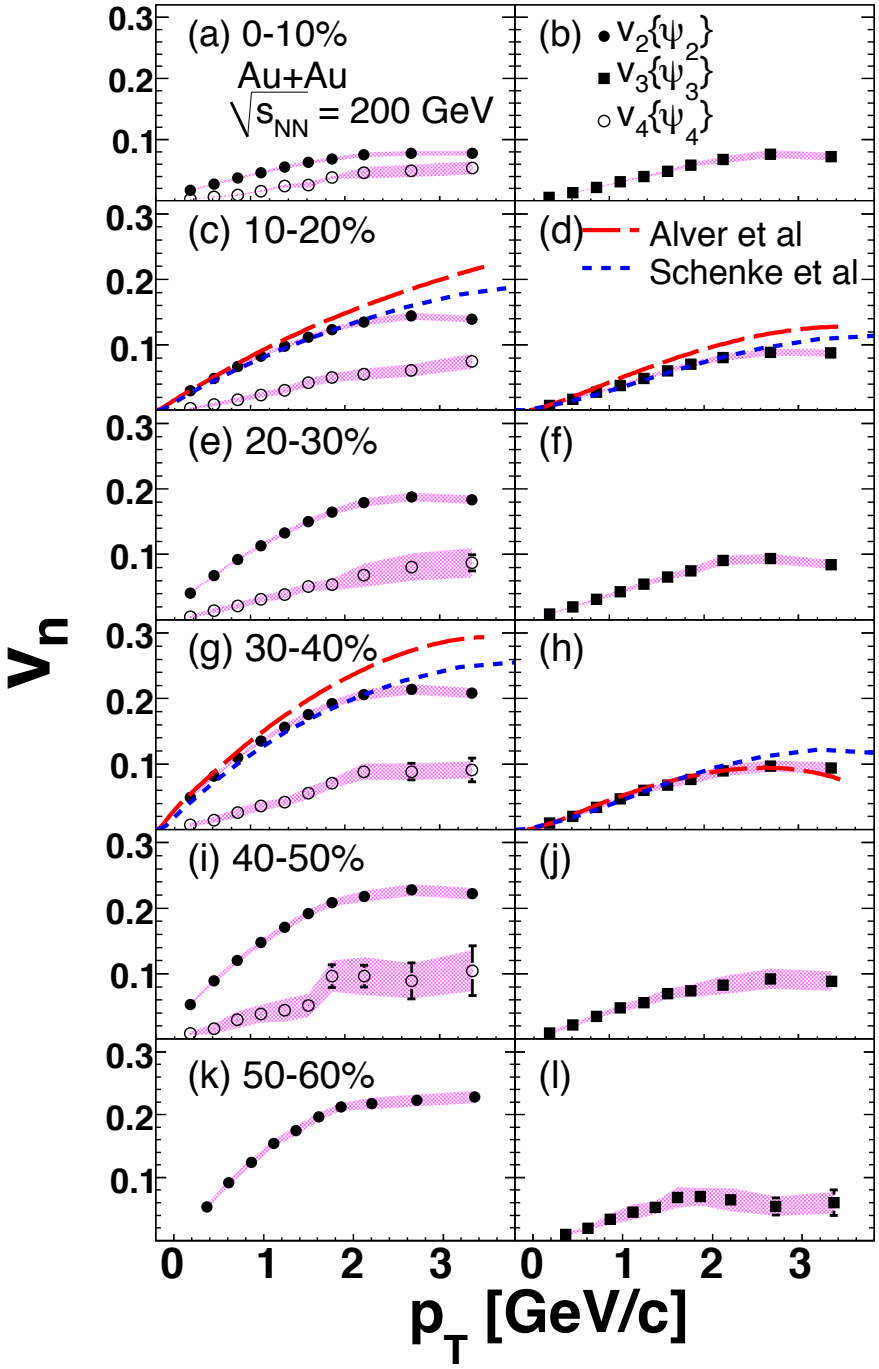

Figure 6.5: Measurements of v_2, v_3, v_4 with respect to ψ_n from [68].

We use Fig. 6.6 as an example of the result of the background subtraction. Inclusive photon triggers at 2–3 GeV/c are associated with inclusive charged hadron at 1–2 GeV/c. The centrality is 0–20%. The left column includes v_2 modulation of the background shape; the middle column is modulated by v_2 and v_3, and right column is v_2, v_3 and v_4. Adding in background v_n one by one shows the effect of each v_n.

The left column uses the standard v_2 modulated background only. The first row shows the per trigger yield Au+Au correlation function, with the blue curve representing the underlying event background to be subtracted. Using Eq. 6.5, the jet function is calculated and plotted in the second row as black points. The red points are the p+p correlation function as a reference. With v_2 modulated background subtraction, the double peak structure is clearly seen. The third row shows the Fourier spectra of the Au+Au jet function (plotted in black points) and compared with the two different p+p cases. The solid red line represents the unmodified p+p and red dashed line represents p+p with awayside jets fully quenched.

Moving to the second column, v_3 modulation is included in the background. The top panel shows that the background function has a different shape compared to the v_2 only case. The jet function after subtraction in the second row shows that the double peak structure is significantly reduced, and there is a pedestal under the jet correlation function. This should be expected, since add in those terms modulating the background function leave the total jet yield, re[resemted bu $C + 0$ imcjamged/ Ot os pm;u tje sja[e pf tje ket fimctopm wjocj cjages/

The Fourier spectrum in the third row shows that the third harmonic in the jet function is significantly reduced, which is not surprising since we now include v_3 in the flow background. As a crosscheck, the C_0 term in both cases (v_2 and $v_2 + v_3$) are the same, which is because adding in another v_n contribution in Eq. 6.2 will only change the shape of the jet function, not the total yield integrated over 2π.

In the right column of Fig. 6.6, we also include the v_4 modulation. The subtracted jet function in the second panel does not have a clear double peak structure. It looks more like a broadened and suppressed jet sitting on a flat pedestal.

The pedestal structure can be understood as follows. In all three different background cases shown in Fig. 6.6, the background level, b_0, is fixed to the same value determined by absolute normalization. Since add in extra v_n terms do not change the total background, but only changes the shape, this means the total yield of the jet function is also the same with different v_n background shape. This is verified in the Fourier spectra that C_0 is the same in all three

cases. Since the yield does not change, but the shape of the jet function does, the enhancement seen as ridge and shoulder for background with v_2 only is redistributed when higher harmonics are included in the background. This redistribution of the extra yield recovers the ridge and shoulder and leads to the pedestals seen in the second and third columns of Fig. 6.6.

6.4 Motivation and Verification of the p+p reference

From the standard two particle correlation analysis, we know that the correlation function can be written as

$$CF(\Delta\phi) = JF(\Delta\phi) + FL(\Delta\phi) \tag{6.4}$$

or we can rewrite Eq. 6.4 as

$$JF(\Delta\phi) = CF(\Delta\phi) - FL(\Delta\phi) \tag{6.5}$$

We assume after removing the flowing background contributions, $FL(\Delta\phi)$ in Eq. 6.5, what's left should resemble a p+p–like jet. This is inspired by the high p_T correlation function studies from PHENIX [23] and [24].

In the previous sections, we use unmodified p+p jets and awayside fully quenched p+p jets as two baselines. We claim that the Fourier spectra of any awayside–modified p+p like jets should lie in between the Fourier spectra of these two baselines. We tested several scenarios of jet modifications to see if the claim holds. In Fig. 6.7, several scenarios are illustrated. We have black(red) curves which represented the unmodified (awayside fully quenched) p+p jet. The Fourier spectra are plotted in the right hand side with the same color. We then varied the shape and yield of awayside jet. The first case is shown in green where the width of the awayside is unchanged, but the awayside yield is suppressed by 0.5. In the second case, the yield of the awayside is unchanged, but the width is broadened by 50%, which is shown in blue. The last case has awayside width broadened by 50% and yield suppressed by 50%, plotted in yellow.

The right hand side of Fig. 6.7 show that the Fourier spectra of the three jet scenarios all fall between the black and red points, thus support the use of these two extreme cases for comparison with Au+Au which are the two extreme case we used here. The awayside fully quenched case can be thought of as an awayside jet that is extremely broad. As visible in blue, even if the awayside yield is unchanged, once the width is broader, the Fourier spectrum starts to approach the fully quenched awayside case.

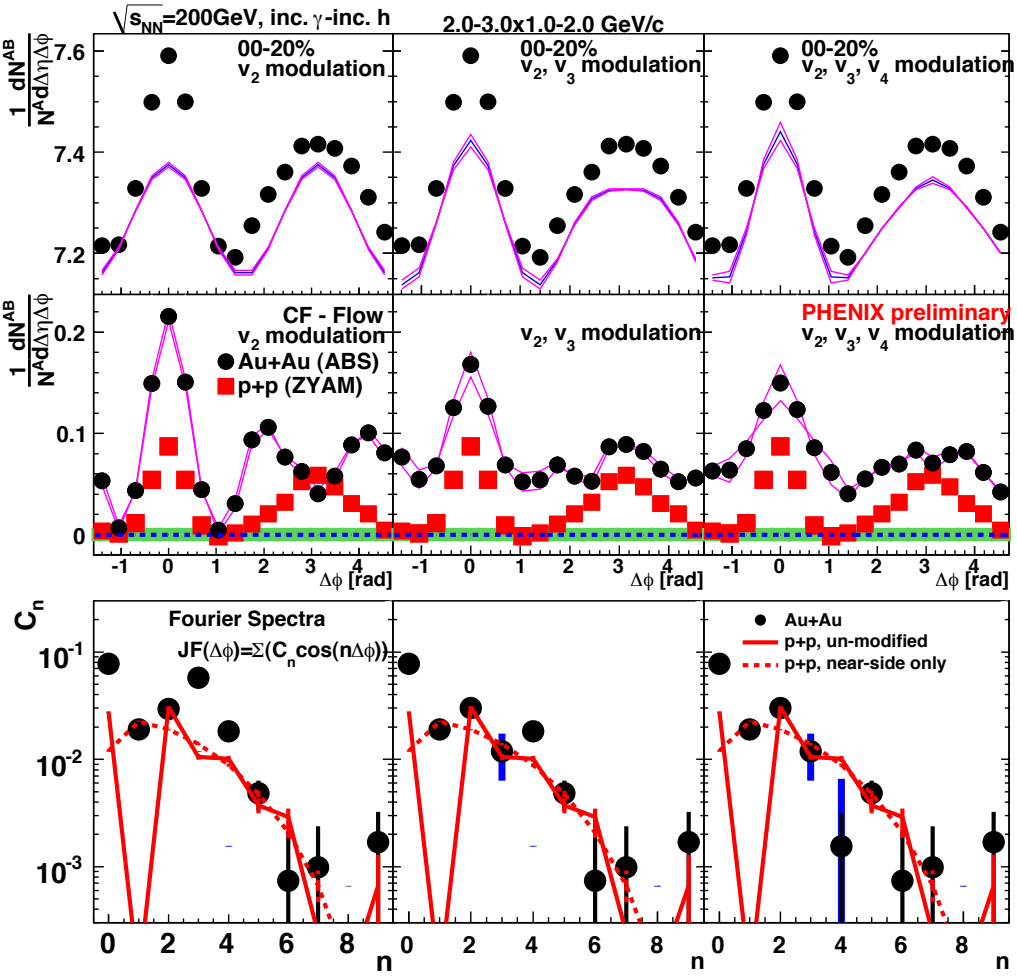

Figure 6.6: Correlation functions with different v_n modulated underlying event background subtracted. The left column: v_2 modulation; middle column: v_2 and v_3 modulation; right column: v_2, v_3 and v_4 modulation. Top panel: correlation function with v_n modulated underlying event background; middle panel: jet function with v_n modulated background subtracted; bottom panel: Fourier spectra of the jet function.

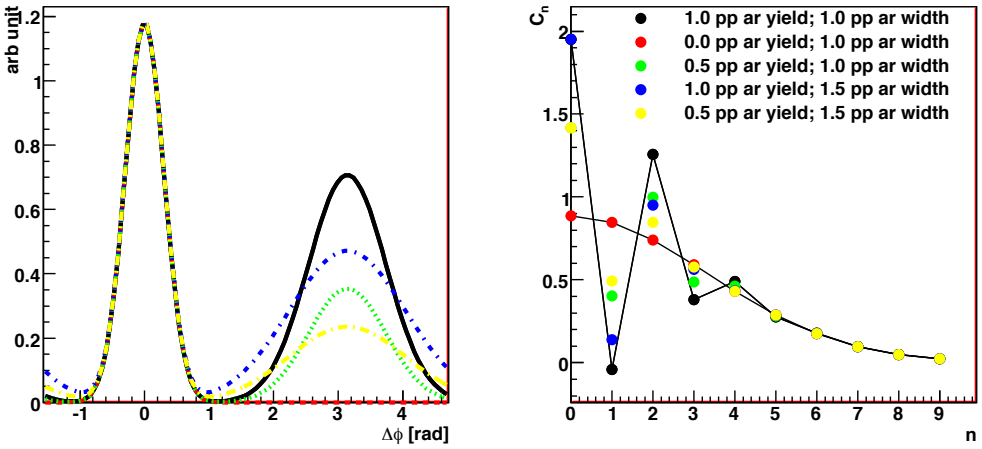

Figure 6.7: Fourier Spectra in different simulated p+p like jet scenarios. Black: unmodified p+p jet; red: awayside jet yield is fully suppressed; green: awayside yield is suppressed by 50%; blue: awayside jet width is broadened by 50%; yellow: the awayside jet yield is suppressed by 50% and the jet width is broadened by 50%.

6.5 Au+Au Compared with p+p

In this section, we start with the Fourier spectra and see the effect in the v_n subtraction.

To study the v_n effect, we first transform all the correlation functions in Eq. 6.4 in to Fourier spectra, say

$$CF(\Delta\phi) = \Sigma C_n^{CF} \cos(n\Delta\phi) \tag{6.6}$$
$$FL(\Delta\phi) = \Sigma C_n^{FL} \cos(n\Delta\phi) \tag{6.7}$$
$$JF(\Delta\phi) = \Sigma C_n^{JF} \cos(n\Delta\phi) \tag{6.8}$$

So for each Fourier coefficient, C_n, Eq. 6.4 can be written to be as

$$C_n^{CF} = C_n^{FL} + C_n^{JF} \tag{6.9}$$

or we can rearrange the equation

$$C_n^{JF} = C_n^{CF} - C_n^{FL} \tag{6.10}$$

From Eq. 6.2, we only use v_2, v_3, and v_4 and a constant term in the flow underlying background. When doing the subtraction shown in Eq. 6.10, only C_0, C_2, C_3, C_4 will be modified. The rest of the harmonics are untouched.

After we did the subtraction, we compare C_n in Au+Au with the corresponding term C_n from the two p+p reference baseline. If after v_n background subtraction, what's left in Au+Au falls in between the two p+p reference, we can assume the jet component left in Au+Au should be a "p+p–like jet shape". If what's left is beyond the two p+p reference, then this will indicate some extra contributions other than the bulk and jet contribution exists.

Fig. 6.8 is the C_0 term. C_0 corresponds to the total per trigger yield integrated over 2π. We see all the Au+Au points are significantly above the p+p reference lines here. This is not surprising since we know at low partner p_T, there are more particles in Au+Au than in p+p, as seen in this analysis and reported by PHENIX earlier [23]. This extra yield was originally the ridge and shoulder, these structures are no longer observed. Nevertheless, the total particle yield in Au+Au correlations is higher than the totally uncorrelated underlying events (which is determined by absolute normalization) and unmodified jet can provide

In Fig. 6.9, after removing the uncorrelated v_2 terms from the underlying event, the remaining C_2 due to jets in Au+Au lies in between the two p+p references. This suggests that C_2 in Au+Au can be explained by the p+p like jet; for C_2, there is only bulk and jet.

In Fig. 6.10, the C_3 the central values still fall between the two p+p references, but the systematic error bar is large enough to cover the two references. curves. This plot suggests that the third harmonic could be described by the bulk v_3 and the normal jet contribution only. If this is true, then the three peak structure (ridge plus two shoulders) is due to the bulk v_3, since after subtraction, only the jet–like structure remains.

The v_4 case, shown Fig. 6.11, is different. We applied v_4 obtained [68] and the result is surprising. Unlike Fig. 6.9 and Fig. 6.10, all the Au+Au points are below the p+p references, and are consistent with 0, except for the associated particle $p_T = 3$–5 GeV/c. This is very surprising, since if C_4 is consistent with 0, then it indicates that the bulk v_4 describe everything in Au+Au collisions, and the jet component has no contribution to the fourth harmonic at all. We don't have good explanation for this at this moment.

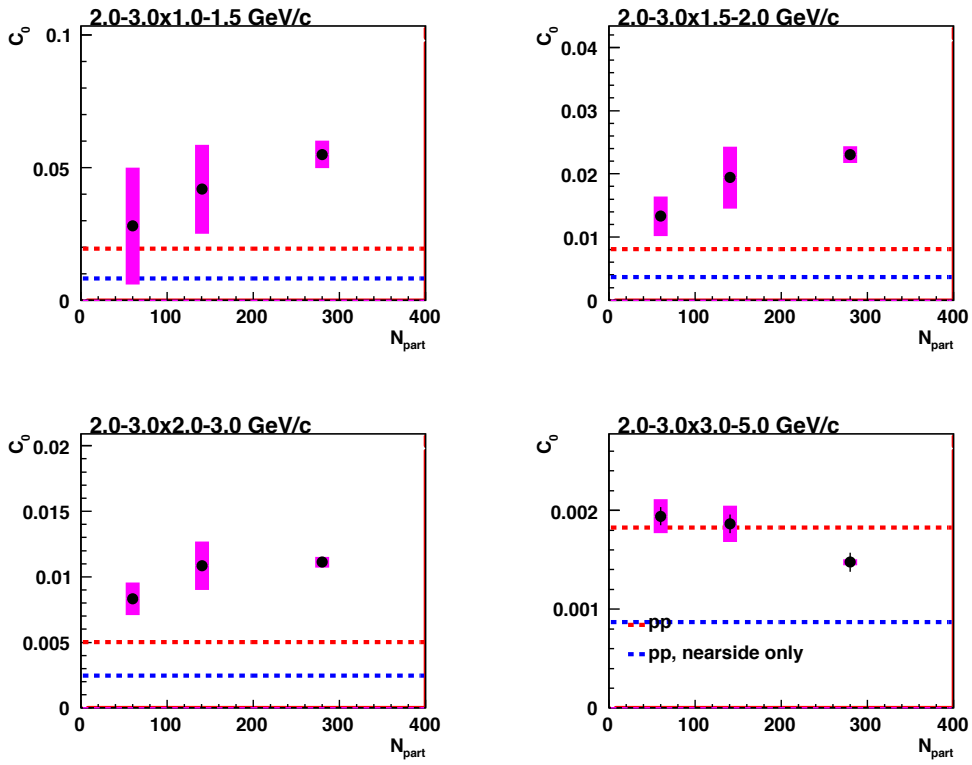

Figure 6.8: C_0 from Au+Au in different as a function of N_{part} compare with two p+p references in different partner p_T.

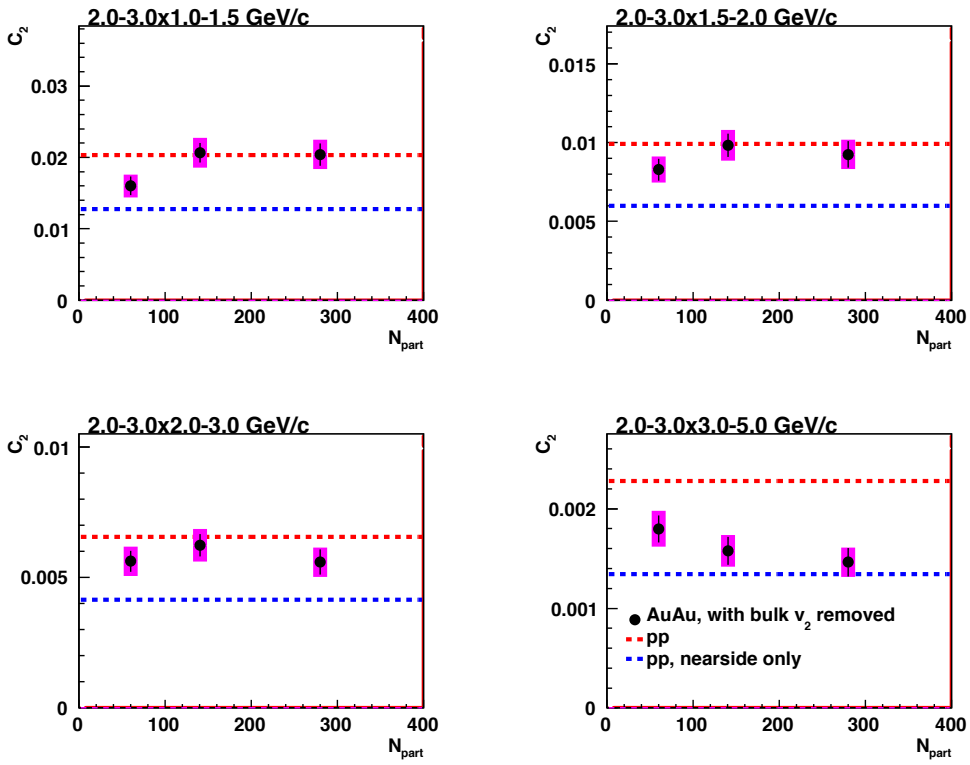

Figure 6.9: C_2 from Au+Au in different as a function of N_{part} compare with two p+p references in different partner p_T.

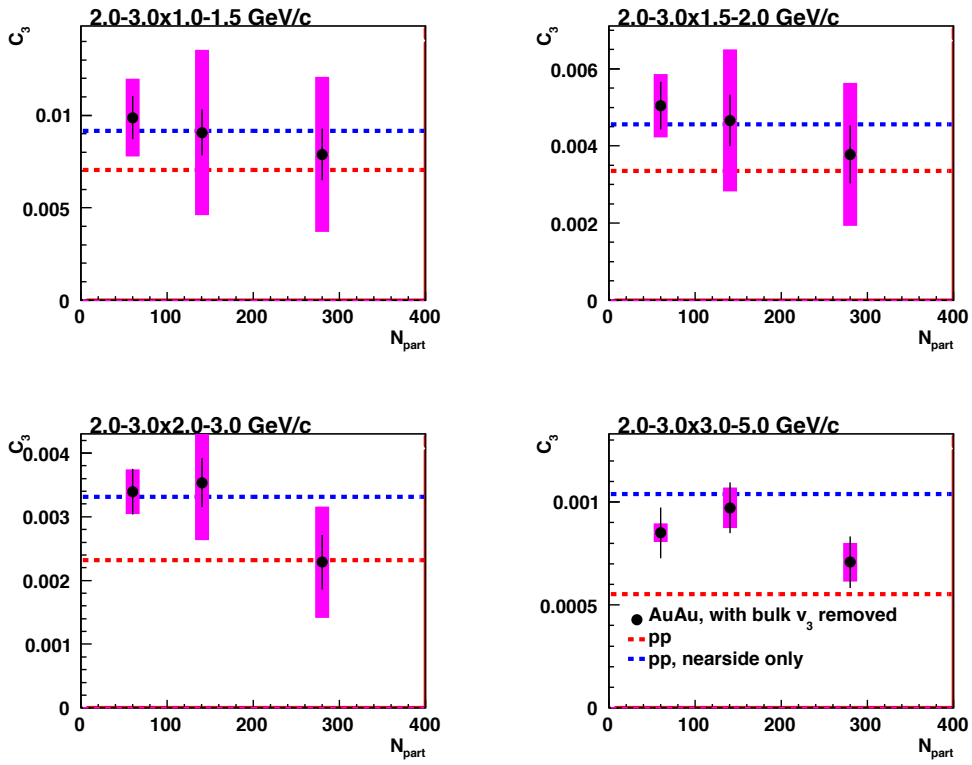

Figure 6.10: C_3 from Au+Au in different as a function of N_{part} compare with two p+p references in different partner p_T.

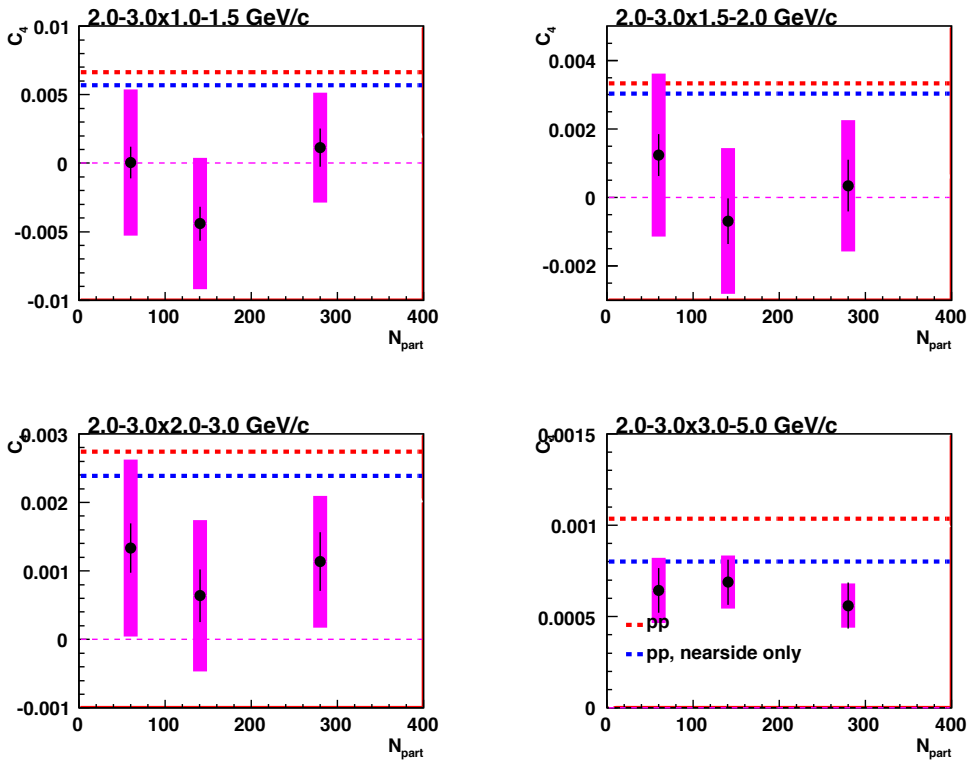

Figure 6.11: C_4 from Au+Au in different as a function of N_{part} compare with two p+p references in different partner p_T.

Part IV

Discussion

Chapter 7

Discussion

7.1 QGP: the Most Perfect Fluid

When the two nuclei undergo non–central collisions, or have a nonzero impact parameter, b, the colliding area forms an almond shape. This hot dense region equilibrates, expands and cools, and numerous particles are produced. The pattern of the particle emission depends on the mean free path of the particles, l, and the the size of the system, R. When l is not much smaller than R, the emission pattern can be assumed to be the superposition of many nucleon–nucleon collisions, which are azimuthally isotropic. When $l \ll$ R, then the behavior of a system in equilibrium can be described by relativistic hydrodynamics, and the emission pattern is mainly influenced by the shape of the system.

When system is locally thermalized, as described in Chapter 1.3, the system can be described by hydrodynamics. When the system expands, the particles flow collectively. This flow is due to the pressure gradients in the system. In the almond shape colliding area, the pressure should to be the greatest at the short direction, which is along the impact parameter.

As a result, we can measure the angular distribution of particles with respect to the event plane as:

$$\frac{dN}{d\phi} \propto 1 + \sum (2v_n \cos n(\phi - \psi_n)) \tag{7.1}$$

The Fourier coefficients, v_n, can provide a lot of information on the properties of quark–gluon plasma, and can be compared with hydrodynamical calculations.

7.1.1 v_2 and Geometry

PHENIX measured v_2 in Au+Au and Cu+Cu collisions [18]. The v_2 of inclusive charged hadrons is measured as a function of p_T, as shown in Fig. 7.1. In Fig. 7.1 (a) and (b), v_2 increases from central to mid–central collisions, in parallel with the increased geometrical anisotropy. The v_2 increases with p_T up to 3 GeV/c and then appears to saturate.

Cu+Cu is a smaller system than Au+Au. When both systems have a similar number of participants during the collision, the two may have different geometric shapes. In order to remove the geometrical effect of the system, the v_2 is normalized by the eccentricity, ε. Since p_T integrated v_2 is assumed to be proportional to the eccentricity of the system, it can be used as a proxy of eccentricity [18].

After normalizing by eccentricity (or the p_T integrated v_2), all v_2 values fall along a universal curve, independent of the colliding system and centrality as shown in Fig. 7.1 (c). This implies that the expansion of the system is universal, and suggests a rapid thermalization of the system at the partonic level [77, 78].

7.1.2 v_2 and Quark Number Scaling

v_2 as a function of p_T for different particle species are shown in Fig. 7.2 (a) [18]. v_2 of identified particles fall into two groups: mesons and baryons. At $p_T < 2$ GeV/c, v_2 of the mesons is larger than for baryons. At $p_T > 2$ GeV/c, the v_2 of mesons begins to saturate while the v_2 of baryons continues increasing and shows some signs of saturation at 3 GeV/c. Fig. 7.2 (b) is the same data, but plotted vs transverse kinetic energy, KE_T, where $\mathrm{KE}_T = m_T - m$. KE_T takes into account relativistic effects and the particle mass, and is a better way to check scaling with the energy. We see that all mesons line up together, as do the baryons.

We can take a step further and plot the v_2 per valence quark:

$$v_2^{meson}(p_T) = 2v_2^{quark}(p_T/2) \tag{7.2}$$

$$v_2^{baryon}(p_T) = 3v_2^{quark}(p_T/3) \tag{7.3}$$

Fig. 7.3 shows the v_2/n_q vs p_T/n_q or KE_T/n_q scaling. After scaling by number of quarks, where $n_q = 2$ for mesons and 3 for baryons, v_2/n_q vs KE_T/n_q of all particles align together and show a universal trend, visible in Fig. 7.3 (b). On the other hand, Fig. 7.3a, which is plotted vs p_T, does not show similar scaling properties. The fact that the flow scales with the quark content rather

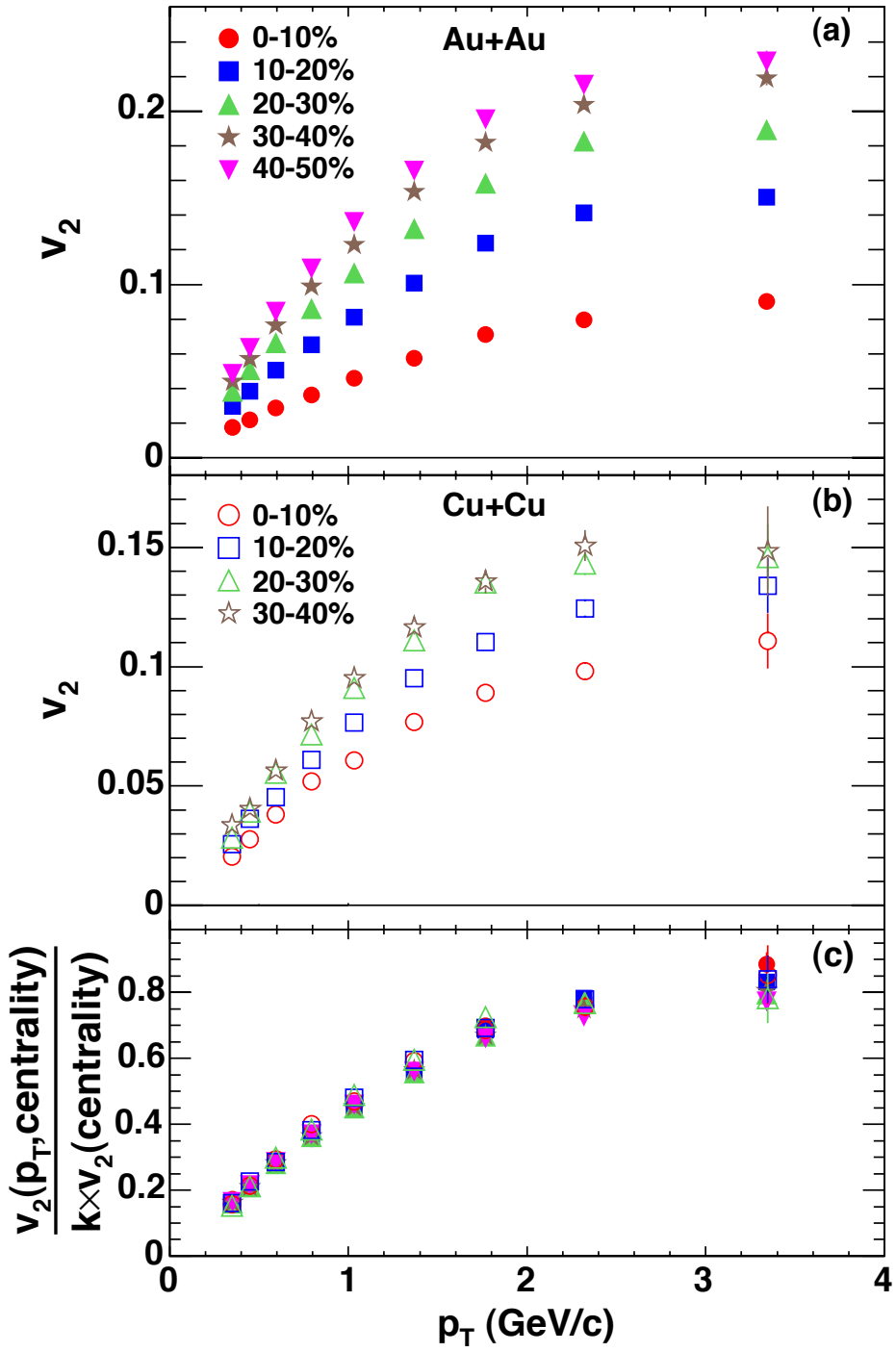

Figure 7.1: v_2 measurement in (a)Au+Au; (b)Cu+Cu; (c)v_2 scaled with p_T integrated v_2 [18]

than the mass of the hadrons, suggests that quarks are the relevant degrees of freedom when the pressure gradients are built up. The magnitude of v_2 implies that the collective flow is built up very quickly, before the expansion of the system restores geometrical symmetry.

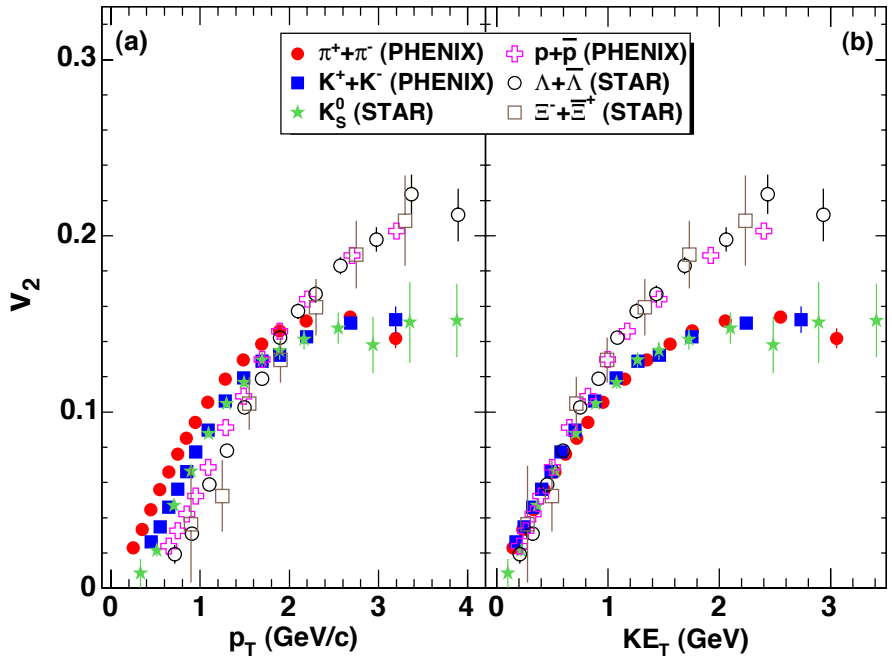

Figure 7.2: (a) v_2 vs p_T and (b) v_2 vs KE_T of identified charged hadrons in min–bias Au+Au collisions [18]. STAR data from [79, 80]

7.1.3 How Perfect is QGP? Extracting η/s

The significant flow, v_2, observed indicates the system expands collectively, and that it thermalized rapidly [77, 78]. This is can be described by the relativistic hydrodynamics. But by assuming the system as perfect fluid, where there is no viscosity, the hydrodynamic models predict a stronger v_2 than data [17]. Earlier calculations indicates that by introducing small but nonzero viscosity to the system, it can reduce the v_2 [81]

When using relativistic hydrodynamics to calculate v_2, several parameters are necessary: the thermalization time, τ_0, where the hydrodynamics starts; τ_f, where the hydrodynamics stops; the initial state of the system when hydrodynamics starts. Here we focus on the initial state of the collision. There are two kinds of initial conditions. One is the Glauber model, which assumes

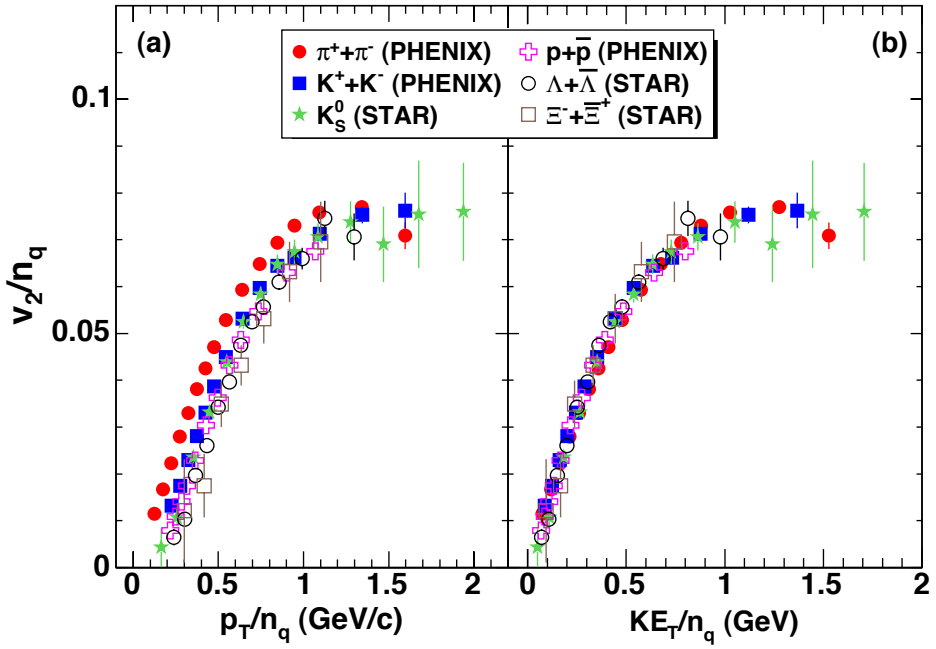

Figure 7.3: Quark number scaling of identified charged hadrons: (a) v_2/n_q vs p_T/n_q and (b) v_2/n_q vs KE_T/n_q [18]. STAR data from [79, 80]

that the nuclei consist of individual nucleons with nucleons distributed according to Woods–Saxen function. The other model is the Color Glass Condensate (CGC), which assumes that in the nuclei, the density of gluons is saturated. So the initial condition is determined by the gluon distribution inside the nuclei.

If the QGP behaves like a liquid, this raises the question of what the shear viscosity of this liquid might be. The shear viscosity, η, is the property of the liquid which describes the energy dissipation. The larger the viscosity, the easier energy gets lost. For perfect liquid, the shear viscosity is zero, which means energy can go through the medium without any dissipation.

But the QGP is not a normal "liquid". It has a high temperature, consists of quarks and gluons, and the interaction is described by QCD. With Anti–di–Sitter/Conformal Field Theory (AdS/CFT), people can transform the strong coupling problem into a 5–dimensional gravity dual, where the strong–coupled field theory is approximated as a gravitational field near a black hole. By this AdS/CFT correspondence, people calculate that there is a minimum value for the ratio of the shear viscosity over the entropy density, which is given by [82]

$$\frac{\eta}{s} = \frac{1}{4\pi} \tag{7.4}$$

Eq. 7.4 tells us that there is a universal lower bound of the ratio η/s. Even though the ratio of η/s has a lower bound, the viscosity of the quark gluon plasma could still be large. So it is an important experimental goal to measure it.

Fig. 7.4(a) and Fig. 7.4(b) compare relativistic hydrodynamical calculations for v_2 with two different initial conditions, Glauber and CGC [83]. The v_2 data is from STAR [84]. The calculations show that if the viscosity to entropy ratio is zero, which is the case for a perfect fluid, both initial states over–estimate the measured v_2 values.

Further calculations assume different values of η/s, from 0.08 $(1/4\pi)$ to 0.24. The effect of the viscosity brings the calculated v_2 down. The most interesting aspect of Fig. 7.4(a) and Fig. 7.4(b) is that with some finite viscosity, both Glauber and CGC describe the v_2 trend equally well. For the Glauber initial state, the best value is $\eta/s = 1/4\pi$, while $\eta/s = 2/4\pi$ for the CGC initial state.

From these calculations, we know that the QGP has a small but finite η/s, which is close to the value of the universal lower bound of a quantum system, $\eta/\mathrm{s} = 1/4\pi$. Also, depending on the assumptions of different initial states, Glauber or CGC, the value of η/s is different. A key issue over the past several years has been how to remove this degeneracy with additional experimental information.

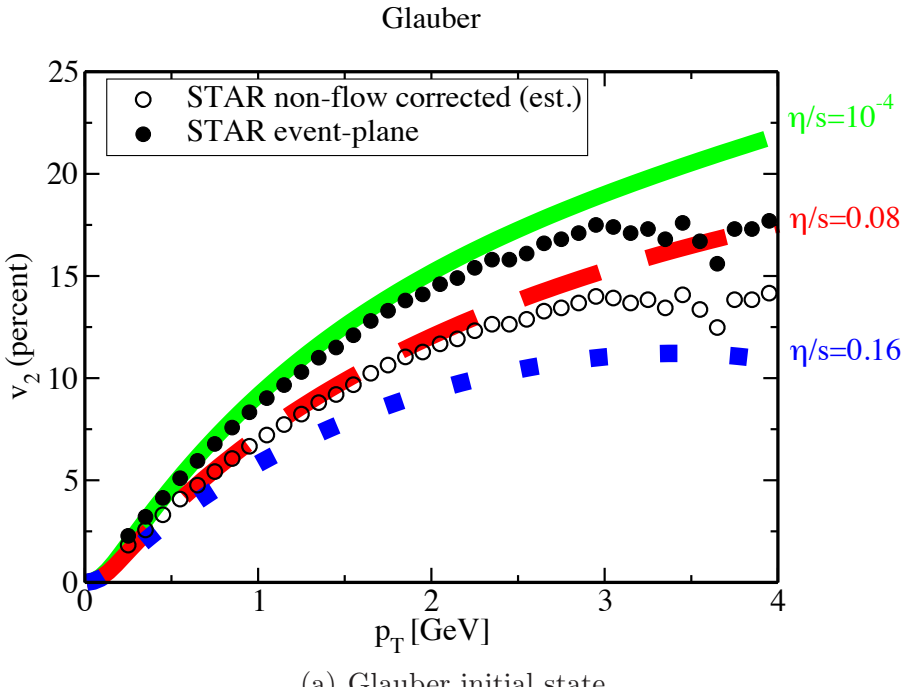

(a) Glauber initial state

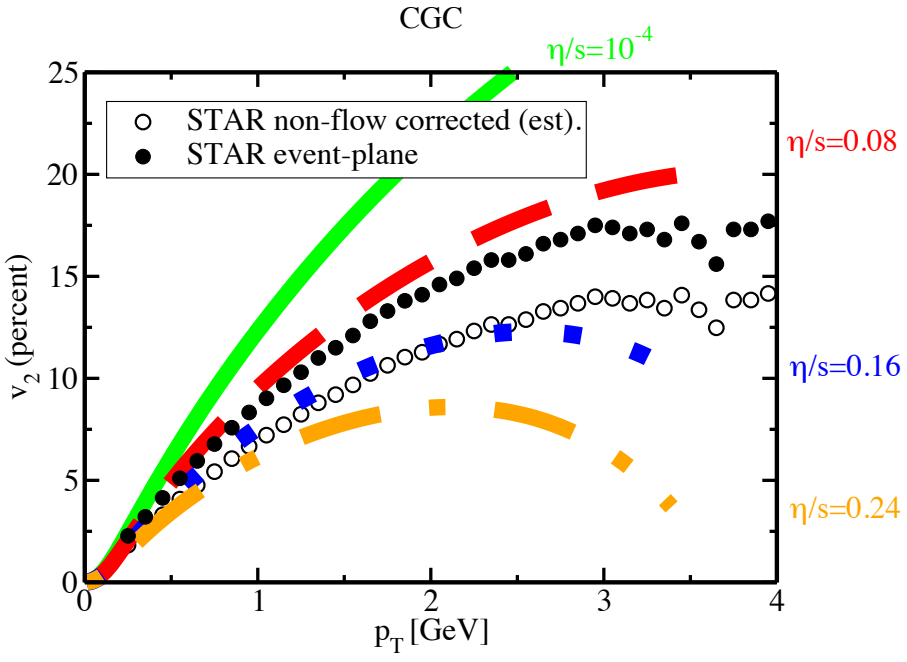

(b) CGC initial state

Figure 7.4: Flow calculations with different initial state conditions with various η/s [83]. The data is from STAR [84]

7.1.4 Further Constraints on η/s: v_n

To further constrain η/s, we need more parameters. The two different initial states (Glauber and CGC) give different values for η/s when compared with v_2. Comparing hydrodynamic calculations to higher harmonics ($n > 2$) will provide additional constraints to distinguish between models and initial conditions.

Fig. 7.5 compares the $v_2\{\psi_2\}$ and $v_3\{\psi_3\}$ as a function of N_{part} with several theoretical calculations [72, 74, 70]. Alver et al. [72] assumed an energy profile using two initial conditions, Glauber and MC–KLN. The Glauber initial state condition was described previously in section 5.8, the energy profile is described by a Woods–Saxon function. MC–KLN [85, 86] is a particular implementation of the Color Glass Condensate, where the energy density is determined by gluon density in the transverse plane. The gluon density peaks at the center of the nuclei and decreases at the edge of the nuclei. Fluctuations are introduced in both initial conditions. These two initial conditions are paired with different η/s values: $\eta/s = 1/4\pi$ for Glauber and $2/4\pi$ MC–KLN respectively, as the two combinations describe v_2 equally well. Petersen et al. [74] starts with Glauber initial conditions. Then the interaction is simulated by the Lund model [87] followed by fragmentation of color tubes, which is also known as the UrQMD transport model [9, 10]. The results are evolved with ideal hydrodynamics ($\eta/s = 0$) event–by–event. At late hadron cascade stage when the system is dilute, the system is gradually transit from hydrodynamics to transport model. B. Schenke *et al.* [70] use event–by–event Glauber initial conditions to fully account for fluctuations in the initial positions of nucleons in the Au nuclei, and then evolves the medium with 3+1 dimensional viscous hydrodynamics, where several values of η/s have been used.

All models are compared with $v_2\{\psi_2\}$ and $v_3\{\psi_3\}$. All calculations describe $v_2\{\psi_2\}$ very well at $p_T = 0.75$ GeV/c as shown in Fig. 7.5(a). At $p_T = 1.75$ GeV/c, the MC–KLN calculation (red points) does not describe the data well at low N_{part}.

For $v_3\{\psi_3\}$ at $p_T = 0.75$ GeV/c, shown in Fig. 7.5(c) and (d), all calculations with Glauber initial conditions show good agreement with data. However, the MC–KLN calculation (red points) are significantly below the data. The deviation is even larger at higher p_T. By contrast, models with Glauber initial conditions with $\eta/s = 1/4\pi$ still describe the data relatively well. This shows the constraining power of v_3 to differentiate among the models.

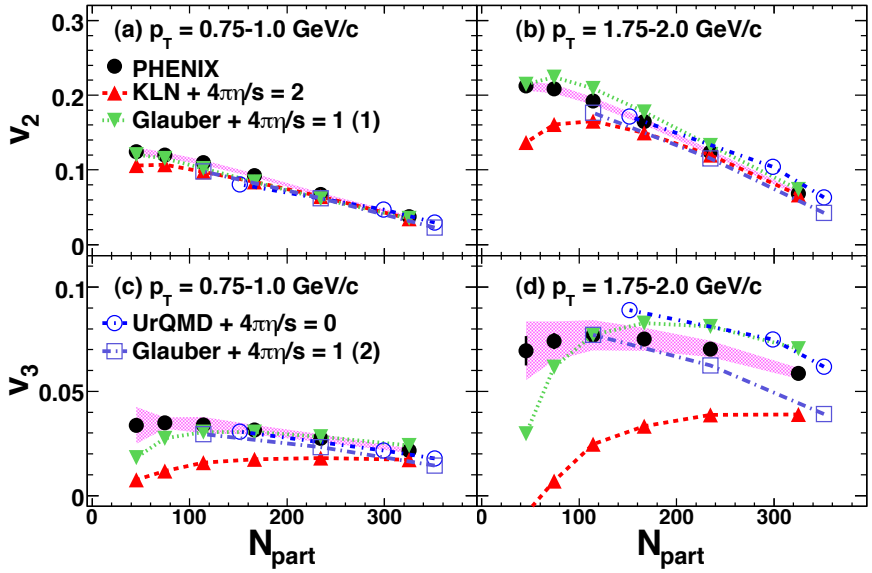

Figure 7.5: v_2 and v_3 compared with various theory calculations in Au+Au [68]

7.2 v_n in Two Particle Correlation: the Ridge and Shoulder

7.2.1 The Ridge and Shoulder with v_2–modulated Background Subtraction

With v_2–modulated underlying event background subtraction in the two particle correlation analysis, the novel structures of the ridge and shoulder are studied extensively in Chapter 4. Both the ridge and shoulder have some properties in common. Both yields strongly depend on the size of the medium and the yield increases with the size of the system. The spectra and truncated mean p_T show that both the ridge and shoulder are much softer than jets in p+p collisions. This tells us that neither the ridge nor the shoulder arise directly from hard scattering. The truncated mean p_T of the ridge and shoulder are closer to the bulk, which indicates that the origin of both should be related to the medium. The truncated mean p_T of the ridge and shoulder are also consistent with one another across various centralities, hinting that the mechanism for producing the ridge and shoulder is independent from the size of the medium.

Both the ridge and shoulder have inspired several theoretical explanations. Most of these theories treat the two phenomena separately. There are several physical pictures proposed to explain the production of the ridge: Jet–medium interactions may result in a momentum kick to particles in the bulk medium, boosting their momentum and producing a correlation with a traversing fast parton [38]. A correlated emission model describes radiation of soft gluons by a parton penetrating the medium; these gluons and their resulting hadronic fragments are boosted by longitudinal flow of the medium [39]. The Glasma model treats the ridge as arising from the flux tube formed early in the collision; longitudinal expansion elongates the ridge in η [40].

The shoulder structure has been suggested to arise from passage of a sound wave as the medium responds to shocks deposited by jet energy loss [41, 42, 43]. However, there is considerable debate as to whether it is possible to observe the resulting Mach cone–like structure [44, 45].

7.2.2 The Ridge, Shoulder and Higher Order v_n Background Modulation

The idea of non–zero odd harmonics, especially v_3, changes the picture for the ridge and shoulder [67]. After higher harmonics are measured using a reaction plane defined at large η [68], we have a better way to describe the shape of the underlying event background.

After subtracting the underlying event, including the modulation of higher harmonics, from two particle correlations, both the ridge and shoulder disappear, as shown in Fig. 6.6. Instead of the ridge and shoulder, the jet function looks like a di–jet with a suppressed and possibly broadened awayside on top of a flat pedestal.

Fourier coefficients, C_n with $n > 0$, as defined in Eq. 6.1, are used to describe the shape of the correlation function. After subtracting backgrounds with higher harmonic modulations, the Fourier coefficient of the corresponding harmonics in Au+Au is consistent with the sum of a jet–like structure and the medium, as shown in Fig. 6.9, Fig. 6.10 and Fig. 6.11.

This tells us that the correlation function can be mostly described by the medium and jets. In other words, the ridge and shoulder arose because we did not consider the background shape correctly. However, v_n is a shape parameter. When integrated over 2π, the $v_n \cos n\Delta\phi$ term is zero, which means v_n changes the shape of the background, but not the absolute background level. In Fig. 6.6, the background level is fixed using the absolute normalizations [76]. This is a crucial step, because we calculate explicitly the background level of

the "totally uncorrelated" underlying background pairs. No matter how many v_n we include in the subtraction, the background level never changes.

This makes Fig. 6.8 an important result. Fig. 6.8 describes the total yield of the correlation function in Au+Au. At low partner p_T, the total yield in Au+Au is larger than in p+p collisions. This tells us that this extra yield comes neither from the uncorrelated background pairs nor from the jets.

Even though Fig. 6.8 shows that there is significant yield which is not from jets or the underlying event, we cannot separate this extra yield from the jets. The reason is that the awayside jet is suppressed, and we cannot tell the exact level of suppression. However, we can use studies of the ridge and shoulder shown in Fig. 4.19 to represent the extra yield or the pedestal. The general trend of the ridge and shoulder yields is an increase with N_{part}. In Fig. 4.28, the truncated mean p_T of the ridge and shoulder are roughly consistent with each other. So we know the truncated mean p_T of the pedestal, which should be the sum of the ridge and shoulder, and should be the same as the ridge and shoulder. This tells us the pedestal is slightly harder than the bulk, but softer then the hard scattering components, indicating that the source of this extra yield may come from some jet–medium interaction, which gives the medium extra energy and makes the truncated mean p_T slightly larger than the bulk medium.

7.2.3 Ridge, Shoulder and the Energy Loss

If the yields in the ridge and shoulder are coming from extra energy deposited in the medium, a natural question is where this energy comes from? One possible source is from the energy loss of the awayside jet.

In Fig. 4.13, we extract the yield of the awayside jet via the fitting method. It is clearly shown that the head region, or the awayside jet yield, is suppressed compared to p+p. This jet suppression is seen in all partner p_T bins. At the same time, the yield in the shoulder region increases while the head region is suppressed. Qualitatively, this is consistent with the idea of energy or momentum conservation, where the energy lost in the head region is recovered in the shoulder region.

However further studies do not agree with this simple assumption. We use p_T weighted yields to describe the momentum in all the components, which is shown in Fig. 4.25 and Fig. 4.26. In Fig. 4.26, the p_T of the associated particles is 1–5 GeV/c. Conservation of momentum tells us that the momentum lost by the high p_T associated particles must be recovered as low p_T particles. What we see in Fig. 4.26 is that the momentum carried by the near and awayside are both larger than the p+p case. But the increase of the nearside is much

larger than the increase of the awayside, indicating a momentum imbalance. Thus, conservation of momentum does not hold, and the observed increase in yield must come from a mechanism as yet unknown.

Part V

Conclusion

Chapter 8

Conclusion

Inclusive photon-inclusive charged hadron $\Delta\eta$-$\Delta\phi$ correlations have been measured. The underlying event background has been removed in order to study the properties of the jet pairs. When subtracting the background pairs with v_2 only modulations, exotic structures have been found in both the near side, the "ridge", and the away side, the "shoulder". The properties of the "ridge" and "shoulder" are very similar to one another in yield, spectra and truncated mean p_T. The truncated mean p_T of the ridge and shoulder are both softer than jet fragments in p+p collisions, and are slightly harder than inclusive charged hadrons. This indicates these two structures may come from some jet-medium interactions.

In order to study the effect of higher harmonics of the underlying event collective flow, higher harmonics have been measured using two methods: the reaction plane method and the two particle correlation method. The new measurement of higher harmonics provides two key pieces of physics. The first is an additional constraint in quantifying the viscosity, or η/s, of the quark-gluon plasma. When using v_2 to quantify η/s, both Glauber and CGC initial state conditions describe the data well, but each correspond to a different η/s: $\eta/s = 1/4\pi$ for Glauber and $2/4\pi$ for CGC. With v_3, the data favors Glauber initial state with $\eta/s = 1/4\pi$.

The second impact of quantifying the higher harmonics is the impact of including them in the underlying event shape. Including higher harmonics in the subtraction of background under the jet function cause the "ridge" and "shoulder" disappear. The resulting jet function does show away side jet suppression and broadening.

There is extra yield observed as a pedestal in the jet functions when including the higher harmonic contributions. Since including higher harmonics do not change the yield, the source of the pedestal is mostly coming from particles originally assigned to the ridge and shoulder when consider only v_2

modulations in the shape of the background.

In conclusion, when jets pass through the medium, the away side jet is suppressed and the shape is broadened. This also brings out extra particles with spectra slightly harder than the medium, but softer than jet fragments. These are probably from the jet-medium interaction.

Bibliography

[1] K. Nakamura and P. D. Group, Journal of Physics G: Nuclear and Particle Physics **37**, 075021 (2010)

[2] S. Bethke, The European Physical Journal C - Particles and Fields **64**, 689 (2009)

[3] D. J. Gross and F. Wilczek, Phys. Rev. Lett. **30**, 1343 (1973)

[4] H. D. Politzer, Phys. Rev. Lett. **30**, 1346 (1973)

[5] F. Karsch, Lecture Notes on Physics **583**, 209 (2002)

[6] E. V. Shuryak, Sov. Phys. JETP **47**, 212 (1978)

[7] E. V. Shuryak, Physics Letters B **78**, 150 (1978)

[8] P. F. Kolb and R. Rapp, Phys. Rev. C **67**, 044903 (2003)

[9] S. A. Bass *et al.*, Prog. Part. Nucl. Phys. **41**, 255 (1998)

[10] M. Bleicher *et al.*, J. Phys. G **25**, 1859 (1999)

[11] R. J. Glauber, Phys. Rev. **100**, 242 (1955)

[12] P. Stankus, Annual Review of Nuclear and Particle Science **55**, 517 (2005)

[13] S. Turbide, R. Rapp, and C. Gale, Phys. Rev. C **69**, 014903 (2004)

[14] A. Adare *et al.* (PHENIX Collaboration), Phys. Rev. Lett. **104**, 132301 (2010)

[15] D. dEnterria and D. Peressounko, The European Physical Journal C - Particles and Fields **46**, 451 (2006)

[16] A. Adare *et al.* (PHENIX Collaboration), Phys. Rev. C **81**, 034911 (2010)

[17] K. Adcox *et al.*, Nuclear Physics A **757**, 184 (2005)

[18] A. Adare *et al.* (PHENIX Collaboration), Phys. Rev. Lett. **98**, 162301 (2007)

[19] A. Adare *et al.* (PHENIX Collaboration), Phys. Rev. Lett. **105**, 062301 (2010)

[20] A. Adare *et al.* (PHENIX Collaboration), Phys. Rev. Lett. **101**, 232301 (2008)

[21] S. S. Adler *et al.* (PHENIX Collaboration), Phys. Rev. Lett. **97**, 052301 (2006)

[22] A. Adare *et al.* (PHENIX Collaboration), Phys. Rev. Lett. **98**, 232302 (2007)

[23] A. Adare *et al.* (PHENIX Collaboration), Phys. Rev. C **78**, 014901 (2008)

[24] A. Adare and other (PHENIX Collaboration), Phys. Rev. Lett. **104**, 252301 (2010)

[25] B. I. Abelev *et al.* (STAR Collaboration), Phys. Rev. C **80**, 064912 (2009)

[26] M. Harrison, T. Ludlam, and S. Ozaki, Nuclear Instruments and Methods in Physics Research Section A: Accelerators, Spectrometers, Detectors and Associated Equipment **499**, 235 (2003)

[27] M. Adamczyk *et al.*, Nuclear Instruments and Methods in Physics Research Section A: Accelerators, Spectrometers, Detectors and Associated Equipment **499**, 437 (2003)

[28] B. B. Back *et al.*, Nuclear Instruments and Methods in Physics Research Section A: Accelerators, Spectrometers, Detectors and Associated Equipment **499**, 603 (2003)

[29] K. H. Ackermann *et al.*, Nuclear Instruments and Methods in Physics Research Section A: Accelerators, Spectrometers, Detectors and Associated Equipment **499**, 624 (2003)

[30] K. Adcox *et al.*, Nuclear Instruments and Methods in Physics Research Section A: Accelerators, Spectrometers, Detectors and Associated Equipment **499**, 469 (2003)

[31] M. Allen *et al.*, Nuclear Instruments and Methods in Physics Research Section A: Accelerators, Spectrometers, Detectors and Associated Equipment **499**, 549 (2003)

[32] C. Adler, A. Denisov, E. Garcia, M. Murray, H. Strobele, and S. White, Nuclear Instruments and Methods in Physics Research Section A: Accelerators, Spectrometers, Detectors and Associated Equipment **499**, 433 (2003), the Relativistic Heavy Ion Collider Project: RHIC and its Detectors

[33] K. Adcox *et al.*, Nuclear Instruments and Methods in Physics Research Section A: Accelerators, Spectrometers, Detectors and Associated Equipment **499**, 489 (2003)

[34] L. Aphecetche *et al.*, Nuclear Instruments and Methods in Physics Research Section A: Accelerators, Spectrometers, Detectors and Associated Equipment **499**, 521 (2003)

[35] J. T. Mitchell *et al.*, Nuclear Instruments and Methods in Physics Research Section A: Accelerators, Spectrometers, Detectors and Associated Equipment **482**, 491 (2002)

[36] C. Adler *et al.* (STAR Collaboration), Phys. Rev. Lett. **90**, 082302 (2003)

[37] B. Alver *et al.*, Phys. Rev. Lett. **104**, 062301 (2010)

[38] C.-Y. Wong, Phys. Rev. C **78**, 064905 (2008)

[39] C. B. Chiu and R. C. Hwa, Phy. Rev. C **79**, 034901 (2009)

[40] A. Dumitru, F. Gelis, L. McLerran, and R. Venugopalan, Nuclear Physics A **810**, 91 (2008)

[41] H. Stoecker, Nucl. Phys. **A750**, 121 (2005)

[42] J. Casalderrey-Solana, E. V. Shuryak, and D. Teaney, J. Phys. Conf. Ser. **27**, 22 (2006)

[43] R. B. Neufeld, Phys. Rev. C **79**, 054909 (2009)

[44] R. B. Neufeld, Eur. Phys. J. **C62**, 271 (2009)

[45] B. Betz *et al.*, J. Phys. G **35**, 104106 (2008)

[46] A. Adare *et al.* (PHENIX), Phys. Lett. **B649**, 359 (2007)

[47] B. B. Back *et al.* (PHOBOS), Phy. Rev. Lett. **94**, 122303 (2005)

[48] S. Afanasiev *et al.* (PHENIX Collaboration), Phys. Rev. C **80**, 024909 (2009)

[49] B. B. Back *et al.*, Phys. Rev. Lett. **91**, 052303 (2003)

[50] A. M. Poskanzer and S. A. Voloshin, Phys. Rev. C **58**, 1671 (1998)

[51] K. Miki, S. Esumi, T. Isobe, and Y. Miake, "π^0 and direct photon v_2 in run4 $\sqrt{s_{NN}} = 200$ gev au+au collisions at rhic-phenix," AN518

[52] M.SHIMOMURA, H.Masui, S.Esumi, and Y.Miake, "High p_t charged hadron v_2 in au + au collisions at $\sqrt{s_{NN}} = 200$ gev," AN473

[53] A. Adare *et al.* (PHENIX Collaboration), Phys. Rev. C **80**, 024908 (2009)

[54] A. Adare *et al.* (PHENIX Collaboration), Phys. Rev. D **76**, 051106 (2008)

[55] S. S. Adler *et al.* (PHENIX Collaboration), Phys. Rev. D **74**, 072002 (2006)

[56] S. S. Adler *et al.* (PHENIX Collaboration), Phys. Rev. C **69**, 034910 (2004)

[57] S. S. Adler *et al.* (PHENIX Collaboration), Phys. Rev. Lett. **95**, 202001 (2005)

[58] J. Adams *et al.* (STAR Collaboration), Phys. Rev. Lett. **97**, 162301 (2006)

[59] T. Renk, Phys. Rev. C **80**, 044904 (2009)

[60] A. Majumder, Phys. Rev. C **75**, 021901 (2007)

[61] V. S. Pantuev(2007), arXiv:0710.1882 [hep-ph]

[62] S. S. Adler *et al.* (PHENIX), Phys. Rev. C **71**, 051902 (2005)

[63] T. Renk, Phys. Rev. C **78**, 014903 (2008)

[64] S. S. Gubser, S. S. Pufu, and A. Yarom, Phys. Rev. Lett. **100**, 012301 (2008)

[65] V. Roy and A. K. Chaudhuri, J. Phys. G **37**, 035105 (2010)

[66] A. D. Polosa and C. A. Salgado, Phys. Rev. C **75**, 041901 (2007)

[67] B. Alver and G. Roland, Phys. Rev. C **81**, 054905 (2010)

[68] A. Adare *et al.* (PHENIX Collaboration)(2011), 1105.3928

[69] K. Adcox *et al.* (PHENIX Collaboration), Phys. Rev. Lett. **89**, 212301 (2002)

[70] B. Schenke, S. Jeon, and C. Gale, Phys. Rev. Lett. **106**, 042301 (2011)

[71] M. Csand, T. Csrg, A. Ster, B. Lrstad, N. Ajitanand, J. Alexander, P. Chung, W. Holzmann, M. Issah, and R. Lacey, The European Physical Journal A - Hadrons and Nuclei **38**, 363 (2008)

[72] B. H. Alver, C. Gombeaud, M. Luzum, and J.-Y. Ollitrault, Phys. Rev. C **82**, 034913 (2010)

[73] B. Alver, M. Baker, C. Loizides, and P. Steinberg(2008), 0805.4411

[74] H. Petersen, G.-Y. Qin, S. A. Bass, and B. Müller, Phys. Rev. C **82**, 041901 (2010)

[75] R. A. Lacey *et al.*, Phys. Rev. C **82**, 034910 (2010)

[76] A. Sickles, M. P. McCumber, and A. Adare, Phys. Rev. C **81**, 014908 (2010)

[77] E. Shuryak, Nuclear Physics A **750**, 64 (2005)

[78] U. Heinz and P. Kolb, Nuclear Physics A **702**, 269 (2002)

[79] J. Adams *et al.* (STAR Collaboration), Phys. Rev. Lett. **92**, 052302 (2004)

[80] J. Adams *et al.* (STAR Collaboration), Phys. Rev. Lett. **95**, 122301 (2005)

[81] D. A. Teaney, Journal of Physics G: Nuclear and Particle Physics **30**, S1247 (2004)

[82] G. Policastro, D. T. Son, and A. O. Starinets, Phys. Rev. Lett. **87**, 081601 (2001)

[83] M. Luzum and P. Romatschke, Phys. Rev. C **78**, 034915 (2008)

[84] B. I. Abelev *et al.* (STAR Collaboration), Phys. Rev. C **77**, 054901 (2008)

[85] T. Lappi and R. Venugopalan, Phys. Rev. C **74**, 054905 (2006)

[86] H.-J. Drescher and Y. Nara, Phys. Rev. C **76**, 041903 (2007)

[87] B. Andersson, G. Gustafson, G. Ingelman, and T. Sjstrand, Physics Reports **97**, 31 (1983)

Appendix A

Flow background shape

A.1 Introduction

In two particle correlations, in order to extract the underlying flow background, it is important to understand the shape of the flow background. We know the single particle azimuthal distribution can be written as Eq. A.1

$$\frac{dN}{d\phi} = \frac{N}{2\pi}\left(1 + 2\Sigma v_n \cos n(\phi - \psi_n)\right) \tag{A.1}$$

, where v_n is the n-th order of anisotropy measured respect to ψ_n, the n-th order of event plane.

Originally, we only consider the simpler form where only the v_2 term exists as

$$\frac{dN}{d\phi} = \frac{N}{2\pi}\left(1 + 2v_2 \cos 2(\phi - \psi_2)\right) \tag{A.2}$$

and the particle pair distribution will be like Eq. A.3

$$\frac{dN^{AB}}{d\Delta\phi} = \frac{N^A N^B}{2\pi}\left(1 + 2v_2^A v_2^B \cos(2\Delta\phi)\right) \tag{A.3}$$

In reference [68], we know v_2, v_3 and v_4 all have significant contributions. It is important to consider their contribution in the pair distribution. What we try to do here is start with a more general Eq. A.1, and then derive the generalized Eq. A.3.

A.2 Derivation

For single particle distribution, we have the following expression Eq. A.4 and Eq. A.5 (only show v_2 and v_3, but without losing the generality):

$$\frac{dN^A}{d\phi} = \frac{N^A}{2\pi}\left(1 + 2v_2^A \cos 2(\phi - \psi_2) + 2v_3^A \cos 3(\phi - \psi_3)\right) \tag{A.4}$$

$$\frac{dN^B}{d\phi} = \frac{N^B}{2\pi}\left(1 + 2v_2^B \cos 2(\phi - \psi_2) + 2v_3^B \cos 3(\phi - \psi_3)\right) \tag{A.5}$$

so when integrated Eq. A.4 over 2π, we have

$$\begin{aligned}
& \int_0^{2\pi} \frac{dN^A}{d\phi} d\phi \\
= \; & \frac{N^A}{2\pi} \int_0^{2\pi} \left(1 + 2v_2^A \cos 2(\phi - \psi_2) + 2v_3^A \cos 3(\phi - \psi_3)\right) d\phi \\
= \; & \frac{N^A}{2\pi} 2\pi \qquad \text{(A.6)} \\
= \; & N^A \qquad \text{(A.7)}
\end{aligned}$$

which gives us the total multiplicity N^A.

For particles A and B distributed as Eq. A.4 and Eq. A.5, the pair distribution, $\frac{dN^{AB}}{d\Delta\phi}$, where $\Delta\phi = \phi^B - \phi^A$ or $\phi^B = \phi^A + \Delta\phi$, can be written as Eq. A.8

$$\frac{dN^{AB}}{d\Delta\phi} = \int_0^{2\pi} d\phi^A \frac{dN^A}{d\phi^A} \frac{dN^B}{d\phi^B} \tag{A.8}$$

So here we explicitly calculate Eq. A.8:

$$
\begin{aligned}
&\frac{dN^{AB}}{d\Delta\phi} \\
= &\int_0^{2\pi} d\phi^A \frac{dN^A}{d\phi^A}\frac{dN^B}{d\phi^B} \\
= &\int_0^{2\pi} d\phi^A \left(\frac{N^A}{2\pi}(1+2v_2^A\cos 2(\phi^A-\psi_2)+2v_3^A\cos 3(\phi^A-\psi_3)\right) \\
&\left(\frac{N^B}{2\pi}(1+2v_2^B\cos 2(\phi^B-\psi_2)+2v_3^B\cos 3(\phi^B-\psi_3))\right) \\
= &\frac{N^A}{2\pi}\frac{N^B}{2\pi}\int_0^{2\pi} d\phi^A \left(1+2v_2^A\cos 2(\phi^A-\psi_2)+2v_3^A\cos 3(\phi^A-\psi_3)\right) \\
&\left(1+2v_2^B\cos 2(\phi^A+\Delta\phi-\psi_2)+2v_3^B\cos 3(\phi^A+\Delta\phi-\psi_3)\right) \\
= &\frac{N^A}{2\pi}\frac{N^B}{2\pi}\int_0^{2\pi} d\phi^A(1+2v_2^A\cos 2(\phi^A-\psi_2) \\
&+2v_3^A\cos 3(\phi^A-\psi_3) \\
&+2v_2^B\cos 2(\phi^A+\Delta\phi-\psi_2) \\
&+2v_3^B\cos 3(\phi^A+\Delta\phi-\psi_3) \\
&+4v_2^Av_2^B\cos 2(\phi^A-\psi_2)\cos 2(\phi^A+\Delta\phi-\psi_2) \\
&+4v_2^Av_3^B\cos 2(\phi^A-\psi_2)\cos 3(\phi^A+\Delta\phi-\psi_2) \\
&+4v_3^Av_2^B\cos 3(\phi^A-\psi_2)\cos 2(\phi^A+\Delta\phi-\psi_2) \\
&+4v_3^Av_3^B\cos 3(\phi^A-\psi_2)\cos 3(\phi^A+\Delta\phi-\psi_2))
\end{aligned}
\tag{A.9}
$$

We now integrate Eq. A.9 term by term:

$$\int_0^{2\pi} 1 d\phi^A = 2\pi$$

$$\int_0^{2\pi} 2v_2^A\cos 2(\phi^A-\psi_2)d\phi^A = 2v_2^A\times 0 = 0$$

$$\int_0^{2\pi} 2v_3^A\cos 3(\phi^A-\psi_3)d\phi^A = 2v_3^A\times 0 = 0$$

$$\int_0^{2\pi} 2v_2^B \cos 2(\phi^A + \Delta\phi - \psi_2) d\phi^A \;=\; 2v_2^B \times 0 = 0$$

$$\int_0^{2\pi} 2v_3^B \cos 3(\phi^A + \Delta\phi - \psi_3) d\phi^A \;=\; 2v_3^B \times 0 = 0$$

$$\begin{aligned}
&\int_0^{2\pi} 4v_2^A v_2^B \cos 2(\phi^A - \psi_2) \cos 2(\phi^A + \Delta\phi - \psi_2) d\phi^A \\
&= 4v_2^A v_2^B \int_0^{2\pi} d\phi^A \frac{1}{2} \left[\cos(4\phi^A - 4\psi_2 + 2\Delta\phi) + \cos(2\Delta\phi)\right] \\
&= 4v_2^A v_2^B (\frac{1}{2}) \left(0 + 2\pi \cos(2\Delta\phi)\right) \\
&= 4\pi v_2^A v_2^B \cos(2\Delta\phi) \qquad \text{(A.10)}
\end{aligned}$$

$$\begin{aligned}
&\int_0^{2\pi} 4v_3^A v_3^B \cos 3(\phi^A - \psi_3) \cos 3(\phi^A + \Delta\phi - \psi_3) d\phi^A \\
&= 4\pi v_3^A v_3^B \cos(3\Delta\phi) \qquad \text{(A.11)}
\end{aligned}$$

$$\begin{aligned}
&\int_0^{2\pi} 4v_2^A v_3^B \cos 2(\phi^A - \psi_2) \cos 3(\phi^A + \Delta\phi - \psi_3) d\phi^A \\
&= 4v_2^A v_3^B \int_0^{2\pi} d\phi^A \frac{1}{2} [(\cos(5\phi^A - 2\psi_2 + 3\Delta\phi - 3\psi_3) \\
&\quad + \cos(-\phi^A - 2\psi_2 - 3\Delta\phi + 3\psi_3)] \\
&= 4v_2^A v_3^B (\frac{1}{2})(0 + 0)) \\
&= 0 \qquad \text{(A.12)}
\end{aligned}$$

$$\int_0^{2\pi} 4v_3^A v_2^B \cos 3(\phi^A - \psi_3) \cos 2(\phi^A + \Delta\phi - \psi_2) d\phi^A = 0 \qquad \text{(A.13)}$$

so the final result of Eq. A.9 is

$$\begin{aligned}
&\frac{dN^{AB}}{d\Delta\phi} \\
= &\int_0^{2\pi} d\phi^A \frac{dN^A}{d\phi^A}\frac{dN^B}{d\phi^B} \\
= &\frac{N^A}{2\pi}\frac{N^B}{2\pi}(2\pi + 0 + 0 + 0 + 0 + 4\pi v_2^A v_2^B \cos(2\Delta\phi) + 0 + 0 + 4\pi v_3^A v_3^B \cos(3\Delta\phi)) \\
= &\frac{N^A N^B}{2\pi}(1 + 2v_2^A v_2^B \cos(2\Delta\phi) + 2v_3^A v_3^B \cos(3\Delta\phi)) \qquad \text{(A.14)}
\end{aligned}$$

To check the final pair distribution, we integrate Eq. A.14 over 2π, then we have

$$\begin{aligned}
&\int_0^{2\pi} \frac{dN^{AB}}{d\Delta\phi} d(\Delta\phi) \\
= &\int_0^{2\pi} \frac{N^A N^B}{2\pi}\left(1 + 2v_2^A v_2^B \cos(2\Delta\phi) + 2v_3^A v_3^B \cos(3\Delta\phi)\right) d(\Delta\phi) \\
= &\frac{N^A N^B}{2\pi}(2\pi) \\
= &N^A N^B \qquad \text{(A.15)}
\end{aligned}$$

which is exactly what we expect when we have two complete un-correlate particles A and B.

For a generalized form of Eq. A.14, we have

$$\begin{aligned}
&\frac{dN^{AB}}{d\Delta\phi} \\
= &\frac{N^A N^B}{2\pi}(1 + \Sigma 2 v_n^A v_n^B \cos(n\Delta\phi)) \qquad \text{(A.16)}
\end{aligned}$$

especially in the case we have v_2, v_3, v_4, Eq. A.16 become

$$\begin{aligned}
&\frac{dN^{AB}}{d\Delta\phi} \\
= &\frac{N^A N^B}{2\pi}(1 + 2v_2^A v_2^B \cos(2\Delta\phi) + 2v_3^A v_3^B \cos(3\Delta\phi) + 2v_4^A v_4^B \cos(4\Delta\phi)) \qquad \text{(A.17)}
\end{aligned}$$